

**Dispersive measurement of a metastable phase qubit using a
tunable cavity**

by

Jed Douglas Whittaker

B.S., Brigham Young University, 2003

M.S., Brigham Young University, 2004

A thesis submitted to the
Faculty of the Graduate School of the
University of Colorado in partial fulfillment
of the requirement for the degree of
Doctor of Philosophy
Department of Physics

2012

This thesis entitled:

Dispersive measurement of a metastable phase qubit using a tunable cavity

written by Jed Douglas Whittaker

has been approved by the Department of Physics

Raymond Simmonds

Charles Rogers

Date_____

The final copy of this thesis has been examined by the signatories, and we find that both the content and the form meet acceptable presentation standards of scholarly work in the above mentioned discipline.

Abstract

Whittaker, Jed Douglas (Ph.D., Physics)

Dispersive measurement of a metastable phase qubit using a tunable cavity

Thesis directed by Dr. Raymond W. Simmonds

A metastable phase qubit was measured using a tunable cavity by two methods: a tunneling measurement followed by magnetometry readout by the cavity, and a non destructive dispersive measurement of the qubit by the cavity. The Purcell Effect was observed as a decrease in the energy relaxation time of the qubit in the vicinity of the cavity, and could be manipulated by dynamically tuning the cavity. The observed dispersive shift of the cavity did not match the two-level system model for nonlinear qubits. Instead, a three-level model of the qubit was needed to describe the data, necessitated by the weakly nonlinear nature of the metastable phase qubit. The cavity was also used to directly observe the photons radiated by a tunneling measurement.

for my parents

Acknowledgements

The long road to producing this work has been far from lonely, and I am fortunate to have been supported by what feels like an army of mentors. Not least among these is my advisor, Ray Simmonds, who constantly pointed to the next horizon with vigor and excitement. From Ray I learned about taking complex problems and paring them down to their essential elements in order to plan a clear path forward, about the utility of both rough and precise calculation, and about the importance of clear, concise communication. Ray's desire to have me solve problems and answer questions in my own way and by experimentation has helped me to become a more independent and productive researcher, though he was always excited to get in the lab and explore. I learned much from our many impromptu lab sessions. He always encouraged me to seek knowledge that I lack from those who are experts, and pointed me towards the many experts at NIST who could authoritatively answer my questions.

Through my years at NIST I have had the privilege to work with excellent people in the Simmonds group, who have contributed greatly to this work and who I will thank in a roughly chronological manner. Shane Allman, with whom I have shared an office for over eight years, has always been willing to grind through the details of a problem and help me fill in the cracks in my knowledge and see clearly where I am. Kevin Osborn showed me how to make my first cryogenic resonator measurements, Josh Strong first showed me how to run/get angry at a dilution refrigerator, and Kat Cicak introduced me to cleanroom work and taking binders full of process notes. Adam Sirois

was always interested in talking about the big picture with me, and often helped me gain perspective. Mika Sillanpää designed and fabricated the device used for tomography measurements reported on in Chapter 7, and Jae Park contributed the calculated full tomography plots in Figure 3.10; I appreciate them sharing their work with me. Fabio Altomare taught me the nuts and bolts of qubit manipulation and measurement, and spent many, many hours helping me understand what we were doing as well as helping me think about the architecture of the control and data taking software I wrote. Anche, tante grazie per le cene con la famiglia! Dale Li offered support not just by always being willing to attack a problem at the white board, but by making sure I was laughing now and again. John Teufel gladly offered his strong and valuable knowledge of cryogenic microwave measurements, as well as his talent for cutting through silly ideas with a clear, friendly question. Joe Aumentado and Lafe Spietz designed, built, and helped me use the SQUID amplifier that allowed me to graduate in 2012; otherwise I'd still be averaging traces! Joe's interest in and knowledge of experimental methods has made him a valuable resource for this work. Fabio da Silva shared his cleanroom experience while we were in the trenches, and has been patient and helpful as I have been transferring my measurement knowledge to him.

The outstanding cleanroom staff at NIST-Boulder has been crucial to the success of this work. Gene Hilton never ceased to amaze me with his depth of fabrication knowledge, which he was always willing to share, and possesses a powerful balance of precision and practicality in his work. Paul Dresselhaus seemed to always be there to help wrestle with equipment in a bind, and Jim Beall helped me find creative solutions to fabrication problems. Gene, Paul, Jim, Jay Koch, Norm Bergren, and Maggie Crews together worked tirelessly in the Sisyphean way required to keep the NIST-Boulder cleanroom a productive and convenient place to build experiments. Thanks also to Dan

Schmidt for his willingness to brainstorm about the practical problems of experimental work and show me machining methods that helped me get the job done. Markus Ansmann, as a graduate student at UCSB in the Martinis group, was very helpful as I was bringing up the FPGA-based microwave sequencer (Section 6.2.1) for which he wrote the server software; I am grateful for his time on the phone with me. I am also grateful to my undergraduate and master's thesis advisor, Robert Davis at Brigham Young University, for starting me on this journey by giving me the opportunity to discover experimental physics and helping me publish early.

Thanks to IARPA for funding the final years of my dissertation, and NIST for funding all the rest. Many thanks to the United States taxpayer!

Contents

List of Tables	xiii
List of Figures	xiv
1 Introduction	1
1.1 Quantum computing	1
1.2 Superconducting qubits	3
1.3 Circuit quantum electrodynamics	5
1.4 Overview of dissertation	7
2 The nonlinear quantum electrical resonator	8
2.1 Linear LC resonator	8
2.1.1 Circuit description	8
2.1.2 Quantum description	10
2.2 Nonlinear Josephson resonator	11
2.2.1 Circuit description	11
2.2.1.1 The Josephson junction	12
2.2.1.2 Junction in an LC resonator	15
2.3 Phase qubits	19
2.3.1 Metastable qubit hysteresis and anharmonicity	19

2.3.2	Stable phase qubit (transmon)	21
2.4	Circuit Quantum Electrodynamics	25
2.4.1	Jaynes-Cummings Hamiltonian	25
2.4.2	The dispersive shift and the three level qubit	28
2.4.3	The Purcell effect	31
3	Control and measurement of the metastable phase qubit	34
3.1	Qubit control	34
3.1.1	Potential control	34
3.1.2	Bloch sphere manipulations and tomography	38
3.1.3	T_1 measurement and the π -pulse	42
3.1.4	Ramsey fringe measurement	44
3.1.5	Tomography	44
3.2	Tunneling measurement and flux-state readout	48
3.2.1	Tunneling measurement	49
3.2.2	Ring-down	49
3.2.3	Retrapping	50
3.2.4	Tunneling advantages and disadvantages	52
3.2.5	Standard DC SQUID readout	52
3.2.5.1	Schematic description	52
3.2.5.2	Advantages and disadvantages	54
3.2.6	Tunable cavity readout	56
3.2.6.1	Schematic description	56
3.2.6.2	Advantages of the tunable cavity	60
3.3	Dispersive measurement	61
3.3.1	Jaynes-Cummings and the dispersive shift	61

3.3.2	The AC Stark shift	62
4	Design and modeling of the device	64
4.1	Metastable phase qubit design	64
4.1.1	Junction, inductor, and capacitor design	65
4.1.2	Bias line design	67
4.2	Tunable cavity design	69
4.2.1	Junction, inductor, and capacitor design	69
4.2.2	A single photon in the tunable cavity	72
4.3	Qubit-cavity coupling	74
4.3.1	Tee inductor coupling	74
4.3.2	EM simulations of splitting	75
4.4	Summary of design values	76
5	Sample fabrication	78
5.1	Wiring and insulating layers	78
5.2	Josephson junction	79
5.2.1	Junction technology development	79
5.2.1.1	Via junctions	79
5.2.1.2	Trilayer junctions	81
5.2.2	Shadow evaporated junctions	82
5.3	Packaging	85
5.3.1	Box	85
5.3.2	Wire bonds and spurious resonances	85
6	Experimental setup	88
6.1	Dilution refrigerator	88

6.1.1	Wiring schematic	88
6.2	Signal generation	92
6.2.1	Microwave generation and pulse shaping	92
6.2.2	Flux control, filtering, and bias tees	94
6.3	Signal detection	96
6.3.1	SQUID amp	99
6.3.2	Network Analyzer	101
6.3.3	IQ mixer	101
6.3.4	Data acquisition card	104
6.4	Control program architecture	105
7	Tunneling measurements	108
7.1	Device with DC SQUID	108
7.1.1	Steps	108
7.1.2	Spectroscopy	109
7.1.3	Rabi, T_1 , Ramsey	111
7.1.4	Tomography	112
7.2	Device with tunable cavity	114
7.2.1	Tunable cavity characterization	114
7.2.2	Qubit steps	117
7.2.3	Measure pulse and retrapping	118
7.2.4	Spectroscopy, AC Stark shift	119
7.2.5	Rabi, T_1 , Ramsey	123
7.2.6	The Purcell effect	125
7.2.7	Tunneling photons poisoning the cavity	128
7.2.8	Multiplexing	130

8	Dispersive measurements	132
8.1	Metastable phase qubit and tunable cavity device	132
8.2	Spectroscopy	133
8.3	Rabi oscillations and T_1	135
8.4	State discrimination	138
8.5	Dispersive shift data	141
9	Conclusions and future work	142
9.1	Summary of results	142
9.1.1	Demonstration of full qubit control	142
9.1.2	Tunneling readout with a tunable cavity	142
9.1.3	Tunneling measurement photons in the cavity	143
9.1.4	Multiplexing tunable cavities	144
9.1.5	Dispersive measurement with a tunable cavity	144
9.2	Future work	144
9.2.1	Device design/measurement setup improvements	144
9.2.2	Bifurcation measurement	147
9.2.3	Tunable cavity states and anharmonicity	147
9.2.4	Multiplexing and cavity damping	148
9.3	Final thoughts	149
10	Appendix A	150
10.1	Qubit with DC SQUID process sheet	150
10.2	Qubit with tunable cavity process sheet	168
10.3	Multiplexed tunable cavities process sheet	173
	Bibliography	207

List of Tables

- 4.1 Summary of design values 76
- 6.1 Calibration file format 104
- 9.1 Cold attenuators 146

List of Figures

1.1	Types of superconducting qubits	3
2.1	Driven LC resonator circuit schematic	8
2.2	Quantum harmonic oscillator	11
2.3	Nonlinear resonator circuit	12
2.4	The Josephson junction	13
2.5	Current-biased Josephson junction tilted washboard potential	14
2.6	Potential of the nonlinear LC resonator	17
2.7	Biased nonlinear resonator potential and wavefunctions	18
2.8	Circuit schematics for the metastable and stable phase qubits	19
2.9	Metastable qubit potentials for different β_{LS}	20
2.10	The effect of β_L on f_{01} spectroscopy and on α_r	21
2.11	Stable phase qubit	22
2.12	Stable phase qubit potential	24
2.13	Jaynes-Cummings Hamiltonian energy levels	27
2.14	Dispersive shift	30
2.15	Purcell effect	33
3.1	Metastable phase qubit potentials	35

3.2	Metastable phase qubit steps	37
3.3	Metastable phase qubit S-curve	38
3.4	Mapping the two-level system to the Bloch sphere	39
3.5	Driven Rabi oscillations	40
3.6	T_1 measurement	42
3.7	π -pulse frequency components	43
3.8	Ramsey fringe measurement	45
3.9	Tomography of an arbitrary state	47
3.10	Tomography sweep	48
3.11	Tunneling measurement	49
3.12	Voltage pulse from ring-down	50
3.13	The retrapping process	51
3.14	The anti-retrapping measure pulse	51
3.15	Qubit/DC SQUID circuit schematic	53
3.16	Qubit state readout	53
3.17	DC SQUID flux response	54
3.18	Tunneling readout sequence	55
3.19	Qubit/tunable cavity circuit schematic	56
3.20	Tunable cavity spectroscopy for different β_{LS}	57
3.21	Dip resonator quality factor	58
3.22	Dip resonator and peak resonator	59
3.23	Flux magnetometry using the tunable cavity	60
3.24	Tunable cavity control	60
3.25	Dispersive shift in the cavity	62
3.26	The AC Stark shift	63

4.1	How L_{Qu} and C_{Qu} affect qubit spectroscopy	66
4.2	Bias coil Norton equivalent circuit	67
4.3	Two bias line designs	69
4.4	Tunable cavity with series inductance L_s	70
4.5	Tunable cavity Q and spectroscopy for changing L_s	72
4.6	T_1 decay and cavity rise time	73
4.7	Simplification of tunable cavity circuit	74
4.8	Passive coupling with inductors	75
4.9	EM simulation of cavity splitting	75
5.1	Optical micrographs of the three designs	78
5.2	Via junction fabrication	80
5.3	Via junction scanning electron micrograph	81
5.4	Trilayer junction fabrication	82
5.5	$4 \mu\text{m}^2$ trilayer junction scanning electron micrograph	83
5.6	Shadow evaporation junction fabrication	83
5.7	Shadow evaporated junction micrographs	85
5.8	Chip mounted in box/circuit board combo	86
5.9	Ground plane wire bonds	87
5.10	Transmission measurements with and without crossover bonds	87
6.1	Fridge wiring schematic	89
6.2	FPGA controlled microwave pulse electronics	92
6.3	Microwave pulse electronics	93
6.4	Rising edge of a flux pulse from the Tektronix AWG5014B	94
6.5	Custom bias tee	96

6.6	Simplified signal detection schematic	96
6.7	Resonator measurement imperfections	98
6.8	The SQUID amplifier	99
6.9	SQUID amplifier bias changes and gain compression	100
6.10	SQUID amplifier gain and SNR	101
6.11	IQ mixer nonidealities	103
6.12	Gage data acquisition card background	105
6.13	Control and data taking program architecture	106
7.1	Via-style junction metastable phase qubit steps	109
7.2	Via-style metastable phase qubit spectroscopy	110
7.3	Via-style metastable phase qubit Rabi oscillations and T_1	111
7.4	Via-style metastable phase qubit Ramsey fringes	112
7.5	Full tomography data	113
7.6	Tomography data of $\pi/2$ state decay	113
7.7	Tunable cavity spectroscopy	115
7.8	Tunable cavity power sweep and fit	116
7.9	Tunable cavity IQ plot	116
7.10	Qubit steps taken with a tunable cavity	117
7.11	Square measure pulse and retrapping	118
7.12	Anti-retrapping measure pulse contrast	119
7.13	Qubit spectroscopy taken with a tunable cavity	120
7.14	Qubit spectroscopy with and without cavity	121
7.15	High power spectroscopy	121
7.16	AC Stark shift data	122
7.17	Rabis oscillations in a metastable phase qubit	123

7.18	S-curves and π -pulse duration	124
7.19	T_1 in a metastable phase qubit	125
7.20	Ramsey fringe experiment on a metastable phase qubit	126
7.21	Purcell effect on a qubit from a tunable cavity	127
7.22	Pulse sequence for measuring ring down photons	129
7.23	Ring down photons in cavity	129
7.24	Multiplexed tunable cavities	131
8.1	Tunable cavity spectroscopy, moving qubit	133
8.2	Flux sensitive tunable cavity spectroscopy, moving qubit	134
8.3	Dispersive spectroscopy	134
8.4	Dispersively measured Rabi oscillations	136
8.5	Dispersively measured time domain Rabi oscillations	136
8.6	Dispersively measured T_1	137
8.7	IQ noise and state discrimination	138
8.8	IQ noise standard deviation	139
8.9	State discrimination and detuning	139
8.10	Dispersive shift in the tunable cavity	141
9.1	Tunable cavity anharmonicity	148

1

Introduction

1.1 Quantum computing

The twentieth century has seen the esoteric thought experiments about single quantum particles from the fathers of quantum mechanics, like Bohr and Einstein, become a laboratory reality. For example, the wave-particle dual nature of electrons has been demonstrated using a Young's double slit experiment, recording the measurement locations of individual electrons[1]. Similar experiments have been done with atoms[2][3]. Bohr's extension of Young's double slit experiment included a spring connected to one of the slits in order to gain information about which path the quantum particle took, a thought experiment intended to further explore his ideas about complementarity. This experiment has also been performed in the laboratory using an atom interferometer[4], and even in the case where an analogue to the spring's stiffness was tuned to explore the boundary between the classical and the quantum[5].

Interest in controlling single quantum objects has grown considerably in recent decades as supporting technologies have matured, such as lasers and detectors. The 2012 Nobel Prize in physics, given to Serge Haroche and David J. Wineland for “for ground-breaking experimental methods that enable measuring and manipulation of individual quantum systems.” Both Haroche

and Wineland built and manipulated systems made of a single quantum two-level system coupled to a quantum harmonic oscillator. Besides the fundamental physical and philosophical questions that individual quantum system experiments answer, practical applications are becoming apparent, namely quantum computing. First proposed by Richard Feynman[6] in 1982 as a way to simulate physics that cannot be simulated with classical computers, building a quantum computer has become an important technological priority for governments and scientists around the world.

The fundamental unit of quantum computing is the quantum bit, or “qubit.” Physical implementations of qubits vary, as will be discussed, but there are universal attributes qubits share. In 2000, DiVincenzo outlined his “requirements for the implementation of quantum computation” [7], which have become widely accepted. These requirements are:

1. A scalable physical system with well characterized qubits
2. The ability to initialize the state of the qubits to a simple fiducial state, such as $|000\dots\rangle$
3. Long relevant decoherence times, much longer than the gate operation time
4. A “universal” set of quantum gates
5. A qubit-specific measurement capability

A variety of quantum systems are being explored as possible qubit implementations, with varying levels of success. Molecular proton spins have been controlled with NMR to perform a simple factoring operation[8]. Trapped ions have been used to make rudimentary quantum processors[9] and work is progressing toward scaling to bigger processors[10]. Full quantum control of a single Bose-Einstein condensate qubit made on a chip has been demonstrated[11], as well as entanglement interactions between Bose-Einstein qubits[12] made on more traditional optical lattices. A quantum algorithm has been run using photons and linear optical circuits[13]. Full quantum control over self-assembling semiconducting quantum dots has also been shown[14]. Superconducting qubits,

a subset of which are the subject of this work, have also been used to run rudimentary quantum algorithms[15][16] and to measure non-local quantum correlations[17].

Each of these implementations has strengths and weaknesses, which may be categorized according to the DiVincenzo criteria. One of the strengths of superconducting qubits is related to scalability. Part of the scalability criterion is that one must be able to couple many qubits, building a quantum processor. Because superconducting qubits are made using microfabrication, many may be readily produced on the same wafer simultaneously, and they are easily coupled through microfabricated circuit elements. The circuit nature of superconducting qubits also allows them to be both flexible in design as well as flexible in operation, as they may be made tunable over hundreds of linewidths. Many other implementations, such as those based on atoms and traps or physical cavities, have quite limited tunability, usually on the order of a single linewidth.

1.2 Superconducting qubits

Superconducting qubits may be classified as either charge qubits, flux qubits, or phase qubits, shown in Figure 1.1. These qubits are named not for how the quantum state is encoded, but for

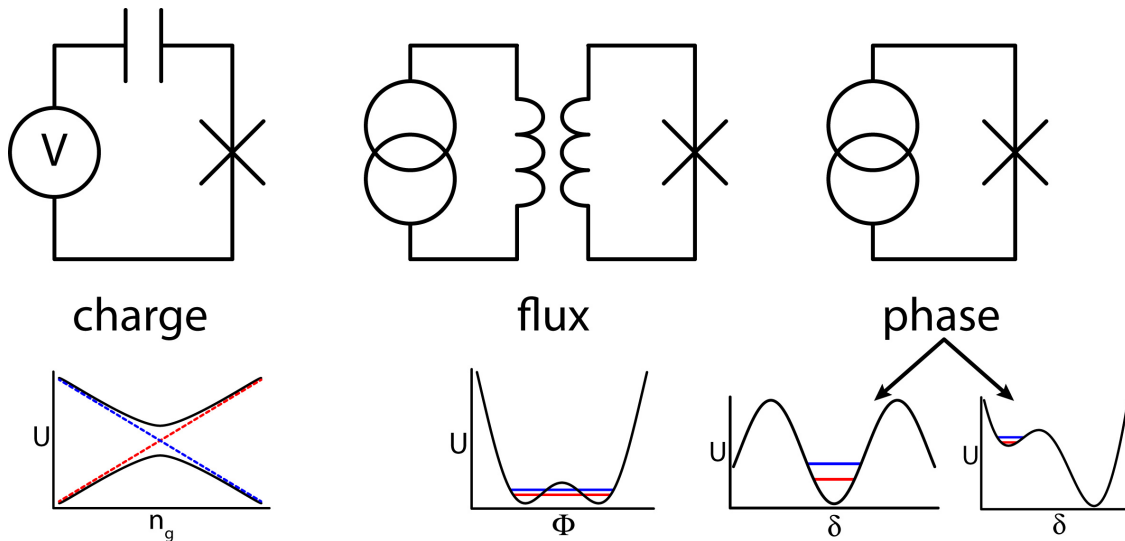


Figure 1.1: Types of superconducting qubits - The three types of superconducting qubits, with their corresponding potential energies plotted below. The name of each qubit type corresponds to its control variable.

what variable is used to control the quantum state. The potential for each qubit is plotted against the name variable for each qubit type in Figure 1.1.

Charge qubits are based on the nonlinearity of the Cooper pair box, made from two parallel Josephson junctions and a gate capacitor, and were first made and measured in the late 1990s[18][19]. While very anharmonic, and therefore very easily addressable qubits, they are very susceptible to charge noise and have therefore fallen out of favor as a qubit implementation.

Flux qubits are made from a single Josephson junction in parallel with an inductor, which was later replaced by a second junction, that allows flux from an external source to be coupled in. This qubit was first made and measured in 2000[20][21]. The potential well of the flux qubit is double valued, with a small barrier between wells. Since there is an inductor instead of a gate capacitor, the flux qubit is insensitive to charge noise. While it may be susceptible to flux noise, it has the advantage of being able to be tuned to a “sweet spot,” where it is flux insensitive.

Phase qubits are, at their core, simply a Josephson junction attached to a current bias, with the bias controlling the quantum mechanical phase across the junction. The current bias is tuned to control the spacing between energy levels, which changes both the transition frequency of the lowest two levels and the relative difference between the lowest two transitions, or relative anharmonicity. While they have a very controllable anharmonicity, there tend to be regions where they are sensitive to flux noise. Phase qubits were first made and measured in 2002[22].

Since their introductions, the charge and phase qubits have evolved some common features. First, most designers have gone towards using a flux bias and an inductance to control their qubits, moving away from noisier direct coupling to source instrumentation. Second, they now both include a shunting capacitor in parallel with the junction. For the charge qubit this was done to make it insensitive to charge noise by making it wholly insensitive to charge; the control variable hence became the quantum mechanical phase across the junction. Since this leads to a periodic cosine-shaped potential where the state inhabits only one well, in this work it will be referred to by the

general name “stable phase qubit,” although in the literature it is referred to as the “transmon.” The current-biased phase qubit adopted a shunting capacitor as needed to keep the qubit frequencies in a convenient range as junction sizes shrank to reduce dielectric losses from spurious two level systems, though the phase variable was still maintained as the control variable. The multi-well nature of this type of phase qubit can lead to metastable well states, so this type of phase qubit will be referred to by the general name “metastable phase qubit,” though in the literature it is referred to simply as the “phase qubit.” Chapter 2 will discuss the similarities and differences between these two types of phase qubits in detail.

Because of the ease of coupling between superconducting qubits, care must be taken when manipulating a measuring a single qubit in the midst of many other qubits so that the others are not disturbed during the procedure. One must be able to individually manipulate and measure a qubit, to the exclusion of all the other qubits. If this ability has not been achieved the system is not fully scalable, even though many qubits have been printed and connected on a wafer. Metastable phase qubits have traditionally been measured using a tunneling measurement, which will be described in detail in Section 3.2, which destroys the qubit state and sends a chirped microwave pulse to anything to which it is coupled. Because of its destructive nature, the tunneling measurement is not a feasible measurement for scaling up to a many qubit quantum processor. A nondestructive measurement is needed, which can be done using a cavity coupled to a qubit. Such a measurement of a metastable phase qubit will be demonstrated in this work, for the first time.

1.3 Circuit quantum electrodynamics

As superconducting qubits have moved from basic characterization experiments to quantum control experiments with an eye toward quantum computation, the field has also emulated cavity quantum electrodynamics (CQED), the study of quantum spins coupled to quantum oscillators, with its own version, circuit quantum electrodynamics (cQED). In cQED, a qubit is coupled to

a cavity, just like the cQED version where an atom is coupled to a cavity. This was first done in the single photon regime in 2005 using a charge qubit placed in a transmission line cavity[23]. This elegant experiment was performed with a projection measurement that did not destroy the qubit, leaving it ready to be used again, starting from its projected state. Later experimenters have used cQED architectures to explore the quantum nature of the linear cavity[24]. However, when considering DiVincenzo's scaling requirement for quantum computation, fixed cavities become impractical as their finite bandwidth limits the number that may be used in a given frequency space, since all coupled qubit/cavity systems suffer loss from the qubit to the environment through the cavity via the Purcell effect. A cavity behaves as a narrow-band filter between the qubit and the environment, and will enhance loss from the already short-lived superconducting qubit to the environment anytime the qubit and cavity are close to resonance. This hole in the qubit's frequency range limits the available bandwidth and makes scaling up such systems difficult.

In this work, a tunable cavity is used to measure and read out the state of a metastable phase qubit in a nondestructive, projective measurement. This brings the advantages of cQED-type measurement to metastable phase qubits for the first time. The tunable cavity is also a solution to the limited bandwidth problem due to the Purcell effect losses near fixed cavities. One could tune the cavity into resonance with a qubit or qubits only when needed for measurement; it may be detuned out of the way at other times to free up bandwidth for other operations, limiting loss via the Purcell effect. In this work we perform rudimentary qubit operations with a metastable phase qubit, but for the first time use a tunable cavity system for measurement. Using a cavity, tunable or not, to measure a metastable phase qubit is an improvement because it is nondestructive to the measured qubit and to any other coupled quantum systems. The tunable cavity is also an improvement over fixed cavity cQED as the cavity may be dynamically moved in frequency space to avoid loss. These two features, cavity measurement and tunability, make the device presented in this work both new and useful.

1.4 Overview of dissertation

This work is organized as follows. Chapter 2 provides the theoretical background for phase qubit physics by considering the addition of a Josephson junction to an electrical quantum harmonic oscillator. Circuit quantum electrodynamics is introduced and discussed in the context of a weakly anharmonic qubit, deriving the dispersive shift from the Jaynes-Cummings Hamiltonian. The Purcell effect is also derived and discussed. Chapter 3 describes the control and measurement of the metastable phase qubit, for both tunneling measurement and dispersive measurement. Chapter 4 covers the design and modeling of the device. Chapter 5 describes the fabrication of the device, including packaging. Chapter 6 is an overview of the experimental setup, including wiring setup, instrument function, and system characterization. Chapter 7 presents data taken using tunneling measurements, including tomographic control and measurement, observation of the Purcell effect, and a measurement of photons generated by a tunneling measurement entering the cavity. Chapter 8 presents data from dispersive measurements, including state discrimination data. Chapter 9 is a summary of results and suggestions for future work.

2

The nonlinear quantum electrical resonator

2.1 Linear LC resonator

2.1.1 Circuit description

The electrical simple harmonic oscillator is a very natural place to start describing superconducting qubits, as it shares many of their features and components. Figure 2.1 is the simplest form of the parallel inductor-capacitor (LC) resonator, as it doesn't have any resistive loss components.

Using Kirchhoff's Laws, one can write down the differential equation for this circuit,

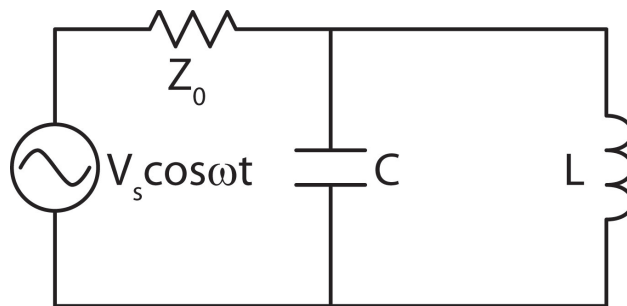


Figure 2.1: Driven LC resonator circuit schematic - Schematic for a driven linear LC resonator without internal loss.

$$\ddot{I}_L + \frac{1}{Z_0 C} \dot{I}_L + \frac{1}{LC} I_L = \frac{V_s \cos(\omega t)}{Z_0 LC}. \quad (2.1)$$

This is of the same form as the standard driven simple harmonic oscillator,

$$\ddot{x} + 2\beta\dot{x} + \omega_0^2 x = A \cos(\omega t). \quad (2.2)$$

The similarity of these two equations allows us to surmise that the resonant frequency of the system is $\omega_0^2 = 1/LC$, and that the damping is provided through the capacitor by source impedance as $2\beta = 1/CZ_0$. Note that this source of damping needs to be minimal for achieving high quality factor LC resonators, even in the present case where the inductive and capacitive portions of the circuit are assumed to be lossless. If superconductors are used for wiring, no resistive loss need be included in the circuit. But in real superconducting LC circuits there is always loss from dielectrics in and near the capacitor, the magnitude of which is dependent both on the material properties[25] and the capacitor geometry[26]. Loss is usually represented in the circuit schematic as a resistor in parallel with the capacitor. Minimizing loss during circuit design will be discussed in Chapter 4.

The total energy of a non-driven parallel LC resonator is just the sum of the energy in the inductor and the energy in the capacitor. Doing the change of variables $I_L = \Phi/L$, $V_C = Q/C$ on this sum transforms it to a proper Hamiltonian, as Φ and Q are canonically conjugate variables,

$$T + U = \frac{1}{2} L I_L^2 + \frac{1}{2} C V_C^2 \rightarrow H = \frac{\Phi^2}{2L} + \frac{Q^2}{2C} \quad (2.3)$$

This Hamiltonian is completely classical, corresponding to circuits operated in the classical regime ($\hbar\omega_0 \ll k_B T$). However, if an LC resonator is operated cold enough, a quantum mechanical description is necessary.

2.1.2 Quantum description

In order to explore the quantum properties of the LC resonator[27], rewrite the Hamiltonian using quantum mechanical operators as

$$\hat{H} = \frac{\hat{\Phi}^2}{2L} + \frac{\hat{Q}^2}{2C}. \quad (2.4)$$

This change of variables gives us an expression that can be directly rewritten as quantum mechanical operators, with flux analogous to position and charge analogous to momentum. These operators obey the commutation relation

$$[\hat{Q}, \hat{\Phi}] = i\hbar. \quad (2.5)$$

As a quantum harmonic oscillator, the Hamiltonian may also be written in the more general way[28]

$$\hat{H} = \hbar\omega_0 \left(a^\dagger a + 1/2 \right) \quad (2.6)$$

with the annihilation and creation operators

$$a = \sqrt{\frac{C\omega_0}{2\hbar}}\Phi + i\sqrt{\frac{1}{2\hbar C\omega_0}}Q, \quad a^\dagger = \sqrt{\frac{C\omega_0}{2\hbar}}\Phi - i\sqrt{\frac{1}{2\hbar C\omega_0}}Q, \quad (2.7)$$

where $\omega_0 = 1/\sqrt{LC}$. This simple harmonic oscillator Hamiltonian can be solved exactly for the wavefunctions[28]

$$\psi_n(\Phi) = \left(\frac{C\omega_0}{\pi\hbar 2^{2n}(n!)^2} \right)^{1/4} e^{-\frac{C\omega_0\Phi^2}{2\hbar}} H_n \left[\sqrt{\frac{C\omega_0}{\hbar}}\Phi \right], \quad (2.8)$$

where H_n is the n^{th} Hermite polynomial. The first five states are plotted in Figure 2.2.

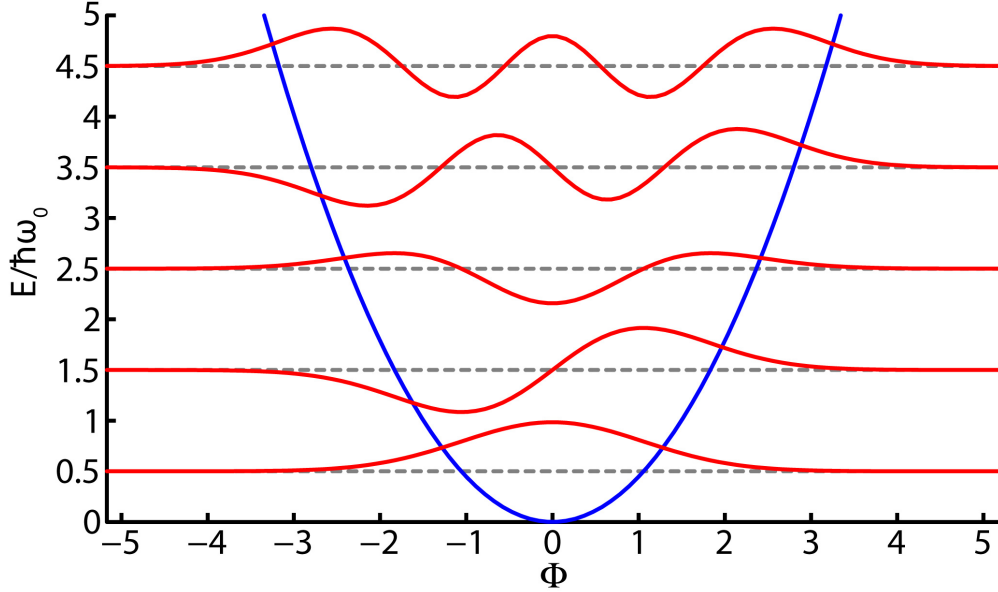


Figure 2.2: Quantum harmonic oscillator - Quantum harmonic oscillator potential well and first 5 energy levels (dotted grey), as well as their corresponding wavefunctions (red).

2.2 Nonlinear Josephson resonator

2.2.1 Circuit description

While the LC resonator has discrete quantum levels which may be observed at sufficiently low temperature, those levels are evenly spaced in energy and therefore not easily individually addressable. Thus, the quantum LC resonator does not meet the DiVincenzo criterion that requires well-defined qubits [7] for performing quantum computations. But by deforming the potential using an appropriate nonlinear element, the resulting oscillator can be made to have individually addressable levels and become a quantum computation element candidate. The nonlinear, and sometimes described as dissipationless, element added to superconducting circuits is the Josephson junction, shown in a resonator circuit in Figure 2.3a as an X. The Josephson junction will be described in more detail below. The geometric inductance L_g allows the junction's critical current to be controlled by an externally applied flux, tuning the circuit's resonant frequency. The ratio between L_g and the zero-bias effective junction inductance L_{J0} also sets the hysteresis of the qubit potential wells, as we shall see below in Section 2.3.1. The shunting capacitor C_s allows the resonant

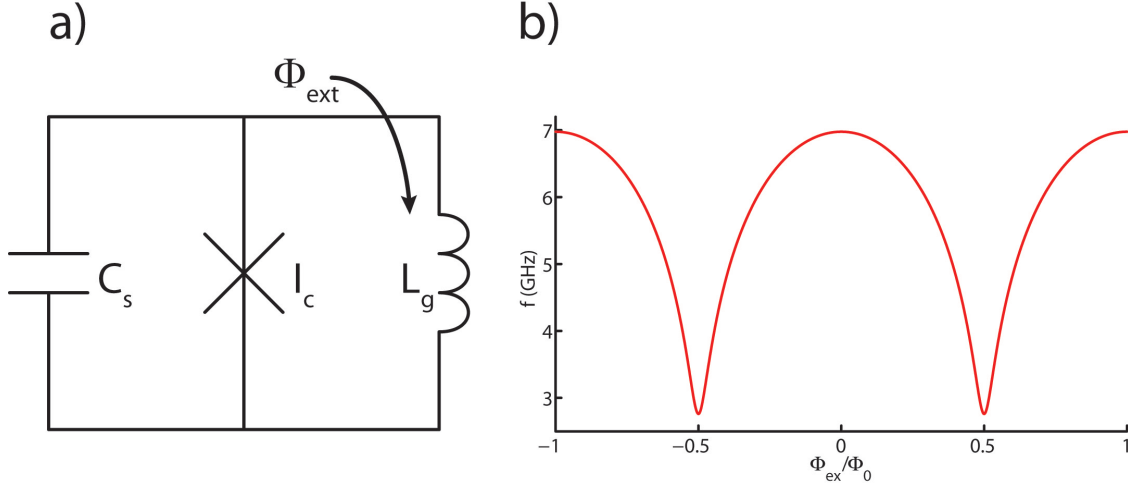


Figure 2.3: Nonlinear resonator circuit - a) Schematic for a nonlinear resonator based on a Josephson junction. The geometric inductance L_g allows flux (Φ_{ex}) to be coupled into the loop in order to tune the junction's critical current I_c . The shunting capacitor C_s allows the resonant frequency of the circuit to be chosen by the designer. b) The Josephson junction's effective inductance L_J changes with applied external flux Φ_{ex} , changing its resonant frequency in a periodic way.

frequency of the circuit to be altered to meet design parameters. If a particular materials system within the shunting capacitor has a lower loss than the Josephson junction being used then the capacitor's participation ratio may be increased (by increasing the value of the capacitance) to increase the resonator's lifetime. A large inductance placed in series with the Josephson junction may also be used to lower the junction's participation ratio and increase the resonator's lifetime. Design choices to minimize loss are discussed in detail in Chapter 4.

2.2.1.1 The Josephson junction

The aluminum/aluminum oxide/aluminum ($Al/AlO_x/Al$) insulating barrier, shown in Figure 2.4a, has become commonly used as a Josephson junction in superconducting quantum computing applications because of its low loss and ease of fabrication. In a superconducting Josephson junction the insulating barrier is thin enough to allow the overlap of electron pair wave functions, such that a pair may move across the barrier without any applied voltage. Electron pairs in

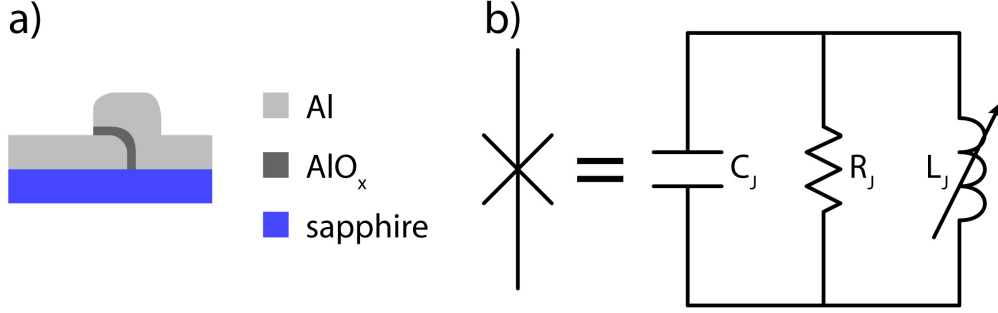


Figure 2.4: The Josephson junction - a) The $Al/AlO_x/Al$ Josephson junction. b) The Josephson junction can be modeled by the parallel combination of a variable inductor, a capacitor, and a resistor. The junction capacitance is typically $50 \text{ ff}/\mu\text{m}^2$.

Josephson junctions behave according to the Josephson current and voltage relations

$$I = I_c \sin \delta, \quad \frac{\partial \delta}{\partial t} = \frac{2e}{\hbar} V, \quad (2.9)$$

where δ is the quantum mechanical phase difference of the electron pair wavefunction across the junction and I_c is the critical current of the junction. I_c is the current at which a current-biased junction switches from a zero voltage state to a voltage state. A more detailed description and derivations of the Josephson relations may be found in [29]. Josephson junctions may be described using a circuit model, as a variable inductance in parallel with their intrinsic capacitance and loss, the loss being modeled as a resistor as in Figure 2.4b.

While tunnel barriers have a supercurrent branch, where the drive current is less than I_c , that is lossless at DC, there seems to always be loss at RF frequencies due to defects in the tunnel barrier or nearby dielectrics[25][30]. Research on this loss has suggested that minimizing dielectric material around the device as well as reducing the area of the junction is desirable for long-lived Josephson resonators. It is clear that for large area junctions ($\gtrsim 5 \mu\text{m}^2$) on sapphire the loss is dominated by two-level systems (TLSs) present in the junction dielectric, as they tend to manifest themselves as spectroscopic splittings whose coupling and loss may be readily quantified for a given device. For these large junctions, the density of spectroscopically visible TLSs decreases as the area

of the junction decreases, until it becomes rare to see any TLSs over the whole spectroscopy range when the junction area $\lesssim 1 \mu\text{m}^2$. Due to the time-intensive nature of spectroscopy scans, TLSs coupled weaker than a few tens of MHz are often not seen with typical scan resolutions, although they may still be present. These weakly coupled TLSs may be detected using a T_1 vacuum Rabi measurement, described in [31].

A single Josephson junction, without a shunting capacitor or geometric inductance, will make a tilted-washboard potential when DC current biased, as shown in Figure 2.5, according to $U(\delta) = (I_c\Phi_0/2\pi)(\cos\delta - (I/I_c)\delta)$, where δ is the gauge-invariant phase across the junction, and I_c is the junction critical current[32][33]. The slope of the tilt increases with increasing bias I , and can be thought of a ball on a tilted washboard in a viscous fluid[29]. The critical current I_c is analogous to the point when the tilt is great enough for the ball to start rolling down the washboard.

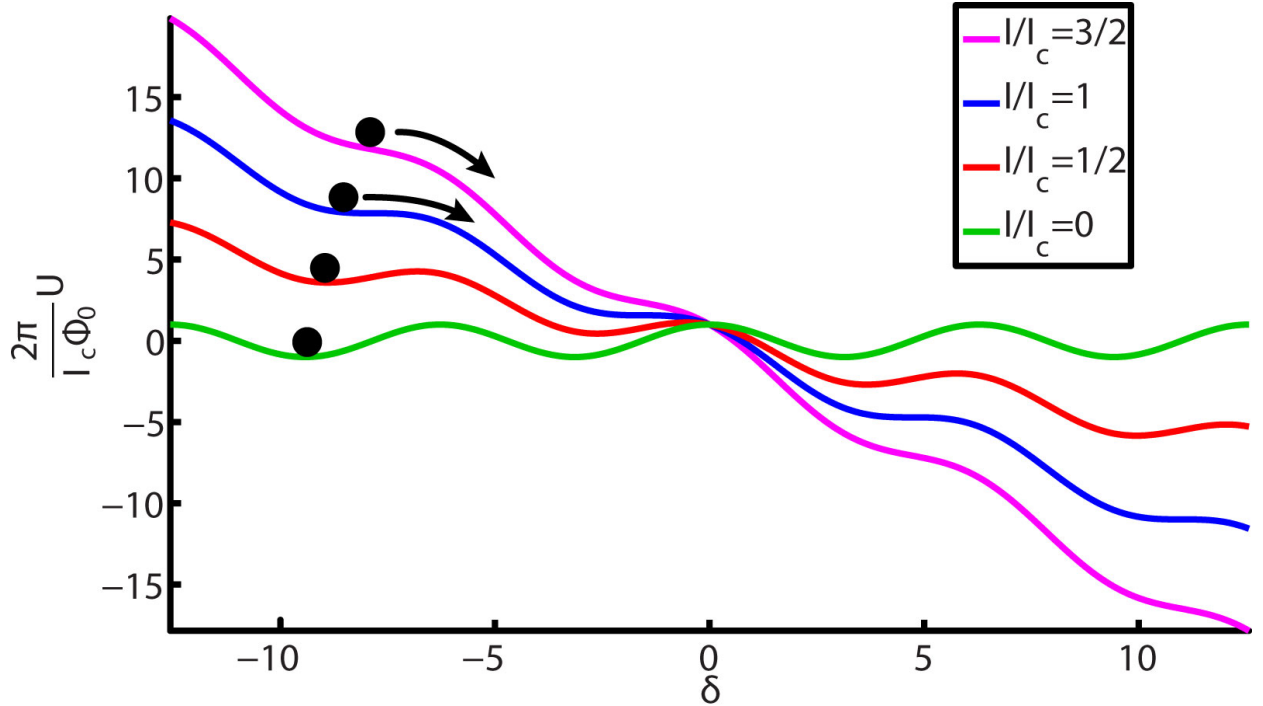


Figure 2.5: Current-biased Josephson junction tilted washboard potential - When a Josephson junction is DC current-biased the cosine potential ($U(\delta) = (I_c\Phi_0/2\pi)(\cos\delta - (I/I_c)\delta)$) is tilted in proportion to the applied current. When $I \geq I_c$, the particle tunnels, rolling down the washboard potential.

2.2.1.2 Junction in an LC resonator

Placing a junction in parallel with an LC resonator makes it an anharmonic, tunable resonator by combining the properties of both systems. The effective inductance of the Josephson junction is given by[29]

$$L_J = \frac{\Phi_0}{2\pi I_c \cos \delta}, \quad (2.10)$$

and classically contributes to the total circuit inductance in parallel to the LC elements to give a plasma frequency

$$\omega_p = \frac{1}{\sqrt{\frac{L_J L_g}{L_J + L_g} C_s}}. \quad (2.11)$$

Using the flux quantization condition $\delta = 2n\pi - 2\pi\Phi_{ex}/\Phi_0$ and the Josephson current equation $I = I_c \sin \delta$ one can write down the transcendental equation to find the phase δ at a given applied flux Φ_{ex}

$$\delta = 2\pi \frac{\Phi_{ex}}{\Phi_0} - \beta_L \sin \delta, \quad (2.12)$$

where $\beta_L = 2\pi L_g I_c / \Phi_0 = L_g / L_{J0} = E_{J0} / E_L$. Solving this equation gives a phase δ_0 that can be used in Equation 2.10 to get L_J and therefore a plasma frequency, giving the spectroscopy plotted in Figure 2.3b.

In order to further understand this circuit, we find the potential landscape of this circuit. We start by writing down the current expressions for each element, noting that Kirchhoff's Voltage Law says that $V = V_L = V_C = V_J$,

$$I_L = -\frac{1}{L_g} \int V dt, \quad I_C = C_s \dot{V}, \quad I_J = I_c \sin \delta. \quad (2.13)$$

We can use this in writing down Kirchhoff's Current Law to get

$$I_L = I_J + I_C \rightarrow C_s \dot{V} + I_c \sin \delta + \frac{1}{L_g} \int V dt = 0 \quad (2.14)$$

The Josephson Voltage relation, $V = (\Phi_0/2\pi) \dot{\delta}$, allows us to write this in terms of the junction phase δ

$$C_s \frac{\Phi_0}{2\pi} \ddot{\delta} + I_c \sin \delta + \frac{\Phi_0}{2\pi L_g} \int \dot{\delta} dt = 0 \quad (2.15)$$

Multiplying by $\Phi_0/2\pi$ and doing the integral gives a constant of integration term $(2\pi/\Phi_0)I_{DC} = (2\pi/\Phi_0)\Phi_{ex}/L_g$ which can be used to describe the current source as an external DC flux. Writing this out gives

$$C_s \left(\frac{\Phi_0}{2\pi} \right)^2 \ddot{\delta} + \frac{\Phi_0}{2\pi} I_c \sin \delta + \left(\frac{\Phi_0}{2\pi} \right)^2 \frac{1}{L_g} \delta + \left(\frac{\Phi_0}{2\pi} \right)^2 \frac{2\pi \Phi_{ex}}{L_g \Phi_0} = 0. \quad (2.16)$$

This equation is of the form $m\ddot{x} + dU(x) = 0$, the equation of motion for a 1-D particle in a potential, with $m \leftrightarrow C_s (\Phi_0/2\pi)^2$ and $x \leftrightarrow \delta$. This analogy shows us that the potential of our circuit is

$$U = \int dU d\delta = \int \left(\frac{\Phi_0}{2\pi} I_c \sin \delta + \left(\frac{\Phi_0}{2\pi} \right)^2 \frac{1}{L_g} \delta + \left(\frac{\Phi_0}{2\pi} \right)^2 \frac{2\pi \Phi_{ex}}{L_g \Phi_0} \right) d\delta \quad (2.17)$$

$$U = -\frac{\Phi_0}{2\pi} I_c \cos \delta + \left(\frac{\Phi_0}{2\pi} \right)^2 \frac{1}{2L_g} \delta^2 + \left(\frac{\Phi_0}{2\pi} \right)^2 \frac{2\pi \Phi_{ex}}{L_g \Phi_0} \delta, \quad (2.18)$$

with the resulting constant of integration dropped because it is just an energy offset. We can clean up this equation using the Josephson energy $E_{J0} = (\Phi_0/2\pi)I_c$ and the geometric inductive energy $E_L = (\Phi_0/2\pi)^2 / 2L_g$ to write

$$U = \underbrace{-E_{J0} \cos \delta}_{U_{JJ}} + \underbrace{E_L \delta^2}_{U_{LC}} + \underbrace{E_L 4\pi \frac{\Phi_{ex}}{\Phi_0} \delta}_{U_{\Phi_{ex}}}. \quad (2.19)$$

In this form the three parts of the potential are clear: the cosine junction contribution U_{JJ} , the parabolic LC resonator contribution U_{LC} , and a linear slope piece from the external flux bias $U_{\Phi_{ex}}$. They are shown in Figure 2.6 both a) separated and b) together as the folded washboard potential of the nonlinear oscillator.

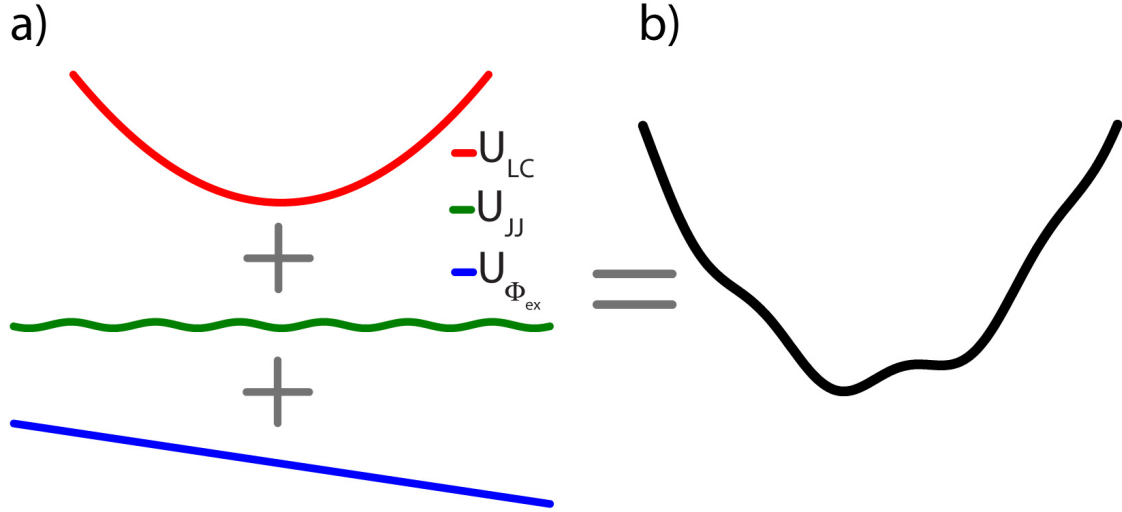


Figure 2.6: Potential of the nonlinear LC resonator - a) The separate pieces of the potential equation sum to give b) the nonlinear resonator's folded washboard potential.

The time-independent Schrödinger equation,

$$\hat{H}|\psi_n\rangle = E_n|\psi_n\rangle, \quad (2.20)$$

allows us to solve for the steady-state quantum states in an arbitrary potential. $|\psi_n\rangle$ and E_n are the eigenfunctions and eigenenergies of the system. Since the Hamiltonian for a particle in a one dimensional potential, analogous to our anharmonic LC oscillator, is

$$\hat{H} = -\frac{\hbar^2}{2m} \frac{d^2}{dX^2} + U(X), \quad (2.21)$$

we may write the qubit Hamiltonian as

$$\hat{H} = -\frac{\hbar^2}{2C_s} \left(\frac{2\pi}{\Phi_0} \right)^2 \frac{d^2}{d\delta^2} + U(\delta). \quad (2.22)$$

Putting this in the time-independent Schrödinger equation gives

$$E_n |\psi_n(\delta)\rangle = -E_C \frac{d^2}{d\delta^2} |\psi_n(\delta)\rangle + \left(-E_{J0} \cos \delta + E_L \delta^2 + E_L 4\pi \frac{\Phi_{ex}}{\Phi_0} \delta \right) |\psi_n(\delta)\rangle, \quad (2.23)$$

where $E_C = e^2/2C_s$. This equation is most easily solved numerically, using the techniques described in [34] and [35]. The resulting eigenenergies and eigenstates are plotted with the potential for the circuit parameters $\Phi_{ex}/\Phi_0 = 0.65$, $\beta_L = 3.0$, $E_{J0}/E_C = 3600$, and $E_L/E_C = 600$ in Figure 2.7. The relative anharmonicity

$$\alpha_r = (E_{12} - E_{01})/E_{01} \quad (2.24)$$

is, in a sense, a measurement of the addressability of qubit states; the greater the relative anharmonicity, the more distinct the energy levels. For the wells in Figure 2.7, $\alpha_{01-shallow} = 3.6\%$ and $\alpha_{01-deep} = 0.6\%$, so the lower two states in the shallow well are better separated than the lower two states in the deep well. This is equivalent to saying that the shallow well is more anharmonic than the deep well.

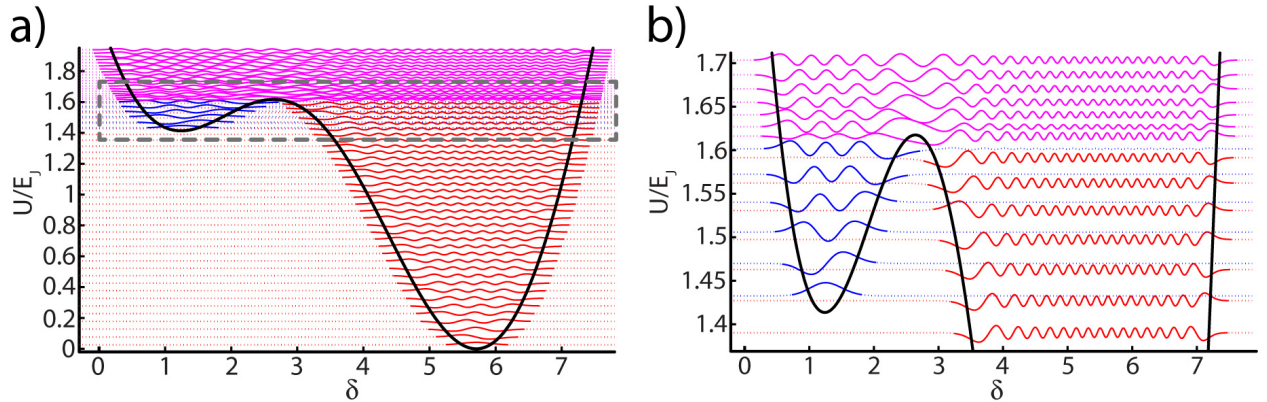


Figure 2.7: Biased nonlinear resonator potential and wavefunctions - a) The first 80 wavefunctions, found by numerically solving the time-independent Schrödinger equation. b) Detail, showing the shallow well states. The wavefunctions are plotted with partial dotted lines and different colors for clarity. Any potential energy offset has been removed.

2.3 Phase qubits

The nonlinear resonator is the generalization of the phase qubit, which exists in the lower two states of a single well. There is a great deal of flexibility in design of phase qubits because the parameters of all three circuit elements may be tuned for operation in different regimes. Two common regimes are seen in the metastable and stable phase qubit designs, shown in Figure 2.8. The metastable qubit has a strong quadratic term from its geometric inductance that allows it to have multiple wells available to it under the right flux bias conditions, giving rise to its “metastable” nature. However, the stable phase qubit has negligible geometric inductance and is therefore a simple cosine potential; the qubit does not have other unique wells available to it, giving it a more “stable” nature.

2.3.1 Metastable qubit hysteresis and anharmonicity

The metastable phase qubit has the same Hamiltonian as the nonlinear Josephson resonator described above, but has the constraint that $\beta_L > 1$, where there exist bias conditions with more than one well. As β_L is increased, the maximum number of available wells increases in a stepwise manner, though the number of available wells for a given β_L depends on the applied flux. The effect of β_L is seen in Figure 2.9. The circuit is hysteretic any time there are two or more wells.

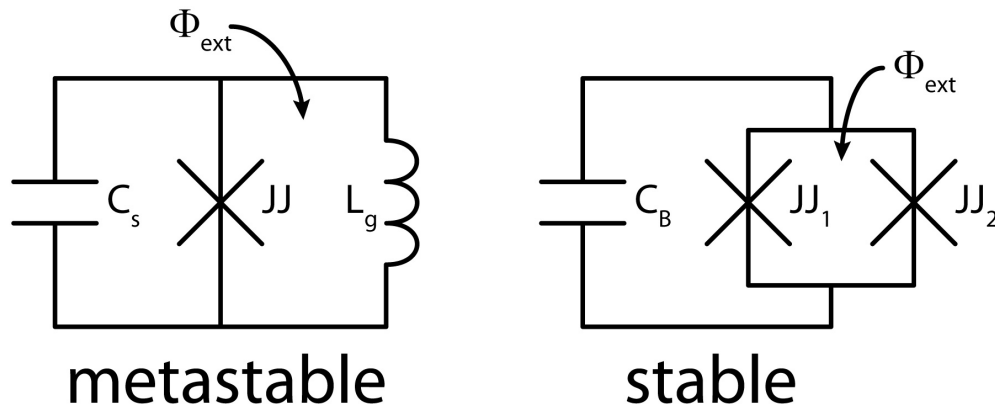


Figure 2.8: Circuit schematics for the metastable and stable phase qubits - The stable phase qubit is a metastable phase qubit without a large geometric inductance L_g .

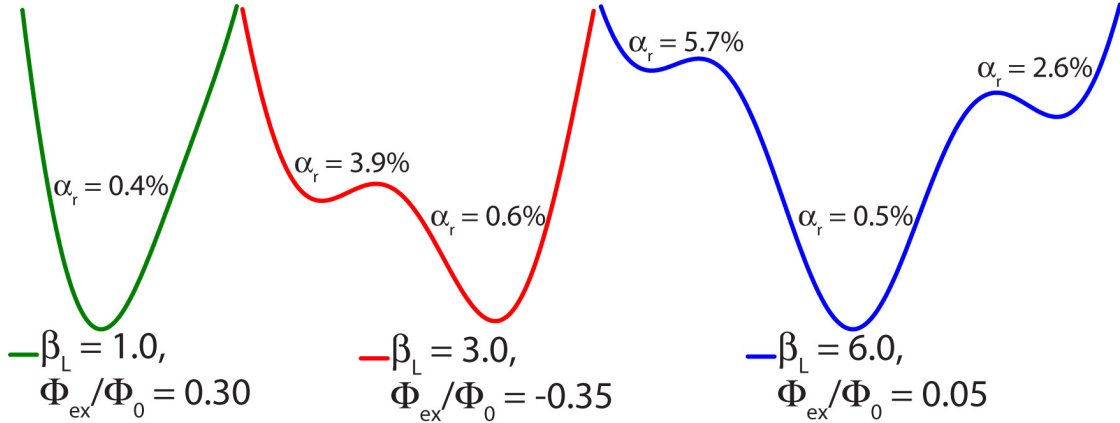


Figure 2.9: Metastable qubit potentials for different β_L s - Changing β_L changes the maximum number of available wells. The relative anharmonicity α_r of each well is also reported, demonstrating that the deep wells tend to be more harmonic than the shallow wells. Applied fluxes were chosen for each plot to most clearly show the maximum number of available wells for each β_L . The different β_L values were obtained by holding the junction critical current fixed and changing the geometric inductance.

Note that for the case where $\beta_L = 6$, a particle leaving the left well may go to either the middle well or the right well.

The relative anharmonicity α_r of each well in Figure 2.9 shows that the deep wells have weaker anharmonicity than the shallow wells. This suggests that the shallow wells are more desirable places for the qubit to be defined since high anharmonicity corresponds to the $0 \rightarrow 1$ transition being very separated from the other transitions in frequency space. A well separated transition is more easily addressable, which is advantageous for quantum computing applications[7].

One way to visualize the β_L - α_r relationship is to plot the f_{01} spectroscopy for different values of β_L while holding E_{J0} and E_C constant, as in Figure 2.10a. It is clear that the spectroscopy curve steepness increases with decreasing β_L , which had the effect of increasing the qubit's susceptibility to flux noise. The change in α_r with flux is also steeper. The spectroscopy plots in Figure 2.10a have dots on each plot indicating at what flux the qubit will tunnel out of the $|0\rangle$ state 0.1% of the time after sitting at the operate flux for $10 \mu\text{s}$. Although the plots in Figure 2.10b suggest large anharmonicities, the relative anharmonicity of the metastable phase qubit is rarely seen to be $\gtrsim 7\%$, since the $|1\rangle$ state tunnels long before the $|0\rangle$ state begins to tunnel.

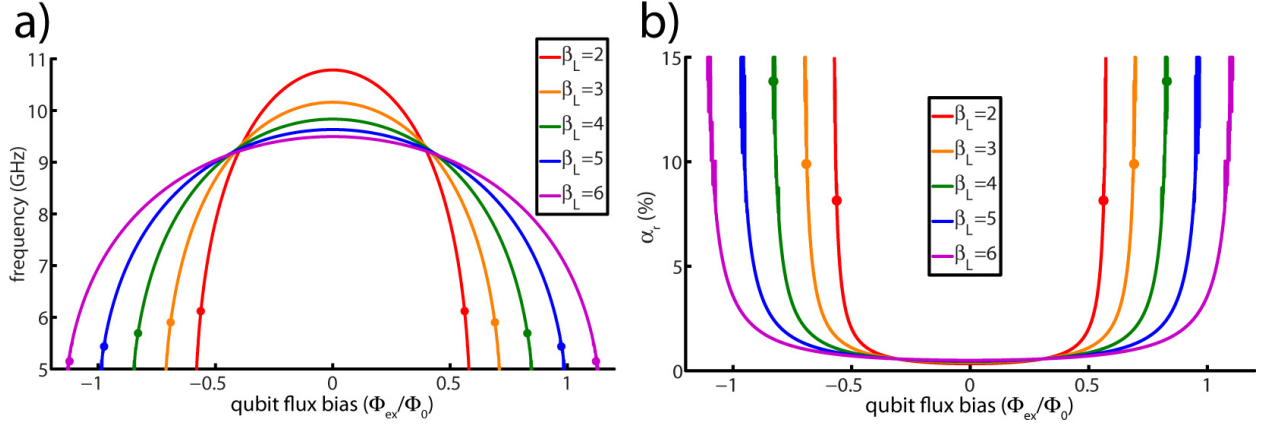


Figure 2.10: The effect of β_L on f_{01} spectroscopy and on α_r - a) Numerically solving the Schrödinger equation for the f_{01} transition at different values of β_L shows that the slope of the spectroscopy increases as β_L decreases. This leads to an increase in sensitivity to external flux noise. The dots on each plot are where the qubit will tunnel out of the $|0\rangle$ state 0.1% of the time after sitting at the operate flux for 10 μs . b) Also solving for the f_{12} transition gives the dependence of the relative anharmonicity α_r , whose steepness also increases as β_L decreases. The same 0.1% points are marked, but only for the low β_L plots since at this point in the higher plots the $|1\rangle$ state is already gone.

2.3.2 Stable phase qubit (transmon)

The stable qubit, also known as the transmon, essentially eliminates the large geometric inductance L_g in favor of a second Josephson junction, which mostly just suppresses the δ^2 and δ terms from Equation 2.19 (except for stray inductance from the wiring connecting the junctions, which is small and usually ignored). There is also a gate capacitor C_g , whose name was inherited from its charge qubit ancestry and is now simply the capacitance to the ground plane. These two features combine to give the Hamiltonian

$$\hat{H} = 4E_C (\hat{n} - n_g)^2 - E_J \cos \hat{\varphi}, \quad (2.25)$$

where \hat{n} is the Cooper pair number operator, n_g is the charge on the gate capacitor, $\hat{\varphi}$ is the operator for the gauge-invariant phase across the junctions, and $E_C = e^2/2(C_J + C_B + C_g)$, where C_B is the shunting capacitor[36]. The E_J term is a combination of the two junctions, including

asymmetries and the effect of the applied flux Φ_{ex} :

$$E_J = (E_{J1} + E_{J2}) \cos\left(\pi \frac{\Phi_{ex}}{\Phi_0}\right) \sqrt{1 + d^2 \tan^2\left(\pi \frac{\Phi_{ex}}{\Phi_0}\right)}, \quad (2.26)$$

where $d = (E_{J2} - E_{J1}) / (E_{J1} + E_{J2})$ accounts for asymmetry between the junctions.

Because charge qubits had coherence times limited by charge noise, the stable phase qubit was developed by increasing the ratio E_J/E_C to be much $\gg 1$, making them charge insensitive and allowing us to ignore the n_g term in the Hamiltonian[37]. The charge insensitivity has the gate capacitor C_g behaving simply as an external coupling capacitor, and could be neglected in the Hamiltonian if desired. The $E_J/E_C \gg 1$ design choice greatly increased energy relaxation and decoherence times, though at the cost of a bit less anharmonicity. A schematic drawing of the circuit, taken from [37], is shown in Figure 2.11a.

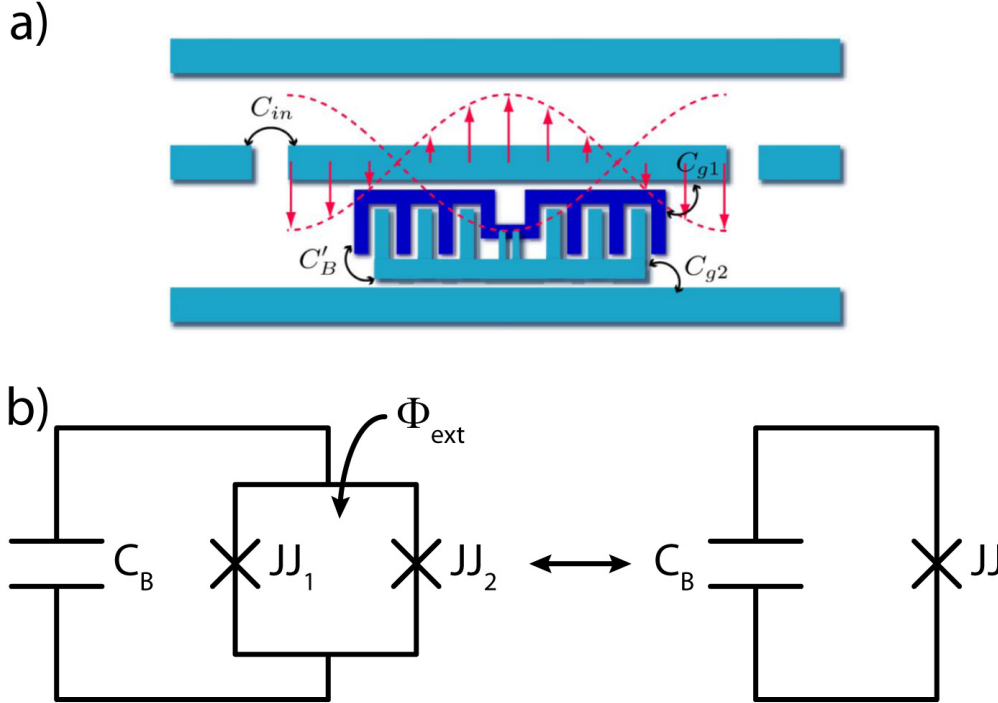


Figure 2.11: Stable phase qubit - a) Schematic drawing of the stable phase qubit, taken from [37]. b) The traditional circuit diagram for the stable phase qubit. Combining the split junctions as in Equation 2.26 allows us to redraw the circuit in a simpler form.

While the stable phase qubit is often discussed including the gate capacitor, it can be ignored as being simply an external coupling capacitor. The split junctions can be thought of as one junction, as in Equation 2.26, simplifying the circuit greatly. The circuit is redrawn in Figure 2.11b, which is just an LC resonator with the inductor replaced by a Josephson junction. Thus, exchanging the inductive term of the LC resonator Hamiltonian (Equation 2.4) with the Josephson energy $-E_J \cos \delta$ gives us the new Hamiltonian

$$H = E_C \frac{d^2}{d\delta^2} - E_J \cos \delta. \quad (2.27)$$

Note that the amplitude of the cosine in the junction term is modulated by E_J , which depends on the external flux Φ_{ex} according to Equation 2.26. This is essentially the nonlinear Josephson resonator Hamiltonian (Equation 2.22), without the δ and δ^2 terms, which is equivalent to setting the geometric inductance to infinity. While the stable phase qubit does have some geometric inductance because the loop containing the two junctions has dimension, the loop is small enough that the δ and δ^2 terms are negligible.

While this Hamiltonian may be solved analytically using the Mathieu functions[37], the result is cumbersome to use numerically. Approximating the cosine potential using a Taylor expansion, followed by time-independent perturbation theory on the Schrödinger equation, gives a more tractable solution. The expanded cosine term

$$E_J \cos \delta \simeq E_J \left(1 - \frac{\delta^2}{2} + \frac{\delta^4}{24} \right) \quad (2.28)$$

gives a δ^2 term that may be used as part of the unperturbed Hamiltonian since this allows a

standard harmonic oscillator equation

$$H \simeq \underbrace{E_C \frac{d^2}{d\delta^2} + E_J \frac{\delta^2}{2}}_{H_0} - \underbrace{E_J \left(1 + \frac{\delta^4}{24}\right)}_{H'}. \quad (2.29)$$

The known harmonic oscillator Hamiltonian uses the ladder operators b and b^\dagger , which can be used to write the approximated Hamiltonian

$$H \simeq \underbrace{\sqrt{8E_C E_J} \left(b^\dagger b + \frac{1}{2}\right)}_{H_0} - \underbrace{E_J - \frac{E_C}{12} (b + b^\dagger)^4}_{H'}. \quad (2.30)$$

The first order corrections to this Hamiltonian are

$$E_j^{(1)} = -\frac{E_C}{12} \langle j | (b + b^\dagger)^4 | j \rangle = -\frac{E_C}{12} (6j^2 + 6j + 3) \quad (2.31)$$

and

$$|j\rangle^{(1)} = -\frac{E_C}{12} \sum_{i \neq j} \frac{\langle i | (b + b^\dagger)^4 | j \rangle}{E_i - E_j} |i\rangle. \quad (2.32)$$

The first six approximated energy levels are plotted in Figure 2.12.

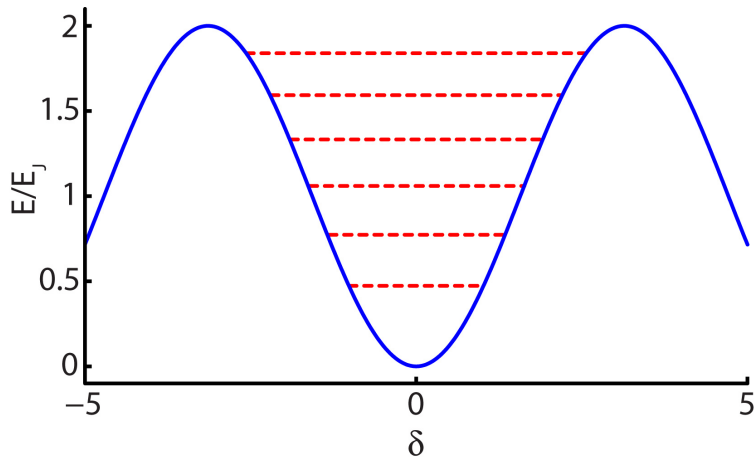


Figure 2.12: Stable phase qubit potential - First order corrected energies of the stable phase qubit's potential, found using time-independent perturbation theory on the expanded cosine term. Energy offsets have been removed.

2.4 Circuit Quantum Electrodynamics

Circuit quantum electrodynamics (cQED), the interaction of a superconducting qubit with a quantum harmonic oscillator, has been demonstrated in both stable phase qubits[38][39] and metastable phase qubits[40][41]. Stable phase qubits have been built directly into transmission line resonators, which have been used as both a storage and state transfer element as well as a measurement/readout mechanism. Metastable phase qubits have been coupled to both lumped element resonators and transmission line resonators, and have also been used in state storage and state transfer experiments. They have also been read out using lumped element resonators[42], but until this work they had yet to be used to directly measure metastable phase qubits.

2.4.1 Jaynes-Cummings Hamiltonian

The simplest form of cQED is the two-level qubit system interacting with a harmonic oscillator cavity, described by the Jaynes-Cummings Hamiltonian

$$H_{JC} = \underbrace{\frac{1}{2}\hbar\omega_q\sigma_z}_{H_q} + \underbrace{\hbar\omega_r\left(a^\dagger a + \frac{1}{2}\right)}_{H_r} + \underbrace{\hbar g\left(a^\dagger + a\right)\sigma_x}_{H_{int}}, \quad (2.33)$$

where ω_q and ω_r are the qubit and harmonic oscillator frequencies, g is the coupling between them, σ_z and σ_x are the spin operators for the qubit state, and a and a^\dagger are the ladder operators for the harmonic oscillator. Using the substitution $\sigma_x = \sigma_+ + \sigma_-$ and taking the rotating wave approximation to get rid of counter-rotating/anti-resonant (such as $a\sigma_-$, which lowers both the qubit and the cavity resonator states simultaneously) gives the simplified form

$$H_{JC} = \frac{1}{2}\hbar\omega_q\sigma_z + \hbar\omega_r\left(a^\dagger a + \frac{1}{2}\right) + \hbar g\left(a^\dagger\sigma^- + a\sigma^+\right). \quad (2.34)$$

Use of the rotating wave approximation is justified by being in the strong coupling regime[43], where the decay rate of the qubit is much less than the coupling between the qubit and the cavity, and the coupling is less than the cavity resonant frequency ($1/T_1 \ll g \ll f_{cav}$). This Hamiltonian may be solved exactly[43], having the eigenstates

$$|+, n\rangle = \cos \theta_n |e, n\rangle + \sin \theta_n |g, n+1\rangle, \quad (2.35)$$

$$|-, n\rangle = -\sin \theta_n |e, n\rangle + \cos \theta_n |g, n+1\rangle, \quad (2.36)$$

where g and e are the ground and excited states of the qubit and

$$\theta_n = \frac{1}{2} \tan^{-1} \left(\frac{2g\sqrt{n+1}}{\Delta_{01}} \right), \quad \Delta_{01} = \omega_q - \omega_r. \quad (2.37)$$

The eigenenergies of the system are

$$E_{\pm, n} = \hbar\omega_r \pm \frac{\hbar}{2} \sqrt{4g^2(n+1) + \Delta_{01}^2}, \quad (2.38)$$

with the ground state having the energy

$$E_{g, n} = \frac{\hbar\Delta_{01}}{2}. \quad (2.39)$$

This spectrum is a ladder of two level systems, where the n th rung holds $n+1$ excitations in one of its two states, with the exception of the lone ground state. The spectrum is plotted in Figure 2.13 for the $|\Delta_{01}| \gg g$ and $|\Delta_{01}| \ll g$ regimes. The two-level ladder rungs are clear in both situations.

The effect of the cavity on the qubit and the qubit on the cavity can be more clearly seen by

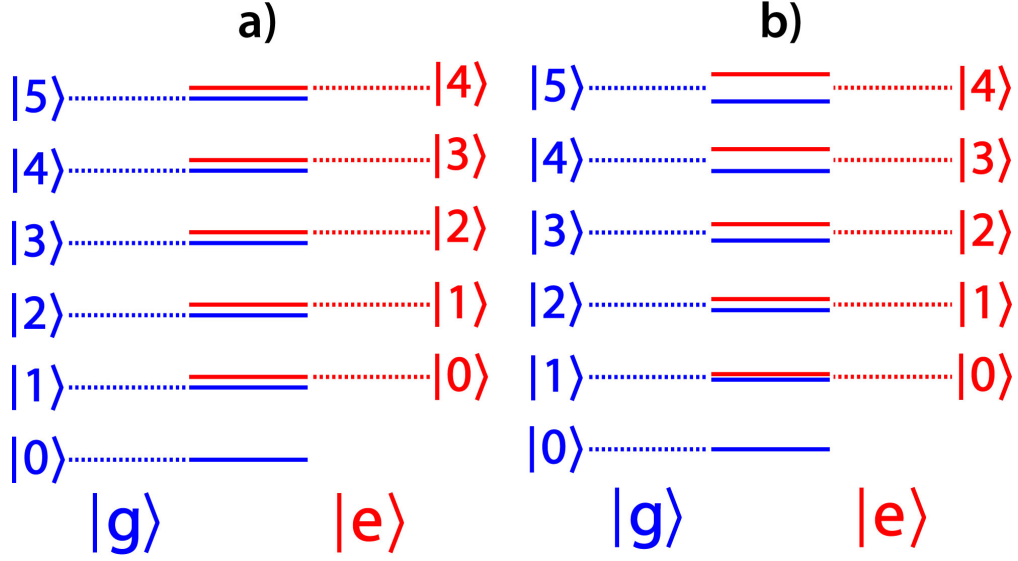


Figure 2.13: Jaynes-Cummings Hamiltonian energy levels - The energy level diagram given by the Jaynes-Cummings Hamiltonian for a two-level system coupled to a cavity. The dressed states are the solid lines, and form a ladder of two level systems where the n th rung holds $n + 1$ excitations, with the exception of the lone ground state rung. a) The $|\Delta_{01}| \gg g$ or dispersive regime, where the combined system has a weak interaction. b) The $|\Delta_{01}| \ll g$, where the levels are strongly shifted as the energy levels from the non-interacting Hamiltonian become degenerate.

making the unitary transformation, following [36],

$$U = e^{\frac{g}{\Delta_{01}}(a\sigma_+ - a^\dagger\sigma_-)}. \quad (2.40)$$

Expanding this to second order in g and applying it to our Hamiltonian gives the approximate expression

$$UHU^\dagger \approx \hbar \left[\omega_r + \frac{g^2}{\Delta_{01}}\sigma_z \right] a^\dagger a + \frac{\hbar}{2} \left[\omega_q + \frac{g^2}{\Delta_{01}} \right] \sigma_z \quad (2.41)$$

From this equation we can see that the cavity frequency is affected by the state of the qubit according to

$$\widetilde{\omega}_r = \omega_r \pm \frac{g^2}{\Delta_{01}}, \quad (2.42)$$

commonly known as the dispersive shift. Rearranging the approximate Hamiltonian to

$$H \approx \hbar\omega_r \left(a^\dagger a + \frac{1}{2} \right) + \frac{\hbar}{2} \left[\omega_q + 2\frac{g^2}{\Delta_{01}} a^\dagger a + \frac{g^2}{\Delta_{01}} \right] \sigma_z \quad (2.43)$$

gives the expression for the effect of the cavity state, or number of photons in the cavity, and the qubit frequency

$$\widetilde{\omega}_q = \omega_q + 2n\frac{g^2}{\Delta_{01}} + \frac{g^2}{\Delta_{01}}, \quad (2.44)$$

where the term $2ng^2/\Delta_{01}$ is the AC Stark shift, and the g^2/Δ_{01} term is the Lamb shift. The AC Stark shift allows an important cavity photon number calibration and will be discussed in the next chapter.

2.4.2 The dispersive shift and the three level qubit

From above, the dressed state energy levels are shifted from the non-interacting Hamiltonian energy levels by the amount $\pm n\hbar g^2/\Delta_{01}$, which depends on the qubit state (\pm). This dispersive shift may be used to measure the state of the qubit by looking at the state of the cavity, or vice versa, though the further the separation between the qubit and the cavity the smaller the shift and the more experimentally challenging it may become to see. For one photon in the system, the dispersive shift corresponds to a frequency change in the cavity of $f = \pm g^2/\Delta_{01}$. This suggests that it is advantageous to increase the coupling g in order to have a larger, and therefore more visible, shift. While this is true, it also must be balanced with the fact that stronger coupling leads to more loss from the qubit to the cavity. This loss, explained as the Purcell effect, is described in Section [2.4.3](#).

This dispersive shift was derived above for a strict two-level system, ignoring the other energy levels that are usually present in both the stable and metastable phase qubit. If the anharmonicity of the potential is sufficiently high, then the influence of the upper levels significantly changes

the dispersive shift for the lowest two levels[37]. To see this effect, derive the energy levels for a three-level system coupled to a cavity, following [44]. The Jaynes-Cummings Hamiltonian can be generalized to a three level system with the Hamiltonian

$$H = H_Q + \hbar\omega_r a^\dagger a + \hbar g \left(a\sigma_+ + a^\dagger\sigma_- \right), \quad (2.45)$$

where

$$H_Q = \begin{pmatrix} 0 & 0 & 0 \\ 0 & \hbar\omega_{01} & 0 \\ 0 & 0 & \hbar\omega_{02} \end{pmatrix}, \quad \sigma_- = \begin{pmatrix} 0 & 1 & 0 \\ 0 & 0 & \lambda \\ 0 & 0 & 0 \end{pmatrix}, \quad \sigma_+ = \begin{pmatrix} 0 & 0 & 0 \\ 1 & 0 & 0 \\ 0 & \lambda & 0 \end{pmatrix}, \quad (2.46)$$

$$\lambda \approx \sqrt{2}, \quad \omega_{12} = \omega_{02} - \omega_{01} < \omega_{01}.$$

Label the eigenbasis as $|q, n\rangle$, where $q = 0, 1, 2$ represent the state of the 3-level qubit system and n is the Fock state photon number for the cavity. Apply second order perturbation theory to the energy states since first order gives no corrections, to get the total energies for the three different qubit states, up to second order

$$E_{0,n} \approx n\hbar\omega_r - n \frac{\hbar g^2}{\Delta_{01}}, \quad (2.47)$$

$$E_{1,n} \approx \hbar\omega_{01} + n\hbar\omega_r + (n+1) \frac{\hbar g^2}{\Delta_{01}} - n \frac{\hbar g^2 \lambda^2}{\Delta_{12}}, \quad (2.48)$$

$$E_{2,n} \approx \hbar\omega_{02} + n\hbar\omega_r + (n+1) \frac{\hbar g^2 \lambda^2}{\Delta_{12}}, \quad (2.49)$$

where $\Delta_{12} = \omega_{12} - \omega_r$. If the cavity is operated in the single photon regime, then the dispersive shift on the cavity due to the qubit state (limited to the $0 \rightarrow 1$ transition) is

$$\Delta\omega = \pm \left(\frac{g^2}{\Delta_{01}} - \frac{g^2}{\Delta_{12}} \right). \quad (2.50)$$

The extra term in the three level shift has a dramatic effect on the shape of the shift curve, as

seen in Figure 2.14. The size of the three level correction clearly depends on the $1 \rightarrow 2$ transition, though if $\omega_{01} \gg \omega_{12}$, then the correction is small and approaches the two level case, though it is always negative. But if $\omega_{01} \approx \omega_{12}$, then the correction is significant. Thus the size of the correction depends on the relative anharmonicity $\alpha = \omega_{01} - \omega_{12}$ of the qubit, making the correction essential to modeling the dispersive shift of the small anharmonicity metastable phase qubit. Note that there is a special regime where the dispersive shift for the three-level model is positive, and corresponds to part of the “straddling regime,” where the cavity frequency is between the f_{01} and f_{12} transition frequencies[37][45]. The behavior in this region is complex, and beyond the scope of this work. For the qubit-cavity system modeled here the straddling regime is between about $0g$ and $4g$. Also indicated on the plot is a grey gradient where the accuracy of this theory is not guaranteed, since it lies outside of the dispersive limit ($|\Delta_{01}| \gg g$).

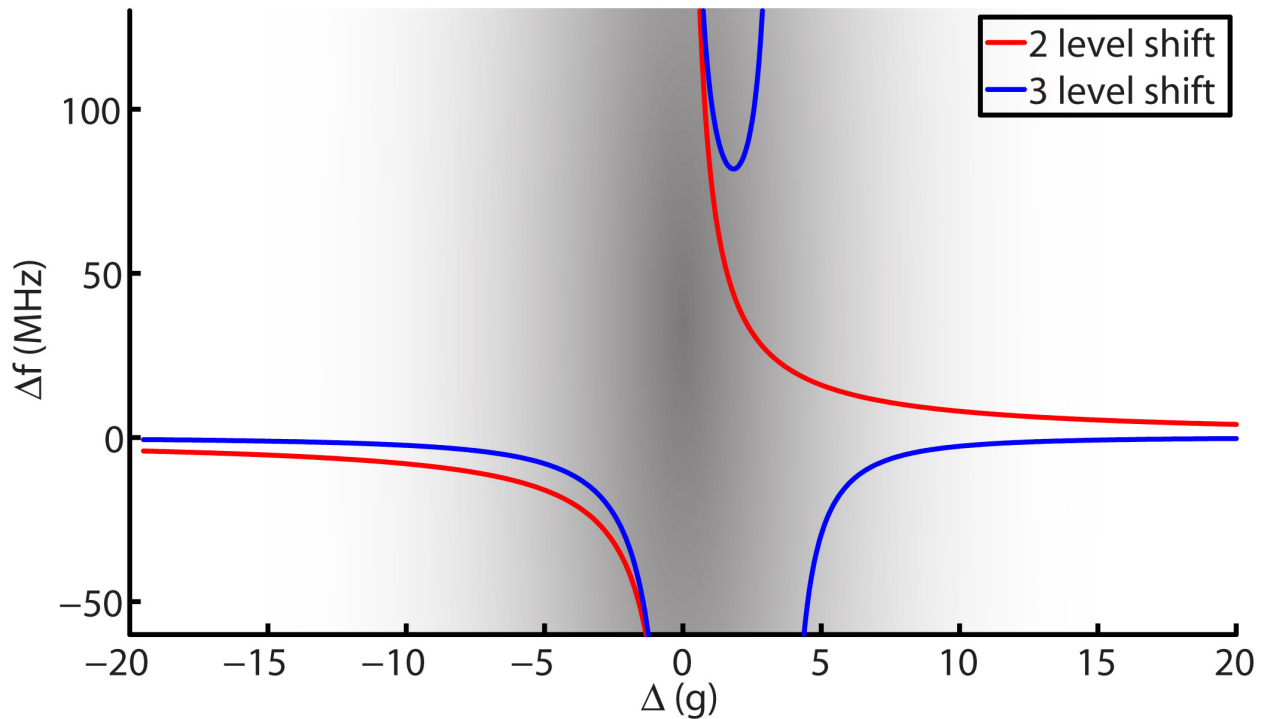


Figure 2.14: Dispersive shift - The dispersive shift on the cavity due to the qubit, comparing the two- and three-level models for a metastable phase qubit with $\beta_L = 3$. Note that the dispersive shift for the three-level model is negative everywhere except in a small region between about $0g$ and $4g$, part of the “straddling regime.” The grey gradient in the middle of the plot is where the dispersive limit does not apply.

2.4.3 The Purcell effect

In 1946 Purcell suggested that a nuclear magnetic spin would be damped through a resonant electrical circuit of quality factor Q , if it were placed inside the resonator and Q were sufficiently small[46]. The free space decay, which is very long for such spins, would be shortened by the factor $3Q\lambda_n^3/4\pi^2V$, where λ_n is the transition wavelength and V is the resonator mode's volume. This effect later found applications in cavity quantum electrodynamics (CQED)[43] and now is being seen in circuit quantum electrodynamics (cQED)[47].

As Purcell's argument was based on Fermi's Golden Rule for spontaneous emission, let us begin there, following [37]. While the qubit energy is decaying into the cavity, the cavity energy is decaying into the surrounding bath. This last decay path obeys the Hamiltonian

$$H = \hbar \sum_k \lambda_k \left[b_k^\dagger a + a^\dagger b_k \right], \quad (2.51)$$

where a and a^\dagger are the cavity ladder operators, b_k and b_k^\dagger are the bath operators for mode k , and λ_k is the coupling strength between the cavity and the bath. Fermi's Golden rule states that the spontaneous emission rate is $\gamma = 2\pi/\hbar |\langle f|H|i\rangle|^2 \rho$, where f and i are the final and initial states, respectively, and ρ is the density of states. Since we are only interested losing a photon from the cavity to the bath this expression may be simplified to

$$\gamma_\kappa = \kappa |\langle f|a|i\rangle|^2, \quad (2.52)$$

where all the coefficients have been folded into $\kappa = \omega_{cav}/Q_{cav}$, the decay rate of the cavity to the bath. Now we need the initial and final states of our system; initially there must be a photon in the qubit only, then finally no photon anywhere since it was absorbed by the bath through the cavity. For the two level atom the loss is $\gamma_\kappa = \kappa g^2/\Delta_{01}^2$. For our three level atom the first two dressed

state wavefunctions, up to second order, are

$$\overline{|0, n\rangle} \approx \left(1 + \frac{g^2 n}{2\Delta_{01}^2}\right) |0, n\rangle - \frac{g\sqrt{n}}{\Delta_{01}} |1, n-1\rangle + \frac{g^2 \lambda \sqrt{n^2 - n}}{\Delta_{01} (\Delta_{01} + \Delta_{12})} |2, n-2\rangle, \quad (2.53)$$

$$\overline{|1, n\rangle} \approx \left[1 - \frac{g^2}{2} \left(\frac{n+1}{\Delta_{01}^2} + \frac{\lambda^2 n}{\Delta_{12}^2}\right)\right] |1, n\rangle + \frac{g\sqrt{n+1}}{\Delta_{01}} |0, n+1\rangle - \frac{g\lambda\sqrt{n}}{\Delta_{12}} |2, n-1\rangle. \quad (2.54)$$

Plugging these into our Fermi's Golden Rule expression gives

$$\gamma_\kappa = \kappa \left| \frac{g(n+1)}{\Delta_{01}} \left(1 + \frac{g^2 n}{2\Delta_{01}^2}\right) - \frac{gn}{\Delta_{01}} \left[1 - \frac{g^2}{2} \left(\frac{n+1}{\Delta_{01}^2} + \frac{\lambda^2 n}{\Delta_{12}^2}\right)\right] - \frac{g^3 \lambda^2 n(n-1)}{\Delta_{01} \Delta_{12} (\Delta_{01} + \Delta_{12})} \right|^2, \quad (2.55)$$

which recovers the two level qubit Purcell effect loss $\gamma_\kappa = \kappa g^2 / \Delta_{01}^2$ when there is only an excitation in the qubit ($n = 0$).

The Purcell effect loss that the qubit sees is purely an external loss. Like Purcell's nuclear magnetic spin, the qubit's total loss will be increased by the presence of the cavity coupled to a bath. The qubit's internal loss occurs through different mechanisms like the dielectric losses described at the beginning of this chapter. Figure 2.15 is a plot of the Purcell model for a metastable phase qubit-cavity system for different quality factor cavities. The loss is strongly enhanced near the degeneracy, but asymptotically approaches the qubit's internal decay time of $T_1 = 1000$ ns.

While the external loss from the qubit through the cavity to the bath can be a dominant mechanism, one should note that the Purcell effect is not just limited to designed electrical cavities. It applies to any mode coupled to the qubit, so it is important that the qubit be well isolated from spurious modes. This isolation usually takes the form of weak inductive coupling to and heavy filtering on the qubit control lines. Ideally, the engineered cavity is the only Purcell decay path. A tunable cavity is more flexible than a fixed cavity, as it may be tuned into resonance for intentional decay or detuned for maximal qubit lifetime.

The Purcell effect suggests that it is best to have a weakly coupled, high quality factor cavity

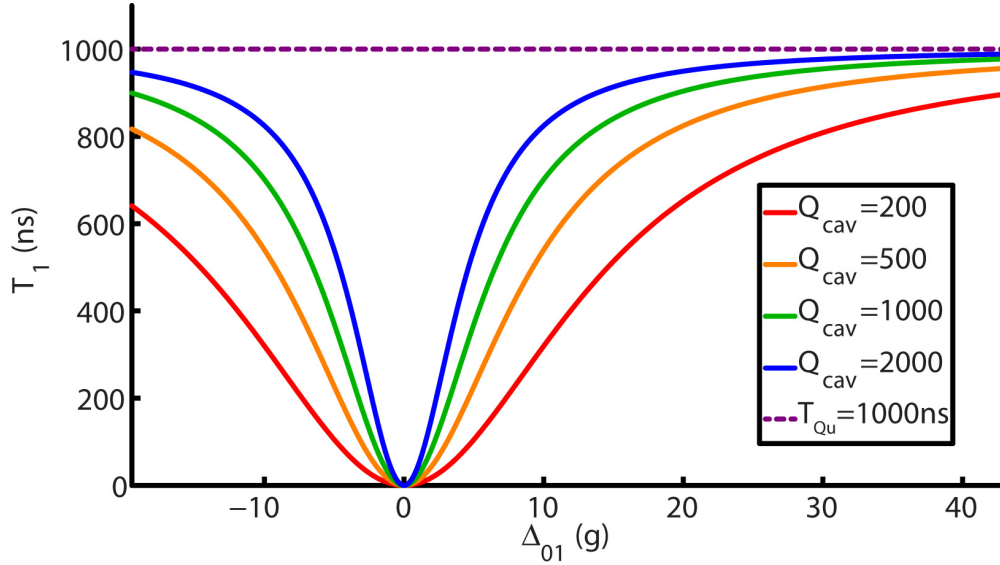


Figure 2.15: Purcell effect - The Purcell effect, showing loss from the qubit to the cavity for different quality factor cavities and a background $T_1 = 1000$ ns.

so that qubit loss is minimized over a broad range of detunings. However, one must also remember that a more weakly coupled qubit-cavity system also requires longer timescales to transfer energy and information. For instance, a qubit that is weakly coupled to the cavity will give small dispersive shifts when being measured by the cavity, requiring more time to achieve the necessary signal-to-noise required by a given experiment. A similar problem occurs when the cavity is weakly coupled to the bath, in our case dominated by a microwave feedline used for measuring the cavity state. If the coupling is weak between the cavity and the feedline, the long ring-up time for the cavity may hide the dynamics of a particular experiment. Thus the experimenter must consider qubit-cavity coupling, cavity-feedline coupling, qubit internal loss, and cavity external loss when designing a circuit to carry out a desired experiment.

3

Control and measurement of the metastable phase qubit

3.1 Qubit control

The metastable phase qubit’s multi-well potential makes it an inherently more challenging control problem than other types of superconducting qubits because the qubit must be reset after each measurement in order to know which well is populated at the beginning of manipulation. The potential control techniques that will be discussed are unique to the metastable phase qubit. However, the general principles of qubit state control presented here may be applied to the other superconducting qubit systems.

3.1.1 Potential control

As discussed in the previous chapter, the shape of the qubit potential may be manipulated by an externally applied flux Φ_{ex} . For $\beta_L \lesssim 4.7$ there are places where the potential is single-valued as well as places where the qubit is double-valued, as shown in Figure 3.1. The single-valued location is used for resetting the qubit to a known state, so this is labeled the “reset”

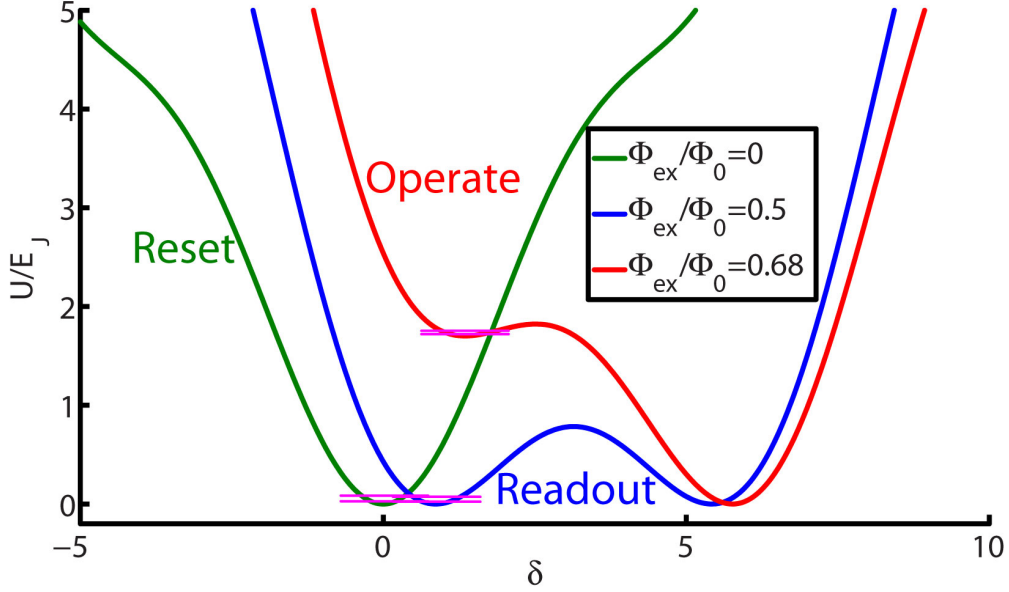


Figure 3.1: Metastable phase qubit potentials - Three metastable phase qubit potentials, one single-valued for resetting the qubit, one symmetric double-valued for reading out the measurement results, and one asymmetric double-valued for operating the qubit. The two energy levels that make up the qubit are shown in magenta. For a qubit with $\beta_L = 3.0$.

potential. While any well may be used for qubit state manipulations, we have already seen that the higher anharmonicity of the shallow well in the double-valued potential is most desirable for quantum computation operations because of its relatively high anharmonicity (Section 2.3.1), and so this will be called the “operate” potential. After qubit manipulations are complete the state is measured using a fast flux pulse (described in detail below) that is calibrated to cause a tunneling event to the deep well only if the qubit was measured in the $|1\rangle$ state. The symmetric double well potential, or “readout” potential, has wells that are separated by a flux quantum Φ_0 , as well as a large barrier between the wells. The two states represented by the two wells correspond to the direction of circulating current in the qubit loop, and the large barrier keeps these states separated over long time scales. The Φ_0 difference between the circulating current states provides plenty of room for distinguishing between the two using flux magnetometry, providing the readout device is sufficiently coupled to the qubit.

In order to properly operate a metastable phase qubit it is important to know what applied flux corresponds to the symmetric single-valued well, the symmetric double valued well, and where

the tunneling event happens. These values are found by measuring the circulating current in the qubit at different flux biases using a magnetometry measurement, yielding data commonly referred to as “steps.” The flux applied to the qubit inductive loop is swept while the total flux in the loop is measured by a SQUID. Figure 3.1 shows the qubit well drifting along the δ -axis as the external flux is changed, moving its minimum value δ_0 . As the flux moves the potential from being multi-welled to being single-welled again a tunneling event will occur and a discontinuous jump in the phase will occur as the previously occupied well disappears. The position of the minimum value of the potential well can be found by setting the derivative of the potential to zero and solving for δ

$$dU = E_J \sin \delta + 2E_L \delta + E_L 4\pi \frac{\Phi_{ex}}{\Phi_0} = 0 \rightarrow \sin \delta = -2 \frac{E_L}{E_J} \left(\delta + 2\pi \frac{\Phi_{ex}}{\Phi_0} \right). \quad (3.1)$$

Since this is a transcendental equation there will be multiple values for δ when the potential is multi-welled, so the correct value δ_0 must be chosen. One way to choose the correct value is to start in a single valued potential that only has one extremum and then always choose the δ value closest to the last one. As long as the flux steps are small enough, this method should always give the δ_0 of the same well, until that well disappears and the minimum phase is single-valued again in the next well. These discontinuities are the steps. The current in the qubit loop can be found using the Josephson current relation with the found value for δ_0 , $I = I_c \sin \delta_0$. The minimum value δ_0 and the current in the qubit are plotted in Figure 3.2. The single-valued potential that can be used for resetting the system occurs at the integer multiples $n\Phi_{ex}/\Phi_0$, while the double-valued potential that can be used for readout occurs at the half-integer multiples $(n/2)\Phi_{ex}/\Phi_0$. While this model shows discontinuities occurring whenever a well disappears at $|I_{qubit}| = I_c$, tunneling of the state to the deep well should occur sooner in real systems. Where the tunneling happens depends on the loss in the system, the temperature of the system, and the time spent in a given well configuration[48][32]. If we approximate the metastable well as a cubic potential, the tunneling

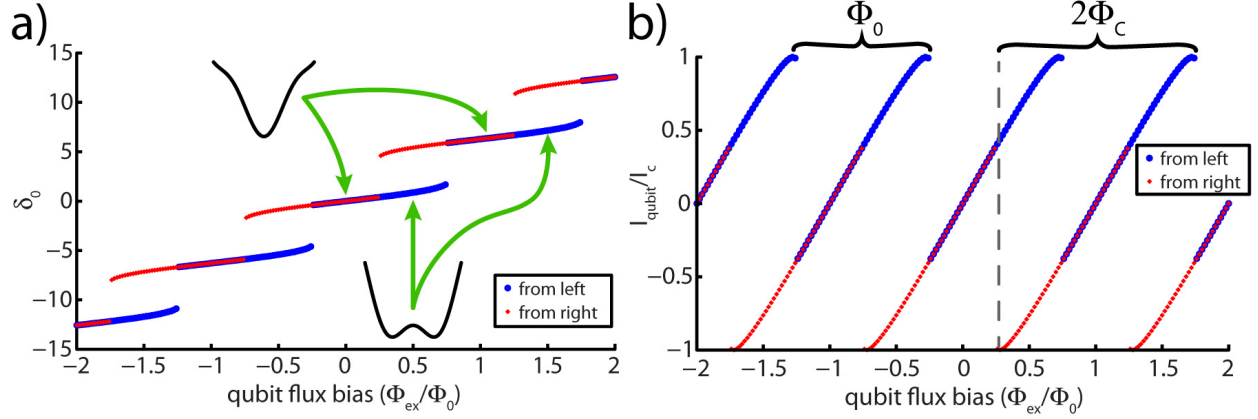


Figure 3.2: Metastable phase qubit steps - a) The phase δ_0 corresponding to the well minima as a function of applied flux Φ_{ex} , showing the discontinuities when wells disappear. b) The current in the qubit calculated from δ_0 . For both plots the symmetric single-valued potential (reset) occurs at the integer multiples $n\Phi_{ex}/\Phi_0$, and the symmetric double-valued potential (readout) occurs at $(n/2)\Phi_{ex}/\Phi_0$. The distance between tunneling events is Φ_0 , while the length of an entire step is $2\Phi_C$.

rate is

$$\Gamma = \sqrt{120\pi 7.2 \frac{\Delta U}{\hbar\omega_p}} e^{-7.2 \frac{\Delta U}{\hbar\omega_p} \left(1 + 0.87Q + 0.052 \left(1 + \frac{2\pi \frac{\Phi_{ex}}{\Phi_0} - \delta_0}{\tan \delta_0}\right)\right)}, \quad (3.2)$$

where ΔU is the barrier height (the distance from the bottom of the metastable well to the top of the barrier), $\omega_p = 1/\sqrt{(L_g \parallel L_{J0})C}$ is the plasma frequency of the circuit, and $Q = \omega_p RC$ is the quality factor of the circuit. The spilling points can be found more precisely by resetting the qubit, moving to an operate flux that is swept to see if the qubit tunnels there, then moving to the readout flux to readout the state. The process is shown schematically in Figure 3.3a. The resulting tunneling probability curve or ‘‘S-curve’’ is plotted in Figure 3.3b. Taking this curve at either end of a step and at the edge of an adjacent step provides enough information to both calibrate the flux axis to a magnetic flux quantum Φ_0 , since the steps are periodic in Φ_0 due to the flux quantization of the loop, as well as determining β_L from the step length $2\Phi_C$.

The flux axis is readily calibrated since the current applied to the bias line can be easily measured from the room temperature electronics, and Φ_0 is read off from the steps data as the difference in flux between tunneling events. The coupling between the bias line and the qubit can then be easily calculated using $M = \Phi_0/I$. Likewise, the hysteresis is found simply by substituting

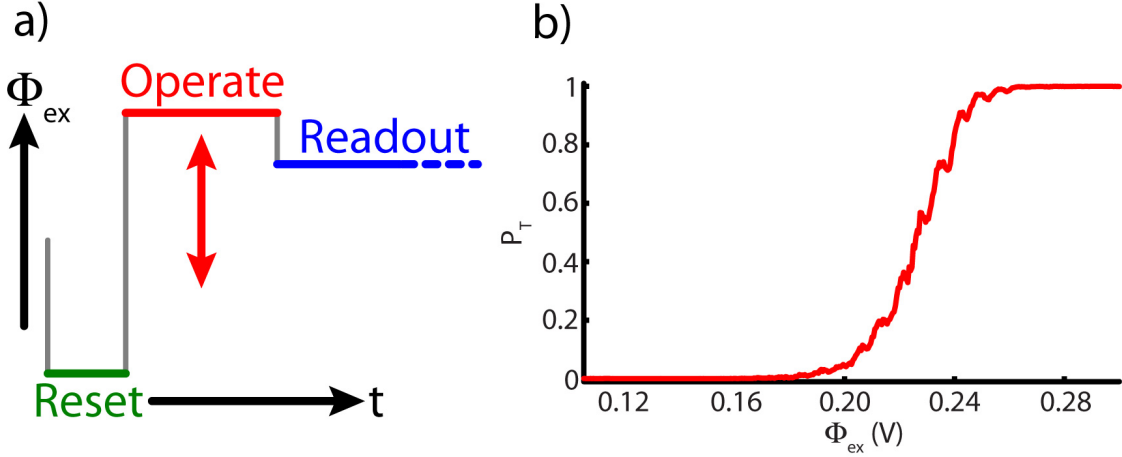


Figure 3.3: Metastable phase qubit S-curve - a) Flux waveform for measuring the S-curve by sweeping the operate flux. b) The S-curve moves continuously from the untunneled to the tunneled state. The little spikes on the S-curve are resonant tunneling events, potential shapes where the ground state energy level in the shallow well is degenerate with a deep well energy level and tunneling is enhanced.

$E_L/E_J = 1/2\beta_L = -\cos \delta/2$ into Equation 3.1, and using the length from the middle of the step to its edge Φ_C to write

$$\tan \delta - \delta = 2\pi \frac{\Phi_C}{\Phi_0}. \quad (3.3)$$

This transcendental equation may be solved for δ , which can be plugged into $\beta_L = -1/\cos \delta$. Since the design value for the geometric inductance L_g is usually very close the actual measured value, one can then calculate the junction inductance $L_{J0} = L_g/\beta_L$.

3.1.2 Bloch sphere manipulations and tomography

Since qubits are two-level quantum systems used for computations that may require any number of manipulations, it is useful to visualize a qubit state as a vector on the three-dimensional Bloch sphere[49], shown in Figure 3.4. The vertical z -axis contains the two eigenstates of the system, where $|0\rangle$ is the ground state and $|1\rangle$ is the excited state. The Bloch vector can be written mathematically as

$$|\psi\rangle = \cos \frac{\theta}{2} |0\rangle + e^{i\varphi} \sin \frac{\theta}{2} |1\rangle. \quad (3.4)$$

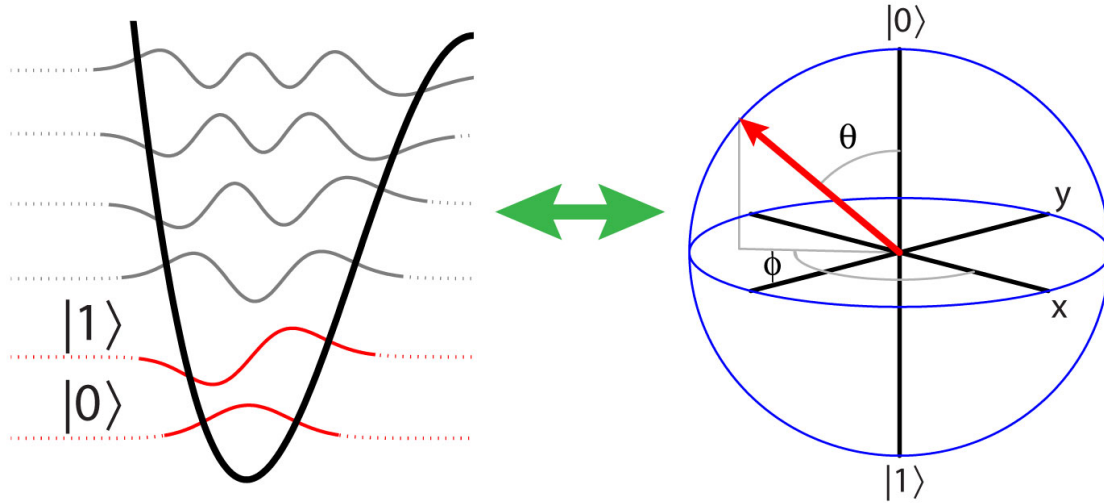


Figure 3.4: Mapping the two-level system to the Bloch sphere - The state of a qubit, a two-level quantum system, can be represented as a vector on the Bloch sphere.

Arbitrary control over the qubit state means having the ability to move the Bloch vector to any location on the Bloch sphere. This is accomplished using a combination of microwave and flux pulses. Flux pulses cause rotations about the z -axis, with the sign of the pulse determining the direction of rotation and the amplitude of the pulse determining the rate of rotation. Microwave pulses cause rotations about an axis in the xy -plane, with the phase of the microwave pulse determining which axis and the amplitude determining the rate of rotation. Duration of both types of pulse determines the total angle of rotation. A simple example of state manipulation is seen by driving Rabi oscillations on a two level system separated by $E_{01} = \hbar\omega_{01}$, using a microwave pulse that oscillates the externally applied flux at frequency $\omega_{01} = (E_1 - E_0)/\hbar$. Any two-level system with an oscillating potential has the Hamiltonian[50]

$$H = H_0 + U(t) = \begin{pmatrix} E_0 & Ae^{i\omega t} \\ Ae^{-i\omega t} & E_1 \end{pmatrix}, \quad (3.5)$$

where A is the amplitude of oscillation. This Hamiltonian has an exact solution. For the driven state at time t , $|\psi\rangle = c_0(t)|0\rangle + c_1(t)|1\rangle$ and the probability for being found in each of these two

states is given by Rabi's formula,

$$|c_1(t)|^2 = P_{|1\rangle} = \frac{A^2/\hbar^2}{A^2/\hbar^2 + (\omega - \omega_{01})^2/4} \sin^2 \left(\sqrt{\frac{A^2}{\hbar^2} + \frac{(\omega - \omega_{01})^2}{4}} t \right),$$

$$|c_0(t)|^2 = P_{|0\rangle} = 1 - |c_1(t)|^2. \quad (3.6)$$

This oscillation between the $|0\rangle$ and $|1\rangle$ states amounts to a rotation of the Bloch vector around the x -axis ($\varphi = 0$), as in Figure 3.5a. This rotation continues as long as the drive is applied.

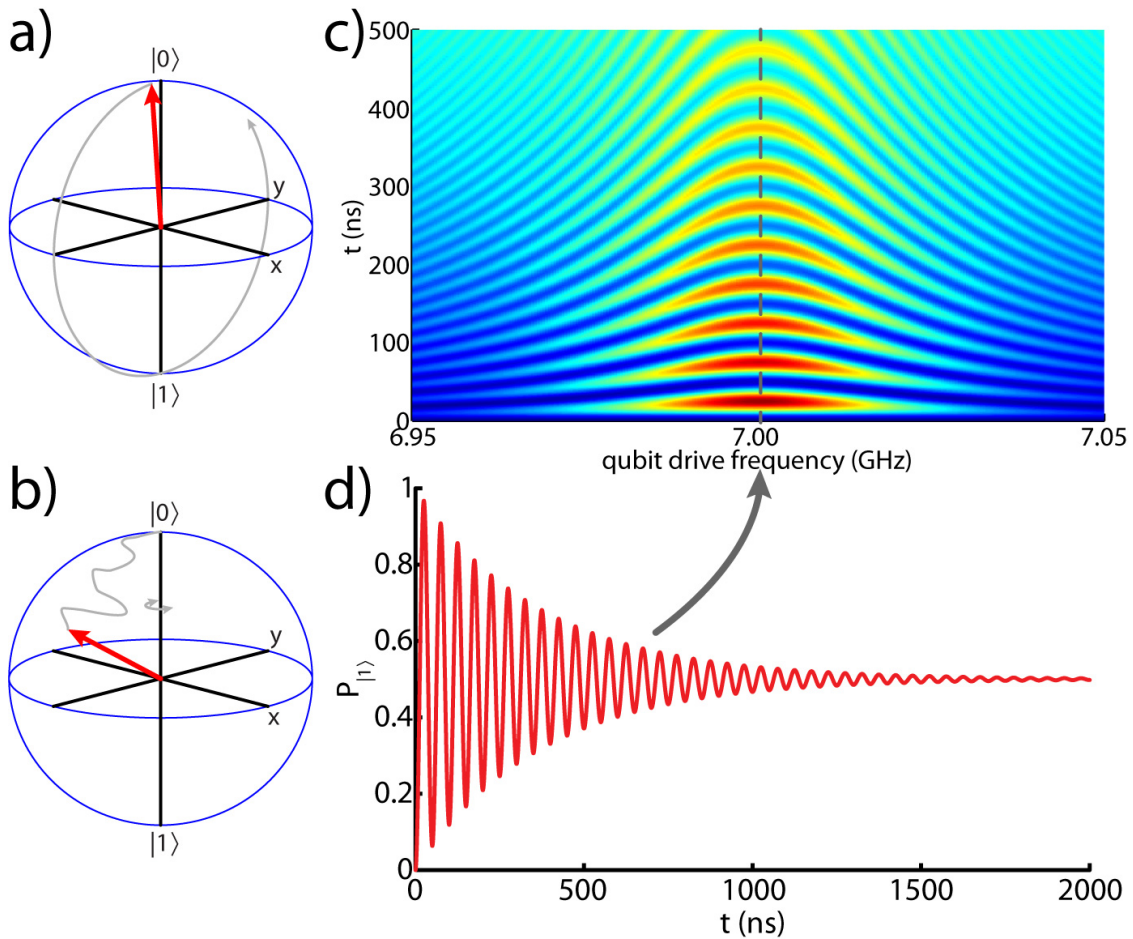


Figure 3.5: Driven Rabi oscillations - a) Bloch sphere representation of driven Rabi oscillations, where the Bloch vector rotates about the x -axis when driven on resonance. b) While Rabis are driven the Bloch vector's axis of rotation changes due to dephasing, equivalent to arbitrary rotations about the z -axis. c) Rabi oscillations at different drive frequencies, calculated from Rabi's formula and including the decay from T' . d) Line cut of c), showing that after a long duration pulse, the probability of being in the $|1\rangle$ state approaches 50%.

From looking at Rabi's formula we can see that the frequency of this oscillation is

$$\Omega_{Rabi} = \sqrt{\frac{A^2}{\hbar^2} + \frac{(\omega - \omega_{01})^2}{4}}. \quad (3.7)$$

On resonance, $\Omega_{Rabi} = A/\hbar$, so Ω_{Rabi} is directly proportional to the drive amplitude A . Off resonance, Ω_{Rabi} increases and the amplitude of the oscillations decreases.

The Rabi oscillation is further modified in the presence of $1/f$ noise and energy decay channels. Low frequency noise (compared to ω_{01}) on the flux bias line causes arbitrary rotations in φ around the z -axis while the flux drive is rotating around the x -axis only, shown in Figure 3.5b, leading to dephasing[51]. The dephasing rate will here be noted as T_2 . When a given x -rotation is much longer than T_2 and is repeated many times, these arbitrary rotations sum to put the Bloch vector always along the equator, in the xy -plane, corresponding to a $|1\rangle$ -state occupation probability $P_1 = 50\%$. The dephasing is also accompanied by the energy decay rate T_1 , which describes the qubit's resonant energy loss to the environment. Taken together these two define a decay constant T' for the Rabi oscillation envelope[52][53]

$$\frac{1}{T'} = \frac{1}{2T_1} + \frac{1}{2T_2}, \quad (3.8)$$

and the combination of this decay constant with Rabi's formula is plotted in Figures 3.5c and 3.5d. The decay envelope around the Rabi oscillations seen in Figure 3.5d suggests that there is a finite timescale during which qubit manipulations may be reliably done. Thus, measurements of T_1 and T_2 are important for understanding the amount of time available to manipulate the qubit state for performing quantum computations.

3.1.3 T_1 measurement and the π -pulse

The energy decay rate T_1 , also known as the longitudinal decay rate because it decays around an xy -plane axis, can be measured by preparing the qubit in the $|1\rangle$ state by using a π -pulse and watching the state decay back down to the $|0\rangle$ state, as seen in Figure 3.6. The T_1 decay follows the functional form $P_{|1\rangle}(t) = e^{-\Delta t/T_1}$, where Δt is the delay between the π -pulse and the measure pulse.

The π -pulse is any drive pulse of appropriate duration and amplitude that moves the qubit from the $|0\rangle$ state to the $|1\rangle$ state, and is best accomplished using a Gaussian shaped pulse[54]. Because Ω_{Rabi} depends on the drive amplitude A , there is a continuum of amplitudes and drive durations that will give a π -pulse. From Equation 3.6 we can see that on resonance, a π -pulse happens when

$$2\frac{A}{\hbar}t = \pi. \quad (3.9)$$

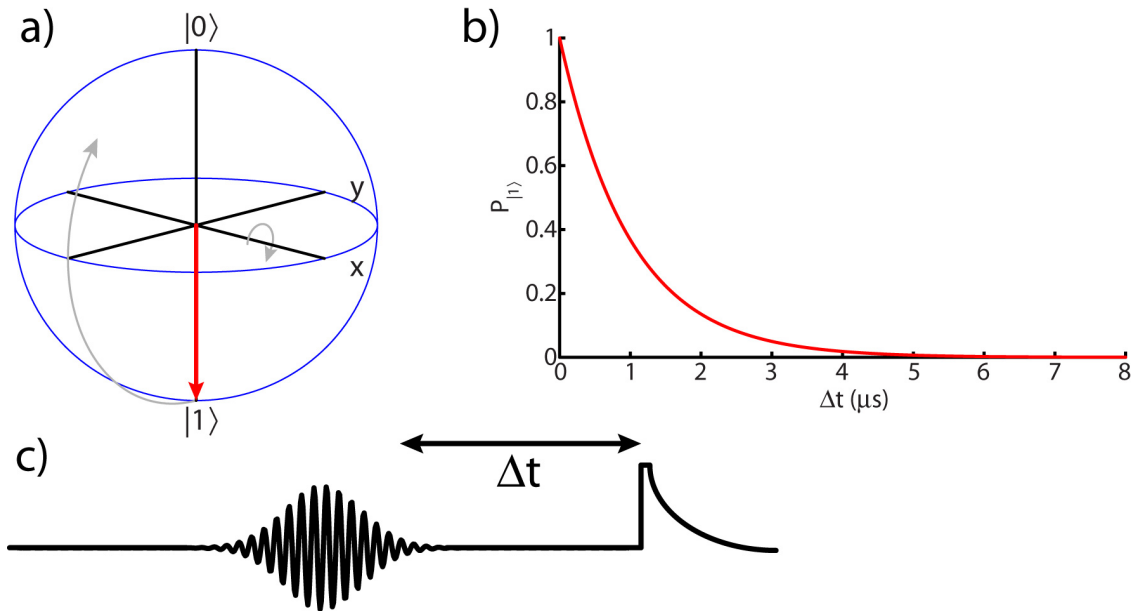


Figure 3.6: T_1 measurement - a) The T_1 measurement involves putting the qubit in the $|1\rangle$ state by applying a π -pulse, then waiting a time Δt , then measuring the state at different values of Δt . b) The calculated decay curve for a T_1 measurement. c) The pulse sequence for the T_1 measurement.

In a perfect two-level system without loss the π -pulse may be chosen to have any combination of amplitude and duration that satisfies Equation 3.9. But we have already seen that the potential usually has more than just two energy levels, and thus care must be taken to only address the bottom two. This means that our π -pulse cannot have significant frequency components that could excite other transitions like the f_{12} or the two-photon $f_{02/2}$ [55]. For the long pulse (120 ns) in Figure 3.7 the FFT shows that it will not excite the $|2\rangle$ state transitions, which represent a qubit with relative anharmonicity $\alpha_r = 1\%$, since the power spectral density at those frequencies is in the noise floor, at least 80 dB below the f_{01} pulse. Since the level spacing, and hence α_r , is different for each DC external flux, the spectral components of the π -pulse must be considered at each flux. Note that if the power spectral density (PSD) of the pulse at $f_{02/2}$ is just 30 dB below the PSD at f_{01} , the $f_{02/2}$ Rabi period will be 1000 times longer than the f_{01} Rabi period, making its population by stray spectral components negligible.

Because of this frequency separation issue it may be tempting to choose a very long π -pulse, like the one in Figure 3.7, so that the pulse is spectrally very narrow. But the energy decay (T_1) and dephasing (T_2) processes described above are also modifying the path of the Bloch vector while the slow π -pulse is applied, and if their time scales are shorter than the π -pulse duration, the qubit will never be able to reach the $|1\rangle$ state. Thus it is important to make the π -pulse long enough

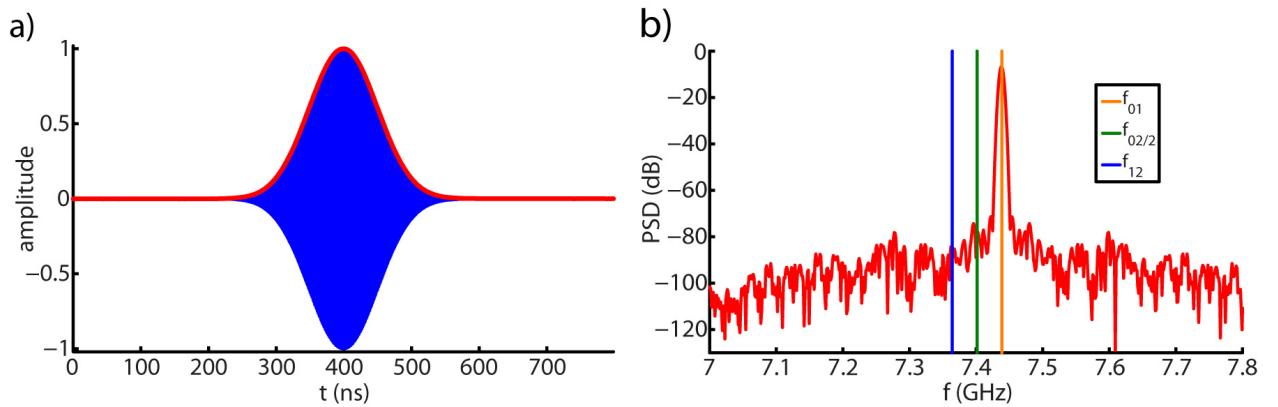


Figure 3.7: π -pulse frequency components - a) 120ns Gaussian π -pulse in the time domain at 7.44GHz. The Gaussian envelope (red) was measured on an oscilloscope and the 7.44GHz sine wave was added. b) FFT of the 7.44GHz, 120 ns Gaussian pulse. For a relative anharmonicity $\alpha_r = 1\%$, the other $|2\rangle$ state transitions are clearly not going to be excited by this pulse as they are in the noise floor.

to exclude undesirable transitions, yet still short enough to make the T_1 and T_2 effects negligible.

3.1.4 Ramsey fringe measurement

The dephasing time T_2 , also known as the transverse decay time because it is the decay rate about the z -axis, is measured using two $\pi/2$ -pulses, with a z -pulse and delay Δt between them, also known as a Ramsey experiment. The $\pi/2$ -pulse is a 90° rotation about the x -axis, as shown in Figure 3.8a. During the delay time the qubit rotates in the xy -plane with a frequency ω_z , proportional the amplitude of the z -pulse, and then a second 90° rotation ($\pi/2$ -pulse) about the x -axis is applied and the state is measured.

The pulse sequence is shown in Figure 3.8b. If the vector doesn't rotate at all during Δt , or if Δt is sufficiently short to make the dephasing insignificant, the second $\pi/2$ -pulse will place the qubit in the $|1\rangle$ state. If the vector rotates to be along the x -axis during Δt , the second $\pi/2$ -pulse will leave the state in the xy -plane. If the vector ends up in the $-y$ direction after Δt , the second $\pi/2$ -pulse will rotate it to the $|0\rangle$ state. While the z -pulse should give deterministic oscillations, over long enough time scales dephasing noise dominates the phase angle ϕ . When the phase position is randomized by this phase noise this rotational bisymmetry gives $P_{|1\rangle} = 50\%$ as the average for a large number of measurements. Thus the Ramsey protocol gives a measurement of the timescale for dephasing, with the functional form[56] $P_{|1\rangle} = 0.5 \cos(\omega_z t) e^{-(t/T_2)^2} + 0.5$, which is plotted in Figure 3.8c for the detuning indicated in the 3D plot by the grey dotted line.

3.1.5 Tomography

A practical summation of the Copenhagen interpretation of quantum mechanical measurement can be found in Dirac's statement "a measurement always causes the system to jump into an eigenstate of the dynamical variable that is being measured"[57]. Taken at face value, this suggests that although a qubit's Bloch vector may point anywhere on the surface of the Bloch sphere, it may

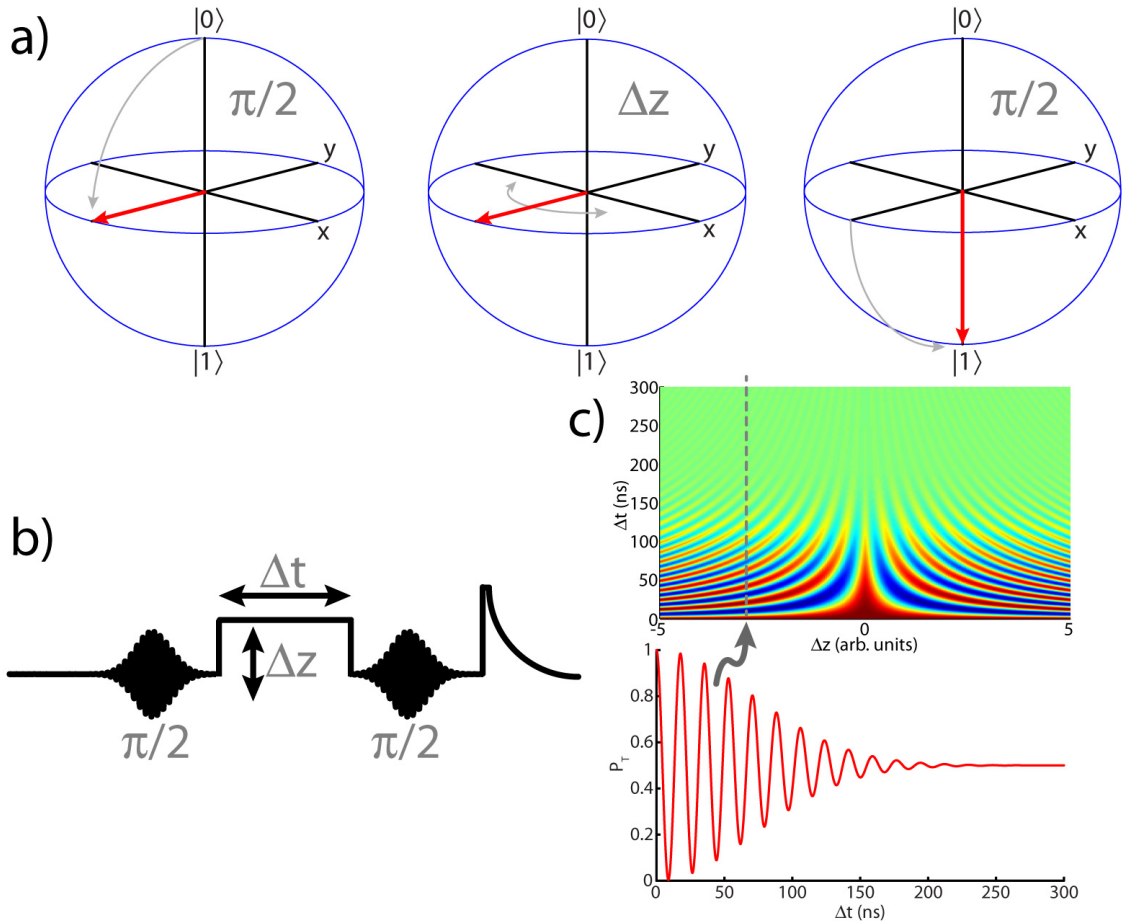


Figure 3.8: Ramsey fringe measurement - a) The T_2 measurement starts by applying a $\pi/2$ -pulse to put the qubit in the xy -plane, then is followed by a z -pulse for a time Δt . The Bloch vector rotates in the xy -plane with a frequency ω_z proportional the amplitude of the z -pulse. A $\pi/2$ pulse is again applied, rotating around the x -axis by 90° , then the state is measured. The case shown is for a null z -pulse and no dephasing. b) Ramsey fringe pulse sequence. c) Ramsey fringes calculated using the functional form $P_{|1\rangle} = 0.5 \cos(\omega_z t) e^{-(t/T_2)^2} + 0.5$.

only be measured to be in either the $|0\rangle$ or $|1\rangle$ state and nothing but the final, measured state of the system may be known; all information about the vector is lost. While this statement is true if only one measurement is made on a given prepared state, by preparing and measuring the same state over and over again one can learn something about the prepared state. Remembering that any wavefunction $|\psi\rangle$ may be written as the sum of eigenvectors in any basis, our qubit's wavefunction can be written in the energy basis as

$$|\psi\rangle = c_0|0\rangle + c_1|1\rangle, \quad (3.10)$$

where $P_{|0\rangle} = |c_0|^2$ ($P_{|1\rangle} = |c_1|^2$) is the probability of a measurement result being in the $|0\rangle$ ($|1\rangle$) state. If repeated enough times $P_{|1\rangle} = 1 - P_{|0\rangle}$ can be well known and tell us the angle θ on the Bloch sphere (Figure 3.4), yet the phase φ is still unknown. This angle can be found using a tomographic measurement technique. Typically, tomography involves measuring the prepared state in different bases, but the same thing can be accomplished by doing an extra known rotation about the x - and y -axis before measurement. Because the extra pulse is known, the position of the qubit state can be deduced from the measurement result. Figure 3.9 schematically shows the tomography procedure. The state to be measured is prepared, then one of three tomography pulses is applied. The three pulses are labeled I , 90_x , and 90_y . I is a null pulse, nothing, so that the angle θ can be measured. 90_x and 90_y are just $\pi/2$ -pulses, though their phases differ by 90° . The 90_x pulse rotates the state about the x -axis by 90° and the 90_y pulse rotates the state about the y -axis by 90° . After performing these rotations, a measurement projects these states onto the z -axis. For a 90° rotation about x -axis, the projection onto the z -axis gives the same result as if the measurement had been projected onto the y -axis. Likewise, a 90° rotation about y -axis followed by a projective measurement onto the z -axis gives the same result as a projective measurement along the x -axis. These two extra rotations, 90_x and 90_y , are nominally equivalent to being able to measure along the y - and x -axes, respectively, thus giving full knowledge of the location of the

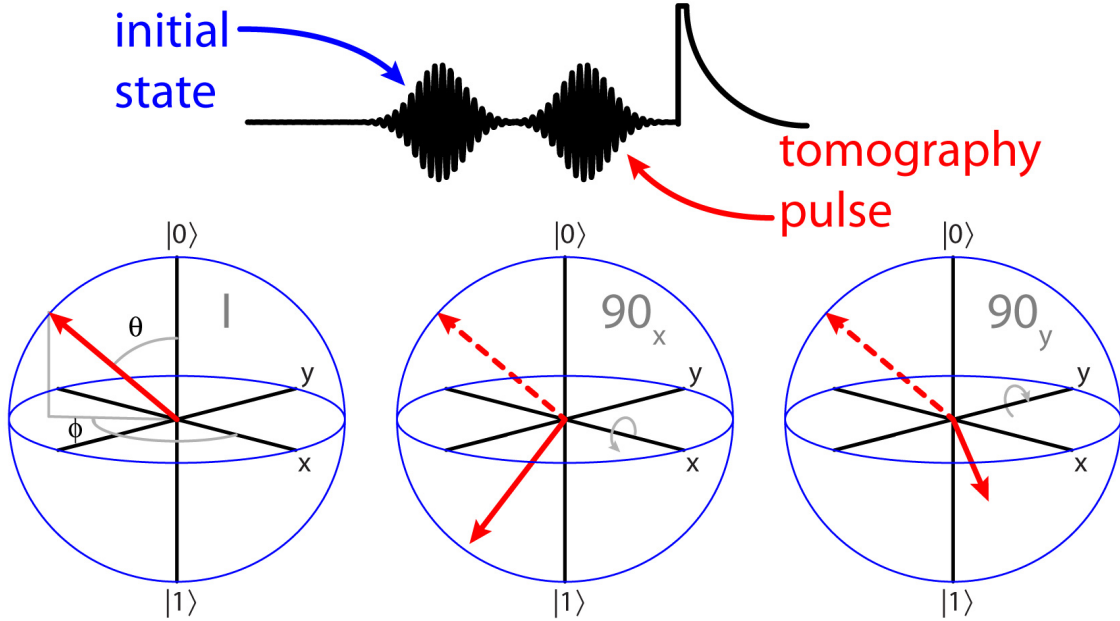


Figure 3.9: Tomography of an arbitrary state - The Bloch vector can be completely described by doing tomographic measurement, which entails doing one of three pulses followed by a measurement: I (no pulse), 90_x , 90_y . The final state after the tomography pulse is applied is the solid red arrow, and the initial state is a dotted red arrow.

Bloch vector. Tomographic measurement has been previously implemented in metastable phase qubits[58].

In order to find precisely the pulses to be used for tomography, one may sweep the phase of the second pulse and use the result as a calibration, as long as the initial states are well known. The prepared states $|0\rangle$, $|1\rangle$, $(|0\rangle + |1\rangle) / \sqrt{2}$, and $(|0\rangle + i|1\rangle) / \sqrt{2}$ can be explored using a tomography pulse whose phase is swept from 0 to 2π . Calculated results for the four different states are plotted on polar plots in Figure 3.10, where the phase is the polar angle and amplitude is the radial variable. This continuous change of phase sweeps the axis of rotation of the tomography pulse through the entire xy -plane. At each phase, the tomography pulse amplitude is also swept through more than one Rabi period, so the entire Bloch sphere is mapped for each prepared state. Note that sweeping pulse amplitude may be replaced with sweeping time, though the energy relaxation time must be sufficiently long for clear data. For the initial state $|0\rangle$, rotations about any axis in the xy -plane for increasing rotation times (or pulse amplitudes) gives identical driven Rabi oscillations. The

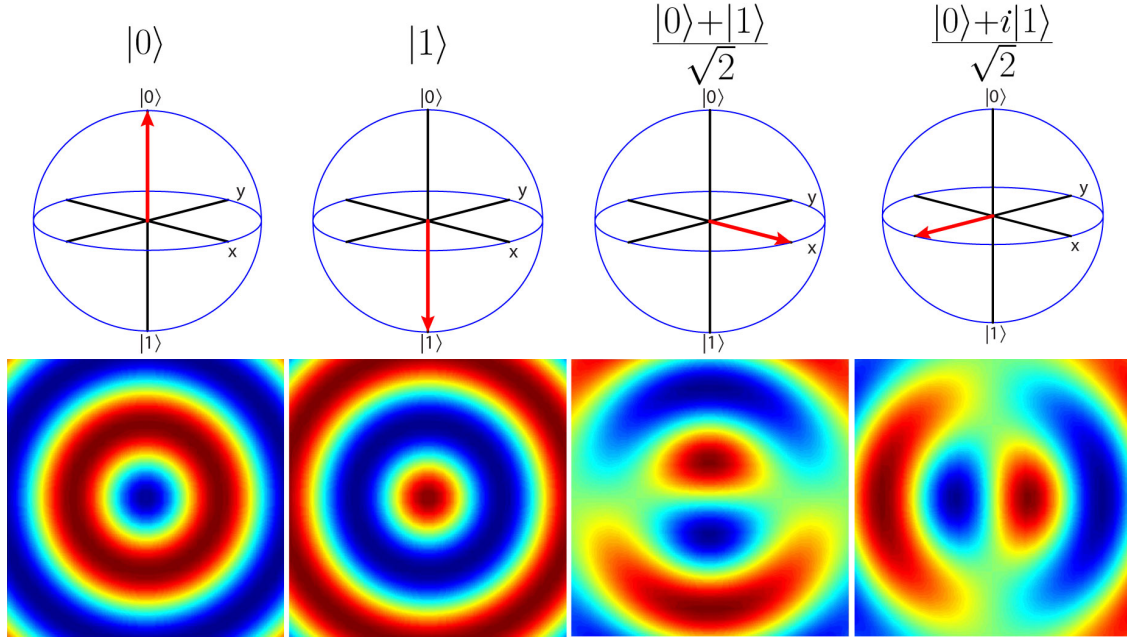


Figure 3.10: Tomography sweep - Calculated tomography, sweeping the tomography pulse amplitude and phase, of the initial states $|0\rangle$, $|1\rangle$, $\frac{|0\rangle+|1\rangle}{\sqrt{2}}$, $\frac{|0\rangle+i|1\rangle}{\sqrt{2}}$. The initial states are shown in the Bloch sphere above each plot. The pulse sequence is shown schematically below.

$|1\rangle$ state plot is the inverse of the $|0\rangle$ state plot, as it is simply Rabi oscillations initiating in the $|1\rangle$ state instead of the $|0\rangle$ state. The $(|0\rangle + |1\rangle)/\sqrt{2}$ and $(|0\rangle + i|1\rangle)/\sqrt{2}$ state plots are a little more complex since when the phase passes through the axis upon which the prepared state lies no change occurs. Rotation about the other axis has the effect of moving the state to either the $|0\rangle$ or $|1\rangle$, depending on the sign of the vector.

3.2 Tunneling measurement and flux-state readout

The qubit manipulations that have been discussed in this chapter may be applied to any superconducting qubit, since the two-level system manifold and Bloch vector representation is common to all of them. While there are measurement/readout schemes that also may be common to all of them, here we describe a tunneling measurement/flux-state readout scheme that is unique to the metastable phase qubit, thanks to the small tunnel barrier between its two wells.

3.2.1 Tunneling measurement

Tunneling measurement is a single-shot, destructive measurement method that takes advantage of the multi-well nature of the metastable phase qubit. After the qubit control manipulations have completed, a fast flux pulse is applied on the order of nanoseconds. This measure pulse is calibrated to cause the qubit to spill into the adjacent well $\sim 95\%$ of the time if it is measured to be in the $|1\rangle$ state, and $\sim 5\%$ of the time if it is measured to be in the $|0\rangle$ state. A schematic picture of the tunneling measurement process is shown in Figure 3.11. The blue curve is the operate potential where the qubit has been manipulated, and the red curve is the potential well during a measure pulse. When a tunneling event occurs the deep well states are occupied; in Figure 3.11 only the two qubit energy levels are plotted.

3.2.2 Ring-down

After a tunneling event, the system is in an energy state far above its ground state, and therefore can be thought of classically as a particle oscillating at high amplitude in the deep well. This

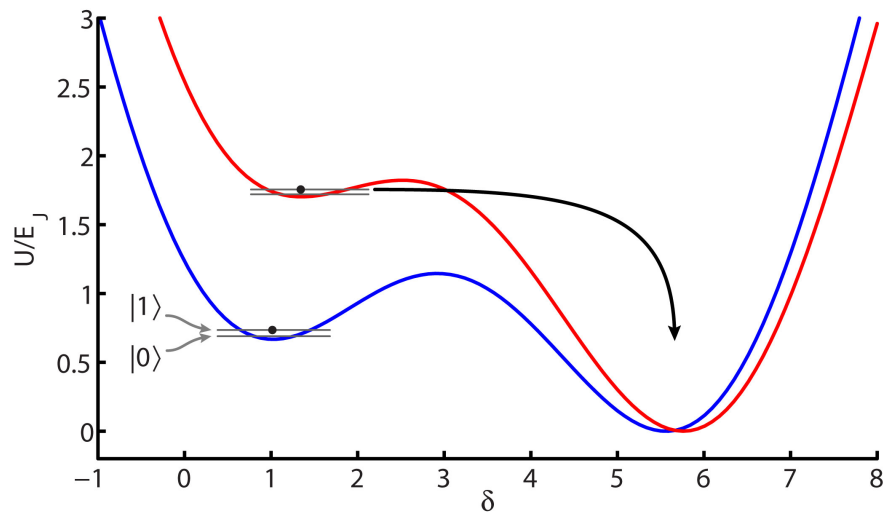


Figure 3.11: Tunneling measurement - A schematic picture of the tunneling measurement process. The fast measure pulse is calibrated so that when the qubit state is measured to be in the $|1\rangle$ -state, then a tunneling event will occur $\sim 95\%$ of the time, and $\sim 5\%$ of the time a tunneling event will occur if it is measured to be in the $|0\rangle$ state. The blue curve is a potential well shape before the measure pulse is applied, and the red curve is the potential well shape while the measure pulse is applied. Only the qubit energy levels are shown.

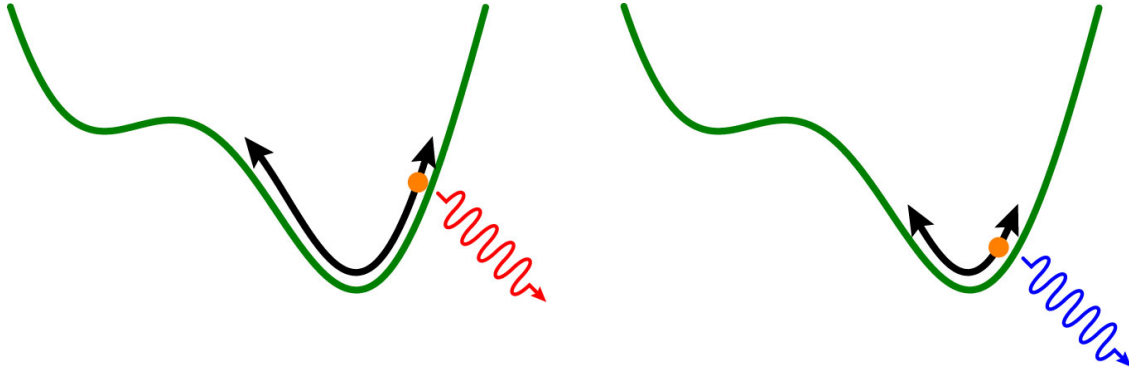


Figure 3.12: Voltage pulse from ring-down - As the particle decays in the deep well it is emitting a chirped voltage pulse to whatever is connected to it, altering any quantum systems. The pulse starts at low frequency and moves to high frequency.

ringing can be thought of classically since the deep well potential is nearly harmonic ($\alpha_r < 1\%$) and has many states. The oscillation changes frequency as it decays since the well is anharmonic, such that the frequency increases as the amplitude of oscillation drops, creating a chirped voltage pulse that often spans several GHz and can effect other quantum systems such as coupled qubits or cavities[59][60][61]. The decay process is shown as the classical particle ringing down in Figure 3.12. Quantum mechanically, the state is decaying by spontaneous emission from one energy level to another in the deep well; the deep well has so many states that it may be thought of as a continuous decay. Solutions to the ring-down radiation problem for multi-qubit systems have included making all measurements simultaneously[59] as well as using narrow linewidth cavities as coupling elements between qubits while keeping the unmeasured qubit(s) detuned from the cavities[61].

3.2.3 Retrapping

The tunneling measurement relies on a rapid energy decay in the deep well during the measure pulse to keep the state from tunneling back into the shallow well and causing a false readout of the $|1\rangle$ state as a $|0\rangle$ state. If the measure pulse finishes and moves the potential back to its original shape before the tunneled state has sufficiently decayed, the state could tunnel back into the shallow well, shown schematically in Figure 3.13. Known as retrapping, this behavior artificially lowers the

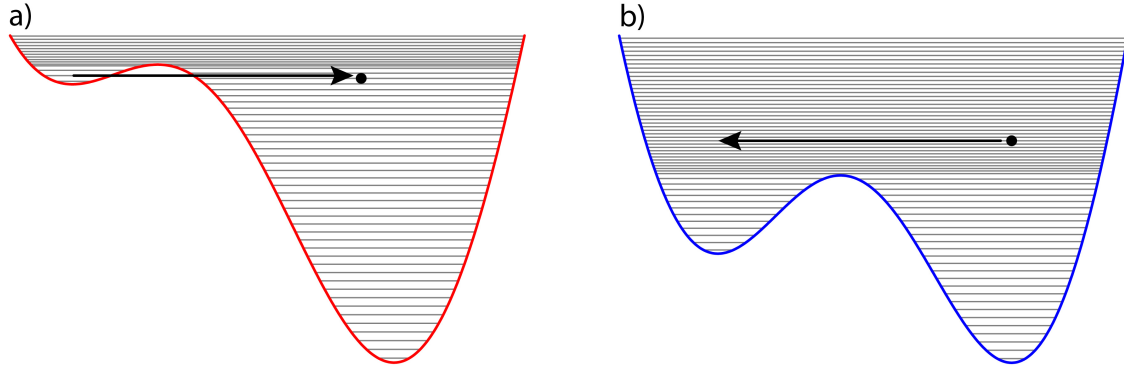


Figure 3.13: The retrapping process - If the particle tunnels, as in a), and the measure pulse moves back to the operate position more quickly than the decay in the adjacent well can move the state below the barrier, as in b), then there is a significant probability that the state will move back to the qubit well. This will make a $|1\rangle$ -state measurement falsely register as a $|0\rangle$ -state, and $P_{|1\rangle} = 1$ will not be realizable at any measure pulse amplitude.

maximum probability achievable for S-curve measurements. Figure 3.14a shows the anti-retrapping measure pulse's effect on retrapping. One solution to this problem is to use an asymmetric anti-retrapping measure pulse. Instead of a hard pulse that is symmetric in time, the anti-retrapping measure pulse rises quickly, then decays slowly to give the state in the right well time to decay to the ground state (Figure 3.14b). While the anti-retrapping measure pulse was not necessary for devices with lifetimes shorter than a few hundred nanoseconds, it has been crucial for longer-lived devices. The retrapping problem suggests the need for a fast, broadband, tunable damping solution.

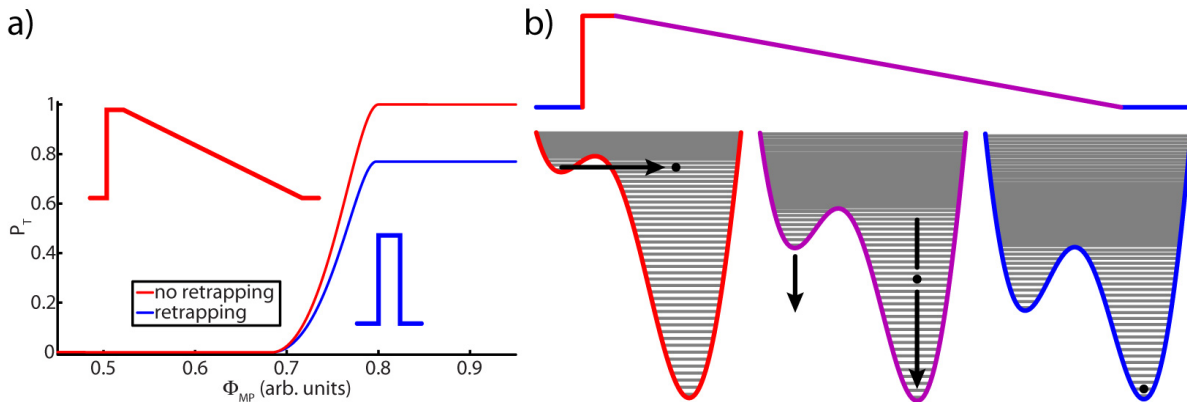


Figure 3.14: The anti-retrapping measure pulse - a) While a fast, symmetric measure pulse will allow retrapping with long-lifetime qubits, an asymmetric anti-retrapping measure pulse keeps a tunneled $|1\rangle$ -state measurement in the appropriate well. b) The potential slowly changes from the shallow measure pulse to the deep operate potential.

3.2.4 Tunneling advantages and disadvantages

Using tunneling measurement with metastable phase qubits has been successful because it provides a single-shot, high-fidelity quantum measurement [55] that can be later read out from a stable double-well configuration. Also, since there is no measurement being conducted on the qubit during manipulation (besides environmental loss, which can be thought of as a continuous weak measurement that is always present), the effect of such “Heisenberg microscope” measurements [43] need not be taken into account (such as the AC Stark shift when performing dispersive measurement with a cavity [62]), simplifying the qubit dynamics. Yet tunneling measurement of the metastable phase qubit has a few major flaws. First, crosstalk between two coupled qubits during measurement has been observed both through a coupling capacitor [59] and through a cavity coupling them [61]. Such crosstalk suggests that either great efforts need to be made to dynamically decouple qubits when one is being measured, or accept that all the coupled phase qubits must be measured simultaneously, placing significant limitations on their utility in quantum information processing. Second, tunneling measurements are destructive, requiring a potential well reset pulse afterwards and precluding the use of measured qubits in subsequent operations. Third, the readout of the tunneling measurement requires moving the qubit flux to the double-well configuration for the readout of its flux state. This is another step that must be added to the reset and operate steps and thus increases the total time required to do one manipulation/measurement cycle.

3.2.5 Standard DC SQUID readout

3.2.5.1 Schematic description

Coupling a DC SQUID to a metastable phase qubit allowed the fast measurement scheme [63] that has become the standard method of metastable phase qubit operation. The long term stability of the symmetric double well potential allowed the readout of DC SQUIDs using a simple, slow current ramp. Figure 3.15 is a wiring schematic for a standard metastable phase qubit coupled to

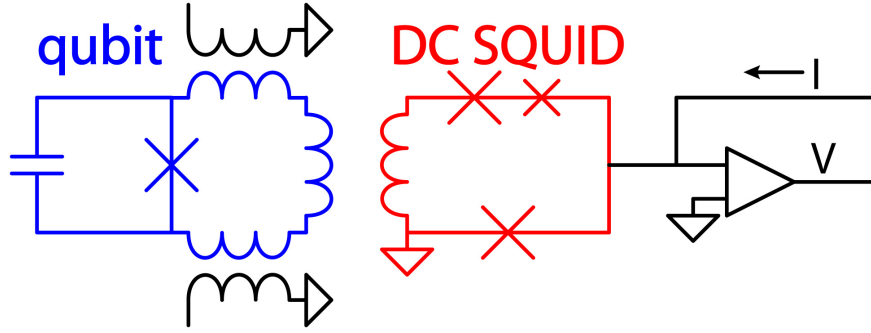


Figure 3.15: Qubit/DC SQUID circuit schematic - A metastable phase qubit coupled to a DC SQUID, which is used for readout. The DC SQUID is driven with a current ramp, and a threshold detector watches the voltage to look for a switching event.

a DC SQUID readout, including qubit control lines.

As already described above, after the fast measure pulse the flux bias is changed to the stable double-well potential at $\Phi_{ex}/\Phi_0 = 0.5$, shown in Figure 3.16. This separates the result of the fast measure pulse, effectively freezing it, so it may be read out on much longer time scales than the stability of the previous metastable well. Since the two wells are separated by a flux quantum, an inductively coupled DC SQUID is used to distinguish whether the phase particle is in the left or right well, corresponding to having measured the logical $|0\rangle$ and $|1\rangle$ qubit states.

The DC SQUID is efficiently designed using three Josephson junctions with different critical currents such that its response to applied flux is asymmetric, with flux sensitivity at zero applied flux, as seen in Figure 3.17. If there were only two symmetric junctions there would be no flux sensitivity at zero flux bias, necessitating another flux bias line to offset the DC SQUID to a flux-sensitive place.

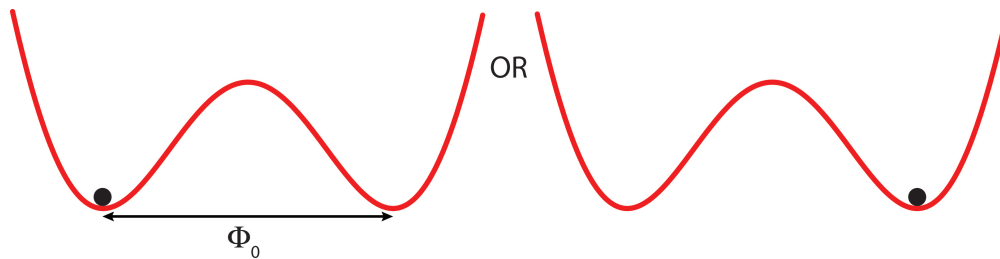


Figure 3.16: Qubit state readout - The qubit is biased to a stable double-well potential, separated by a flux quantum Φ_0 for readout. The current to the SQUID is ramped during readout, looking for the tunneling event that will describe the double-well flux state.

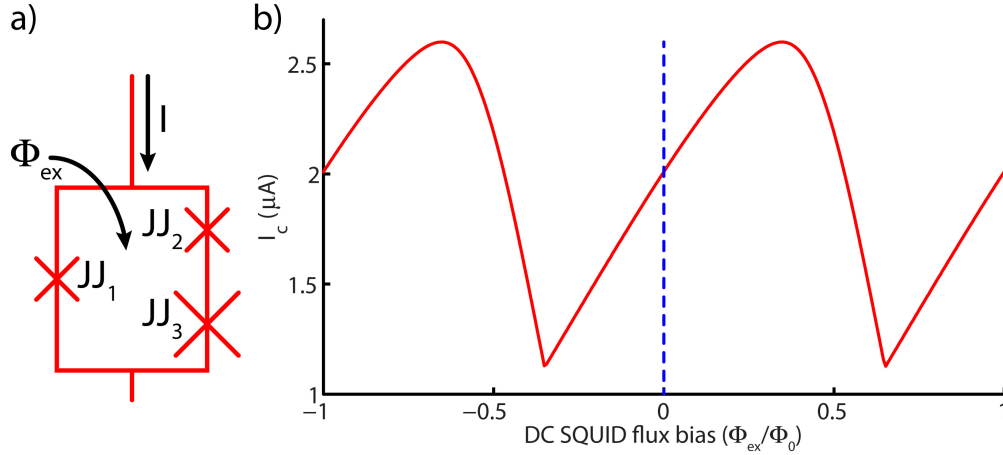


Figure 3.17: DC SQUID flux response - a) A DC SQUID with 3 different Josephson junctions has an asymmetric flux response curve b), with flux sensitivity at zero applied flux (blue dotted line).

The temporal sequence of qubit initialization, operation, measurement, and readout with the DC SQUID is shown in Figure 3.18, and is largely the same as the basic method outlined in Section 3.1.1. The qubit is reset in a single-well potential, moved to the operate flux where operations are performed, then the qubit is measured using a fast flux pulse. After moving to the symmetric double well potential, the DC SQUID flux readout is accomplished by ramping the applied current until the SQUID switches to its voltage state. A timer is started at the beginning of the current ramp, and stops when the switching event happens and the voltage across the SQUID crosses a preset threshold. The switching event will happen earlier if the qubit is in the flux state that is Φ_0 greater than the other, since the SQUID's critical current will be suppressed by the extra Φ_0 of flux.

3.2.5.2 Advantages and disadvantages

DC SQUID readout has been very successful for systems of a few qubits, as it provides stable, high signal-to-noise single-shot readout using low-cost electrical components. But as the superconducting phase qubit community moves toward many-qubit quantum processing, it is clear that the DC SQUID will be prohibitive for the following reasons. First, the DC SQUID is directly coupled to the outside world, and thus is a potential source of noise. The noise seen by the qubit from the

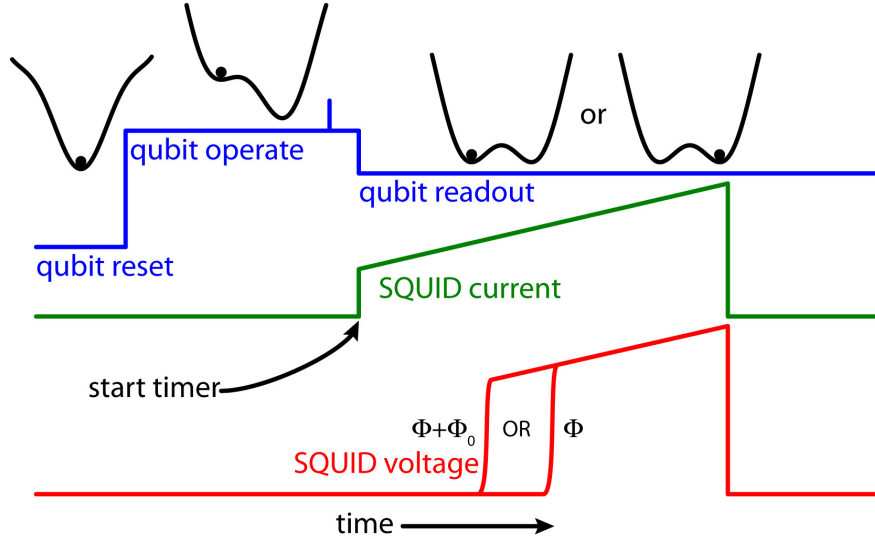


Figure 3.18: Tunneling readout sequence - The qubit is initialized by moving the particle to the reset well. Qubit operations are carried out at the operate flux, and fast measurement happens directly after. The qubit is then moved to the stable double well for readout, where the DC SQUID current is ramped until switching. The time between when the timer starts and when the switching occurs reveals the qubit flux state, and therefore the result of the measurement.

SQUID can be decreased by careful design and bias tuning [64], and by decreasing their coupling. Yet if they are too decoupled, the flux quantum change in the qubit loop will be a very flux small change in the DC SQUID loop, and the two states will be indistinguishable, within the noise of the switching DC SQUID. Thus, the switching noise is a fundamental limitation of the DC SQUIDs, setting the limit on how much it can be decoupled from the qubit. Ideally, the qubit would be completely decoupled from its environment until the time of readout, so decoupling the readout device as far as possible from the qubit is desirable.

The switching current readout method used with DC SQUIDs has the further disadvantage that it emits Josephson radiation while in the voltage state according to $f_J/V = 2e/h = 483.6$ THz/V. This radiation has the potential to disturb adjacent qubits whose states one does not wish to perturb while reading out the original qubit, so the DC SQUID is less practical for multiple qubit processors that need to measure qubits at different times. Additionally, because the DC SQUID is directly coupled to the room temperature world and thus requires heavy filtering to minimize noise, there is a limit on how quickly the readout can be done, set by the filtering. Typical readout times

are in the tens of microseconds, much longer than the T_1 s of even the best metastable phase qubits. Finally, the dependance of the DC SQUID on three Josephson junctions quadruples the number of junctions per qubit that must be engineered. Even in a stable junction fabrication process, variability in the fabrication of Josephson junctions makes it desirable to minimize the number of junctions necessary to build a device.

3.2.6 Tunable cavity readout

3.2.6.1 Schematic description

The tunable cavity has a very similar circuit schematic to the metastable phase qubit 3.19, and is similar in behavior. The main difference is that the ratio of the geometric inductance to the Josephson inductance (β_L) is less than 1, making it single valued at all flux biases. In contrast, the metastable phase qubit has $\beta_L > 1$, making it hysteretic with multiple potential wells at some or all flux biases. Regardless of β_L , the tunable cavity is always periodic in Φ_0 , as seen in Figure 3.20.

Another significant difference between the metastable phase qubit and the tunable cavity is the type and amount of coupling to the microwave line.

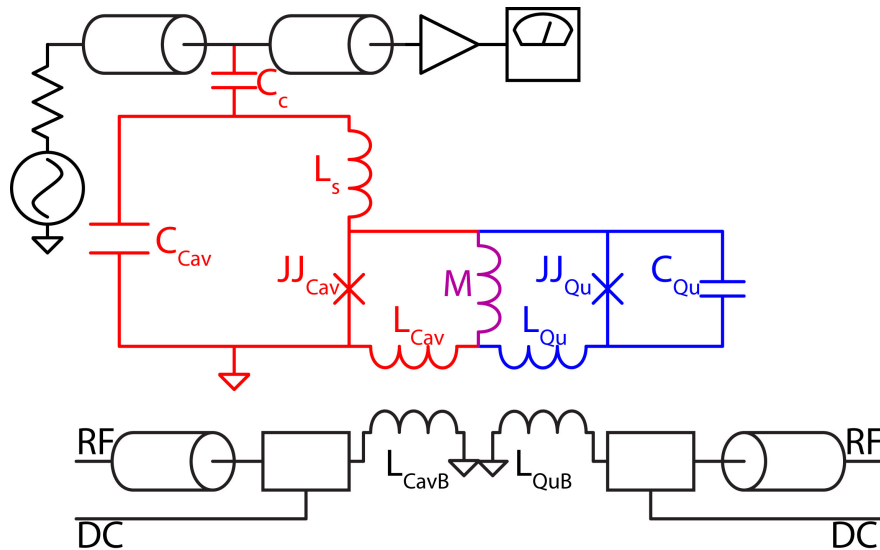


Figure 3.19: Qubit/tunable cavity circuit schematic - The circuit schematic for the tunable cavity coupled to a metastable phase qubit

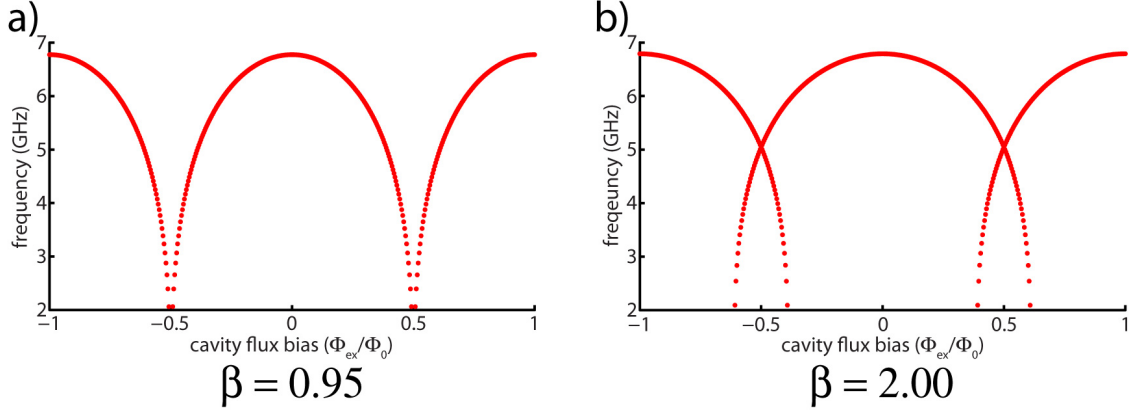


Figure 3.20: Tunable cavity spectroscopy for different β_L s - Tunable cavity spectroscopy for a) $\beta_L = 0.95$ (single valued) and b) $\beta_L = 2.00$ (hysteretic).

While our phase qubits are typically weakly coupled with an external quality factor of $Q_{ext} \sim 10^6$ for isolation, the tunable cavities reported here are coupled strongly with $Q_{ext} = 200 - 1000$ so that they respond quickly. They are also coupled to the microwave feedline through a single capacitor on a tee, so they appear as Lorentzian dips when making a transmission measurement. The form of the S_{21} scattering matrix element for a Lorentzian dip is

$$S_{21} = \frac{S_0 + 2iQ \frac{\omega - \omega_0}{\omega_0}}{1 + 2iQ \frac{\omega - \omega_0}{\omega_0}}, \quad (3.11)$$

where the measured quality factor Q and the dip height S_0 can be written in terms of internal and external quality factors using

$$\frac{1}{Q} = \frac{1}{Q_{int}} + \frac{1}{Q_{ext}}, \quad S_0 = \frac{Q_{ext}}{Q_{int} + Q_{ext}}. \quad (3.12)$$

The internal losses include dielectric losses in the shunting capacitor and Josephson junction, while the external losses occur through the coupling capacitor to the 50Ω microwave feedline. These are largely independent loss channels, and may be somewhat engineered, although the mechanisms of internal loss are still being explored and are not completely controllable yet. However, the external loss through the coupling capacitor to the feedline may be readily designed by changing

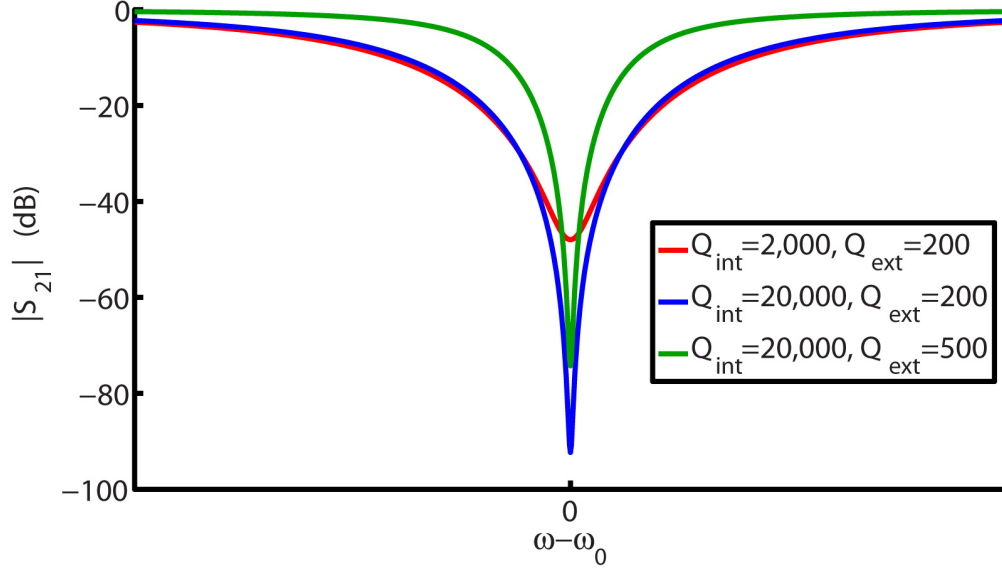


Figure 3.21: Dip resonator quality factor - The internal and external quality factors, Q_{int} and Q_{ext} , in a dip resonator change the shape of the resonance somewhat independently. As the Q_{int} increases the dip gets deeper without its width changing much. When Q_{ext} is increased, the dip narrows significantly, without losing much depth. Note, however, that changing Q_{ext} affects the dip depth more than changing Q_{int} affects the dip width.

the value of the coupling capacitor. The effects of different internal and external quality factors on the dip resonance are shown in Figure 3.21. During measurement and readout the cavity is simply a means for transferring information about the qubit state to the outside world. It is therefore ideal to have no internal loss ($Q_{int} \rightarrow \infty$) and use the external loss to control the speed with which the information is transferred. This means that decreasing dielectric and Josephson junction losses is important for the cavity as well as the qubit, and that the trade-off between suppressing qubit loss via the Purcell effect and increasing information transfer speeds must be balanced for a particular application.

The dip resonator has an unambiguous signal if its amplitude is measured, but its phase trace in frequency space starts and ends at 0° , as seen in Figure 3.22a. One could sweep a frequency range and use the trace to detect the resonator’s frequency, but a more efficient way to detect a frequency shift is to just look at one frequency and measure either amplitude or phase. Amplitude is symmetric about the resonant frequency for both dip and peak resonators, so a single amplitude

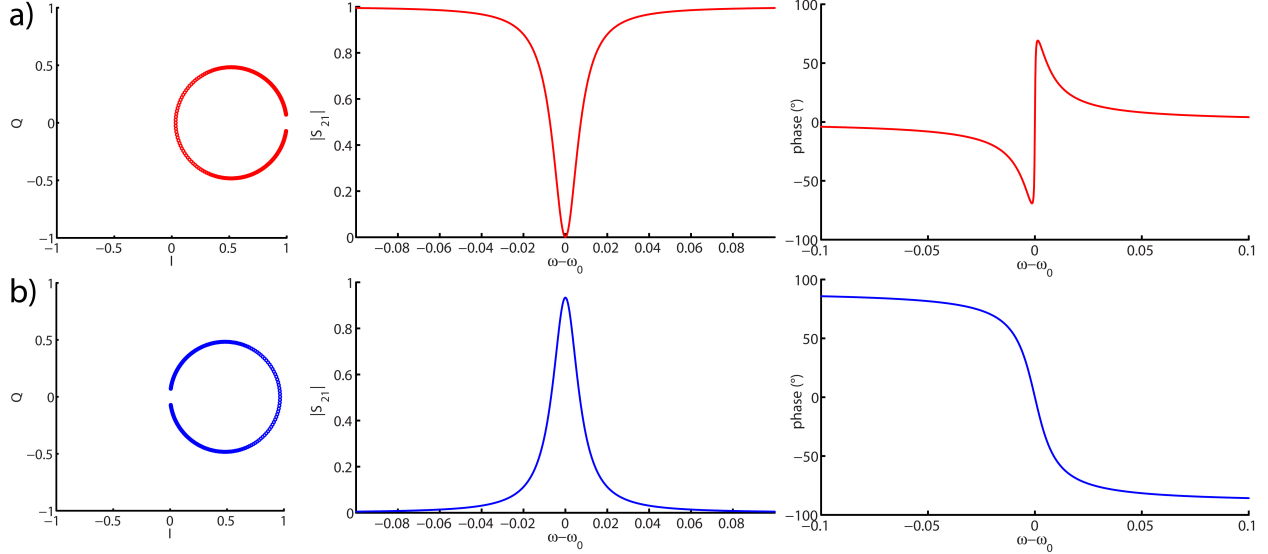


Figure 3.22: Dip resonator and peak resonator - a) Dip resonator frequency response plotted in IQ space, in amplitude, and in phase. b) a peak resonator plotted in IQ space, in amplitude, and in phase. The transformation $I_{peak} = 1 - I_{dip}$, $Q_{peak} = -Q_{dip}$ can be used to move between them.

measurement would not indicate the direction of frequency change. The frequency change direction for a dip resonator, when measured as phase, is clear for small changes from the resonant frequency, but can be ambiguous for large frequency shifts. The clearest frequency shift measurement is done by measuring the phase of a peak resonator. This does not, however, limit circuit designs only to peak resonators since the simple transformation $I_{peak} = 1 - I_{dip}$, $Q_{peak} = -Q_{dip}$ allows a dip resonator to be plotted as a peak resonator, where I_{dip} and Q_{dip} are the measured values of the dip resonance and I_{peak} and Q_{peak} are the transformed values. The phase data from the tunable cavity reported in this work are all presented with this transformation applied.

The tunable cavity can be used to do both flux magnetometry readout for the tunneling measurement scheme, like the DC SQUID, as well as dispersive measurement. Performing flux magnetometry with the tunable cavity depends on it being biased to a spot that is sufficiently flux sensitive to clearly show a frequency change when the qubit flux changes by Φ_0 , schematically shown in Figure 3.23. Dispersive measurement also involves detecting a frequency change in the cavity, but the change is due to the energy state of the qubit and not the flux in the qubit loop. Since the cavity frequency directly follows the qubit state, dispersive measurement is performed

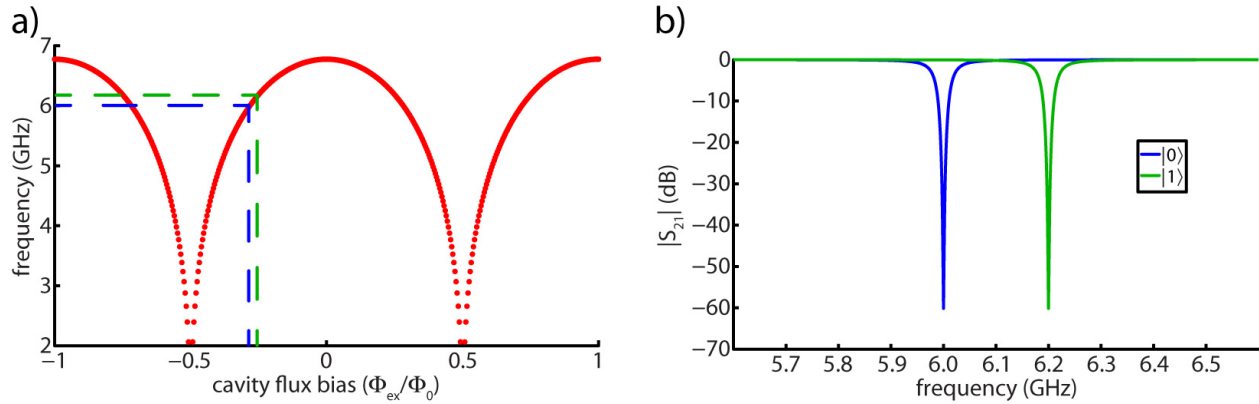


Figure 3.23: Flux magnetometry using the tunable cavity - a) By biasing the tunable cavity to a sufficiently flux sensitive place one may readout the flux state of the qubit, distinguishing between the readout states representing the $|0\rangle$ and $|1\rangle$ qubit states. b) In practice this means driving the cavity at one of the two possible resonances and measuring the power returned to readout the flux state. Note that this may also be done using the phase of the cavity, instead of the amplitude.

during the operate part of the flux ramp, and doesn't require a separate readout flux level and corresponding readout time. Schematic pulse sequences for the two methods are shown in Figure 3.24.

3.2.6.2 Advantages of the tunable cavity

The tunable cavity has the potential to remedy many of the problems with DC SQUID readout. Since the tunable cavity is driven with small amplitude microwaves, there is no emitted Josephson radiation from switching to the voltage state. Because it can be operated without being directly wired to room temperature electronics, the tunable cavity can also be much more decoupled from the environment than the DC SQUID. Also, the strong coupling to the qubit required by the DC

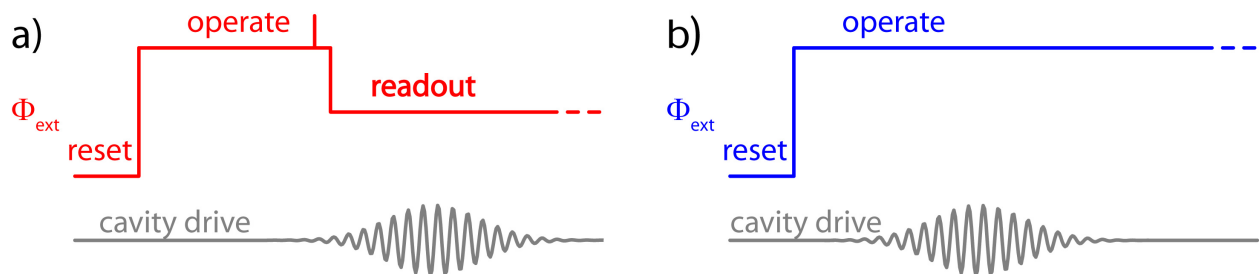


Figure 3.24: Tunable cavity control - Control of the tunable cavity for a) the tunneling measurement scheme and b) the dispersive measurement scheme. Note that the tunable cavity can be placed in an arbitrary place during the operate time

SQUID to overcome its switching noise limitations is not necessary for a tunable cavity since its state discrimination is limited by the amplifier chain and the cavity flux sensitivity, which may be tuned to overcome remaining noise.

Another advantage of the tunable cavity is its speed; it can be read out as fast as the amplifier noise will allow. Using a low noise amplifier, such as a SQUID amplifier[65][66][67], right at the output of the tunable cavity can increase the signal to noise ratio to down near the quantum limit, speeding up the data taking rate.

The tunable cavity may also be frequency multiplexed with other tunable cavities to reduce the number of lines required to operate a quantum processor. Although frequency multiplexing has been demonstrated with DC SQUIDS[68][69], it requires extra circuitry on chip that may become cumbersome with a large number of devices. Tunable cavities are effective for multiplexing[70] low temperature devices and require little more chip real estate than unmultiplexed DC SQUIDS.

A final advantage of doing readout with an tunable cavity is that it can be used for qubit state transfer[71][72] and storage experiments[40][39]. This can be done while still using the tunable cavity as a readout element, though these experiments usually require high quality factor cavities. Either one would have to accept a slow measurement/readout or perform experiments robust enough for a low quality factor cavity. Another option would be to use an tunable coupler[73][74] instead of a coupling capacitor between the microwave feedline and the tunable cavity to dynamically change its external quality factor.

3.3 Dispersive measurement

3.3.1 Jaynes-Cummings and the dispersive shift

As was shown in Chapter 2, the dispersive shift on the cavity as a result of the qubit state for a two-level qubit is $\delta\omega_r = \pm g^2/\Delta_{01}$. This corresponds to a phase shift $\delta\phi = \pm \tan^{-1} (2g^2/\kappa\Delta_{01})$ [23];

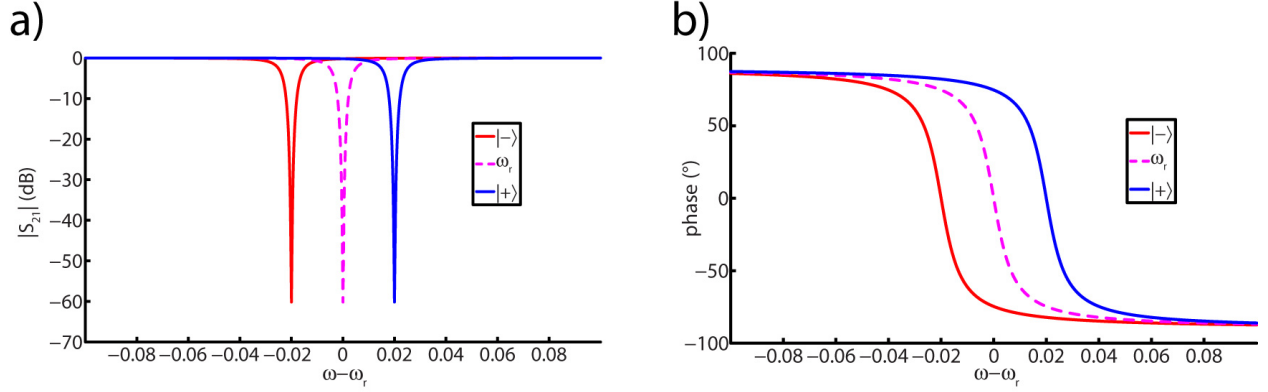


Figure 3.25: Dispersive shift in the cavity - The dispersive shift of the cavity from its center frequency ω_r due to the qubit state $|\pm\rangle$.

both effects are plotted in Figure 3.25. For the three level qubit, these values become $\delta\omega_r = \pm [g^2/\Delta_{01} - g^2/\Delta_{12}]$ and $\delta\phi = \pm \tan^{-1} (2/\kappa [g^2/\Delta_{01} - g^2/\Delta_{12}])$. The separation of the two curves clearly depends on three factors: the coupling g , the detuning Δ_{01} , and the quality factor $Q = \omega_r/\kappa$, since the width of the dip or the slope of the phase change near resonance changes with Q . Strong couplings quickly increase the separation between states since the shift goes as g^2 , though they come at the cost of a larger straddling regime (the region where $\omega_q \approx \omega_r$) and greater loss through the cavity. The detuning factor is only linear, but it is clear that large detunings will have smaller separation. For a device with a low quality factor, large detunings will be particularly challenging to see. Practically, it is easy to become limited by amplifier noise since measurement with photon numbers on the order of one helps reduce dephasing due to a qubit frequency shift as a result of the AC Stark shift.

3.3.2 The AC Stark shift

As the number of photons in the cavity increases, the qubit frequency changes because of the AC Stark shift $\Delta f_{ac} = 2ng^2/2\pi\Delta_{01}$ [62]. The linearity of the shift with photon number allows a nice calibration of the photon number to power applied to the cavity. This calibration is essential to operating in the single photon regime, since it is exceedingly difficult to know what power is being

applied to the cavity, with any precision, since there is usually a long and complex path between the microwave generator and the device at the bottom of a dilution refrigerator. Figure 3.26a shows the Stark shift of a qubit at two different frequencies. The slope of either of these lines, $\Delta f/P$, can be set equal to the Stark shift divided by drive power P to get a calibration for the number of photons in the cavity n per power P .

$$\frac{\Delta f}{P} = \frac{2ng^2}{P\Delta_{01}} \rightarrow \frac{n}{P} = \frac{\Delta f}{P} \frac{\Delta_{01}}{2g^2}. \quad (3.13)$$

Figure 3.26b is the calibration. Note that the calibrations for the two qubit frequencies are the same; the calibration is valid at any qubit frequency, as long as the power delivered is the same at each frequency.

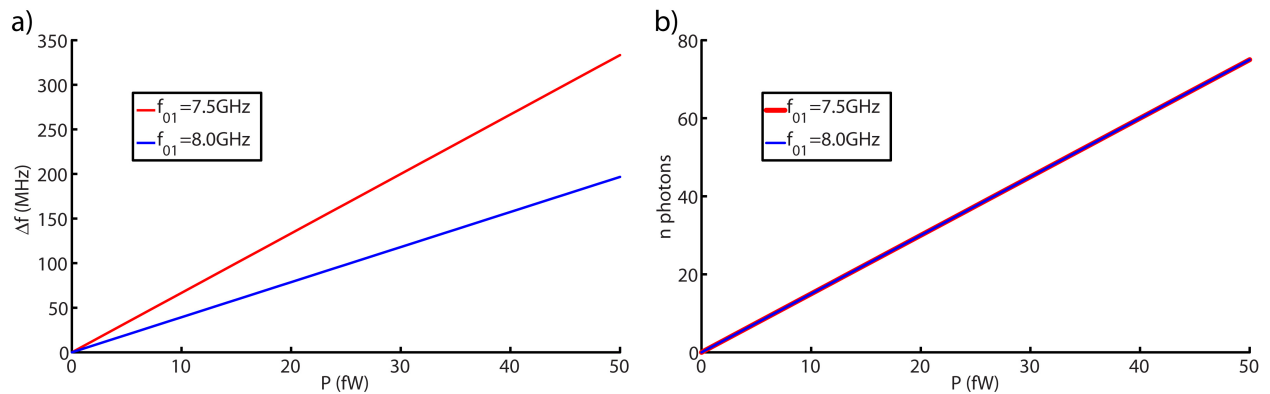


Figure 3.26: The AC Stark shift - As the drive power to the cavity increases, the qubit's frequency is shifted by the Stark effect. a) The Stark shift for two different qubit frequencies, which obeys $\Delta f_{ac} = 2ng^2/2\pi\Delta_{01}$. b) The slope of the shift gives a count for the number of photons in the cavity at a given drive power.

4

Design and modeling of the device

4.1 Metastable phase qubit design

When designing a metastable phase qubit, one must consider the effect of junction size and area, geometric inductance and capacitance values, and coupling to the outside world through bias lines, ground planes, and other circuit elements like cavities. More practical requirements, such as how much current may be driven through the experimental setup, or the microwave range of the available components, must also be considered in the design process. For instance, it is not difficult to design qubits that run at 30 GHz, but a given lab may only have generators and components up to 8 or 18 GHz, limiting the frequency range of devices they may explore.

Each of these decisions affects the others, so it is useful to choose a linear path in the design process, deciding what parameters are essential for a particular experiment and what parameters are less important and may be left subservient to the essential ones. The effect of each parameter on the others must also be explored, and the behavior of the entire circuit must also be considered. The value of electromagnetic simulation software, such as Microwave Office or Sonnet (both of which were used here), cannot be understated in designing predictable devices that give the experimenter the freedom to focus on the science they intend to explore.

4.1.1 Junction, inductor, and capacitor design

The Josephson junction is the heart of any superconducting qubit, and it is often efficient to design the device around a particular junction and desired well shape, described by the parameter β_L . As was previously discussed (Section 2.2.1.1), small area Josephson junctions are desirable for low-loss applications like qubits, since reducing the junction area reduces the number of spurious TLSs seen by the qubit[75]. The size of the junction is usually limited by practical fabrication capabilities. For this work, both ion-milled via-style and shadow evaporated junctions were used, and both were defined using photolithography. Even though spurious TLSs push designers toward small junction areas, the critical current may still be engineered over a large range by changing oxidation times or pressures to control the tunnel barrier thickness. This barrier determines the effective inductance of the junction, which, combined with the geometric inductance, determines the value of β_L . This, in turn, determines range of shunting capacitor values that will put the qubit in the frequency range desired by the experimenter.

In recent years it has become clear that clever circuit design can be used to mitigate materials losses by changing circuit geometry[76]. Capacitors in particular couple to nearby materials which behave as capacitor dielectrics, contributing their intrinsic loss tangents to the capacitor loss, since capacitors rely on electric fields between electrodes to store energy. For interdigitated capacitors (IDCs), simply increasing the spacing between capacitor fingers decreases the electric field density inside the dielectric substrate below them and increases the internal quality factor of IDC LC resonators. Another approach to decreasing loss is to put more energy into less lossy circuit elements by increasing the low-loss element participation ratio. This happens naturally as junction areas shrink since a decrease in critical current must be compensated for by making the geometric inductance larger in order to have the same β_L , which in turn decreases the size of shunting capacitor needed to maintain the same frequency range.

Although small capacitances and large inductances can have loss advantages, how they affect the

shape of the metastable phase qubit spectroscopy must be considered when designing. The effect on the qubit spectroscopy of changing β_L by changing the geometric inductance L_{Qu} was previously shown to be a flattening of the spectroscopy as β_L increases, seen in Figure 2.10 (Section 2.3.1). The effect of L_{Qu} on the spectroscopy when β_L is held constant, allowing I_c to change, and dividing C_{Qu} by the same factor L_{Qu} is changed by in order to keep the frequency the same is shown in Figure 4.1, along with the effect of only changing the shunt capacitor. The geometric inductance on its own has very little effect on the shape of the spectroscopy curve. It is the ratio of inductances β_L that really changes the shape, as was seen in Figure 3.20. The shunting capacitor's largest effect is to shift the qubit frequency higher (lower) for smaller (larger) capacitances, though flattening of the curve occurs for large capacitances. The shape of the spectroscopy curve matters because a flatter curve, with less frequency range, makes the qubit less susceptible to flux noise.

Different capacitor geometries have different advantages and disadvantages. A parallel plate capacitor has the advantage of being an almost purely capacitive component, with very little inductance. If the dielectric between the plates is removed and only vacuum remains, only loss to

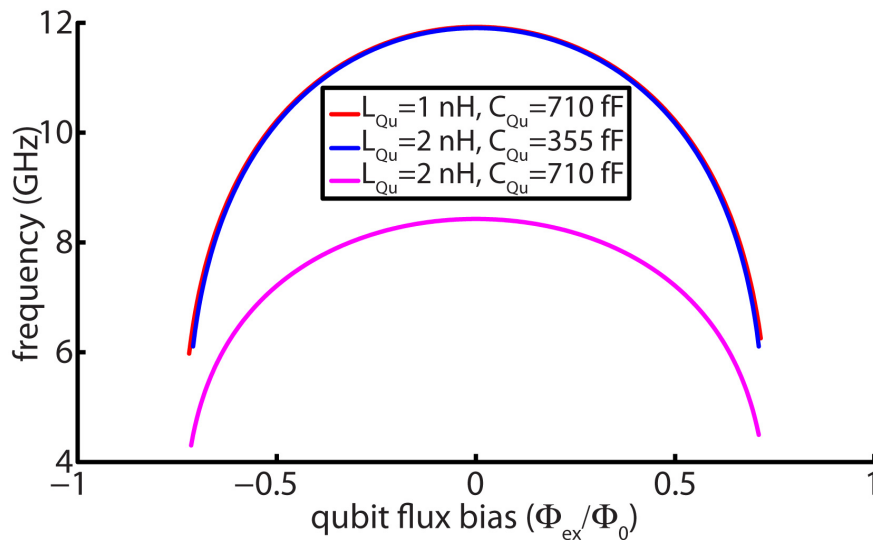


Figure 4.1: How L_{Qu} and C_{Qu} affect qubit spectroscopy - How the geometric inductance L_{Qu} and shunting capacitance C_{Qu} affect the spectroscopy for a constant $\beta_L = 3$. Calculated numerically from the Schrödinger equation. The ends of the spectroscopy are where the $|1\rangle$ state disappears because the barrier between wells is too small; this point is probably unobtainable in practice as a tunneling event is likely to occur very quickly here, before spectroscopy could be taken.

TLs in surface dielectrics contributes to the capacitor loss tangent. But in either case multi-layer processing is required to make a parallel plate capacitor. An interdigitated capacitor may, on the other hand, be made in a single layer, although it requires a large footprint if it is to have large spacing between fingers to decrease the electric field densities in the surface dielectric TLs. It is also quite inductive, requiring a more complex circuit model to describe its behavior along with a decrease in the qubit anharmonicity. Both parallel plate vacuum gap capacitors, described in [77], and interdigitated capacitors were used in this work.

4.1.2 Bias line design

While a seemingly mundane part of design, the bias control line to a qubit or tunable cavity can drastically affect the performance of the device. The bias line can be a significant source of noise if coupled too strongly, so care must be taken to estimate this noise properly in the design phase. Ideally one would like a bias line that is coupled just enough to apply currents necessary to run the experiment, but no more, in order to limit noise. It is important to use an EM solver to properly account for all the currents in a given design, getting an accurate measurement for the coupling.

We can write the Norton equivalent circuit of a bias coil inductively coupled to a parallel LC resonator as shown in Figure 4.2, where

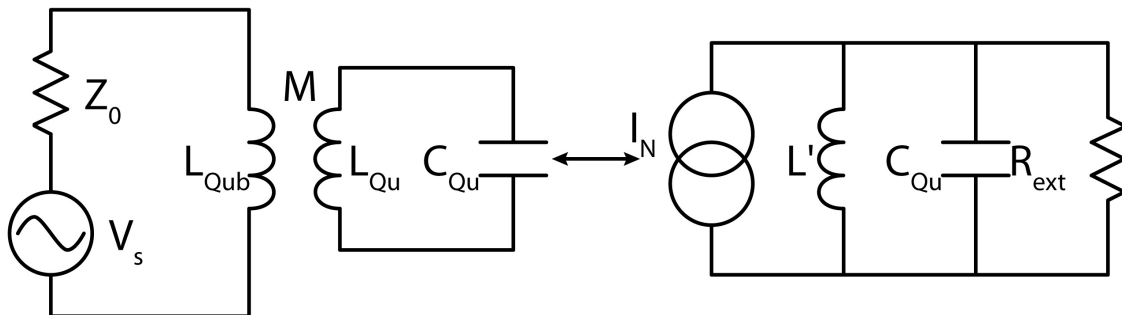


Figure 4.2: Bias coil Norton equivalent circuit - A bias coil inductively coupled to a parallel LC resonator may be transformed into a Norton equivalent circuit.

$$L' = L_{Qu} \left(1 - \frac{\omega (M^2/L_{Qu}) \omega L_{Qub}}{Z_0^2 + \omega^2 L_{Qub}^2} \right), \quad R_{ext} = \frac{L_{Qu}^2 Z_0}{M^2}, \quad (4.1)$$

and

$$I_N = \frac{MV_s}{L_{Qu} \sqrt{Z_0^2 + \omega^2 L_{Qub}^2}} e^{i\theta}, \quad \tan \theta = -\frac{\omega L_{Qub}}{R_{ext}}. \quad (4.2)$$

From this we may write an expression for a resonator's energy decay if the only source of damping is the bias line impedance Z_0

$$T_1 = R_{ext} C_s = \frac{L_{Qu}^2 Z_0}{M^2} C_{Qu}. \quad (4.3)$$

For a resonator with $L_{Qu} = 2.5$ nH and $C_{Qu} = 300$ fF, an $M = 10$ pH coupling gives $T_1 = 938$ ns, while an $M = 1$ pH coupling gives $T_1 = 93.8$ μ s, two orders of magnitude longer. Clearly the $1/M^2$ factor allows for clean isolation of the qubit from the 50Ω feedline when M is sufficiently small.

It is not enough to have a coil with the proper spacing between it and the device; one must also provide a current return path to the ground plane, anchored far away from the coil. In the complex flux environment of a superconducting ground plane, with arbitrary trapped flux gradients from vortices, it is an inaccurate assumption that currents returned to the ground plane near the coil will spread evenly through the ground plane to leave the chip. An uneven distribution of returning currents in the superconducting ground plane can create fluxes in the qubit loop that will not be seen by EM simulators that assume an even distribution of return currents, thus causing sometimes large errors in their calculations of M compared to the real device. Figure 4.3, the layout of the qubit-tunable cavity device measured in this work, shows two bias line designs. The bias line to the qubit L_{QuB} uses the ground plane near the device as a current return, and gave a mutual inductance 5 times higher than calculated by the EM simulations. The tunable cavity bias L_{CavB} design is both gradiometric and has a dedicated current return path wire, which extended all the way to the edge of the chip. It gave a mutual inductance that agreed with EM simulations. The gradiometric coil is positioned to be coupled to the tunable cavity, but not coupled to the qubit.

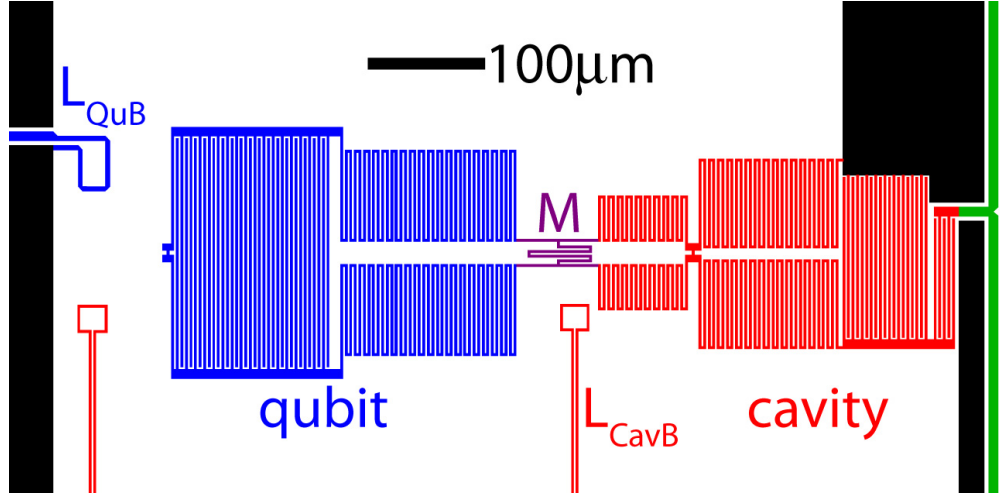


Figure 4.3: Two bias line designs - The layout of the qubit-tunable cavity device measured in this work. The qubit bias line L_{QuB} design sent its return current directly to the ground plane and gave $M = 10$ pH coupling to the qubit, even though EM simulations predicted $M = 1.9$ pH. The tunable cavity bias line L_{CavB} design was both gradiometric and had a dedicated current return path. It gave $M = 1.3$ pH, agreeing well with EM simulation.

4.2 Tunable cavity design

4.2.1 Junction, inductor, and capacitor design

The tunable cavity is, in general, the same circuit as the metastable phase qubit, just with a different β_L value; it is designed to be much more linear than the qubit. As discussed in Section 3.2.6, it is advantageous to have a high internal quality factor cavity so that most of the energy is accessible to the experimenter, instead of being lost to the environment. As discussed above (Sections 2.2.1.1 and 4.1.1), the geometry of the Josephson junction has a strong influence on its loss, as do the materials and geometry of the coupling capacitor. Minimizing loss in the junction for the tunable cavity is the same as for the qubit, so most likely one will choose the same junction for the cavity as for the qubit. The same goes for the tunable cavity's shunting capacitor, though the actual value will most likely be different than the qubit's shunting capacitor. If using an IDC for the tunable cavity shunting capacitor one need not worry about the reduction in anharmonicity due to stray inductance; the tunable cavity can be as harmonic as necessary.

Assuming that the Josephson junction is a source of significant loss, increasing the internal

quality factor means, after doing one's best to make a low-loss junction, decreasing the participation ratio of the junction in the total circuit. One way to do this is to add an inductance in series (L_s) with the inductive loop, as shown in Figure 4.4. This series inductance can be parallelized into an L_{eff} and R_{eff} parallel circuit, with the values

$$L_{eff} = L_s + \frac{L_1 (L_1 + L_s) R_J^2}{(L_1 + L_s) R_J^2 + L_1^2 L_s \omega^2} \quad (4.4)$$

and

$$R_{eff} = \left(1 + \frac{L_s}{L_1}\right)^2 R_J + \frac{L_s^2 \omega^2}{R_J}, \quad (4.5)$$

where $L_1 = L_{Cav} \parallel L_J$. The second term in the R_{eff} expression is small for reasonable loss in the junction ($R_{eff} = 20 \text{ k}\Omega$), so we can write this as

$$R_{eff} \approx \left(1 + \frac{L_s}{L_1}\right)^2 R_J. \quad (4.6)$$

The resonant frequency of the circuit with this extra series inductance, including the coupling

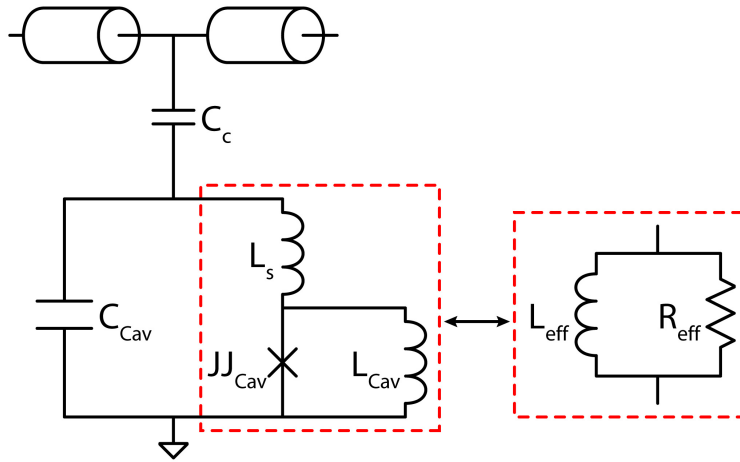


Figure 4.4: Tunable cavity with series inductance L_s - If the loss in the Josephson junction is significant, the internal quality factor of the tunable cavity can be increased by adding a series inductance to the inductive loop. This lowers the participation ratio of the junction in the total circuit. The circuit elements in the red box may be parallelized into an L_{eff} and an R_{eff} circuit.

capacitor, is well approximated by the expression

$$\omega_0 = \frac{1}{\sqrt{(L_1 + L_s)(C_c + C_{Cav})}}. \quad (4.7)$$

Here the capacitance of the small junction is assumed to be included in C_{Cav} . The expression for the internal quality factor of this circuit is

$$Q_{int} = \omega_0 R_{eff} (C_c + C_{Cav}) \approx \omega_0 \left(1 + \frac{L_s}{L_1}\right)^2 R_J (C_c + C_{Cav}). \quad (4.8)$$

The external quality factor of this circuit depends on the output line impedance Z_0 and the coupling capacitance C_c . Its effective resistance can be written as

$$R_{ext} = \frac{2}{Z_0 \omega_0^2 C_c^2}. \quad (4.9)$$

This can be used, along with the expression for L_{eff} , to write the expression for the external quality factor

$$Q_{ext} = \frac{R_{ext}}{\omega_0 L_{eff}} = \frac{2}{Z_0 \omega_0^3 C_c^2} \frac{(L_1 + L_s) R_J^2 + L_1^2 L_s^2 \omega^2}{(L_1 + L_s)^2 R_J^2 + L_1^2 L_s^2 \omega^2}. \quad (4.10)$$

The relationship between the series inductance L_s and the internal quality factor Q_{int} is shown in Figure 4.5a. Using a large L_s clearly increases Q_{int} without changing Q_{ext} very much. Yet applying this method for increasing Q_{int} to the qubit circuit may be problematic as L_s tends to linearize the device as it changes β_L , decreasing its frequency range. This effect may be clearly seen by changing L_s and compensating for the frequency shift by changing the shunting capacitance C_{Cav} and plotting the spectroscopic response, as in Figure 4.5b where $\beta_L < 1$.

For fast, efficient response it is desirable to design $Q_{ext} \ll Q_{int}$, since it is inefficient to have the cavity more internally lossy than the coupling to the feedline; if $Q_{ext} \geq Q_{int}$ then at least half of the energy leaves through unrecoverable channels and is not detected by the experimenter. Since

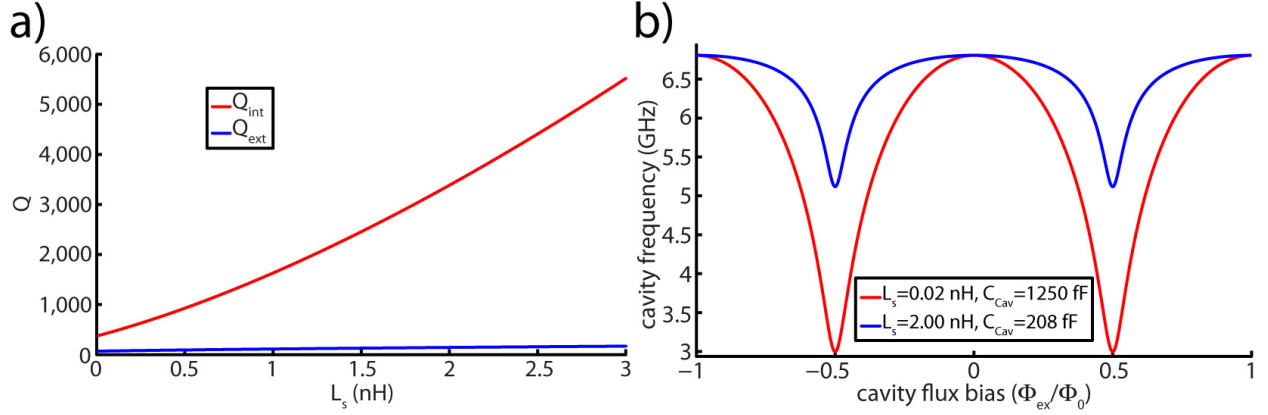


Figure 4.5: Tunable cavity Q and spectroscopy for changing L_s - a) The internal Q_{int} and external Q_{ext} quality factors are plotted for various series inductances L_s . Increasing L_s increases Q_{int} much faster than the increase in Q_{ext} . b) Changing the series inductance L_s changes the shape of the tunable cavity spectroscopy, decreasing its frequency range. The shunting capacitor C_{Cav} is changed to compensate for the frequency shift.

the cavity response time is given by

$$T_{Cav} = \frac{1}{\kappa} = \frac{Q}{\omega_{Cav}}, \quad (4.11)$$

the external quality factor dominates the response time when this design condition is met. For this circuit design, the rise time is therefore controlled by the size of the coupling capacitor. For low T_1 qubits it is important to have a sufficiently fast rise time since as the tunable cavity is ringing up the qubit is decaying, decreasing the signal visibility. Figure 4.6 shows the effect on the $|1\rangle$ state visibility when the qubit is directly measured with the tunable cavity, using the dispersive shift.

4.2.2 A single photon in the tunable cavity

When driven with only one photon, the AC Stark shift is a small effect that may usually be ignored. Also, the dispersive shift shows a simple relationship when the cavity is driven with only one photon; from Equation 2.41 we can see that the dispersive shift also depends on the number

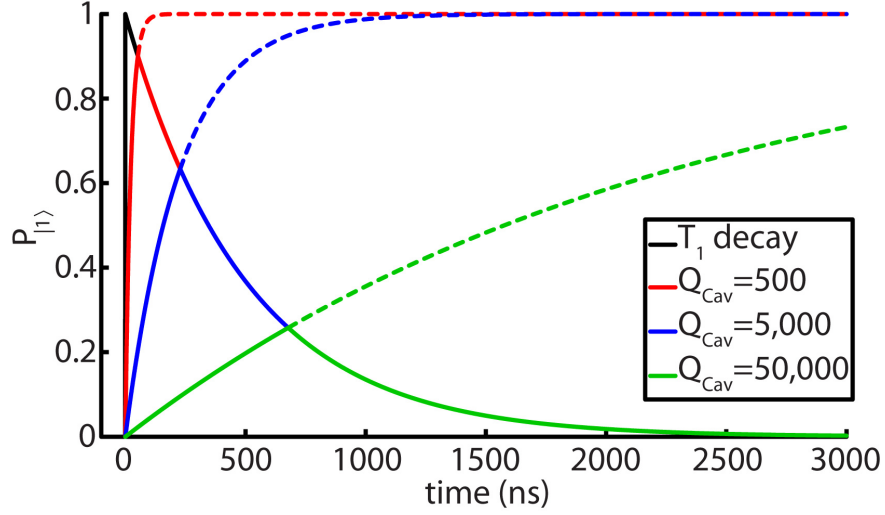


Figure 4.6: T_1 decay and cavity rise time - The the quality factor Q_{Cav} of the cavity, combined with the qubit energy decay time T_1 determines the visibility of the $|1\rangle$ state when the cavity is used to directly measure the qubit in the time domain. For an $f_{01} = 7$ GHz cavity and a qubit with $T_1 = 500$ ns. As Q_{Cav} increases, the visibility decreases.

operator $a^\dagger a$ or the number of photons in the cavity n such that

$$\widetilde{\omega}_r = n\omega_r \pm n \frac{g^2}{\Delta_{01}}. \quad (4.12)$$

This expression is simple with just one photon, though not exceedingly complex with multiple photons. It is useful to know the voltage across the tunable cavity's capacitor that corresponds to a single photon. More practically, it is useful to know what source voltage V_s corresponds to a single photon. The expression for a single photon in an LC resonator with capacitance C_{Cav} is

$$\hbar\omega_r = \frac{1}{2}C_{Cav}V_c^2 \rightarrow V_c = \sqrt{\frac{2\hbar\omega_{Cav}}{C_{Cav}}}, \quad (4.13)$$

where V_c is the voltage across the capacitor C_{Cav} , and ω_{Cav} is the resonant frequency of the cavity. The tunable cavity circuit may be simplified as shown in Figure 4.7. After the circuit

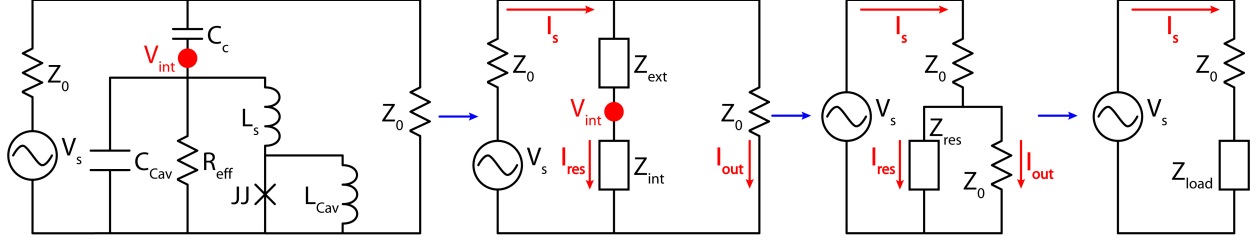


Figure 4.7: Simplification of tunable cavity circuit - The expression for how much source voltage V_s must be applied to get a single photon in the tunable cavity may be found by simplifying the circuit and applying Kirchoff's current law.

simplifications we can define the substitution

$$\alpha = \left(\frac{2}{Z_0 + Z_{Load}} - \frac{1}{Z_0} \right) Z_{int}, \quad (4.14)$$

and then plug it into an expression for the source voltage required for single photon driving

$$V_s = \frac{V_{int}}{\alpha} = \frac{\sqrt{\frac{2\hbar\omega C_{Cav}}{C_{Cav}}}}{\alpha}. \quad (4.15)$$

4.3 Qubit-cavity coupling

4.3.1 Tee inductor coupling

The metastable phase qubit and the tunable cavity may be passively coupled using inductors, either in a transformer configuration or in the equivalent tee circuit, shown in Figure 4.8. The transformer configuration uses a free space coupling, while the tee configuration is an equivalent circuit with shared currents. Since the transformer configuration is best used as a gradiometer for canceling spurious external fields, it requires multiple layer fabrication and a dielectric layer. If, however, one would like to make a single layer device for loss reasons (dielectrics are lossy, as discussed earlier) the tee configuration is the simple, effective inductive coupling choice. It is simple and accurate to calculate the coupling M for the tee design as it is just the inductance of a wire instead of the more complex 3D free space design.

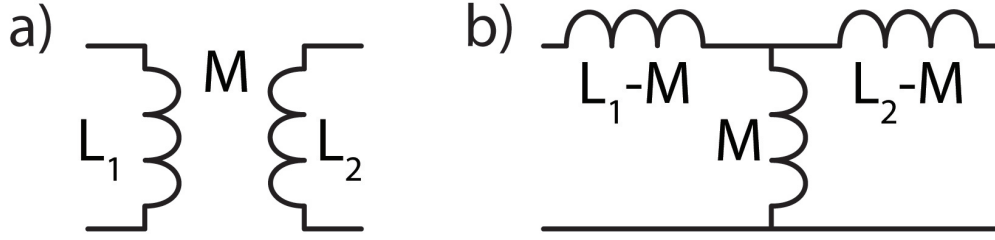


Figure 4.8: Passive coupling with inductors - Two methods for passive inductive coupling between the metastable phase qubit and tunable cavity. a) Transformer coupling relies on open space geometry to transfer current between coils using flux. This method is least susceptible to noise when the coils are gradiometric, which requires multi-layer fabrication with a dielectric layer. b) Tee inductor coupling has equivalent noise susceptibility, but does not need gradiometric design and therefore does not require multi-layer processing.

4.3.2 EM simulations of splitting

Both Microwave Office and Sonnet were used to do simulations of our circuits. Microwave Office has a very nice lumped element schematic simulator that makes fitting a lumped element model to the full EM simulation output very easy. Sonnet has the advantage over the Microwave Office version available to us of being able to model larger spaces, as well as a simple way to place lumped elements on the layout to represent the Josephson junctions. The layout of one circuit is shown in Figure 4.9a. This layout was simulated for an array of lumped element inductances that represent the Josephson junction's response to changing applied fluxes in the qubit, while holding the junction inductance of the tunable cavity fixed. This method accurately predicted the splitting size $2g/2\pi$ for this circuit design, with the results shown in Figure 4.9b. Design control over g is

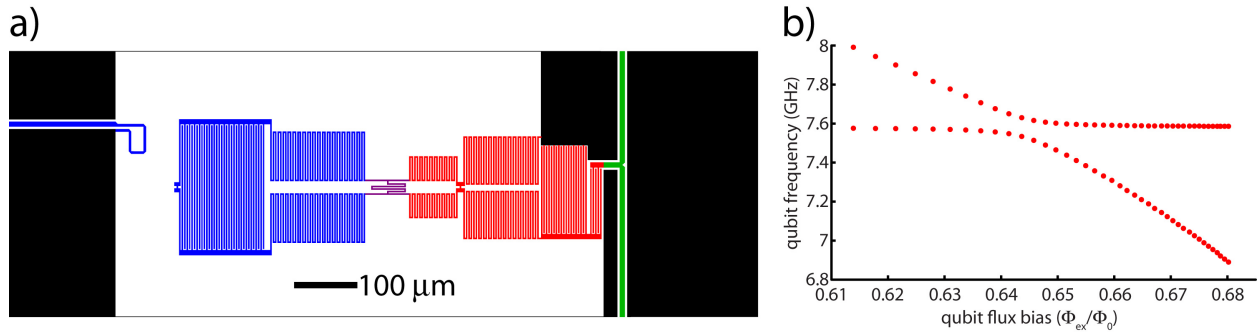


Figure 4.9: EM simulation of cavity splitting - a) The circuit layout used for EM simulation in Sonnet, including the conductor bounding box. b) EM simulation of qubit spectroscopy done using Sonnet, sweeping a lumped element inductance to simulate the response of the junction to applied flux in the qubit, while keeping the tunable cavity junction inductance constant.

Tunable cavity		Qubit	
Element	Value	Element	Value
C_{Cav}	180 fF	C_{Qu}	330 fF
L_{Cav}	680 pH	L_{Qu}	2450 pH
I_c	0.4 μ A	I_c	0.4 μ A
L_{Cavb}	700 pH	L_{Qub}	120 pH
M_{Cavb}	1.3 pH	M_{Qub}	1.9 pH
C_c	19 fF	M	71 pH
L_s	1850 pH		

Table 4.1: Summary of design values.

crucial in designing cQED experiments, as it enters the expressions for the dispersive shift and the AC Stark shift as g^2 .

4.4 Summary of design values

The design values used to make the metastable phase qubit-tunable cavity device (Figure 4.3) are summarized in Table 4.1. The tunable cavity IDC (C_{Cav}) fingers were 2 μ m wide, 140 μ m long, with a 2 μ m gap between them. There were 22 fingers. The capacitor rail on the side opposite the ground plane was 8 μ m, to cut down on stray series inductance in the capacitor. The stray series inductance of the tunable cavity capacitor was calculated as 70 pH. The tunable cavity series inductance L_s was made from a meander inductor with 2 μ m wire widths and 2 μ m spacing between turns, with 31 turns, each turn 80 μ m long. The calculated stray capacitance across the structure was 50 fF. The tunable cavity geometric inductance L_{Cav} was also a meander inductor and had 2 μ m wire widths and 2 μ m spacing between turns, with 20 turns on each side, each turn 38 μ m long. The calculated stray capacitance across the structure was 20 fF. The coupling IDC to the microwave feedline (C_c) had 5 fingers, each 104 μ m long, 2 μ m, with 2 μ m gaps. The microwave feedline was 8 μ m wide with a 4 μ m gap to the ground plane.

The qubit IDC (C_{Qu}) fingers were 2 μ m wide, 200 μ m long, with a 2 μ m gap between them. There were 34.5 fingers. The capacitor rails were 8 μ m to cut down on stray series inductance in

the capacitor. The stray series inductance of the qubit capacitor was calculated as 100 pH, and the stray capacitance to ground was calculated at 30 fF. The qubit geometric inductance L_{Qu} was a meander inductor with 2 μm wire widths and 2 μm spacing between turns, with 39 turns on each side, each turn 80 μm wide. The calculated stray capacitance across the structure was 30 fF.

5

Sample fabrication

5.1 Wiring and insulating layers

Three different circuit designs are shown in Figure 5.1. The DC SQUID readout design, Figure 5.1a, is simply a qubit coupled to a DC SQUID. It is a multi layer design with insulators used to make crossovers, with via-style Josephson junctions and a fixed transmission line cavity. The 100 nm sputtered aluminum layers were wet etched in transene, and the silicon nitride insulators were dry etched in an $O_2 - CF_4$ plasma, tuned to provide 45° sloped edges. It was made on a 3 inch sapphire wafer. The device is described in more detail in [41].

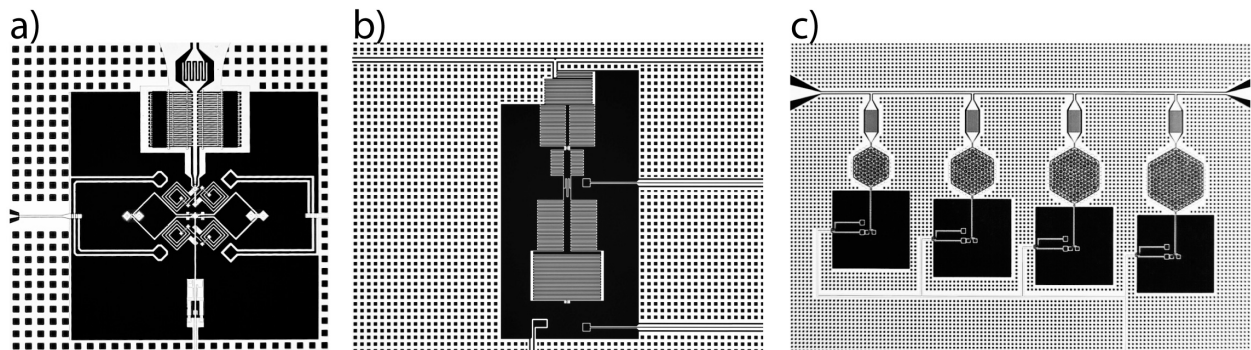


Figure 5.1: Optical micrographs of the three designs - a) Metastable phase qubit readout with a DC SQUID. b) Metastable phase qubit measured/readout with a tunable cavity strongly coupled to the microwave feed line. c) Four tunable cavities multiplexed on a single microwave feedline.

The second design, Figure 5.1b, is a metastable phase qubit coupled to a tunable cavity. It is a simple two layer design, with a wiring layer and a shadow evaporated Josephson junction layer. The 100 nm sputtered aluminum wiring layer was dry etched in a Cl_2 and BCl_3 plasma. All layers were made photolithographically, on a 3 inch sapphire wafer.

The third design, Figure 5.1c, is four tunable cavities without any qubits. This is another multi layer design with crossovers, vacuum gap capacitors, and via-style Josephson junctions. The wiring layers are 100 nm thick sputtered aluminum, the vacuum gap and crossover sacrificial layers were 175 nm thick SiN_x , and the Josephson junction insulating layer was 350 nm thick. The junctions were nominally $6 \mu m^2$ and had critical currents of $1.2 \mu A$. The device was made on a 3 inch sapphire wafer.

5.2 Josephson junction

5.2.1 Junction technology development

Although superconducting Josephson junctions are a decades old technology, using them in coherent quantum devices is a fairly young field, so much experimentation with various fabrication techniques has occurred. The intention here is not to give a broad overview of the field of Josephson junction materials research for superconducting qubits, but to briefly show the progression in the group at NIST Boulder.

5.2.1.1 Via junctions

The early metastable phase qubits at NIST were made from $Nb/AlO_x/Nb$ trilayers[22], though the switch was quickly made to $Al/AlO_x/Al$ via-style junctions[78] as other groups got better results with aluminum, albeit with a completely different device design and junction fabrication procedure[79]. By 2006, when this work began, the via-style $Al/AlO_x/Al$ junction was finishing its run as the workhorse of the metastable phase qubit community. While this technology had yielded

many exciting experiments, its inherently large area junctions proved to be too lossy and had too many TLSs, and thus needed to be replaced by better technologies.

Fabrication of the via-style Josephson junction is shown schematically in Figure 5.2. It starts with a lithographically defined aluminum pad on a substrate, usually a sapphire wafer. A low loss insulator like SiN_x is grown on top, a via is cut down to the aluminum pad, the surface is ion-mill cleaned (or RF cleaned with high kinetic energy[35]), oxidized, then capped with another aluminum layer. After the aluminum layer is lithographically defined, insulator is cut away to expose the underlying aluminum layer so it can be connected to the junction top electrode. If using SiN_x as the insulating layer, after connection to the top electrode it is possible to do a fluorine etch, such as XeF_2 , to remove the remaining insulator and improve the device's loss characteristics. Figure 5.3 is an electron micrograph of a via-style $Al/AlO_x/Al$ Josephson junction and wiring via where the SiN_x dielectric layer has been removed. Note that the wiring crossovers are also suspended instead of resting on a dielectric layer.

The metastable phase qubit coupled to a DC SQUID reported in this work had a $6 \mu m^2$ via-style qubit junction with a critical current around $1 \mu A$ ($L_{J0} = 329$ pH). Its SiN_x dielectric was cut

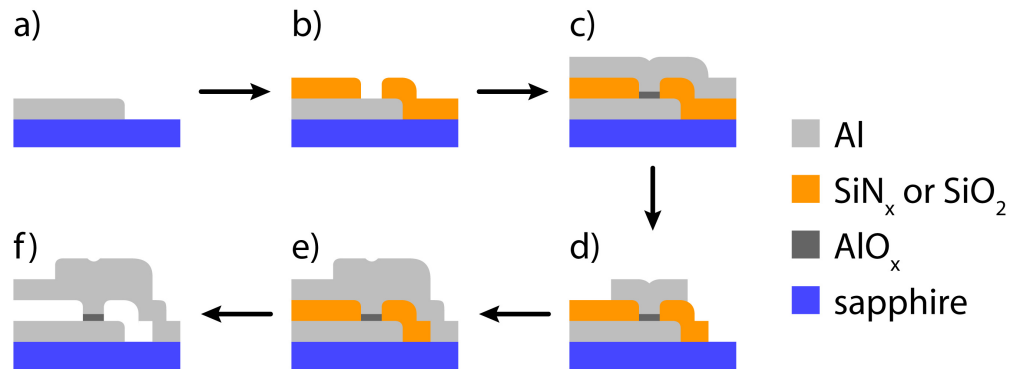


Figure 5.2: Via junction fabrication - a) Al is sputtered and patterned by photolithography on a sapphire surface. b) An insulator is deposited by PECVD and then vias are etched where the junctions will be. c) The vias are ion-mill cleaned or cleaned with a high kinetic energy RF clean, then AlO_x is grown, Al is sputter-deposited, then patterned using photolithography to leave a small island of metal. d) The insulator is patterned and etched using photolithography to enable connection of the junction top electrode to the rest of the circuit. e) Another Al wiring layer is deposited and patterned to connect the junction top electrode. f) If using SiN_x , the remaining insulator may be removed using a fluorine gas etch, leaving vacuum gaps beneath the junction top electrode connections.

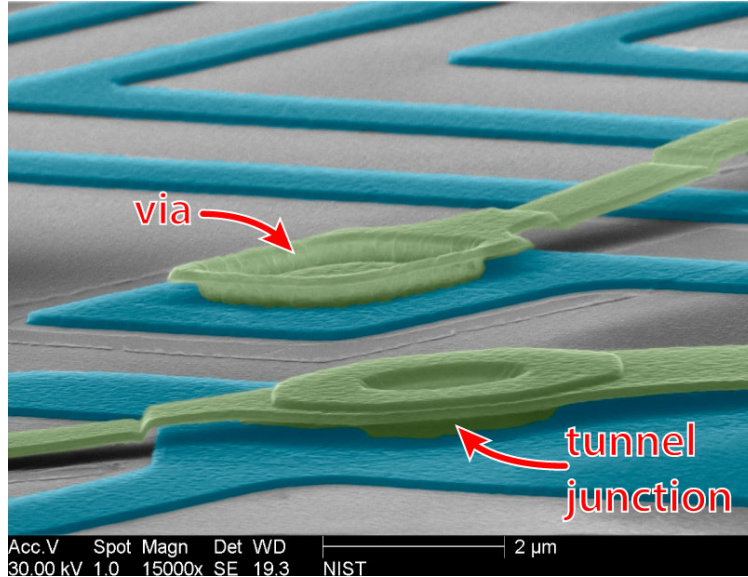


Figure 5.3: Via junction scanning electron micrograph - A via junction with all the SiN_x dielectric layer removed, suspending its top electrode as well as the top electrodes of the wiring via seen in the background.

down to have a minimal footprint, but was not removed from under the top wiring layer.

5.2.1.2 Trilayer junctions

A hypothetically cleaner method for fabricating Josephson junctions is by making them in an $Al/AlO_x/Al$ trilayer, which is then cut to define the junction area and connected to a wiring layer. This allows the junction to be made in one chamber, without ever breaking vacuum, which should lead to a junction with fewer interface defects. A Cl etching system, made by Trion Technology was used to etch the trilayer and define the junction. This system has been problematic and unreliable, though with much work by the cleanroom staff was made reliable for etching of aluminum wiring layers. The trilayer fabrication method is shown in Figure 5.4. The trilayer is made from Al that has been sputtered on sapphire, oxidized, then capped with another sputtered Al layer. The trilayer is etched until just past the tunnel barrier, the base electrode is defined with another lithography and etch step, everything is coated with SiN_x , and a via is cut through to the top electrode. The top Al electrode is sputter deposited, then etched to define wires. The extra insulator is then

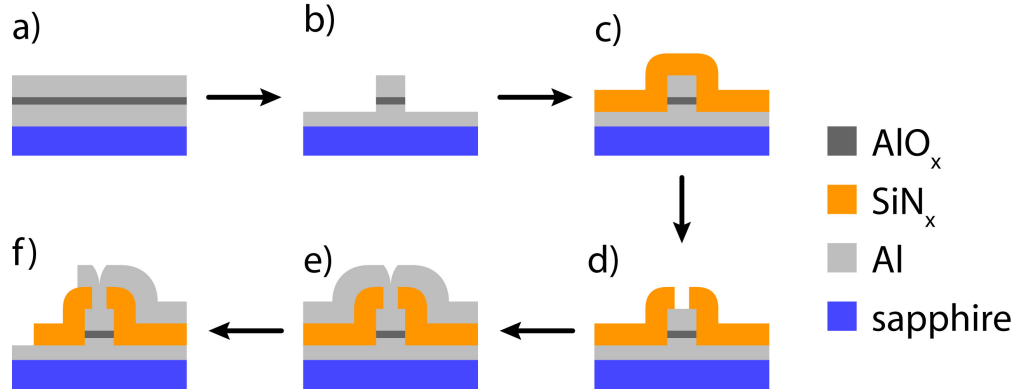


Figure 5.4: Trilayer junction fabrication - a) An $Al/AIO_x/Al$ trilayer is made by sputtering and oxidizing. b) The trilayer is patterned with photolithography and etched using a Cl etcher, which is stopped just after cutting through the oxide layer. c) SiN_x is deposited by PECVD, then d) patterned with photolithography and etched to create a via to the junction. e) An Al wiring layer is deposited by sputtering after an RF clean. f) Finally the Al and then the SiN_x are patterned with photolithography and etched.

removed from the bulk of the wafer, but left under the wiring crossovers. The resulting junction structure is shown in Figure 5.5. The most striking feature of the micrograph is how rough the bottom electrode surface is. This roughness was observed by both optical and electron microscopy immediately after doing the Cl etch that stops just below the tunnel barrier. Devices fabricated with this junction method did not function well at low temperatures, despite having junction normal resistances that matched design parameters. When the chamber for fabricating a more proven technology, shadow evaporated $Al/AIO_x/Al$ junctions, came online at NIST and showed promising results, the trilayer project was abandoned.

5.2.2 Shadow evaporated junctions

Shadow evaporation has been used for decades[80] for making small area Josephson junctions. The procedure is shown schematically in Figure 5.6. The substrate and wiring layer are coated first with a lift off resist (LOR) layer, then standard photoresist. The photoresist is then exposed with a pattern that becomes a bridge over the open substrate when developed, as the LOR is dissolved in the developer. The wafer is then briefly cleaned in an oxygen plasma etch, then loaded into the deposition chamber and cleaned using an ion mill for 60 s. The wafer is tilted at an angle $\pm\alpha$ from

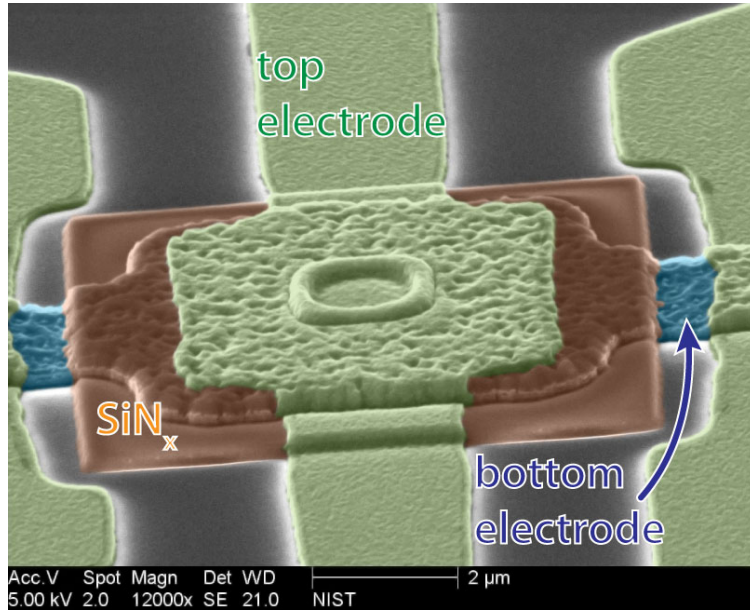


Figure 5.5: 4 μm^2 trilayer junction scanning electron micrograph - The surface roughness of the partially etched trilayer could have limited the reliability of these junctions.

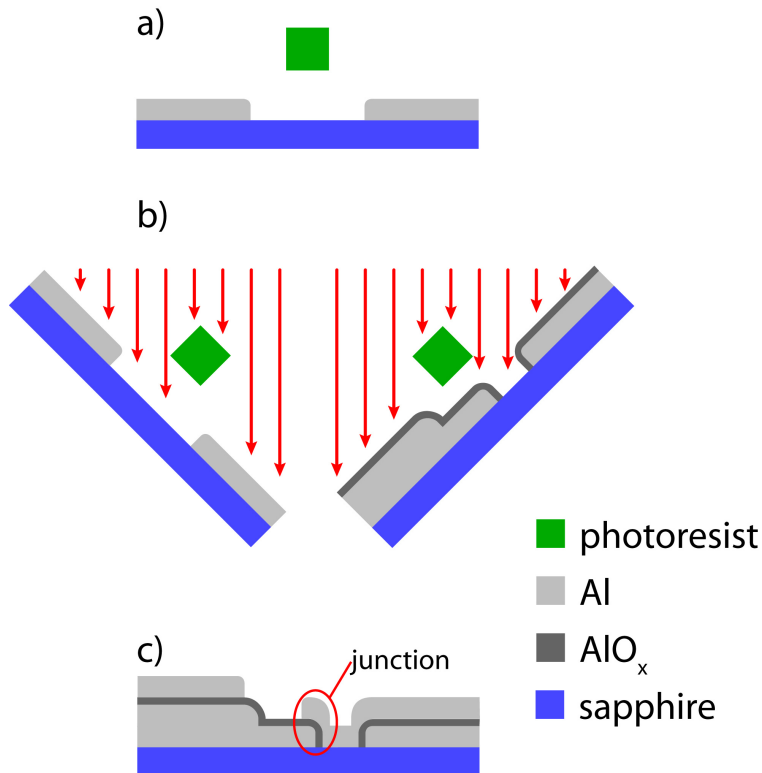


Figure 5.6: Shadow evaporation junction fabrication - a) A photoresist bridge masks the area where the junction will be placed, and the region is ion-mill cleaned for 60 s. b) Al is e-beam evaporated onto the sample at an angle $+\alpha$, then oxidized, then evaporated again at the complimentary angle $-\alpha$. c) The junction remains after lift-off.

perpendicular to the deposition source and an electron beam deposition is performed. Because of the strongly directional nature of electron beam evaporation, only the portion of the substrate in the evaporated atoms' line of sight is coated. The new *Al* surface is oxidized, the sample is rotated to $\mp\alpha$ and a second deposition occurs. The wafer is then lifted off in a gentle (no ultrasonication) stripping process of cold acetone to remove the photoresist, followed by a warm solution to strip the LOR. The resulting junction is shown in Figure 5.7.

The width (W) and length (O) of the overlap region give the nominal area of the junction $A = WO$. The length of the overlap region depends on the angle α according to $O = 2h \tan \alpha - d$, where h is the thickness of the LOR and d is the width of the photoresist bridge. Thus the area of the junction is sensitive to the angle α and may be fine tuned by carefully changing just the angle, allowing precise selection of junction critical currents for small area junctions. As a further refinement, we used our stepper to change the width of the photoresist bridge by using a mask for each side and offsetting one of the masks a small amount on each row of dies on the wafer. Another advantage to this fabrication method is that shadow evaporated junctions may be placed on the wafer as the last fabrication step, keeping the electrostatically and thermally sensitive junctions away from possibly damaging processing steps. The via-style ion mill and the trilayer junctions both have multiple processing steps after the junction is fabricated, including plasma depositions and etches, increasing the possibility for fabrication related damage to the junctions.

Initially, the custom built shadow evaporation chamber at NIST did not have ion mill capabilities for removing the native AlO_x from the wiring layer, so device wiring was made from *Nb*, and thin *Au* pads (30 nm) with a 3 nm *Ti* adhesion layer were deposited on the junction pads to make a clean deposition surface for the junction aluminum. Although this procedure gave reproducible results, the coherence times of the resulting devices were unsatisfactory. An ion mill was installed in the chamber, making all-*Al* devices, without adhesion layers, possible. These devices gave the longest energy relaxation times seen at NIST to that point, and are reported in this work. The

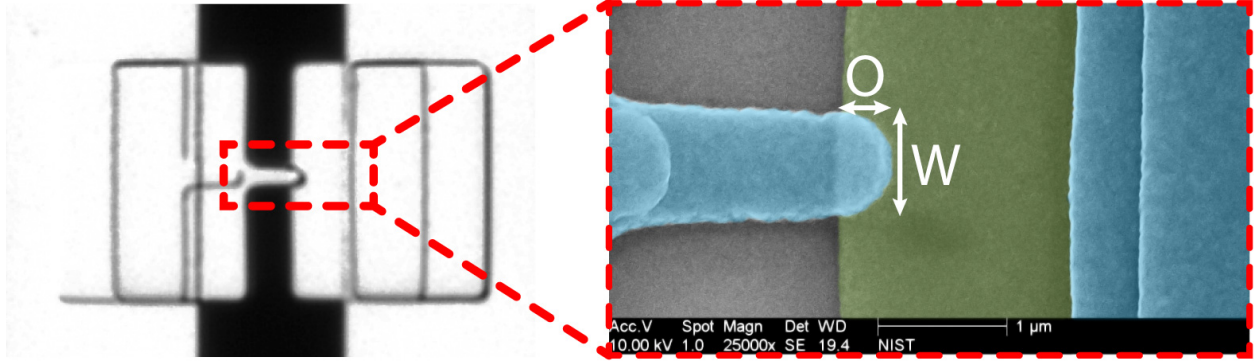


Figure 5.7: Shadow evaporated junction micrographs - A $0.4 \mu\text{m}^2$ $\text{Al}/\text{AlO}_x/\text{Al}$ shadow evaporated Josephson junction, made with photolithography. Optical and scanning electron micrographs. In the electron micrograph, the first deposition is false colored green, and the second deposition is false colored blue.

next generation devices, not reported in this work, had even longer lifetimes, as much as $T_1 = 1.5 \mu\text{s}$. The shadow evaporated qubit junctions for the devices reported here were $0.4 \mu\text{m}^2$ with $\approx 0.4 \mu\text{A}$ ($L_{J0} = 823 \text{ pH}$) critical currents.

5.3 Packaging

5.3.1 Box

Device chips diced from a wafer after fabrication are mounted in custom made boxes, shown in Figure 5.8, featuring twelve 50Ω microwave lines embedded in a 3 layer board. SMA connectors are soldered to the outer edge of the traces, and Al wire bonds are used to connect the traces to the chip. The chip is pressed against the lower ground plane of the board by screws mounted in the lower half of the brass box, shown schematically in Figure 5.8. The box and microwave traces are designed to be free of significant resonant modes in the 2-12 GHz band.

5.3.2 Wire bonds and spurious resonances

The wire bonds connecting the microwave board to the chip connect not just the traces to the chip's bond pads, but also connect the board's ground plane to the chip's ground plane. The number

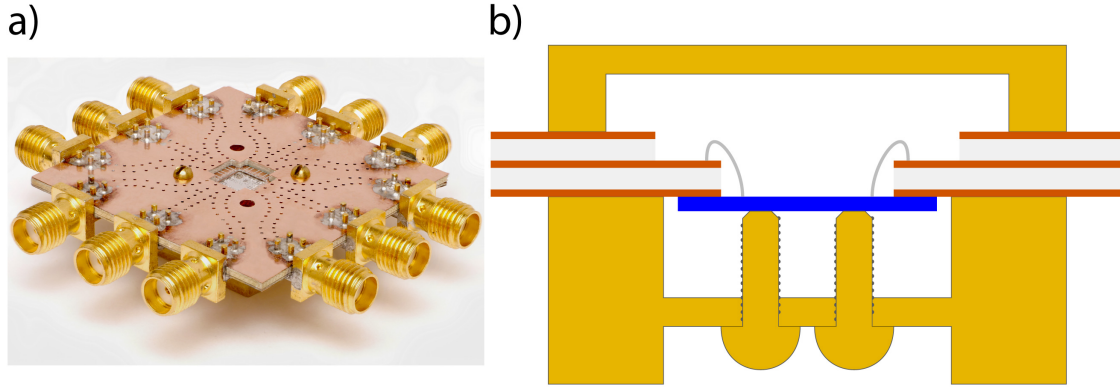


Figure 5.8: Chip mounted in box/circuit board combo - a) Picture of the chip mounted in the box, without the brass lid. b) The chip is pressed against the bottom layer grounding layer of a three layer circuit board, held in place by top and bottom pieces of the brass box. The center board contains traces from near the chip surface to the SMA connectors on the edge. Aluminum wire bonds connect the traces to the chip bonding pads.

and arrangement of these wire bonds can have a dramatic effect on the spectral environment seen by the qubit and the microwave drive and detection instruments[81]. At least three bonds are used per trace connection, in an attempt to maintain a 50Ω impedance between the board and chip. There are also bonds connecting ground planes on chip that have been separated by wiring, as seen in Figure 5.9. This is necessary for devices that only have one wiring layer and/or don't have crossovers between ground planes. When two large ground planes are separated by a long boundary, potential differences in the planes may develop in a phenomenon known as a "slot mode," creating a complex structure in frequency space, with many resonances. This effect is shown in Figure 5.10, where a single layer *Nb* parallel LC circuit with several separated ground planes was measured in transmission at 4 K, with and without crossover bonds connecting the ground planes. Connecting the ground planes is clearly critical, as spurious modes are abundant when they are allowed to float more freely. This could motivate future work into determining if making a dielectric layer just for crossovers significantly increases energy decay rates in coherent devices.

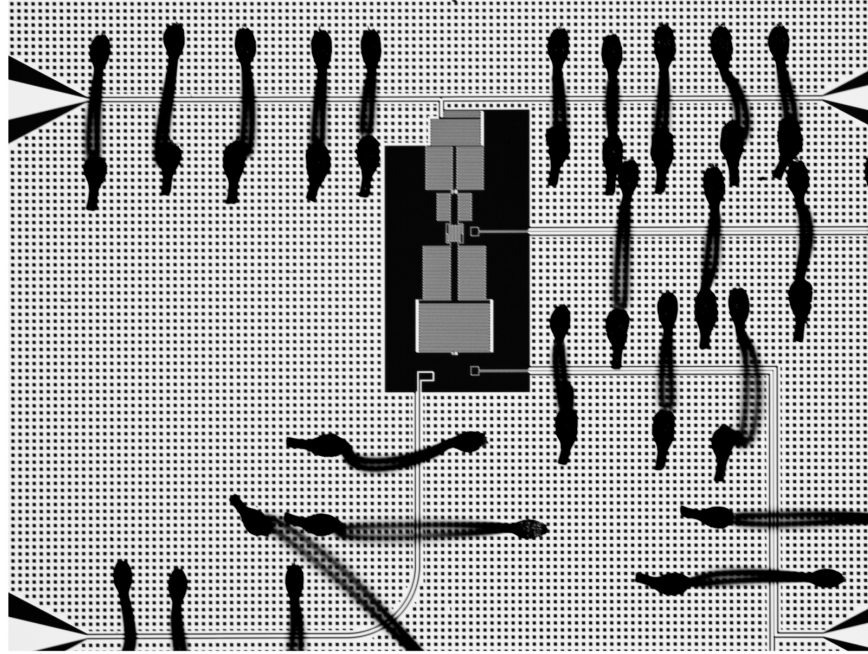


Figure 5.9: Ground plane wire bonds - Optical micrograph of ground planes connected with wire bonds, to suppress spurious slot modes.

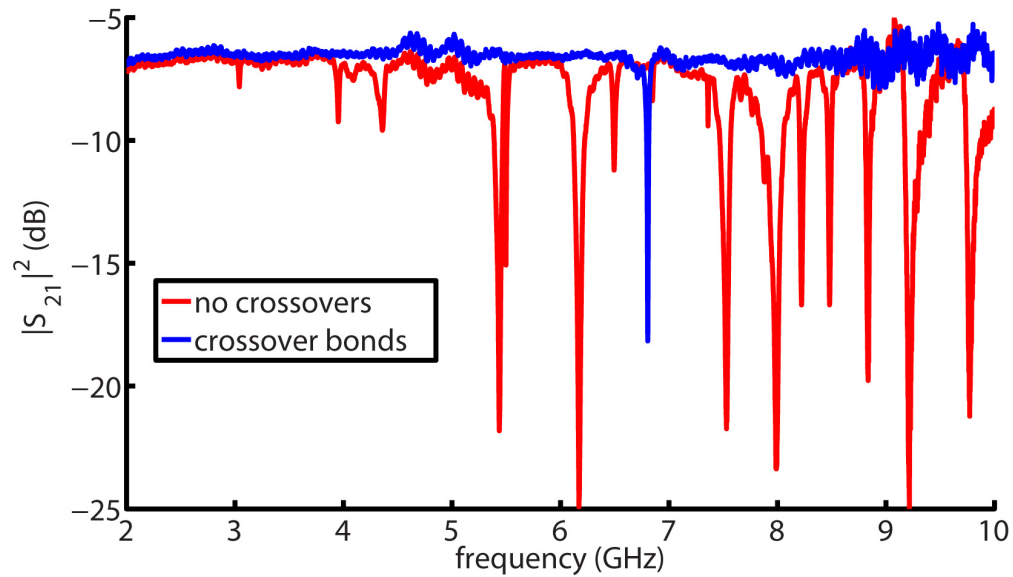


Figure 5.10: Transmission measurements with and without crossover bonds - A lumped element LC resonator made of Nb on SiO_2 measured at 4 K without and then with wire bond crossovers, in two different dunks. When the crossovers were subsequently removed and the sample dunked again, the same no-crossover pattern (red) appeared again.

6

Experimental setup

6.1 Dilution refrigerator

All experiments were performed in an Oxford dilution refrigerator at around 40 mK. The devices were placed in a custom made thermal shield, consisting of a copper can coated on the inside with Eccosorb CR-124 resin to absorb thermal photons radiated at 4 K by the vacuum can. The device boxes are thermally sunk to the thermal shield, which is in turn thermally sunk to the mixing chamber, both through copper braids. Without the thermal shield, thermal photons allow both the f_{12} and the f_{23} transitions to be seen spectroscopically. With the thermal shield, only the f_{01} transition is seen ($f_{02/2}$ can still be seen at high power), demonstrating that radiated 4 K thermal photons have been successfully attenuated below levels that can be seen spectroscopically. The thermal shield was placed in a custom made double-walled Cryoperm magnetic shield, which was placed on the mixing chamber, to prevent arbitrary flux changes from external fields.

6.1.1 Wiring schematic

The fridge wiring schematic for the metastable phase qubit-tunable cavity device is shown in Figure 6.1. The microwave drive and detection circuit to the tunable cavity is drawn in red.

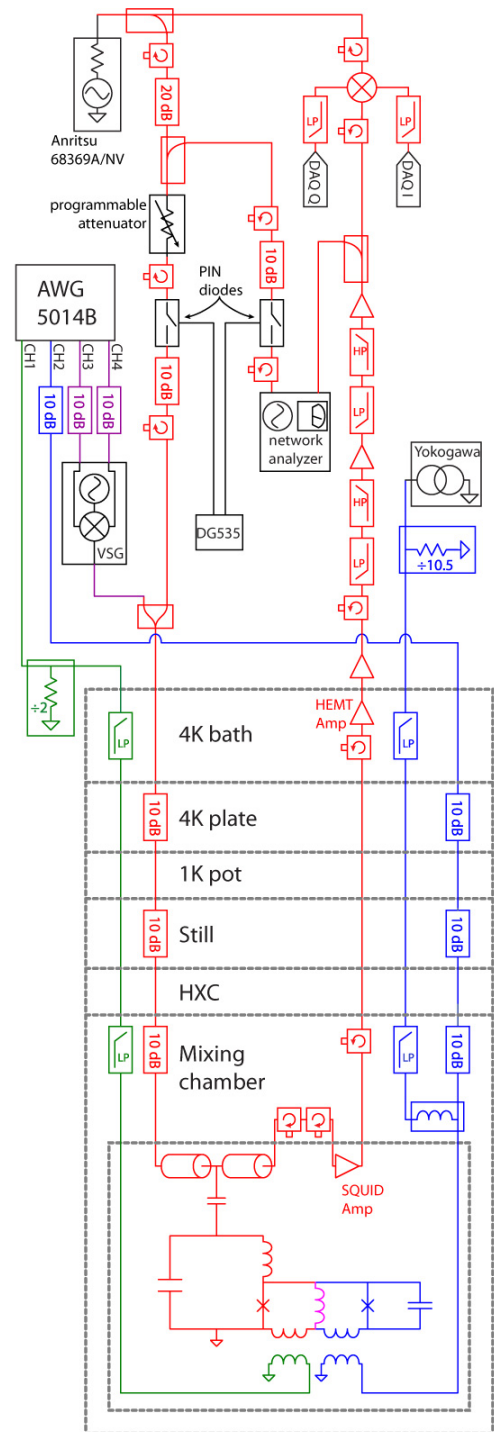
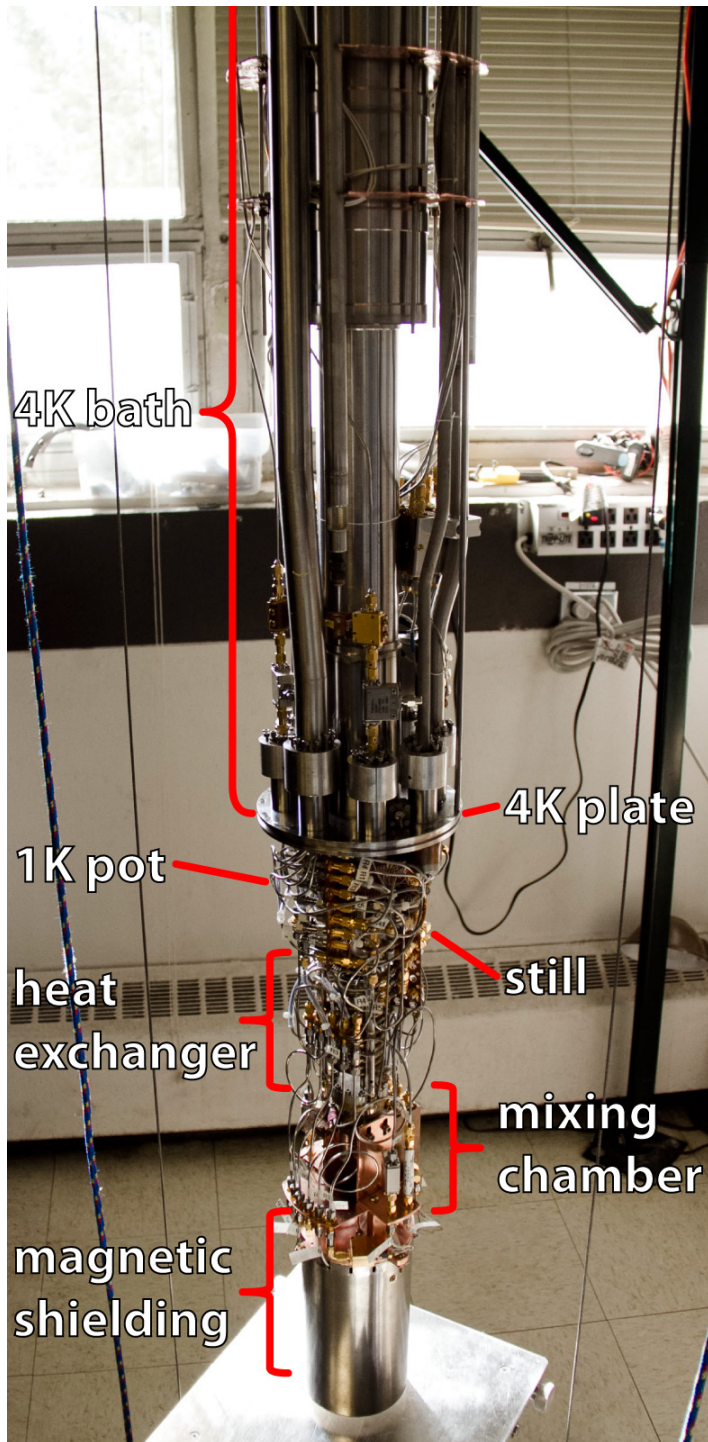


Figure 6.1: Fridge wiring schematic - A picture of the dilution refrigerator at room temperature, with the stages labeled, as well as a schematic of the wiring. The microwave drive and detection circuit for the tunable cavity is drawn in red, with the microwave drive for the qubit, which is combined with the cavity drive, is shown in purple. The flux bias line to the tunable cavity is drawn in green, with the flux bias line to the qubit drawn in blue. The grey dotted box inside the mixing chamber represents the thermal and magnetic shields.

The cavity was driven by a gated generator, which was split to also provide the LO drive for signal detection with an IQ mixer and a two channel data acquisition card. The device output was amplified with a SQUID amplifier at base temperature, a HEMT amplifier at 4 K, and three room temperature amplifiers before being put into the IQ mixer RF input. Cavity drive amplitude was controlled by a programmable attenuator. A network analyzer is also connected to the cavity drive and detection circuit, to be used as secondary source and detection setup for efficient data taking for tunneling measurement readout. The qubit microwave drive, drawn in purple, was combined into the same microwave feedline, with pulses from a vector signal generator shaped by two channels of an arbitrary waveform generator. Tunable cavity flux, drawn in green, was controlled by a third arbitrary waveform generator channel. The qubit flux, drawn in blue, was controlled by both fast and slow sources, combined in a custom bias tee^[35] at base temperature. The fast flux is from a channel of the arbitrary waveform generator (Tektronix AWG5014B), and the slow flux is from a programmable current source (Yokogawa 7651).

The thermal and magnetic shields are represented in Figure 6.1 as the grey dotted box inside the mixing chamber. The two isolators between the circuit and the SQUID amplifier are placed outside these shields because of their magnetic nature. Since both the device and the SQUID amplifier are very sensitive to magnetic flux, it is important to magnetically shield them from the magnetic materials inside the isolators.

Attenuators are placed along the microwave lines at different stages of the dilution refrigerator to decrease the amount of thermal photons seen by the device. The number of photons added by the attenuation at stage i can be calculated using the Bose-Einstein distribution

$$n_i = \frac{1}{e^{\hbar\omega/kT} - 1}. \quad (6.1)$$

This number, minus the photons at the current temperature removed by the attenuator, is then added to the number of thermal photons from the previous stage n_{i-1} divided by the attenuation

value A to get the total number of thermal photons leaving the current attenuation stage n_T ,

$$n_T = \frac{n_{i-1}}{A} + n_i - \frac{n_i}{A} = \frac{n_{i-1}}{A} + \frac{A-1}{A}n_i. \quad (6.2)$$

For the setup shown in Figure 6.1, with 30dB of attenuation, the number of photons reaching the device at 40 mK at 6 and 9 GHz are 0.2 and 0.1 photons, respectively. While this level is small, it is not insignificant. At these levels the thermal population of the $|1\rangle$ state is sufficient to allow the f_{12} transition to faintly appear when doing a high power spectroscopic sweep. Note that at 40 mK the native thermal population at 6 and 9 GHz is 5×10^{-5} and 7×10^{-4} photons, respectively.

Clearly, more attenuation at the mixing chamber would further lower the unwanted thermal population, but two other factors must be considered. First, the room temperature generators must be able to drive enough power to control and measure the cavity and qubit; too much attenuation and there will not be sufficient power reaching the device to perform qubit manipulations when the generator is at its maximum power. The second consideration is the amount of power dissipated at the mixing chamber by the attenuator-if the dissipation is higher than the dilution refrigerator's cooling power the base temperature will rise. While these limitations depend on the specific generators and refrigerators used, one can optimize the attenuator values at each thermal stage using Equation 6.2,

$$\frac{n_{i-1}}{A} \approx \frac{A-1}{A}n_i, \quad (6.3)$$

as a guide. The attenuator values and placements in Figure 6.1 are clearly not optimized. They were chosen to allow for plenty of power to be delivered to the device in case the microwave feedline was undercoupled, a compromise that allowed a small but not insignificant thermal population. An optimized setup would have moved the 10 dB attenuator on the heat exchanger to the mixing chamber, allowing only 0.01 thermal photons at 6 GHz onto the device.

All instruments were triggered by a single pulse generator (Agilent 33220A, not shown in Figure

6.1), which was triggered from a computer using a GPIB command. For flux readout using the network analyzer, the pulse generator was set to burst mode to generate the N samples used to make a histogram with only one GPIB trigger. For dispersive readout the pulse generator was set to continuous mode and data was recorded by the data acquisition card when it was ready. All time sensitive instruments, including the data acquisition card, were synchronized through 10 MHz reference ports to a rubidium frequency standard (SRS FS725).

6.2 Signal generation

6.2.1 Microwave generation and pulse shaping

Full qubit control requires pulses that have a controllable amplitude, phase, and duration. The pulses must also have a high on-off ratio so that manipulations aren't happening when not intended. For the metastable phase qubit with via-style junctions that was read out with a DC SQUID, microwave pulses were made using a two mixer setup controlled with an FPGA. The setup is shown schematically in Figure 6.2. The pulse generation is done in two stages, using two IQ

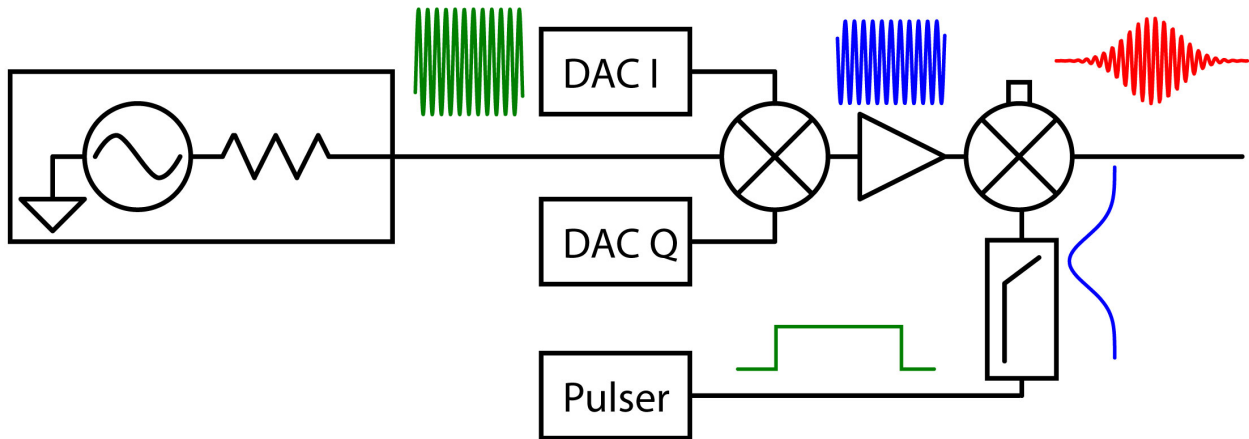


Figure 6.2: FPGA controlled microwave pulse electronics - A continuous wave generator drives the LO port of an IQ mixer, with the IQ ports controlled by an FPGA using 14 bit DACs. This first stage sets the amplitude and phase of the pulse. The second stage, another IQ mixer, is gated with a hard pulse that has been filtered into an approximately Gaussian waveform. This pulser is also controlled by the FPGA using an 8 bit serializer to gain time resolution 1/8 of the FPGA clock period. The output is a roughly Gaussian wavepacket.

mixers. The first mixer is driven by a continuous wave microwave generator (Anritsu 68369A/NV) at +12 to +14 dBm. The I and Q ports are biased by 14-bit DACs controlled by the FPGA and updated once per clock cycle. Changes to I or Q change the amplitude and phase of the output pulse. An amplifier brings the signal back up to the +12 to +14 dBm input power required by the next IQ mixer, which does the time domain pulse shaping. One port is capped with a 50Ω termination, and the other is given a hard pulse, shaped by an approximately Gaussian filter, which sets the duration of the output pulse. The “pulser” is an 8 bit serializer controlled by the FPGA that gives the second stage a time resolution of $1/8$ the FPGA clock period. The FPGA clock is run at 175 MHz, giving a 0.7 ns time step for the pulser. This FPGA-based microwave sequencer was developed by John Martinis during his time at NIST, and the communication software between the sequencer and a control computer was written by his group at UCSB[34].

For the metastable phase qubit-tunable cavity device, microwave pulse control was achieved using a vector signal generator (Agilent E8267D) whose IQ ports were controlled by an arbitrary waveform generator (Tektronix AWG5014B) set to a 1 GS/s sampling rate, as shown in Figure 6.3a. The arbitrary waveform generator was programmed with Gaussian pulse shapes to minimize driving transitions beyond the f_{01} transition, as described in Section 3.1.3. The on-off ratio of the

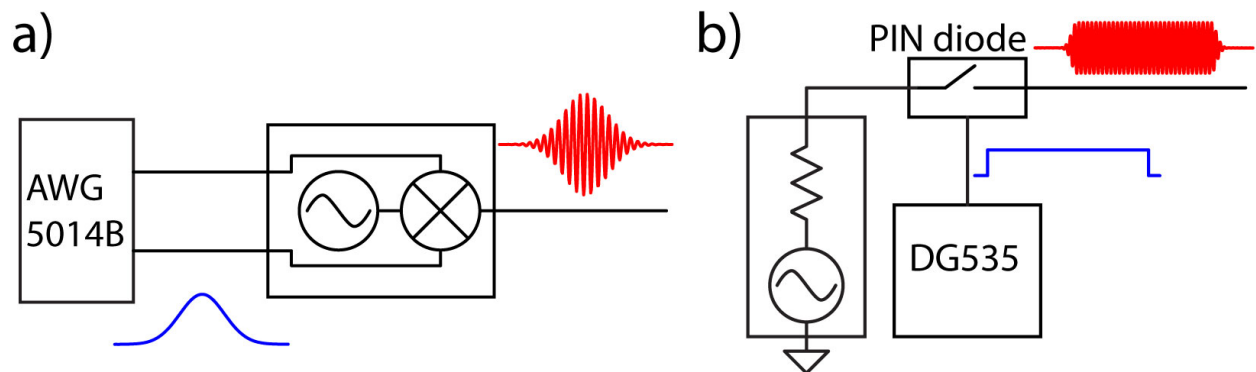


Figure 6.3: Microwave pulse electronics - a) A vector signal generator, shaped by an arbitrary wave generator, generates gaussian pulses with arbitrary rise times and is used for qubit control. b) A simpler setup for driving the tunable cavity uses a PIN diode and digital delay pulse generator with a fast rise time to gate a continuous wave source. Because the tunable cavity is run in a semi-continuous mode, this setup is adequate. The PIN diode setup is also used to gate the network analyzer drive to the cavity.

output was viewed on a spectrum analyzer for calibration, with small DC offset voltages applied by the arbitrary waveform generator in a frequency dependent way to keep the on-off ratio at about 70 dB between 4 and 9 GHz.

The microwave drive required by the tunable cavity is somewhat less demanding, since it is operated in a semi-continuous mode with 5 to 100 μs long pulses (much longer than the qubit pulses) and phase control is not needed. This allows pulses to be generated with a continuous wave generator (Anritsu 68369A/NV) and simply gated by a PIN diode (HP 11720A) with a hard pulse from a digital delay line generator (Stanford Research Systems DG535), as shown in Figure 6.3b. The PIN diode has a typical on-off ratio of 50 dB. This setup was used for driving the cavity during dispersive measurement. The PIN diode setup was also used to gate the network analyzer (Agilent E5071C) when it was being used to drive the cavity for flux readout after tunneling measurement.

6.2.2 Flux control, filtering, and bias tees

For the qubit, both fast and slow flux biases were applied. The fast flux was applied by one channel of the arbitrary waveform generator (Tektronix AWG5014B), attenuated, then injected into a 50Ω microwave line with the stages of attenuation shown in Figure 6.1. At the mixing chamber the signal goes into the RF port of a custom made bias tee, described below. The rise time of the arbitrary waveform is shown in Figure 6.4, for both short and long timescales. The generator

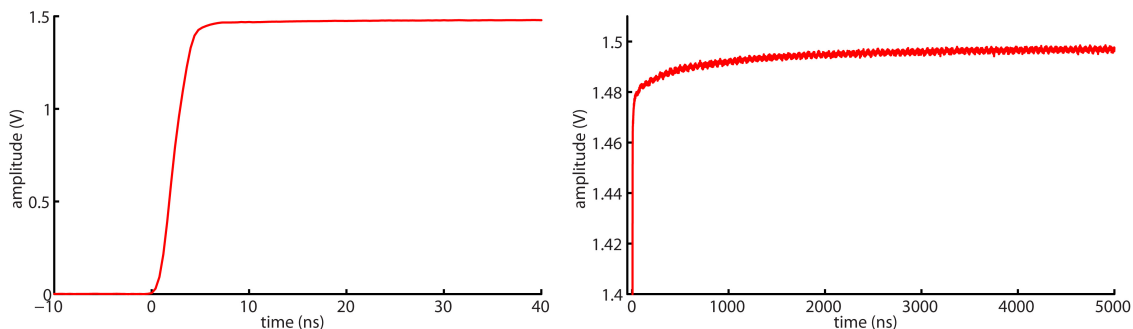


Figure 6.4: Rising edge of a flux pulse from the Tektronix AWG5014B - a) An oscilloscope (4 GHz Tektronix TDS6404) trace of a nominally 1 ns flux pulse spanning 1.5 V. The actual rise time is 3 ns. b) A long oscilloscope trace showing the drift in the generator over microsecond timescales.

does not produce clean step edges on either the nanosecond or microsecond timescale. Although corrections for this instrument may be done to more accurately generate a step edge[82], for this work it was sufficient to wait $3 \mu\text{s}$ for the instrument to settle, then apply a linear correction ramp. The ramp slope was found by biasing the qubit to the shallow well at $P_{|1\rangle} = 0.5$ (for maximum sensitivity) and moving the measure pulse in time across several microseconds. The ramp slope at which $P_{|1\rangle}$ stayed flat was used. The fast flux line for the qubit is not filtered, except by the low temperature attenuators, which only control thermal noise.

The slow flux line to the qubit is driven by a very accurate current source (Yokogawa 7651), which is filtered using a low pass RC filter with a roll-off at ≈ 1 MHz, at 4 K, followed by a 650 MHz low-pass filter encased in copper powder at base temperature. The copper powder absorbs radiation above about 1 GHz. The flux to the tunable cavity is run through the same filtering, though its source is one of the arbitrary waveform generator channels. The $1k\Omega$ resistor in the RC filter ensures that the 50Ω arbitrary waveform generator behaves as a current source. The room temperature attenuators/dividers provide increased resolution by matching the voltage or current needs of the experiment to the full range of the generators. For example, if a current source has a full scale range of 100 mA, but only 2 mA of range is required to move across an entire metastable phase qubit step, then dividing the current source output by 50 would give the highest current resolution available with the generator across the qubit step range.

A bias tee was required for combining the currents for the fast and slow qubit fluxes. A custom bias tee was used here, with the design detailed in [35] and shown schematically in Figure 6.5. Briefly, the bias tee passes fast flux pulses with approximately nanosecond rise times but also allows the pulses to have durations of several microseconds without distortions through the RF port. It allows constant DC signals through the inductive port as well, which filters and high frequency noise. Commercial bias tees often include a capacitive DC block on the RF port which would not allow passage of a several microsecond long pulse without sever distortions.

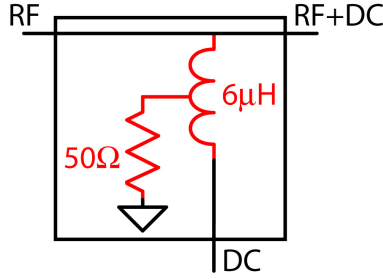


Figure 6.5: Custom bias tee - Bias tee schematic. The 50Ω resistor damps resonances in the $6\mu\text{H}$ conical inductor, and the lack of a capacitor on the RF side allows for wider-band signals such as several-microsecond flux pulses and slow ramps.

6.3 Signal detection

A simplified signal detection schematic is shown in Figure 6.6. The network analyzer or the generator/IQ mixer/data acquisition card may be used as the source/detector pair. There are amplification stages at three temperatures: 40 mK, 4 K, and room temperature. The SQUID amp is a very low noise amplifier, described in more detail below, and it sets the noise temperature of the amplifier chain, since it sits at the lowest temperature of all the amplifiers[83]. Because of a large, previously observed back-action of the SQUID amplifier on the cavity without isolation between them, two 20 dB low temperature isolators are used. For most of the measurements presented here, the SQUID amplifier was biased to a place with a maximal signal to noise ratio and had a gain of about 17 dB and a noise temperature of approximately 600 mK (line loss uncertainties in its measurement could put this number as high at 1 K or as low as 400 mK). The gain $G \approx 17$ dB

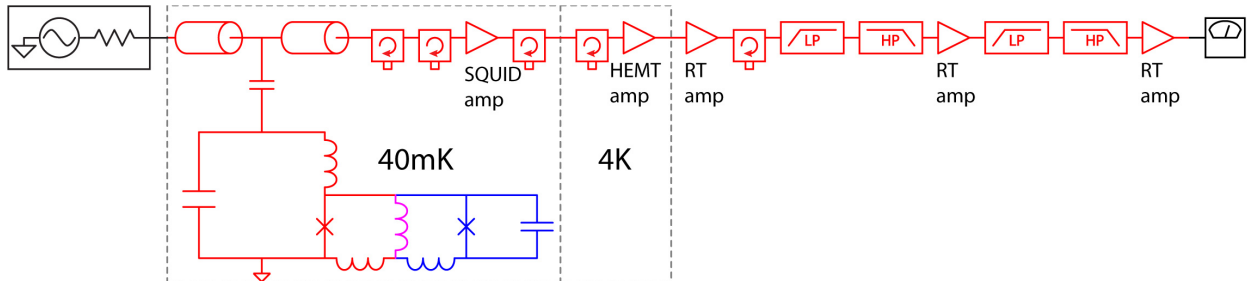


Figure 6.6: Simplified signal detection schematic - The tunable cavity's state is interrogated by a microwave pulse from the source, either a gated generator or a Network Analyzer output. After passing through five amplifier stages, the signal is detected either with an IQ mixer/DAQ card setup or using the Network Analyzer. The noise temperature of the amplifier chain is set by the SQUID amp.

of the SQUID amplifier was estimated using data from two cooldowns; one without the SQUID amplifier and one with the SQUID amplifier, measured with a source and spectrum analyzer. The noise floor $N = -71$ dBm was measured using the spectrum analyzer set to bandwidth $B = 10$ Hz while the source was off. The SQUID amplifier noise temperature was calculated with the expression

$$T_N = \frac{1}{k_B} \left(\frac{N}{GB} - \frac{\hbar\omega}{2} \right), \quad (6.4)$$

where $\omega = 2\pi 6.78$ GHz is the frequency at which the amplifier is operated and k_B is Boltzmann's constant. The largest uncertainties come from the gain measurement.

The HEMT amplifier was purchased from the Caltech radiometer group, a 4-12 GHz LNA with nominally 38 dB of gain and a nominal noise temperature of about $T_N = 4$ K at $T = 20$ K and 7 GHz. Two 20 dB isolators also keep backaction and thermal photons from impinging on the SQUID amplifier from the HEMT amplifier and 4 K components. The three room temperature amplifiers (Mini-Circuits ZVA-183+) have 26 dB of gain from 0.7 to 18 GHz. Because they are so wideband, care must be taken to suppress noise out of the measurement band (~ 5 -7 GHz), so filters are connected between amplifiers. The isolators all have a pass band of 4-8 GHz and 20 dB of isolation. The low pass filters (Mini-Circuits VLF-7200+) allow DC-7.2 GHz to pass, while the high pass filters (Mini-Circuits VHF-3800) allow 4.25-10 GHz to pass. This combination creates a bandpass filter from 4.25-7.2 GHz, right where the tunable cavity is located. Without the filters, the amplifiers exhibit compression of as much as 4 dB because they are saturated by wideband noise.

As this signal detection setup is used to measure a resonator, it is worth considering the effects of non ideal conditions on the measurement outcome of a resonator. An ideal resonator was represented in the plots of Figure 3.22, making perfect circles centered on the real axis and symmetric amplitude traces about the resonant frequency. As described in their paper on resonator measurements[84], Petersan and Anlage state that

Important alterations to the data occur when we take into account several aspects of the real measurement situation. The first modification arises when considering the crosstalk between the cables and/or the coupling structures. This introduces a complex translation $X = (I_0, Q_0)$, of the center of the circle away from its place on the real axis. Secondly, a phase shift θ is introduced because the coupling ports of the resonator do not necessarily coincide with the plane of the measurement. This effect rotates the circle around the origin.

They then give the corrected complex transmission coefficient \tilde{S}_{21} as

$$\tilde{S}_{21} = (S_{21} + X) e^{i\theta}. \quad (6.5)$$

The effects of these modifications to the ideal case are shown in Figure 6.7. The calibration procedure used for the tunable cavity is to detune it as far from the region to be calibrated as possible, do a through calibration, then return the cavity to the desired frequency. This calibration gives data that is close to the ideal, though moving the resonator back noticeably changes both the rotation and origin of the resonance in IQ space in the same way demonstrated in Figure 6.7.

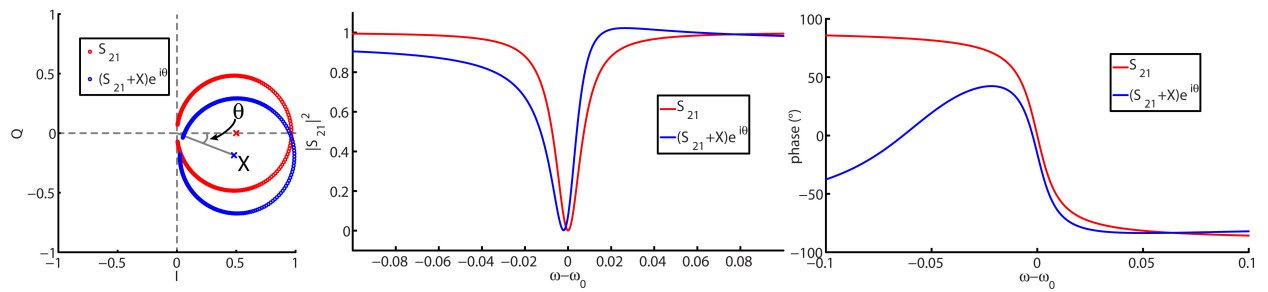


Figure 6.7: Resonator measurement imperfections - The effect of cable/spurious structure crosstalk and measurement plane/port offsets on resonator measurements. The ideal resonator is plotted in red, the non-ideal in blue. The crosstalk offsets the IQ plot by $X = (I_0, Q_0)$ and the measurement plane offset introduces a rotation θ , which combine as $\tilde{S}_{21} = (S_{21} + X) e^{i\theta}$.

6.3.1 SQUID amp

The SQUID amplifier was developed and made at NIST to be a very low noise cryogenic amplifier [65][66][67], mass produced and professionally packaged. The amplifiers are made of Nb , so they function at temperatures below 9 K, though the best performance is at the lowest temperature the amplifier can be placed. Because of its very low power consumption, and therefore small heat dissipation, it can be placed on the mixing chamber without noticeably heating the stage. Figure 6.8a shows a schematic of the SQUID amplifier. This SQUID amplifier is able to amplify effectively at several GHz because the 50Ω input microwave line has been impedance matched to the high impedance SQUID using a quarter wave resonator, which puts a voltage antinode and a current node at the SQUID input coil. The quarter-wave resonator sets the amplification band, limiting it to a few hundred MHz wide, and therefore must be chosen for the frequency of the specific device to be measured. Figure 6.8b shows a photo of the amplifier in its custom box with bias circuitry and without the lid. The bare box and connectors are also shown. Eccosorb CR-124 resin was painted on the box lid to suppress free space box modes. The packaging includes a bias tee for injecting bias current I_b , and a line for the flux bias current I_Φ . These lines are both filtered in the fridge just like the flux bias lines were filtered; with a low pass RC filter at 4 K and a copper powder encased low pass filter on the mixing chamber. These two current drives effect the SQUID amplifier in a

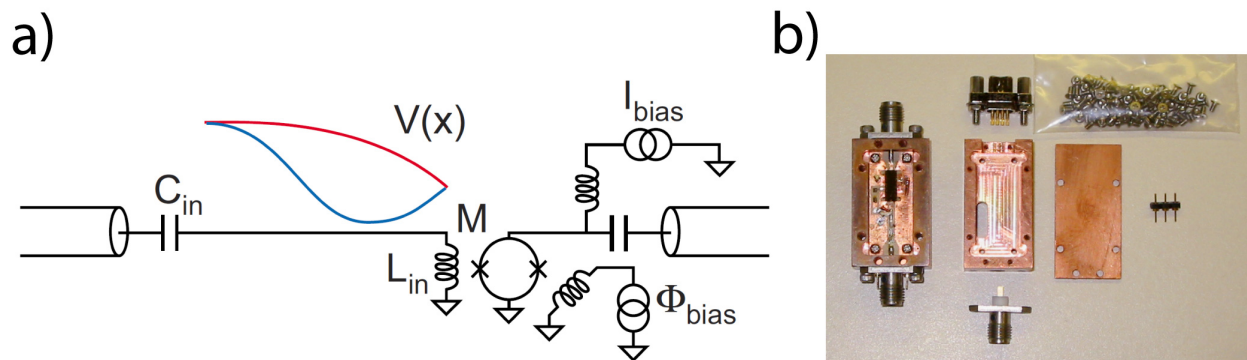


Figure 6.8: The SQUID amplifier - a) Schematic of the SQUID amplifier, taken from [65]. The red and blue lines represent the voltage antinode and current node, respectively, in the quarter wave resonator. b) Photo of a SQUID amplifier packaged in a custom box with bias wiring, showing the components.

complex way, though a rough, heuristic rule is shown in Figure 6.9a. Changing I_b tends to change the overall background gain, while changing I_Φ changes the position in frequency and amplitude of the gain peak. This peak is about 80 MHz wide 3 dB down, and is tunable across ~ 200 MHz. Because of the narrowness of the gain peak, the SQUID amplifier is designed to give gain at specific frequencies. An amplifier with high gain near the top of our tunable cavity's frequency range was chosen. Its gain curve at 6.78 GHz is shown in Figure 6.9b, having a 1 dB compression point at ~ -99 dBm, or ~ 125 fW. As the single photon regime for the tunable cavity at 6.78 GHz is on the order of 1 fW, the amplifier should be far from saturation during our measurements.

The SQUID amplifier bias current I_b and flux current I_Φ must be optimized to get the highest signal to noise ratio (SNR). This is efficiently done by measuring the SNR in high gain regions. A sweep of I_b and I_Φ at 6.78 GHz is shown in Figure 6.10a. Figure 6.10b are signal to noise measurements at two bias currents. These measurements were done by measuring the gain response flux curves with and without a microwave drive using a spectrum analyzer, then taking the difference. The SQUID amplifier bias is optimized when biased at the highest SNR point.

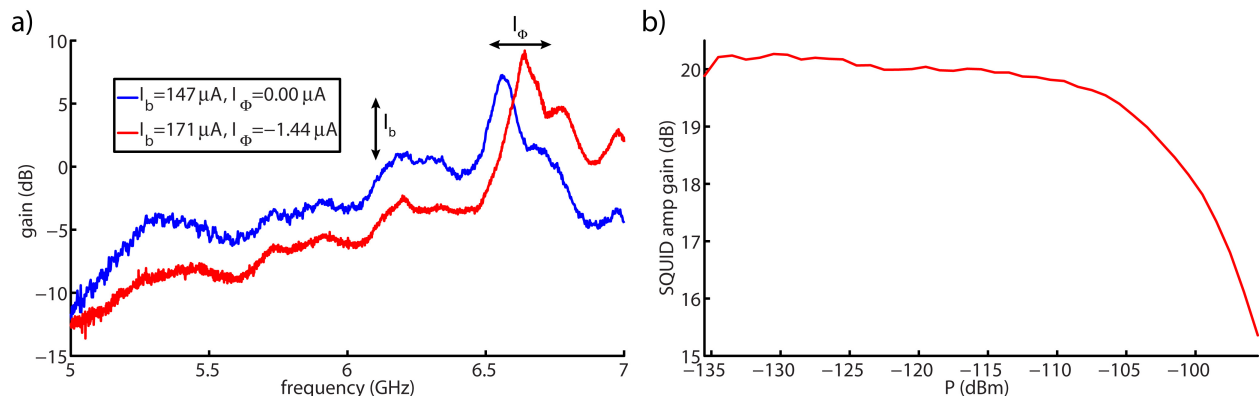


Figure 6.9: SQUID amplifier bias changes and gain compression - a) The high gain region of the SQUID amp is relatively narrow, usually a few hundred MHz, but is somewhat tunable. Roughly, changing the current bias I_b changes the overall background gain, while changing the flux bias current I_Φ changes the position and amplitude of the gain peak. b) The SQUID amplifier's 1 dB compression point is measured here to be about -110 dBm, agreeing with [66], at 6.78 GHz.

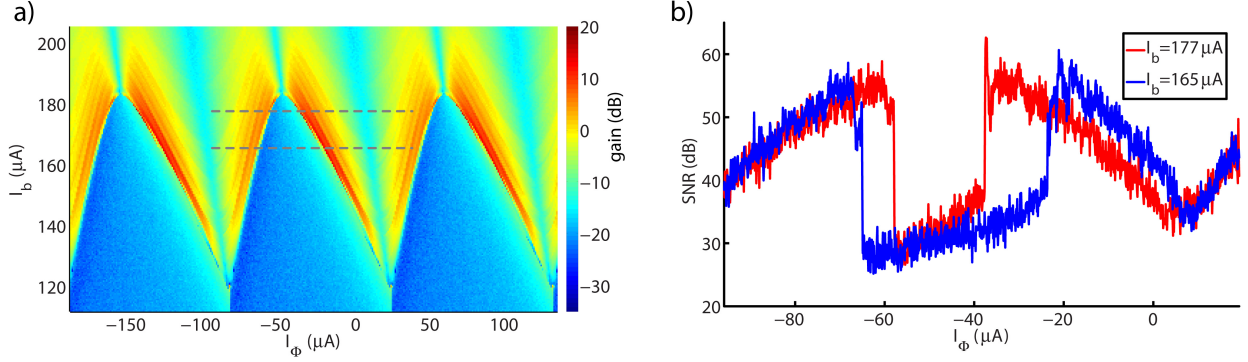


Figure 6.10: SQUID amplifier gain and SNR - a) SQUID amplifier gain was measured as the current and flux bias were swept, while the microwave drive was at 6.78 GHz. b) The signal to noise ratio was measured at the two bias locations indicated in a) by the grey dotted lines.

6.3.2 Network Analyzer

As discussed above, the network analyzer (Agilent E5071C) was used to drive the cavity for flux readout after tunneling measurement, and was gated using a PIN diode. This was necessary since the network analyzer did not have sufficiently controllable or accurate gating on its own, and the drive to the cavity needed to be off when the qubit was being reset or manipulated and measured. The network analyzer was operated in zero span mode, measuring S_{21} , and triggered externally. N points were taken, then uploaded to the control computer for conversion to a histogram, which was then used to calculate an occupation probability. When not in use, the network analyzer was left plugged into the microwave setup, but its output port was turned off.

6.3.3 IQ mixer

For dispersive measurement, the cavity signal is detected using homodyne mixing down to DC with a quadrature-IF double-balanced mixer (Marki IQ-4509). Note that the labeling on the Marki mixers for the I and Q ports is reversed from the way they are being used here. Following Gao[85] and noting that in his equations a and b are swapped, the four port IQ mixer has the two inputs

$A_{LO} = 1$ and $A_{RF} = re^{i\theta}$, and has the two outputs

$$I = I_0 + A_I \cos(\theta), \quad Q = Q_0 + A_Q \cos(\theta + \gamma). \quad (6.6)$$

γ is the phase difference between I and Q , and is nominally $-\pi/2$. Ideally there is no offset in the IQ plane ($I_0 = Q_0 = 0$), and $A_I = A_Q = A$ as one sweeps the phase θ from 0 to 2π , so that I and Q trace out a circle of radius A , centered at the origin. Usually, however, IQ mixers trace out an ellipse, as seen in Figure 6.11a. The ellipse major and minor axes (a and b), along with the angle Φ can be used to characterize A_I , A_Q , and γ with the equations

$$A_I = \sqrt{a^2 \sin^2(\Phi) + b^2 \cos^2(\Phi)}, \quad (6.7)$$

$$A_Q = \sqrt{a^2 \cos^2(\Phi) + b^2 \sin^2(\Phi)}, \quad (6.8)$$

$$\gamma = \alpha_1 - \alpha_2, \quad (6.9)$$

where

$$\alpha_1 = \tan^{-1} \left(\frac{a \sin(\Phi)}{b \cos(\Phi)} \right), \quad (6.10)$$

$$\alpha_2 = \pi - \tan^{-1} \left(\frac{a \cos(\Phi)}{b \sin(\Phi)} \right). \quad (6.11)$$

For a fixed frequency, different powers give different size ellipses, as shown in Figure 6.11b, forming a cone as seen in Figure 6.11c. Each frequency has its own cone. By measuring the ellipse values a , b , and Φ at different frequencies and powers we can come up with the functions $A_I(f, P_{RF})$, $A_Q(f, P_{RF})$, and $\gamma(f, P_{RF})$ that describe each cone. The original RF signal can be found by

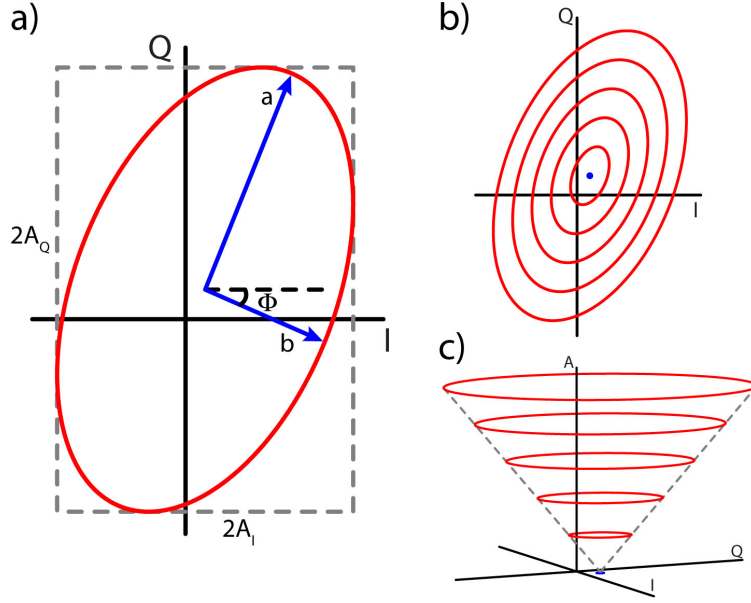


Figure 6.11: IQ mixer nonidealities - a) Parameterizing the ellipse traced out by the IQ mixer at a constant power and frequency. b) For a fixed frequency, decreasing the amplitude A of the signal gives a smaller ellipse, c) which can be represented as a cone. Each frequency has its own characteristic cone.

plugging the values for A_I , A_Q , and γ into

$$r = \begin{cases} \frac{I}{A_I \cos \theta} & (\cos \theta \neq 0) \\ \frac{Q}{A_Q \cos(\theta + \gamma)} & (\cos \theta = 0) \end{cases} \quad (6.12)$$

$$\theta = \begin{cases} \tan^{-1} \frac{\cos \gamma - g}{\sin \gamma} & (I > 0) \\ \tan^{-1} \frac{\cos \gamma - g}{\sin \gamma} + \pi & (I < 0) \end{cases} \quad (6.13)$$

where

$$g = \frac{\cos(\theta + \gamma)}{\cos \theta} = \frac{A_I Q}{A_Q I}. \quad (6.14)$$

The results of the mixer calibration were organized into a single calibration file. Each frequency was one column, representing one ellipse in that frequency's cone. Each power took a 7 row block, so for n powers each column contained the ellipse parameters for a cone of n ellipses. The format of a calibration file with only two different drive powers, and thus only two ellipses per frequency, is shown in Table 6.1. For frequencies and powers between those listed in the calibration file, a

f_1	f_2	\dots	f_N
A_1	A_2	\dots	A_N
I_{01}	I_{02}	\dots	I_{0N}
Q_{01}	Q_{02}	\dots	Q_{0N}
A_{I1}	A_{I2}	\dots	A_{IN}
A_{Q1}	A_{Q2}	\dots	A_{QN}
γ_1	γ_2	\dots	γ_N
f_1	f_2	\dots	f_N
A_1	A_2	\dots	A_N
I_{01}	I_{02}	\dots	I_{0N}
Q_{01}	Q_{02}	\dots	Q_{0N}
A_{I1}	A_{I2}	\dots	A_{IN}
A_{Q1}	A_{Q2}	\dots	A_{QN}
γ_1	γ_2	\dots	γ_N

Table 6.1: Calibration file format - A calibration file for a calibration of N frequencies, done at two powers, making N columns and $2 \times 7 = 14$ rows.

linear interpolation was done for each parameter.

6.3.4 Data acquisition card

The data acquisition card (Gage CS23G8) has two 8-bit channels that may be operated simultaneously as fast as 1.5 GS/s, and includes an onboard averaging feature. This averaging was not a continuous average, but a sum over up to 1024 traces that is transferred to the computer to be divided by the number of samples later. While there is a large increase in speed over transferring one trace at a time for averaging by the computer later, it is still cumbersome compared to a running average as its PCI bus is limited to a 133 MB/s transfer rate. For instance, one $10 \mu\text{s}$ trace at 1.5 GS/s would take at least $110 \mu\text{s}$ to transfer. If a total of around 1,000,000 averages are desired, then the total transfer time is $110 \mu\text{s} \times 1000 = 110 \text{ ms}$. Doing all those averages on the card would be much more efficient as only one transfer would be needed.

The data acquisition card has two undesirable features that are apparent in the data, both seen in Figure 6.12. The most obvious feature is the spike at about $4.5 \mu\text{s}$. This feature is always present, and must be worked around when taking data. Also clear, especially in the time trace

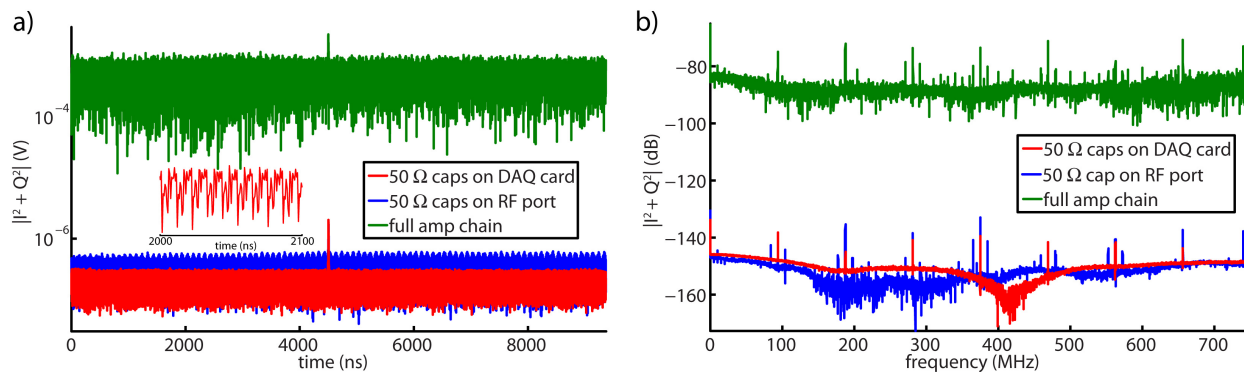


Figure 6.12: Gage data acquisition card background - a) Time traces with just the card, the card and the IQ mixer with the LO port plugged in but not the RF port, and the card with the full amp chain. The inset is a zoomed in portion of the bare card data showing the periodic nature of the background signal. There is also a single spike at about $4.5 \mu\text{s}$. b) FFTs of the time trace data reveal that there is a periodic signal spaced by 93.76 MHz. 10 MHz sidebands appear when the LO port of the mixer is driven, suggesting the generator's clock is bleeding through.

inset, is a periodic spurious background signal, the second feature. The FFT of the background data shows amplitude spikes every 93.76 MHz. Whether this signal is from a source on the card or is being picked up from the environment by the card, it is always present. When the IQ mixer and LO source are added (with the RF port capped) 10 MHz sidebands appear next to the 93.76 MHz-spaced peaks. These most likely are from 10 MHz clock bleeding through the LO port from the generator. Because of their periodicity, these spurious signals may be subtracted from time trace data. All time trace data taken by the DAQ card and shown in this work had this correction applied.

6.4 Control program architecture

The control and data taking program was written in LabView 8.5 and consists mainly of three for loops, schematically shown in Figure 6.13. Instruments were controlled through GPIB and USB ports, with the exception of the data acquisition cards which came with ready made proprietary LabView code for communication through the PCI bus. For each plot, the program saves an ASCII log file with all user-controlled settings and notes written for the specific plot, a JPEG screenshot of the plot for easy reference, an ASCII raw data file containing the data before processing, and an

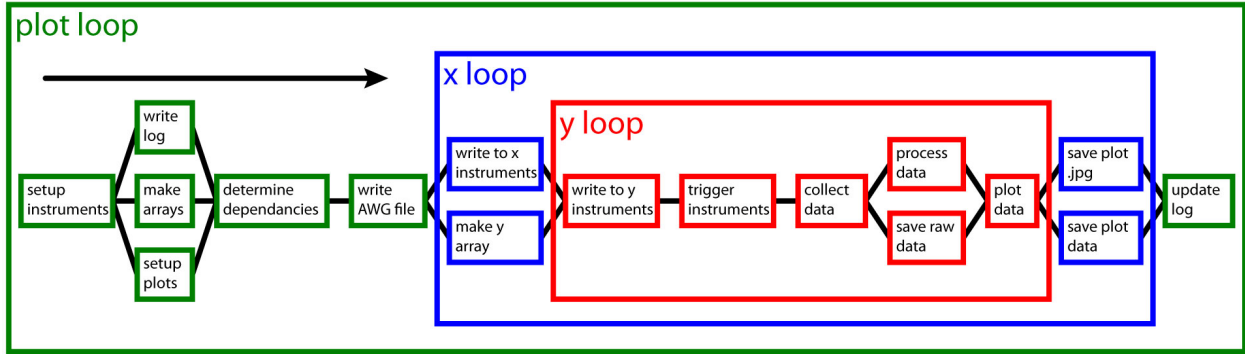


Figure 6.13: Control and data taking program architecture - The control and data taking program mainly consists of three for loops, representing the sweeps on three axes: the y-axis is the inner loop, the x-axis is the middle loop, and the plot axis is the outer loop. The plot axis is where a single value is changed for each new plot. The data flow is left to right.

ASCII plot data file containing the data after processing. The files are named using the convention qbYYMMDD.hhmmss.yVar-xVar-pVar.xxx, where yVar, xVar, are pVar abbreviations for the y-, x-, and plot-axis variables being swept, and .xxx represents the appropriate file extension. The characters after qb are a time stamp, for uniquely labeling the files. After the x-axis and y-axis loops are finished, the log file is updated to reflect any changes to the notes written by the user.

The outer plot loop is where housekeeping for the instruments is done, things like clearing buffers and setting sensitivity ranges. The three axis arrays are made, the plot axes are adjusted, and the log file is written. Dependencies are determined here, and the file containing all points for the Tektronix AWG5014B is written as well. Determining dependencies means both selecting which instruments will need to be updated at each point, but also choosing what non-axis variables need to be changed to accomplish the user's demands. For instance, it is common to take spectroscopy data only in a narrow range around the f_{01} transition since data outside of this range is usually not useful and leads to very large files and long acquisition times. This means that the y-axis drive frequency array depends on the value of the x-axis flux bias according to some previously determined polynomial; the y-axis depends on the value of each x-axis point. This extra logic step can be complex, but is valuable because it improves efficiency; updating every single instrument, whether it changed or not, would be time intensive as some instruments are slow to respond to

changes.

The y -axis array is made for each x -axis loop and sent to the y -axis loop for application. The instruments that change only when the x -axis changes are updated during the x -axis loop. After the y -axis loop finishes, a JPEG screenshot of the plot is taken and the already processed plot data is saved.

During the y -axis loop the pertinent instruments are changed at each y value, the instruments are triggered, a delay occurs while the instruments run, then the computer retrieves the data from the appropriate instrument. The raw data (i.e. histogram data or IQ data) is saved, as well as being processed into the form necessary for plotting, such as occupation probability or phase. The data are then plotted.

For efficient data viewing and analysis a data plotter was also written in LabView 8.5. Using the path to the JPEG screenshot file, it recalls all the information from the log file and all the data from the plot data file. This tool was exceedingly useful for on-the-fly analysis of data for use in later data scans. For example, it readily fits most spectroscopy in order to get a polynomial file relating the flux bias to the f_{01} transition frequency to be used in later scans.

While LabView provides very convenient user interface, efficient plotting and data manipulation tools, and simple, robust instrument communication in its NI-VISA tools, it lacks the flexibility of a scripting platform like Matlab. LabView does have its own scripting language, Mathscript, as well as a port to Matlab, but using a scripting user interface on the program's front panel is very slow as LabView re-compiles the script at each loop iteration. This may be avoided by only writing the Mathscripts in the back panel, but this complicates the user interface and could lead to code corruption. The control and data taking software had front panel scripting user interfaces, but they were disabled when not in use, for faster operation. Most dependencies could be controlled using simple polynomials, which are very efficient to use.

7

Tunneling measurements

7.1 Device with DC SQUID

The data taken with a DC SQUID were done using a via-style junction device, with the purpose of demonstrating control over the entire Bloch sphere. This required characterizing the qubit potential using spilling points, finding the transition frequency f_{01} as a function of applied flux, and driving Rabi oscillations so that π - and $\pi/2$ -pulses may be identified for use in tomography. T_1 was also measured as part of the qubit characterization procedure.

7.1.1 Steps

Qubit steps are the first characterization of a metastable phase qubit, and are described detail in Section 3.1.1. In short, the qubit is kept in its ground state and the DC flux bias is swept to see where the qubit spills into an adjacent well. The sweep is done with the initial well shape at or beyond each extreme of the sweep range in order to find the hysteretic, or multi-well, region. Steps data for the device are shown in Figure 7.1, along with arrows indicating the sweep direction from the two initial states. This data is a combination of two plots, one for each sweep direction, summed and normalized. The color axis of this plot is the number of switching events detected at

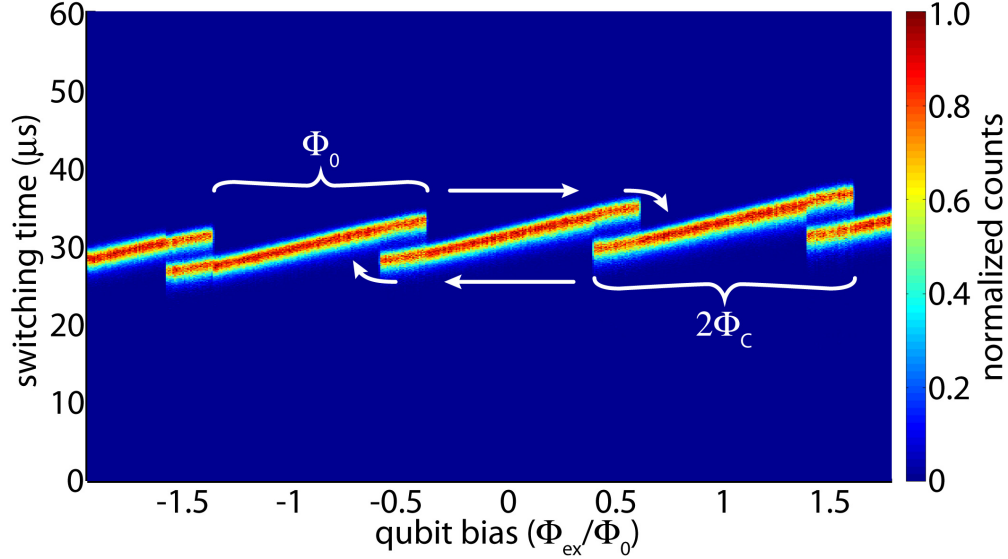


Figure 7.1: Via-style junction metastable phase qubit steps - Qubit steps for characterizing qubit hysteresis, taken using DC SQUID readout. The color axis is the number of voltage switching events. Two datasets have been summed and normalized for clarity, and arrows are included to show the sweep direction. From the steps data one can get values for Φ_0 and Φ_C , which can be used to calculate the coupling between the qubit and bias line M_{QuB} as well as the hysteresis β_L .

a given time for a given flux. The time axis of this plot is proportional to the current in the qubit loop because of the time domain readout procedure outlined in Section 3.2.5.1. From the steps data we can find the coupling M_{QuB} between the bias line and the qubit, as well as β_L . Since the current driven by equipment at room temperature is known and the separation between tunneling events is always Φ_0 , the coupling is $M_{QuB} = \Phi_0/I$. The distance from the middle of a given step to the end of the step is Φ_C . From this steps dataset, $M_{QuB} = 2.3$ pH and $\beta_L = 2.0$. The steps also allow one to find the readout flux, which is in the middle of either of the double well potential regions of the step to be operated on.

7.1.2 Spectroscopy

Another characterization of the qubit's potential well shape may be done by finding the transition frequency between the ground and excited states, f_{01} , for a variety of flux biases. This is easily done by sweeping the qubit drive generator through a range of frequencies at each flux bias and looking at the response. When the drive is on resonance with the qubit, the tunneling rate from

the qubit well to the next well increases. A long drive pulse is used (1 or 2 μs) so that the Rabi oscillations drop down to a constant $P_{|1\rangle} = 0.5$ by the end of the pulse, giving consistent results. If short pulses were used the spectroscopy data would be spotty, since the oscillation could be at a Rabi maximum or minimum when the qubit is measured. Spectroscopy gives a useful relationship between flux bias and f_{01} . Figure 7.2 shows the spectroscopy for the via-style junction metastable phase qubit coupled to a readout DC SQUID. Although several splittings are seen, a dominant splitting is seen at 9 GHz, the location of a transmission line cavity coupled to the qubit. This cavity was used for photon swap experiments[41] which are outside the scope of this work and therefore not discussed. The other splittings are spurious TLSs, described in Section 2.2.1.1, which illustrate the need for small area junctions that show few or no TLS splittings. The presence of so many spurious TLSs in this device required a high resolution spectroscopy plot like the one above to be able to choose a clean region without too many spurious TLSs in which to operate the qubit so that energy exchange with the spurious TLSs will be minimized. The clean region at 8.1GHz was chosen for further characterizing and operating the qubit.

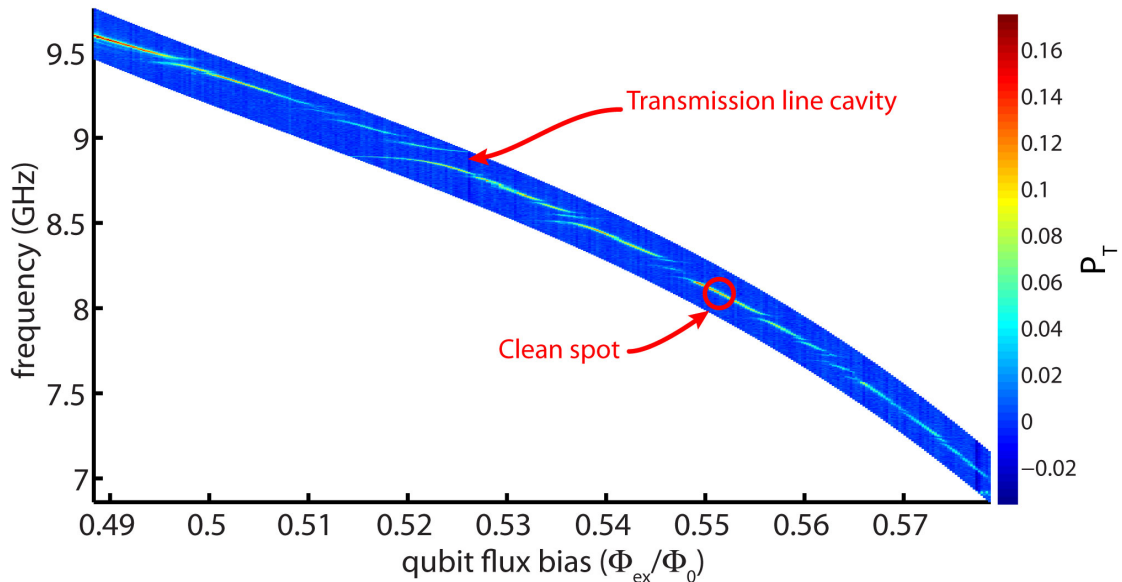


Figure 7.2: Via-style metastable phase qubit spectroscopy - Qubit spectroscopy, with a fixed cavity at 9 GHz. The other splittings are all spurious TLSs. The clean spot at 8.1 GHz was chosen as a spot for performing the other characterizations.

7.1.3 Rabi, T_1 , Ramsey

Rabi and T_1 data were taken after sweeping the drive frequency and power to optimize the microwave signal. The two plots are shown in Figure 7.3. Notice that there is a beating on top of the Rabi oscillations that causes the data to be out of phase with the model between about $t = 150 - 250$ ns, and again at $t = 300 - 400$ ns. This is due to an interaction with a weakly coupled TLS. The TLSs are also partly responsible for the low contrast of 0.45, since they are not just removing energy while the qubit is being driven, but also as the qubit is being measured, as the fast flux pulse moves the qubit across the spectroscopy toward spilling, crossing all the TLSs along the way[25]. The data energy relaxation data are fit with $T_1 = 140$ ns.

Using two $\pi/2$ -pulses with a z -pulse of varying length between them gives the Ramsey fringes seen in Figure 7.4. Fitting the Ramsey fringes near the center of the plot, close to zero detuning, gives $T_2 = 50$ ns, suggesting heavy dephasing since $T_2 \ll 2T_1$. This is somewhat understandable,

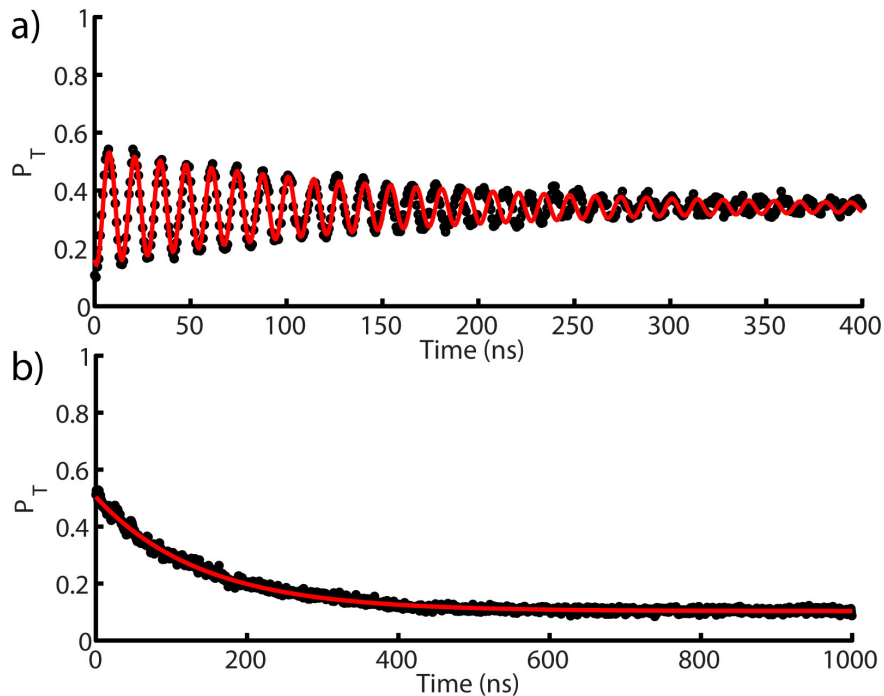


Figure 7.3: Via-style metastable phase qubit Rabi oscillations and T_1 - a) Rabi oscillations, with a contrast of about 0.45. There is a low frequency beating between the qubit and a weakly coupled TLS, evidenced by the data changing phase slightly. b) Energy relaxation measurement, giving $T_1 = 140$ ns.

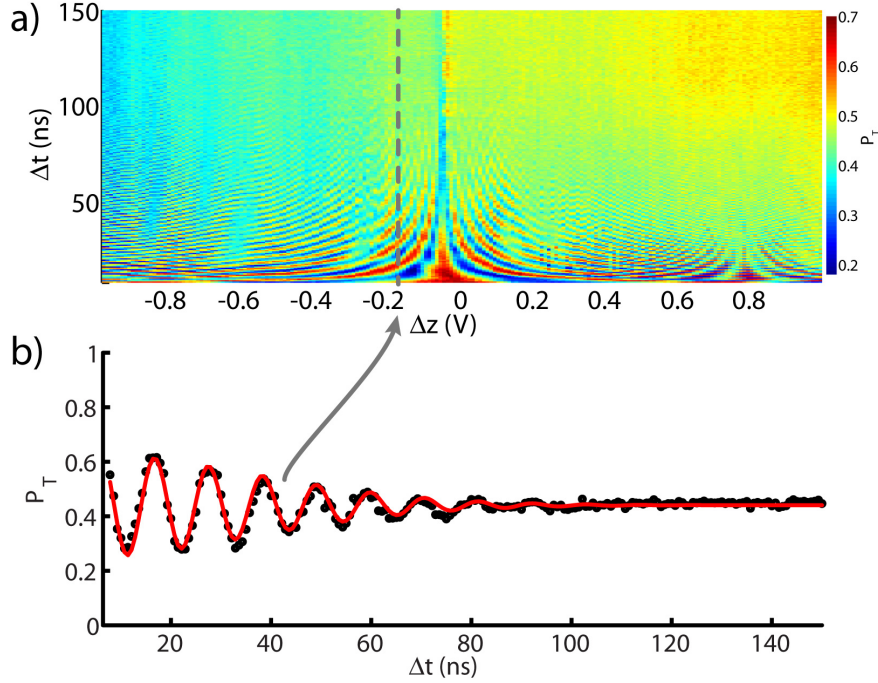


Figure 7.4: Via-style metastable phase qubit Ramsey fringes - a) Ramsey fringes. b) A single trace at z -pulse = -0.18 V and the fit. The result of fitting the curves near the center of the plot gives $T_2 = 50$ ns.

since the data were taken close to spilling, where the spectroscopy slope is steep; the steep slope means that small changes in flux bias from noise make large changes in frequency. Any $1/f$ noise on the bias line will have a large effect on the dephasing due to the steep slope. This device did not have any magnetic shielding around it other than a large mu-metal shield around the fridge at room temperature.

7.1.4 Tomography

Now that the π -, $\pi/2$ -, and z -pulses are known and the time scales shown to be sufficiently long, tomography may be attempted. A full tomographic sweep was done on four different initial states, described in Section 3.1.2. Each of the states $|0\rangle$, $|1\rangle$, $(|0\rangle + |1\rangle)/\sqrt{2}$, and $(|0\rangle + i|1\rangle)/\sqrt{2}$ was prepared, then a second pulse of varied phase and amplitude was applied to do the tomographic inspection of the state. The results for each of these states is plotted in Figure 7.5.

Doing full tomography on an initial state gives far more information than is required to describe

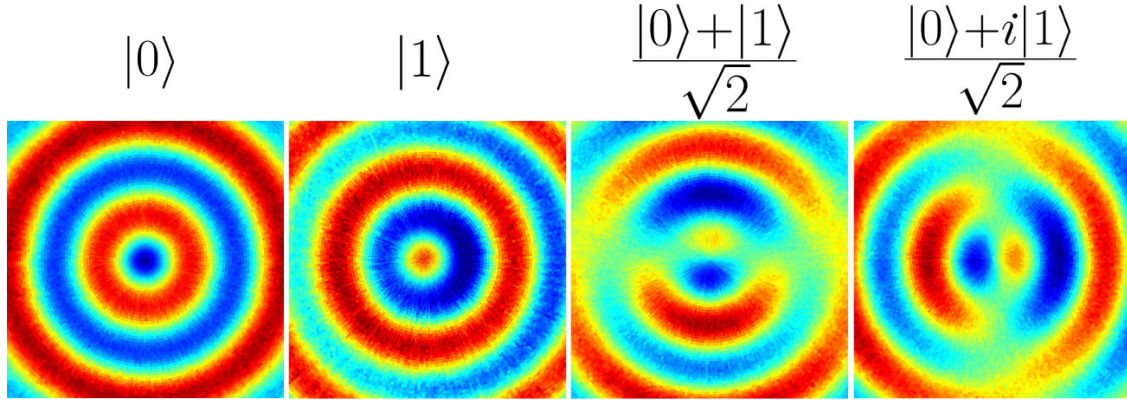


Figure 7.5: Full tomography data - Full tomography on four states, sweeping the tomography pulse amplitude and phase. The initial states are shown above each plot.

the location of the Bloch vector. Doing just three orthogonal pulses is sufficient to fully describe the position of the Bloch vector. The three pulse method ($I, 90_x, 90_y$) was implemented on the initial state $(|0\rangle + i|1\rangle)/\sqrt{2}$ (prepared with a $\pi/2$ -pulse), but with a z -pulse to intentionally detune the potential away from the initial potential's transition frequency and cause the Bloch vector to precess. This precession combines with the energy decay T_1 to trace out a spiral on the Bloch sphere in time. The pulse sequence is shown in Figure 7.6a, the time domain results and a fit for the three tomography pulses is shown in Figure 7.6b, and the plot of the three coordinates from the time domain in a 3D space is shown in Figure 7.6c, with the fit shown in red. This protocol has been

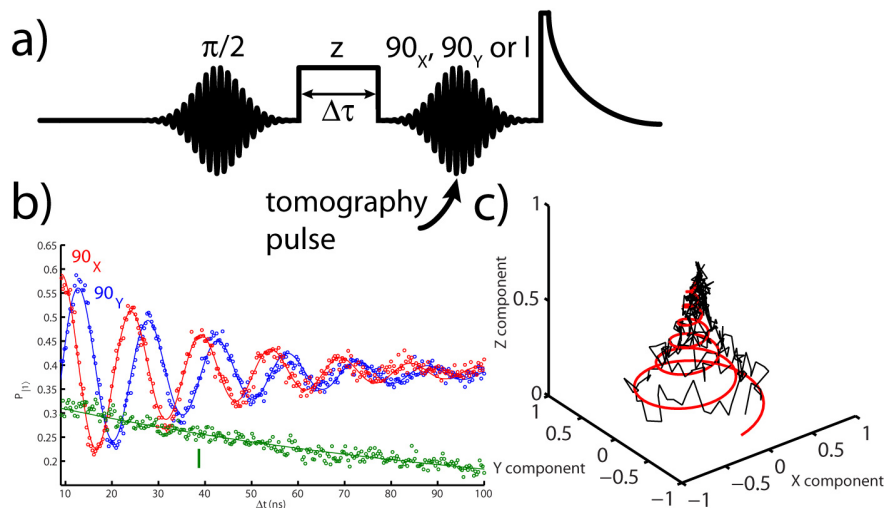


Figure 7.6: Tomography data of $\pi/2$ state decay - Three-pulse tomography of a precessing, decaying $(|0\rangle + i|1\rangle)/\sqrt{2}$ initial state.

previously implemented in metastable phase qubits[58]. This practical application of tomography, combined with the full Bloch sphere plots from Figure 7.5, demonstrate successful implementation of qubit state tomography measurement capabilities.

7.2 Device with tunable cavity

The tunable cavity design was implemented with shadow evaporated junctions on a single wiring layer without depositing any insulators. The purpose of this device was to show that both tunneling and dispersive measurement schemes may be used on the same device. However, as this chapter is concerned with tunneling measurement only, the dispersive data will be shown in the next chapter. Here, in addition to characterizing the tunable cavity, the typical qubit characterizations will be performed: qubit steps, spectroscopy, Rabi oscillations, energy relaxation, and Ramsey fringes.

The resonant nature of the tunable cavity also allows two other characterizations. First, qubit energy loss through the cavity via the Purcell effect is shown to be minimized with the cavity far detuned, then present when it splits the qubit spectroscopy. This not only demonstrates the Purcell effect in this device, but also demonstrates that by using a tunable cavity the intrinsic qubit energy loss rate can be recovered when the cavity is far detune. Second, the extra photons generated from a tunneling event during ring-down in the adjacent potential well are shown to appear in the cavity, which disturbs any prepared cavity states.

7.2.1 Tunable cavity characterization

The cavity spectroscopy was taken using a network analyzer for multiple periods, shown in Figure 7.7. Fitting this data shows that the tunable cavity is single valued with $\beta_L = 0.8$, and has almost 2 GHz of range. As discussed in Section 4.2, the large series inductance L_s that is used to increase the cavity's internal quality factor decreases its frequency range. Since there are multiple periods the flux bias axis can be calibrated in units of Φ_0 , which then allows for a calculation of

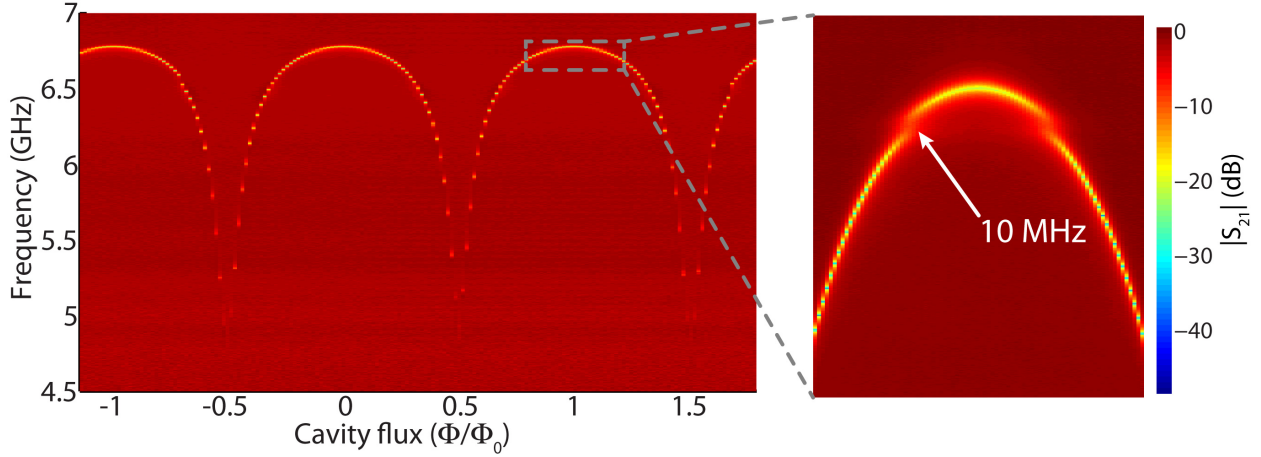


Figure 7.7: Tunable cavity spectroscopy - Flux bias to the tunable cavity was swept, and its frequency measured. Its frequency swings between 4.9 and 6.8 GHz. A fit to the spectroscopy gave $\beta_L = 0.8$ and $I_c = 0.38 \mu\text{A}$, close to the design values. The top of one of the Us is shown in higher resolution, revealing a spurious 10 MHz splitting at about 6.75 GHz.

the coupling between the bias line and tunable cavity. This data gives $M_{CavB} = 1.7 \text{ pH}$, close to the design value. Figure 7.7 also shows a higher resolution magnified view of the top of a tunable cavity curve, revealing a spurious 10 MHz splitting at about 6.75 GHz. This splitting remained in the same location with the same size for several cooldowns, suggesting that it was not a spurious TLS from a materials defect. It is likely a slot mode resonance, resulting from ground planes at different potentials; the crossover bonds used to connect the ground planes (Section 5.3.2) may have not been sufficient to suppress this spurious mode.

Moving the qubit flux while watching the tunable cavity spectroscopy may be used to calculate the cross coupling between the qubit bias line and the tunable cavity. This is useful for creating calibrations that keep the tunable cavity frequency constant while moving the qubit flux. For this device, the coupling between the qubit flux bias and the tunable cavity was $M_{CavQuB} = 0.2 \text{ pH}$.

Figure 7.8a is a power sweep of the cavity when tuned to its maximum frequency at 6.78 GHz. The drive powers in the legend are calculated by knowing the generator power and the loss in the fridge. The highest power trace shows the cavity bifurcating. Figure 7.8b is a Lorentzian fit to one of the traces in the linear regime according to Equation 3.11, with the power to the device at about

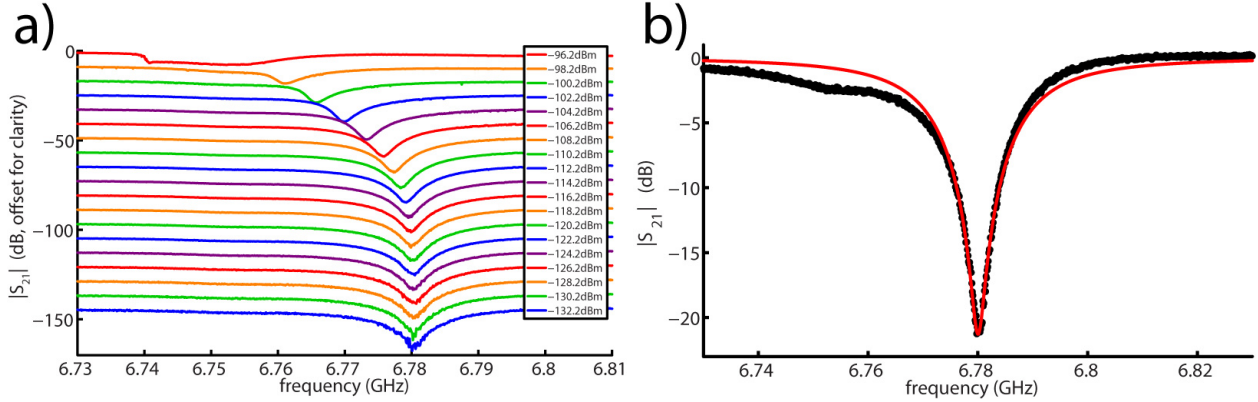


Figure 7.8: Tunable cavity power sweep and fit - a) The tunable cavity is tuned to its maximum frequency at 6.78 GHz, and the drive power to the cavity is swept. The drive powers reported in the legend are calculated from the generator and losses in the fridge, referenced to the plane of the SMA connectors on the box. b) A Lorentzian fit to one of the traces in the low power regime.

-120 dBm. The fit gives $f_0 = 6.780$ GHz, $S_0 = 0.031$, $Q = 278$, $Q_{int} = 8973$, and $Q_{ext} = 287$. The cavity quality factor is clearly dominated by the coupling capacitor and 50Ω line, meaning most of the signal is recovered by the amplifier chain instead of being lost to the environment.

The IQ plot of the tunable cavity while at its maximum frequency is shown in Figure 7.9. The kink in the data is from the 10 MHz spurious resonance at 6.75 GHz, and the resonant frequency of the cavity is marked with a blue dot. The rotation of the IQ circle is a result of impedance mismatches along the microwave line. This could be corrected using Equation 6.5.

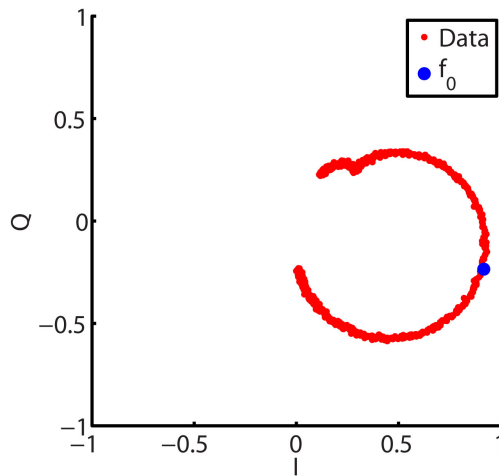


Figure 7.9: Tunable cavity IQ plot - The IQ plot of the tunable cavity at f_{max} , with the resonant frequency marked with a blue dot. The kink is the spurious 10 MHz splitting at 6.75 GHz

7.2.2 Qubit steps

Moving the tunable cavity to a flux sensitive bias allows the cavity to sense changes in the qubit flux state. Figure 7.10 is a composite plot of metastable phase qubit steps measured using the tunable cavity. Data was taken by sweeping a DC bias to the qubit first from the left, then from the right, to get the qubit hysteresis. These two datasets were then added and normalized. The drift in the data is due to spurious cross coupling between the qubit bias and the tunable cavity. As this drift moves the cavity higher in frequency it becomes less sensitive to changes in flux, showing the need to choose a flux sensitive bias point.

Because the qubit steps were taken with a slow DC bias source (measurements on the order of seconds) and not a fast arbitrary waveform generator, the tunneling events happen much earlier than they would if measurements were done on the order of microseconds. Using these rough steps as a guide for determining where to reset, operate, and readout the qubit, one may use fast flux sources to then find the tunneling edges more precisely with an S-curve measurement shown in the inset to Figure 7.10. The arrows point to the three locations where the S-curves need to be

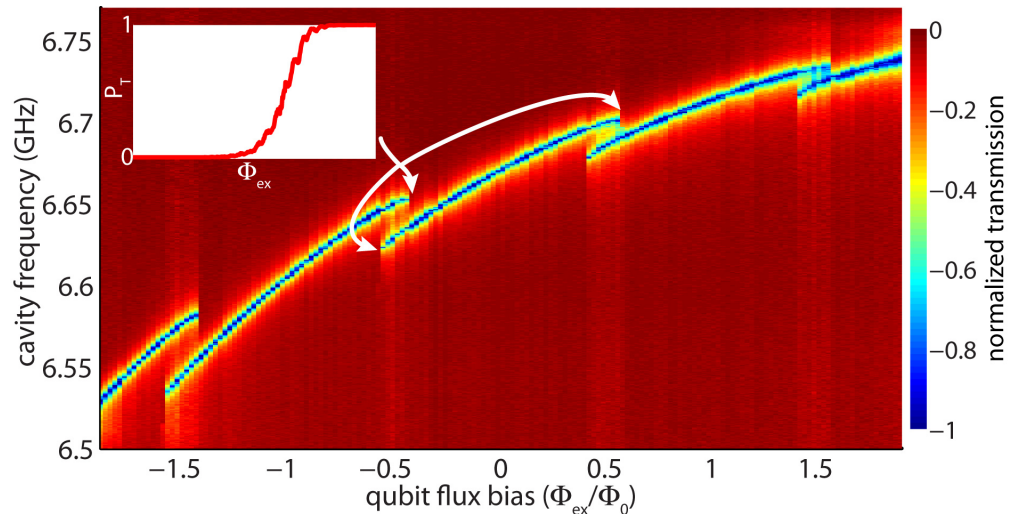


Figure 7.10: Qubit steps taken with a tunable cavity - Qubit steps. The tunable cavity frequency was monitored while the flux bias to the qubit was swept, first from the left and then from the right. The two datasets have been summed and normalized to produce this plot. The drift in the signal is because of spurious coupling between the qubit bias coil and the tunable cavity; the cross coupling was designed to be zero. The inset shows a tunneling S-curve, used for more precisely determining the location of step edges.

taken in order to obtain values for Φ_0 and Φ_C . From the Φ_0 measured here the coupling is found to be $M_{QuB} = 10.8$ pH, more than five times higher than designed. As discussed in Section 4.1.2, this device had a bias coil that did not have a dedicated path return for the return current, which suggests that the return path taken through the ground plane added coupling between the bias line and the qubit. From the Φ_C measured here, $\beta_L = 2.5$ and $I_c = 0.33$ μA . The shadow evaporated junction on the qubit was designed to be identical to the junction on the tunable cavity, and their critical currents agree within 10% of the design value.

7.2.3 Measure pulse and retrapping

As discussed in Section 3.2.1, the tunneling measurement may return errors if a tunneled state tunnels back into the original well, being read out as a $|0\rangle$ even though it was measured to be a $|1\rangle$. This happens when the qubit lifetime is sufficiently long that the tunneled state does not decay before the measure pulse has finished. One solution to this problem is to just make the measure pulse long enough that the tunneled state can decay before the measure pulse is over. The result of this approach is shown in Figure 7.11. The longer measure pulse clearly stops retrapping,

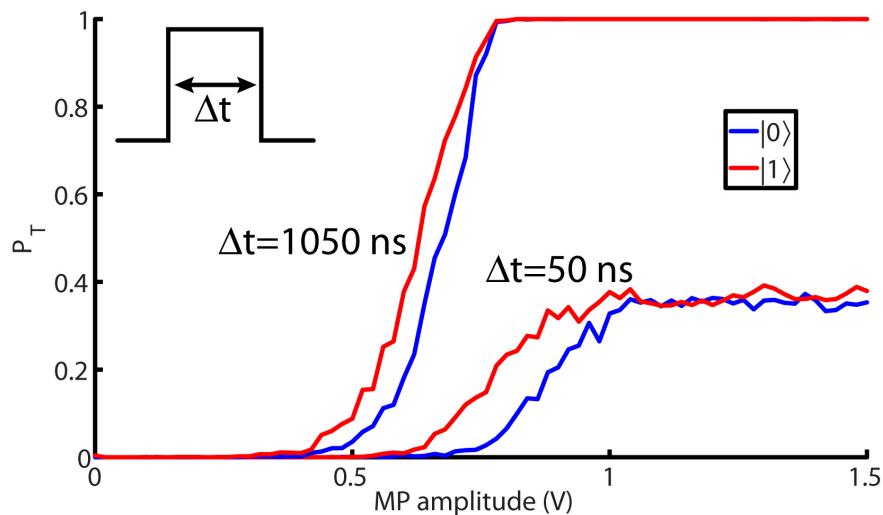


Figure 7.11: Square measure pulse and retrapping - For a 50 ns square pulse, retrapping is definitely occurring, evidenced by a maximum tunneling probability of < 0.4 . The maximum contrast is 0.17. The maximum tunneling probability increases to 1 when the measure pulse is made 1 μs longer, and has a 0.22 maximum contrast.

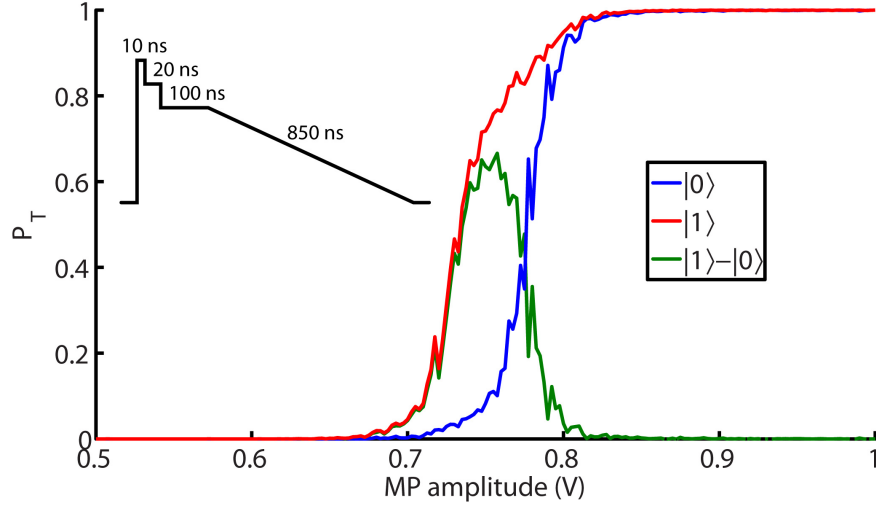


Figure 7.12: Anti-retrapping measure pulse contrast - Using an anti-retrapping measure pulse shape, shown in the inset, gives a much higher contrast of 0.67 between the $|0\rangle$ and $|1\rangle$ states.

but it also gives more time for the $|0\rangle$ state to tunnel through the barrier and give a false $|1\rangle$ state result.

Using an anti-retrapping measure pulse gives much higher contrast, about 0.67, as seen in Figure 7.12. While using the anti-retrapping measure pulse increases contrast, effects that decrease contrast may still be present. These effects include thermal excitation from the ground state and excess flux noise on the bias line.

7.2.4 Spectroscopy, AC Stark shift

To perform spectroscopy measurements, a DC flux source held the qubit at its double well readout spot with no fast fluxes applied. An arbitrary waveform generator was used to apply fast flux pulses to move the qubit to other potential well shapes for qubit manipulations, as well as to apply the measure pulse. This allowed access to the entire qubit step, as shown spectroscopically in Figure 7.13. A slice of the spectroscopy at its highest frequency is shown in the inset. The qubit was driven with enough power to excite transitions beyond the f_{01} transition, which gives a measurement of the relative anharmonicity $\alpha_r = (f_{01} - f_{12})/f_{01} = 0.23\%$ at the highest qubit frequency, also the deepest potential well. This small relative anharmonicity shows that the qubit

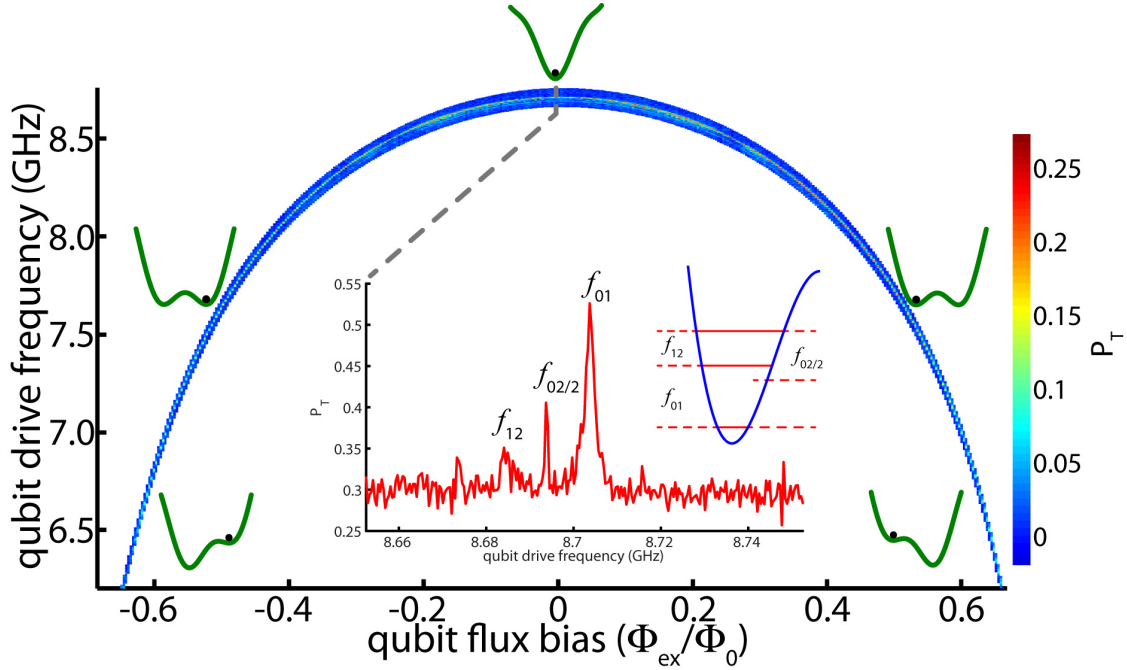


Figure 7.13: Qubit spectroscopy taken with a tunable cavity - Metastable phase qubit spectroscopy, taken using a tunable cavity to readout the flux state after a tunneling measurement. Taken across an entire step. The inset is a slice of the data at the maximum qubit frequency. The device was being driven hard enough to excite higher levels, allowing a measurement of the relative anharmonicity $\alpha_r = 0.23\%$ at the maximum qubit frequency. The qubit potential at different flux states are also shown.

is very harmonic, and thus quite cavity-like, at its highest frequency. The potential configurations at various qubit flux biases are also shown.

This qubit had no spectroscopically visible splittings, as can be seen in a zoomed in portion of the spectroscopy shown in Figure 7.14a, which shows data all the way down past tunneling. This spectroscopy is taken with the tunable cavity at its minimum frequency, $f_{\text{Cav}} = 4.9$ GHz. Figures 7.14b and 7.14c show a small section around the maximum frequency of the cavity with and without the cavity present. The qubit-cavity splitting is $2g/2\pi = 80$ MHz wide. Because of crosstalk between the tunable cavity bias line and the qubit, the flux bias axis of Figure 7.14c was adjusted to match the flux bias axis of Figure 7.14b.

High power spectroscopy was taken to find the $f_{02/2}$ and the f_{12} transitions, and is shown in Figure 7.15. The relative anharmonicity α_r of the qubit varies across this range from about 0.4% to about 3.6%. This weak anharmonicity suggests that when doing dispersive readout, reported

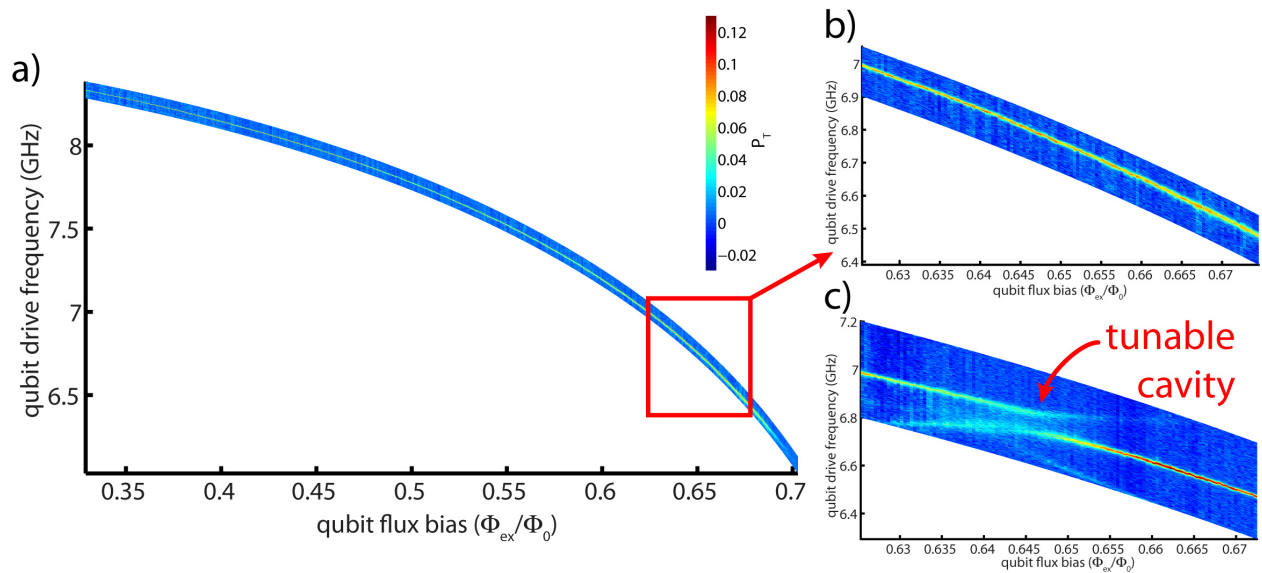


Figure 7.14: Qubit spectroscopy with and without cavity - a) Metastable phase qubit spectroscopy. No splittings seen, and the data goes all the way down to tunneling at around 6.2 GHz. These data have been leveled so that the noise floor of each frequency sweep is at 0. b) Small spectroscopic region, with the cavity detuned to its lowest frequency. c) Cavity at its maximum frequency, interacting with the qubit to cause a splitting $2g/2\pi = 80$ MHz wide. The flux bias axis for the last plot had to be adjusted for spurious crosstalk between the tunable cavity flux bias line and the qubit.

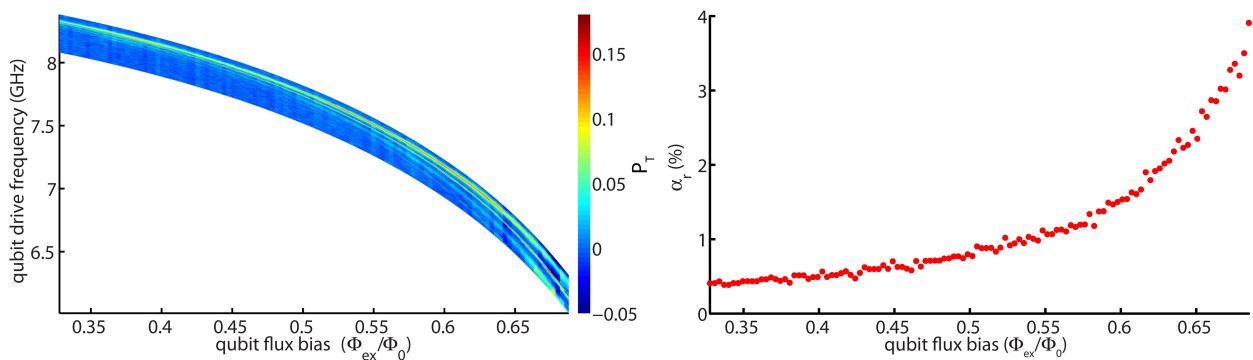


Figure 7.15: High power spectroscopy - High power qubit spectroscopy to measure the relative anharmonicity α_r across much of the spectroscopy range. Thermal activation of the $|1\rangle$ state allows the f_{12} transition to be seen.

in Chapter 8, a three level atom model is needed to model the data, as discussed in Section 2.4.2. Note also that the f_{12} transition is apparent in this data, even though the f_{01} transition is not being simultaneously driven. This is partially due to a native thermal population of the $|1\rangle$ state, allowing the f_{12} transition to appear with only a single tone applied. As discussed in Section 6.1.1, the light attenuation on the fridge was allowing 0.1 to 0.2 thermal photons through to the device, a small but not insignificant population that appears with sufficient drive power.

As derived and explained in Sections 2.4.1 and 3.3.2, the AC Stark shift is the change in qubit frequency f_{01} with the number of photons in the cavity according to $\Delta f_{ac} = 2ng^2/2\pi\Delta_{01}$. For our device the AC Stark shift was measured, with the data shown in Figure 7.16. The fit to the data gives the slope 2.3 photons/ fW , a calibration that may be used to put only one photon on average in the cavity at a time for doing dispersive measurement. The data points at higher power were not included in the fit as the cavity is being driven nonlinear here. The power axis is the estimated power delivered to the reference plane at the SMA connectors on the box holding the device. This power is estimated by measuring the power at the room temperature using a spectrum analyzer and subtracting the value of attenuation between the room temperature fridge input and the reference plane at the box, measured using a network analyzer while the fridge was at room temperature.

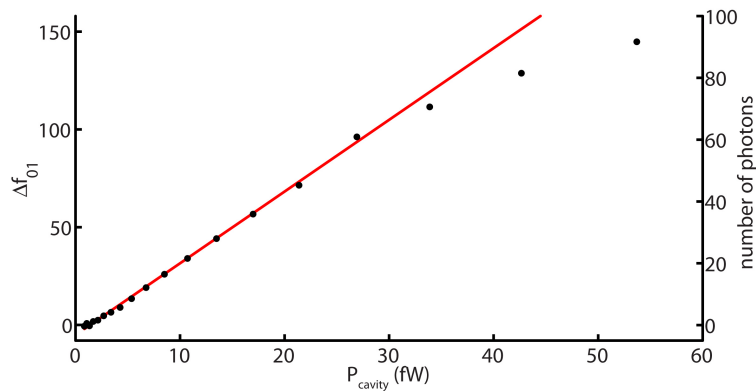


Figure 7.16: AC Stark shift data - The AC Stark shift and fit. For this device, $f_{Qu} = 6.46$ GHz, $f_{Cav} = 6.78$ GHz, and $g/2\pi = 40$ MHz. The fit gave a slope of 2.3 photons/ fW . Higher power points were excluded from the fit as the cavity is nonlinear here.

7.2.5 Rabi, T_1 , Ramsey

Driven Rabi oscillations were measured at several places across the spectroscopy. One of these datasets is presented in Figure 7.17. The first plot shows both the $f_{01} = 7.454$ GHz and the $f_{02/2} = 7.409$ GHz transitions, and is used to find the f_{01} precisely by performing an FFT on each data slice, fitting the periods vs. drive frequency, and finding the drive frequency that gives the maximum period. Figure 7.17b is a longer trace of Rabi oscillations at f_{01} , and is fit to theory. The fit gives $f_{Rabi} = 28$ MHz, with a decay time of $T' = 520$ ns. Sweeping drive amplitude changes the Rabi oscillation frequency linearly, as shown in Figure 7.17c.

The Rabi oscillation data is used to choose a π -pulse for other measurements. As discussed in Section 3.1.3, the duration of the π -pulse needs to be sufficiently long so that it doesn't excite transitions other than the f_{01} transition. While this is best done by measuring the spectral components of the pulse at the qubit's various transition frequencies, the effect of different pulse durations on the $|1\rangle$ state S-curve shows the effect, seen in Figure 7.18. The 29 ns and 43 ns pulse lengths did not significantly populate the higher energy levels since the shape of the beginning of the $|1\rangle$ state S-curve is unchanged[55], though near the top of the S-curve there is a difference between the two.

The 29 ns pulse gives a higher contrast since T_1 effects have less time to effect the qubit during

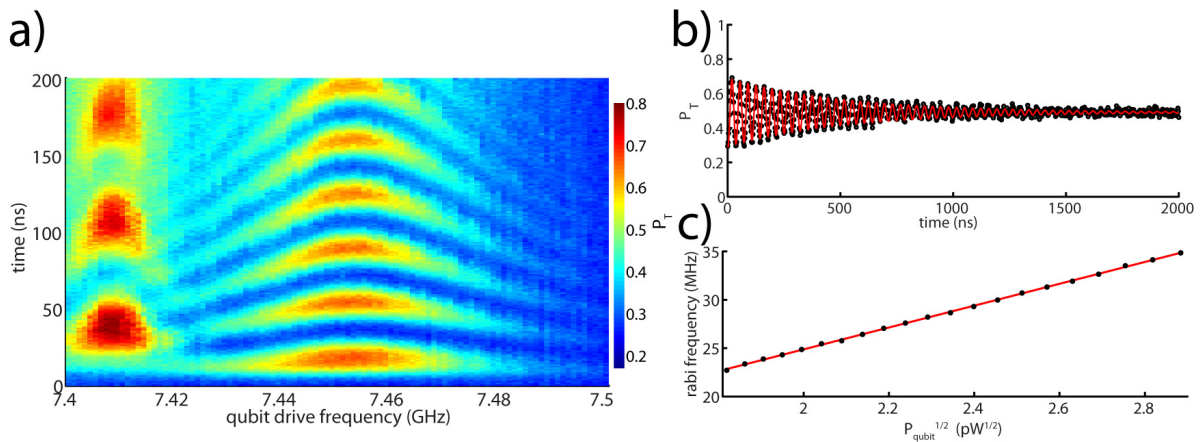


Figure 7.17: Rabis oscillations in a metastable phase qubit - a) Driven Rabi oscillations, sweeping frequency, to find f_{01} precisely. The oscillations on the left side of the plot at 7.409 GHz are the $f_{02/2}$ transition. b) A long, single Rabi oscillation trace at $f_{01} = 7.454$ GHz, fit to theory. c) The change in Rabi frequency with drive amplitude is linear.

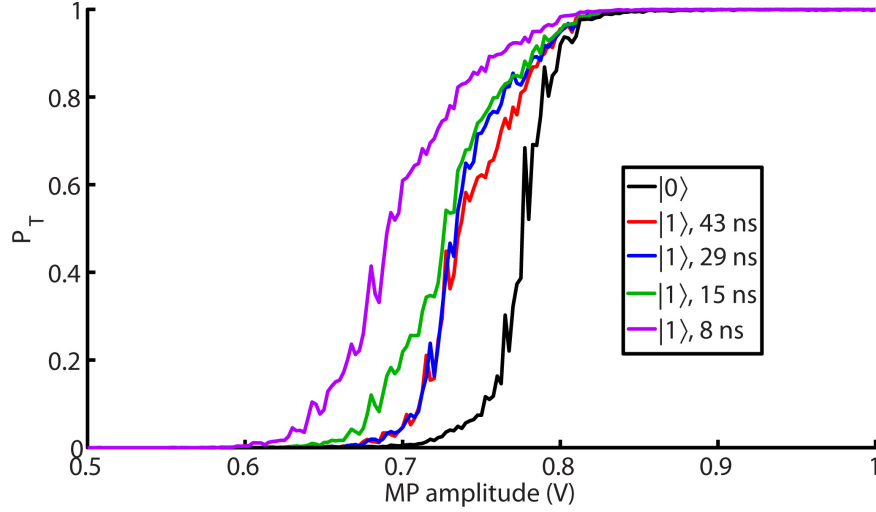


Figure 7.18: S-curves and π -pulse duration - $|0\rangle$ and $|1\rangle$ state S-curves for various π -pulse durations.

the pulse. The 15 ns pulse clearly shows contamination by other frequency components in the beginning of the S-curve while not significantly changing the overall contrast. This contamination is seen at the beginning of the S-curve because the higher, accidentally populated levels are closer to the top of the metastable well's barrier, allowing them to tunnel earlier than the first excited state. While the higher level contamination may not affect the contrast, it will change the energy relaxation rates and the ability to manipulate the qubit in a simple two-level manifold. The 8 ns pulse seems dominated by higher transitions because of its significantly changed S-curve beginning, while offering even higher state contrast. Of these pulses, the 29 ns pulse seems to offer the highest contrast without significant higher level transition contamination.

Now that the π -pulse frequency, amplitude, and duration has been selected, a T_1 measurement may be performed reliably. A T_1 measurement at 8.18 GHz is shown in Figure 7.19, with a fit giving $T_1 = 655$ ns. This data is smoothly decaying, suggesting little to no significant interaction with individual TLSs[31]. From Equation 4.3, showing the loss from the qubit to the bias line, it is clear that part of the loss is due to the five times overcoupling between the qubit bias line and the qubit. For this device, with $M = 10.8$ pH, T_1 would be 938 ns if the bias line were the only loss channel, while if it had ended up as designed then the bias line T_1 limit would have been 23.4 μ s.

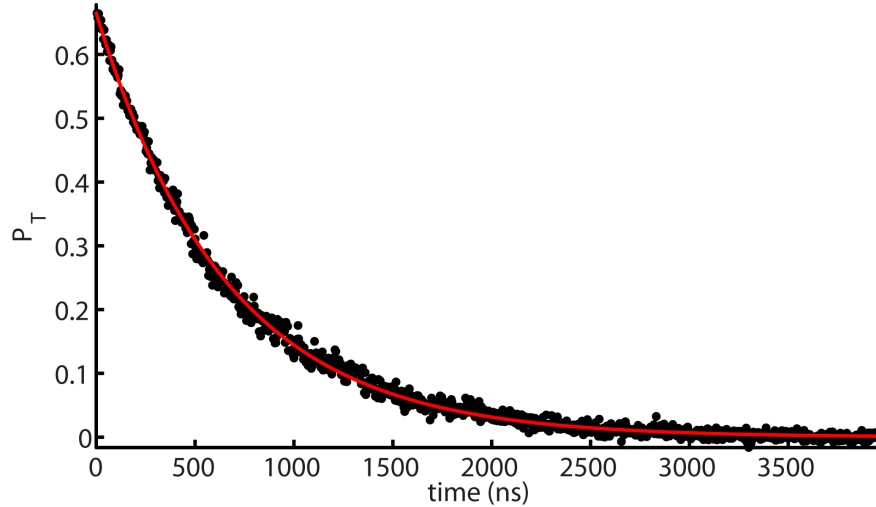


Figure 7.19: T_1 in a metastable phase qubit - A T_1 measurement at $f_{01} = 8.18$ GHz, fit to an exponential with $T_1 = 655$ ns.

While this is a significant improvement in isolation, the qubit is still limited by other loss channels since the measured T_1 is still less than the bias line limited T_1 calculation. The T_1 measurements taken across the qubit spectroscopy will be presented in the next section, where loss through the cavity, characterized by the qubit T_1 , is considered.

Ramsey fringes taken at $f_{01} = 7.39$ GHz are shown in Figure 7.20. When the time traces are fit to $P_{|1\rangle} = 0.5 \cos(\omega_z t) e^{-(t/T_2)^2} + 0.5$ (see Section 3.1.4), the Ramsey frequency changes with z -pulse amplitude linearly, shown in the Figure, with an average $T_2 = 106$ ns. While this is a low coherence time compared to some other qubit types, it is a good coherence time compared to other metastable phase qubits. Some of the decoherence could be due to the strong overcoupling between the qubit flux bias line and the qubit; noise on the bias line is transmitted to the qubit five times more strongly than designed.

7.2.6 The Purcell effect

The Purcell effect in cQED, described in Section 2.4.3, is the energy loss of the qubit to the environment through the cavity. With the tunable cavity circuit we have built here, the Purcell effect may be clearly observed by first moving the cavity far from the qubit and measuring the

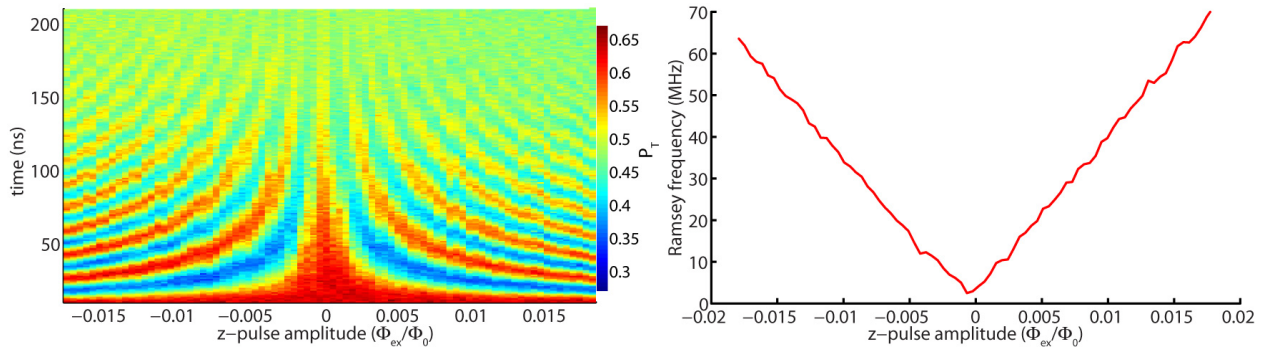


Figure 7.20: Ramsey fringe experiment on a metastable phase qubit - Ramsey fringe measurement at $f_{01} = 7.39$ GHz. Fitting the time traces gives the linear Ramsey frequency plot on the right, as well as giving a Ramsey decay time $T_2 = 106$ ns.

qubit energy relaxation time, then tuning the cavity back in resonance with the qubit to see the loss enhancement appear. The data for this experiment are shown in Figure 7.21. The data were taken for the tunable cavity fully detuned to its minimum frequency at $f_{Cav} = 4.90$ GHz (red dots), then tuned to its maximum frequency $f_{Cav} = 6.78$ GHz (blue dots). Since the energy loss rate γ_P can be found by plugging data from spectroscopy into

$$\gamma_P = \kappa \frac{g^2}{\Delta_{01}^2} = \frac{2\pi f_{Cav}}{Q_{Cav}} \frac{g^2}{\Delta_{01}^2}, \quad (7.1)$$

the intrinsic energy relaxation time (green dots) can be found by doing some simple algebra, $\gamma_q = \gamma_1 - \gamma_P$. Fitting the result to a polynomial allows the resulting curve (green line) to be used to model the two datasets, shown as red and blue solid curves. The values used in these calculations were $f_{Cav} = 4.90$ or 6.78 GHz and $Q_{Cav} = 82$ or 278 , and $g/2\pi = 40$ MHz, numbers obtained from earlier measurements. Clearly the intrinsic energy relaxation time is not simply inversely proportional to frequency as would be expected from dielectric loss mechanisms. The mechanism for this more complicated frequency-loss relationship is unknown.

These two datasets clearly show that by detuning the cavity far from the qubit, the intrinsic qubit loss rate may be nearly recovered. This allows the qubit to be operated with high T_1 s across a large range, overcoming a significant limitation of fixed cavity cQED systems. One may detune

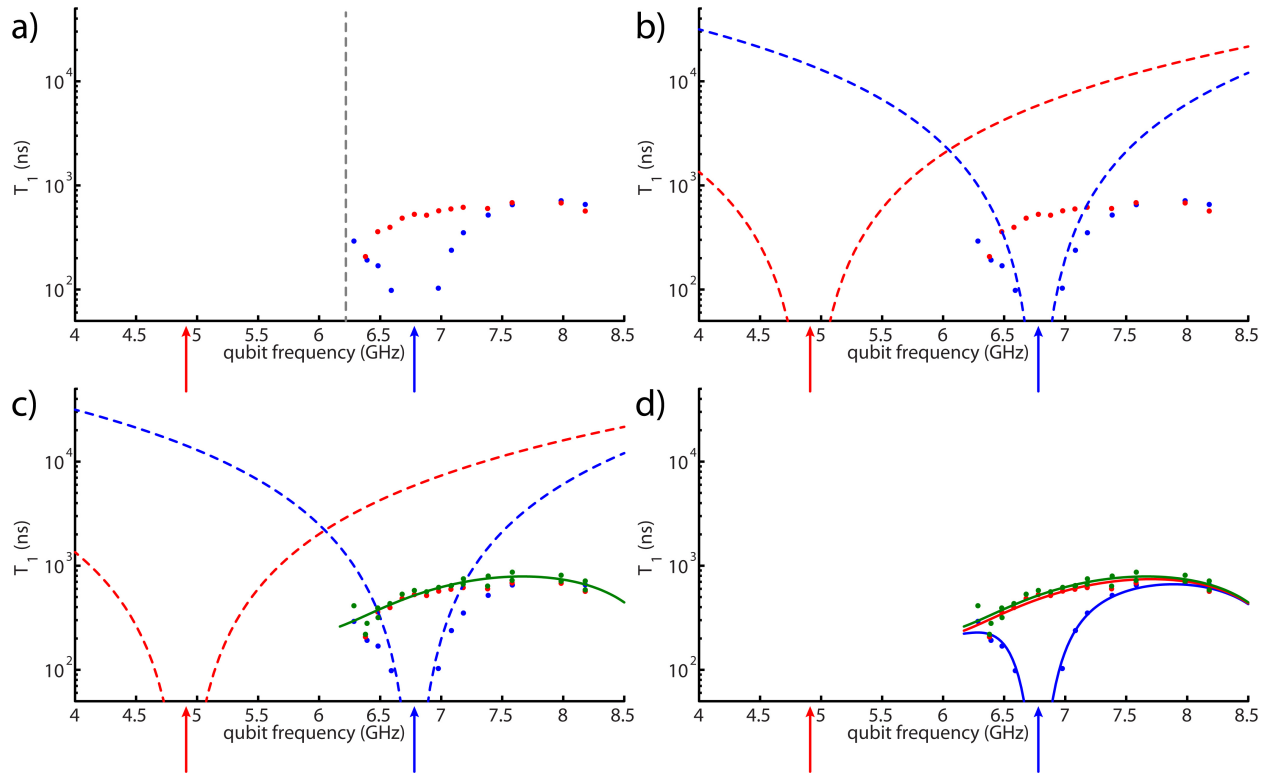


Figure 7.21: Purcell effect on a qubit from a tunable cavity - Qubit T_1 data with the tunable cavity at 4.90 and 6.78 GHz, to see the Purcell effect directly. a) The red and blue arrows indicate the cavity location when $f_{Cav} = 4.90$ and 6.78 GHz, respectively, and the grey dashed line is the minimum available qubit frequency. The procedure for modeling the data is as follows: b) first, the Purcell loss rate γ_P is plotted as red and blue dashed lines using the quality factor found from spectroscopic measurements. Since the overall T_1 is represented in the data, the intrinsic qubit loss rate γ_q is c) then found and plotted as green dots. These dots are fit to a polynomial, the solid green line. d) Finally, the result of the fit to the intrinsic decay time is then used to plot the model corresponding to each dataset as red and blue solid lines. For the red data $f_{Cav} = 6.78$ GHz and $Q_{Cav} = 278$. For the blue data $f_{Cav} = 4.90$ GHz and $Q_{Cav} = 82$. The coupling used was $g/2\pi = 40$ MHz.

the cavity during qubit operations that require long T_1 s, then move the cavity near the qubit for measurement. This specific procedure is clearly possible, though was not attempted with this device.

7.2.7 Tunneling photons poisoning the cavity

As discussed in Section 3.2.1, a tunneling event radiates as the state rings down in the well it tunnels into. Since our tunable cavity is strongly coupled to the qubit, when the frequency of the ringing well is on resonance with the cavity the radiated photons will be transferred into the cavity. This effect has been indirectly observed[61] by watching the state of a second qubit on the other side of a fixed harmonic cavity, but never before by direct observation of the cavity itself.

The pulse sequence used to observe the photons ringing down after tunneling is shown in Figure 7.22. The qubit is reset to its ground state, then the drive to the cavity is turned on to about the single photon level. The qubit is moved to a shallow-well operate flux, a short (5 ns), square measure pulse is applied, then the qubit is returned to the same shallow-well operate flux. After about 4 μ s the qubit is returned to the reset flux and the drive to the cavity is turned off. The cavity is monitored during this entire sequence, and we watch for extra photons to enter the cavity and then decay out to the feedline and amplifier chain. The anti-retrapping measure pulse was not used here, as flux crosstalk from the qubit bias during the long ramp may have altered the results in a complex way.

The data showing ring down photons in the cavity after a tunneling measurement is shown in Figure 7.23. A signal indicating ring down photons present in the cavity is clear when a tunneling event happens. Fitting its decay time gives $T_{decay} = 220$ ns, which is much longer than the cavity response/decay time $T_{Cav} = Q/\omega_{Cav} = 6.5$ ns. This discrepancy implies that the ring down photons are being fed to the cavity over a 200 ns period, as the state slowly decays. This is reasonable since the qubit has been measured to have a T_1 on the order of several hundred

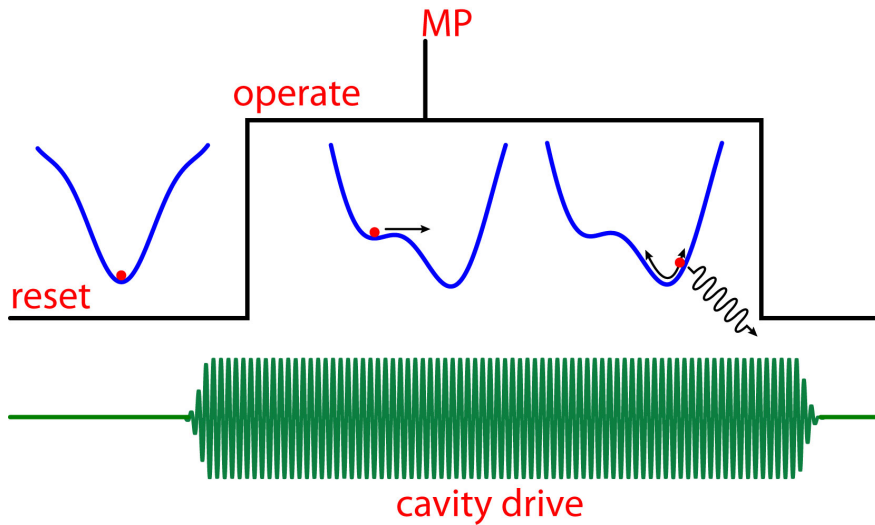


Figure 7.22: Pulse sequence for measuring ring down photons - The qubit is forced to tunnel by a short (5 ns) measure pulse and rings down, all while the cavity is being monitored.

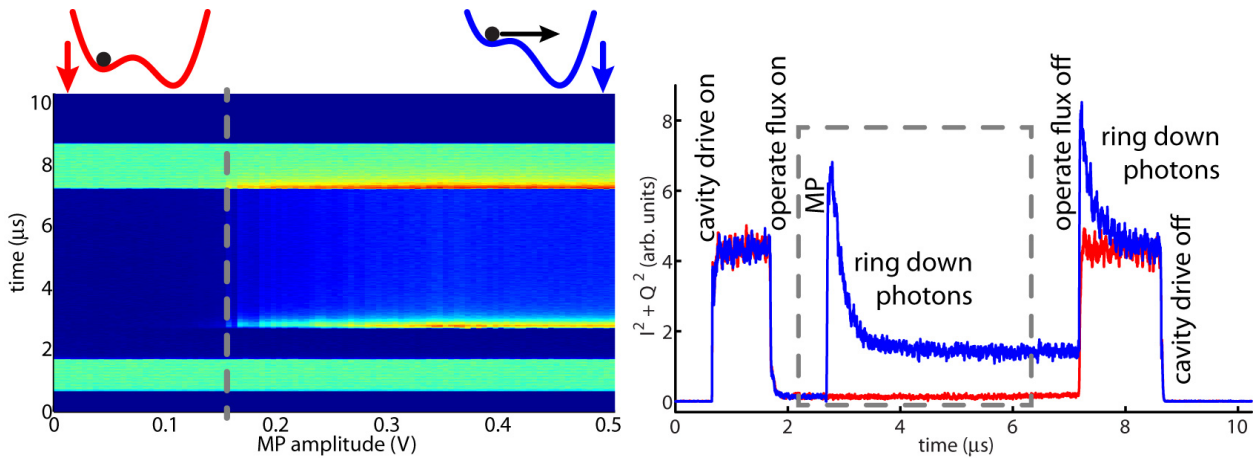


Figure 7.23: Ring down photons in cavity - a) Time traces for an array of measure pulse amplitudes, with the first and last traces plotted in b) to show the signal with and without a tunneling event occurring. The cavity is clearly populated when a tunneling event occurs. A tunneling event occurs again when the operate flux goes back to the reset potential well since the tunneled state now must tunnel back into the original well, again giving ring down photons to the cavity.

nanoseconds near $f_{01} \approx f_{Cav} = 6.78$ GHz. The ring down signal does not go down to its previous level after the measure pulse, since the tunneling event changes the flux state seen by the tunable cavity by Φ_0 , which shifts the frequency of the cavity. Note that the second tunneling event, when resetting the qubit, goes down to the non-measure pulse level. The potential is single valued at the reset spot, so the flux state seen by the cavity is always the same, regardless of whether a tunneling event happened.

7.2.8 Multiplexing

One advantage of microwave readout is that it is easily multiplexed, with little extra chip area used. Although it is not the focus of this work, some early devices were multiplexed to show proof of concept. Figure 5.1c is an optical micrograph showing four tunable cavities with different size vacuum gap shunting capacitors on the same microwave feedline and sharing the same flux bias line. The spectroscopy data from this device is shown in Figure 7.24. These tunable cavities were made with the less reliable via-style Josephson junctions, accounting for the clearly different values of β_L for each device. The multiplexed devices were not pursued further since the complexity of understanding a single device would be further compounded by having four devices moving in the same frequency space. However, this extra complexity will need to be explored in the future if frequency multiplexing for qubit measurement is to be used for efficient wiring schemes when building a quantum processor.

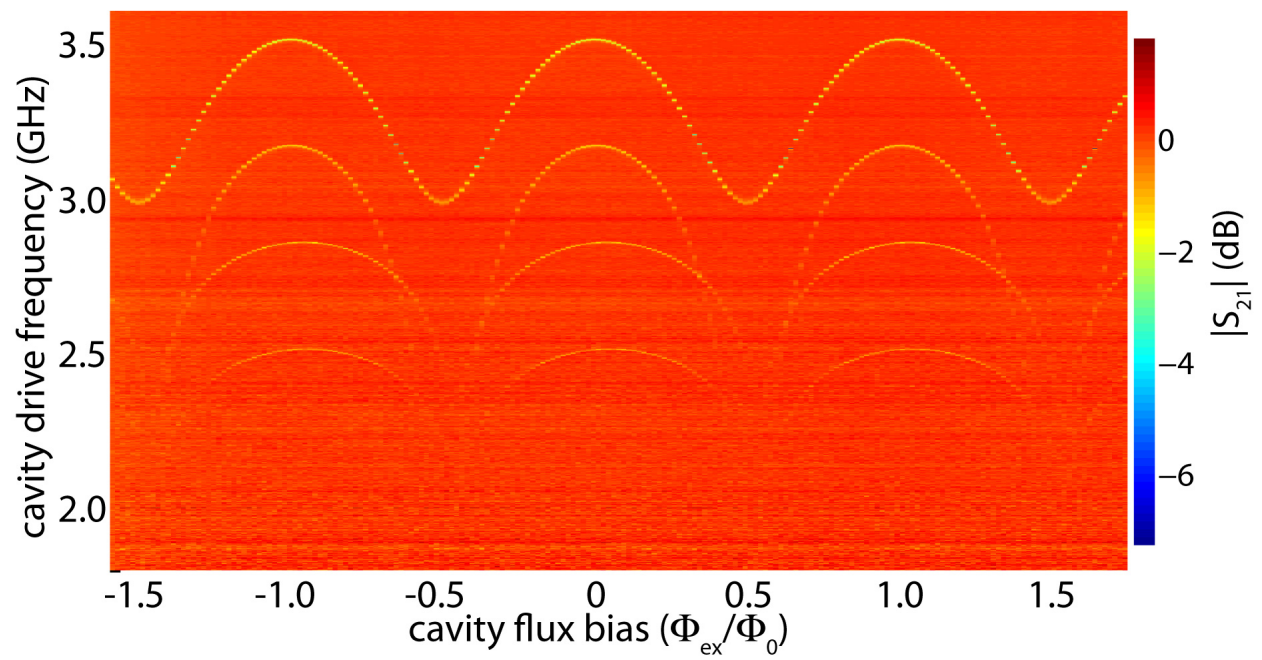


Figure 7.24: Multiplexed tunable cavities - Four tunable cavities with different shunting capacitors multiplexed on the same microwave line.

8

Dispersive measurements

8.1 Metastable phase qubit and tunable cavity device

The device used for the dispersive measurements in this chapter is the same device used for flux readout with a tunable cavity from the last chapter. It is a shadow evaporated $Al/AlO_x/Al$ Josephson junction on a single Al wiring layer. In the last chapter the device was shown to be useful as a flux magnetometer for reading out the qubit flux state after a tunneling measurement. With the device we characterized the qubit, showed that the tunable cavity allows this device to mitigate the Purcell effect losses that are always present in fixed cavity devices, and we directly observed ringdown photons entering the cavity after a tunneling measurement of the qubit. To avoid the drawbacks of tunneling measurement, namely the destruction of the qubit and the emission of ringdown photons after measurement, in this chapter the tunable cavity will be used to dispersively measure the qubit. Dispersive measurement is a non-destructive projection measurement of the qubit state that does not emit the chirped ringdown pulse of the tunneling measurement. The most significant drawback of dispersive measurement is the enhanced loss from the qubit to the environment through the cavity, via the Purcell effect. Since we have already demonstrated that the Purcell effect loss can be mitigated by dynamically tuning the cavity, the demonstration of

dispersive measurement will complete the picture of a technologically useful device for quantum computing applications.

8.2 Spectroscopy

Spectroscopy of the tunable cavity has been presented in the previous chapter, in Section 7.2.1. Cavity spectroscopy data showing the tunable cavity fixed at its maximum frequency while the qubit flux bias is swept is shown in Figure 8.1. At its maximum frequency the tunable cavity is flux insensitive, so any spurious cross coupling between the qubit flux bias and the cavity will have a minimal effect, just as the flux jump from a tunneling event will not be noticeably sensed by the cavity. The zero bias point for the qubit in Figure 8.1 is its maximum frequency, far above the cavity. But when the qubit crosses the cavity at 6.78 GHz on either side of the zero bias point, splittings are seen.

If the tunable cavity is biased to a flux sensitive location, the tunneling events at the step edges will be visible as steps. Figure 8.2 shows tunable cavity spectroscopy, moving the qubit bias, for two different flux sensitive cavity biases. Both plots show both qubit-cavity splittings as well as qubit step edges. The lower frequency cavity bias is more flux sensitive, so the step edge is

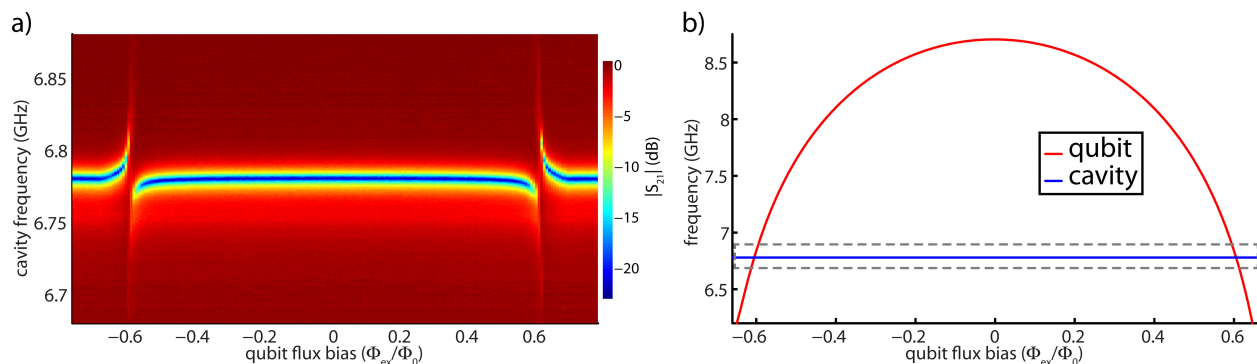


Figure 8.1: Tunable cavity spectroscopy, moving qubit - Holding the cavity fixed at its maximum frequency and sweeping qubit flux. The qubit crosses the cavity twice. Zero flux bias is where the qubit is at its maximum frequency. a) The data over a small frequency range. b) A fit to the qubit spectroscopy is plotted in red and the cavity maximum frequency plotted in blue, with a grey box indicating the region over which the data from a) were taken.

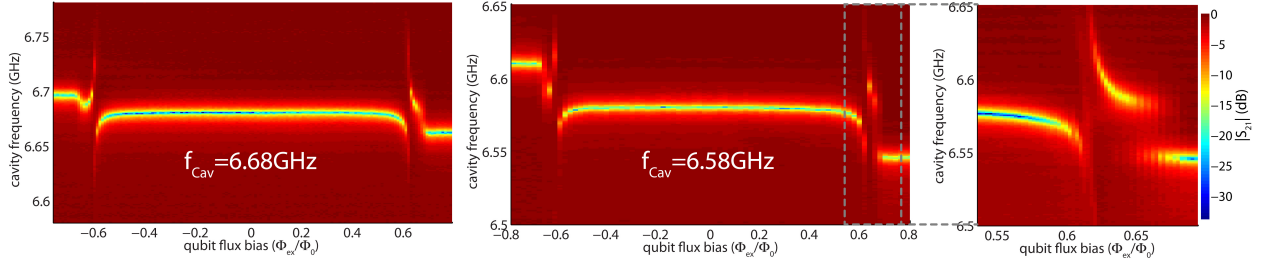


Figure 8.2: Flux sensitive tunable cavity spectroscopy, moving qubit - Holding the cavity fixed at 6.68 and 6.58 GHz and sweeping qubit flux reveals not only the splittings where the qubit and cavity are on resonance, but also the step edges where the qubit tunnels to an adjacent potential well. The crosstalk between the qubit bias and the tunable cavity was calibrated out, fixing the cavity frequency on a given qubit step. The far right plot is a detail of the region in the grey dotted box, more clearly showing a splitting and step edge.

bigger there. The crosstalk between the qubit flux bias line and the tunable cavity was calibrated out so that the cavity frequency would be flat across a given qubit step.

The tunable cavity was then used to measure the qubit dispersively in a spectroscopy measurement, as shown in Figure 8.3. The data were taken by recording the phase of the tunable cavity, driven at low amplitude, while a $2 \mu\text{s}$ spectroscopy pulse is applied to the qubit. The region around the cavity, the “straddling regime” (Section 2.4.2) inside the dotted grey box, is not within the dispersive limit and its behavior is more complex than treated in this work. The straddling regime

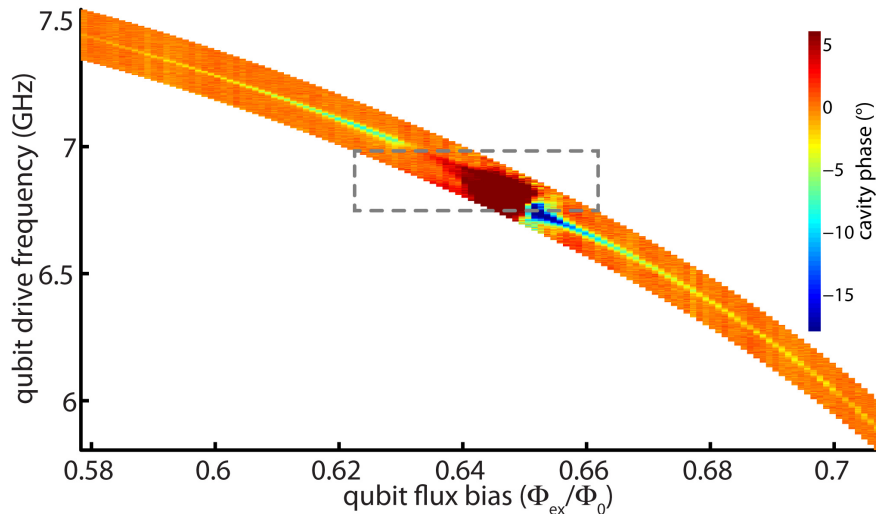


Figure 8.3: Dispersive spectroscopy - The tunable cavity was held fixed at its maximum frequency $f_{cav} = 6.78$ GHz and used to dispersively measure qubit spectroscopy. The “straddling regime” for this device is inside the box of grey dotted lines.

is where the cavity lies between the f_{21} and the f_{01} transition frequencies, and is the only region where the cavity frequency shift may be positive. For this device, when the cavity is at $f_{Cav} = 6.78$ GHz, the straddling regime is $f_{Qu} = 6.78$ to 6.94 GHz. In the dispersive regime, however, the qubit is clearly seen, though the signal fades far from the cavity as Δ_{01} becomes large and the dispersive shift on the cavity becomes small.

8.3 Rabi oscillations and T_1

Rabi oscillations were driven and dispersively measured simultaneously. Data traces were taken in the time domain at each qubit drive pulse length, then combined into the plot in Figure 8.4a. While the qubit drive pulse is on, the qubit is Rabi flopping between the $|0\rangle$ and $|1\rangle$ state in the time domain. Once the drive pulse ends the qubit decays at a rate $1/T_1$ until it is back in the ground state. Taking a line cut along the point where the qubit begins decaying gives the Rabi oscillations in Figure 8.4b. The Rabi oscillation data were fit, giving an oscillation frequency of 27.5 MHz and a decay envelope of 180 ns. Note that the ground state is at about 6° and the $|1\rangle$ state is at about -6° , at the top of the plot; as discussed in Section 2.4.2, the weakly anharmonic metastable phase qubit will have a negative dispersive shift everywhere except in a small region from about $0g$ to $4g$, the straddling regime for this device.

The time domain measurement records not just the qubit state while driven, but also the decay of the state after the qubit drive is turned off. It therefore gives both Rabi oscillation data as well as energy relaxation data, as shown in the time trace in Figure 8.5. The Rabi oscillations in the time domain don't swing all the way between the phase limits for the $|0\rangle$ and $|1\rangle$ states. This is because the cavity response time T_{cav} is on the same order as the Rabi period $T_{Rabi} = 36$ ns. This means that while the Rabi oscillations should be visible in the time domain they will not be faithfully reproduced by the slowly moving cavity.

A time domain T_1 measurement at this flux location is shown in Figure 8.6. The fit to these

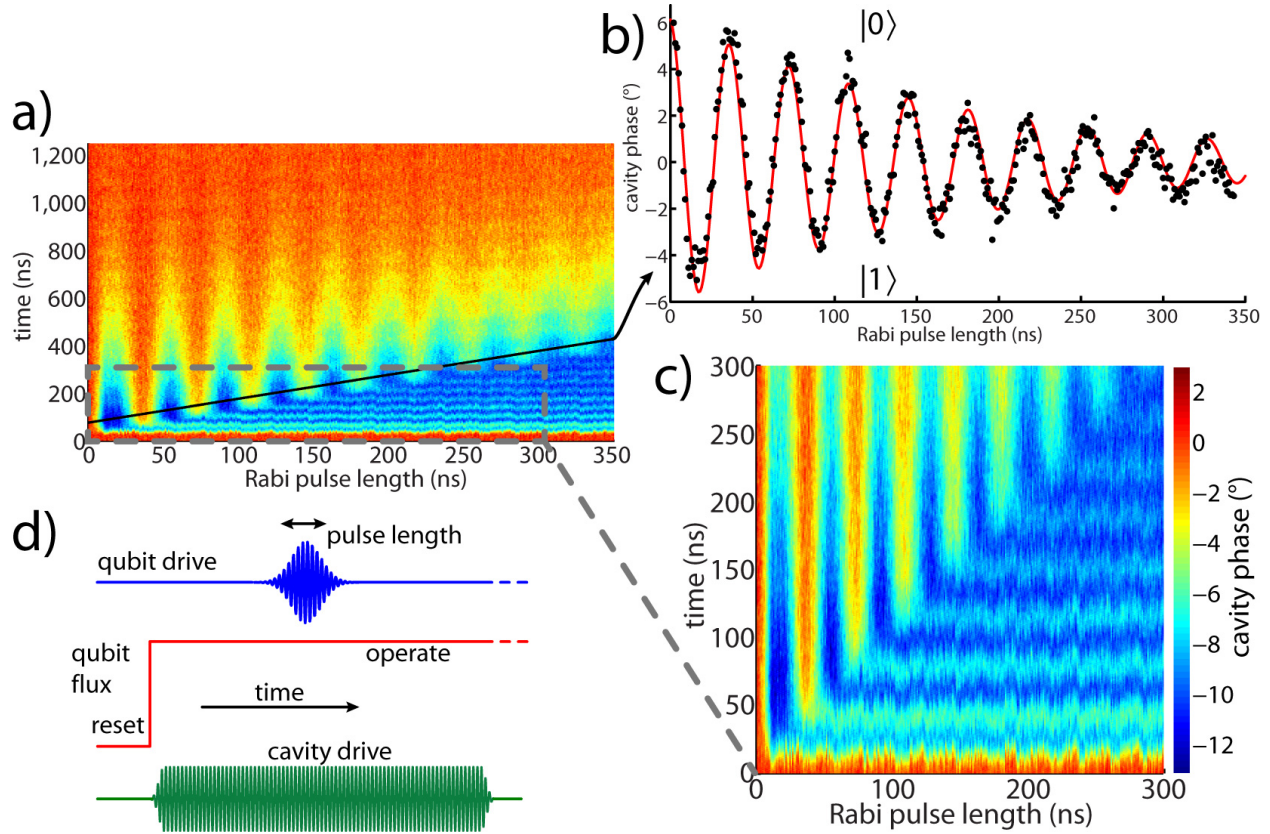


Figure 8.4: Dispersively measured Rabi oscillations - a) Rabi oscillations are driven and measured dispersively. The data are taken in the time domain for each pulse length. The diagonal linecut is b) plotted, fit, and offset to center at 0° , giving a Rabi oscillation frequency of 27.5 MHz and a decay envelope of 180 ns. The cavity phase $> 0^\circ$ when the qubit is in the $|0\rangle$ state. c) A zoom in of the region outlined with grey dotted lines is shown plotted with a 1:1 aspect ratio to emphasize that the Rabi oscillations can be seen in both the time domain and as a function of the drive pulse duration, and the two periods are the same. The data were taken at $f_{01} = 7.18$ GHz. d) The pulse sequence for taking the data.

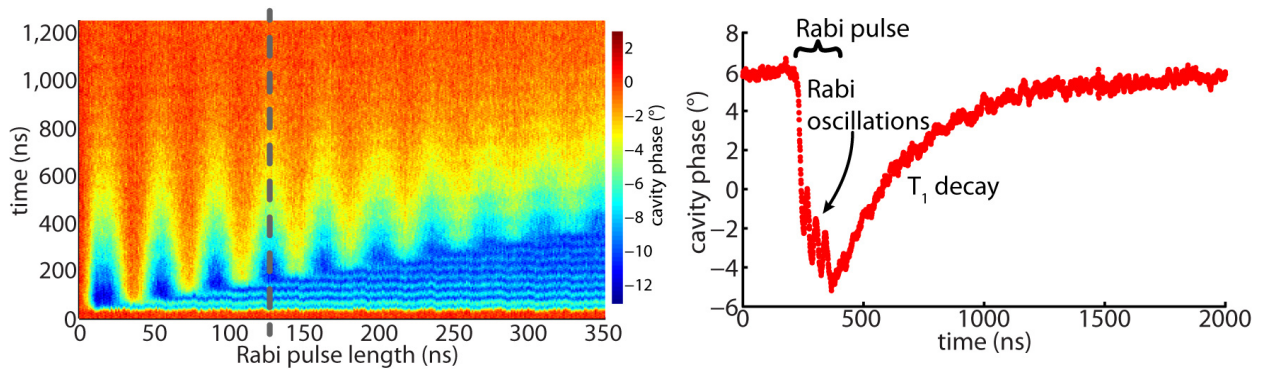


Figure 8.5: Dispersively measured time domain Rabi oscillations - A time trace from the Rabi oscillation data, showing both the driven oscillations and the T_1 decay after the pulse is turned off. The single time trace has been offset in cavity phase to be symmetric about 0° between the $|0\rangle$ and $|1\rangle$ state locations.

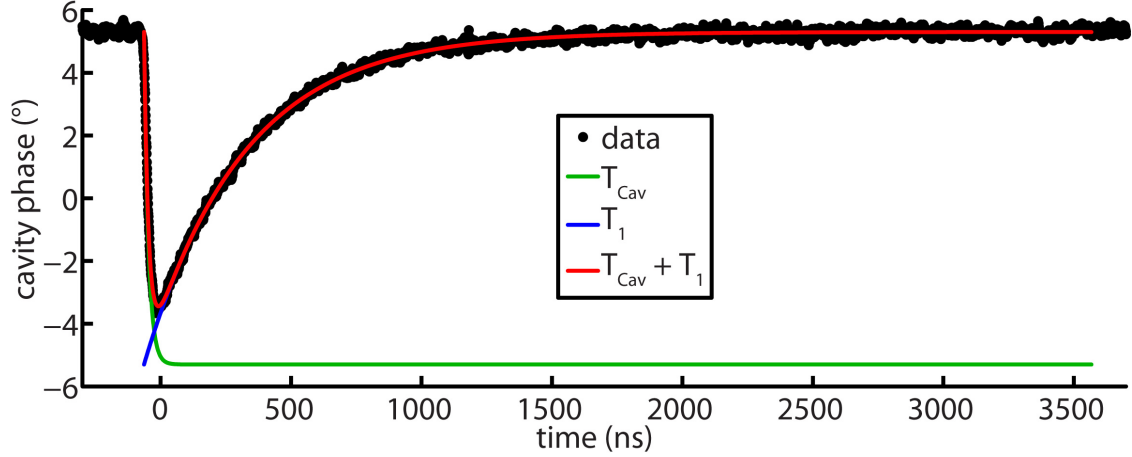


Figure 8.6: Dispersively measured $T_1 - T_1$ data obtained with dispersive measurement at $f_{01} = 7.18$ GHz. The fit gave $T_1 = 380$ ns, a cavity rise time $T_{Cav} = 6.5$ ns, and a total phase swing of $\Delta\phi = \pm 5.3^\circ$.

data give a $T_1 = 380$ ns, much less than the $T_1 = 620$ ns obtained from tunneling measurement when the cavity is far detuned to $f_{cav} = 4.90$ GHz. Even though at this spot ($f_{01} = 7.18$ GHz) the qubit is $+10g$ from the cavity, the Purcell effect is still significantly effecting its decay rate because the cavity is so strongly coupled to the 50Ω feedline, leading to a very low quality factor. The data were also fitted for a cavity rise time, giving $T_{Cav} = 17$ ns. This is a bit higher than the rise time of 6.5 ns calculated from the quality factor of the cavity, though this rise time also includes the 12 ns rise time of the 18 ns Gaussian π -pulse. Since the qubit is decaying while the cavity is ringing up, the data peak does not represent the full phase swing of the dispersive shift. This phase swing may be obtained from the combined T_1 and T_{Cav} fit shown in Figure 8.6, which for this data was $\Delta\phi = \mp 5.3^\circ$. The predicted shift from the three level model for this place was $\Delta\phi = \mp 6.7^\circ$. This 21% difference is not negligible. It may be due to an imperfect preparation of the $|1\rangle$ state by the π -pulse, or it could be that the dispersive shift model we've used has other terms not included here, or maybe the average number of photons in the cavity was less than one.

8.4 State discrimination

The T_1 measurement shown in Figure 8.6 contains points from both the $|0\rangle$ state at the beginning of the time trace and the $|1\rangle$ state at the minimum phase of the time trace. The data points used to calculate the cavity phase can also be plotted on an IQ plot. Figure 8.7a shows the $|0\rangle$ and $|1\rangle$ states plotted for different numbers of averages, showing that the state discrimination improves with increasing averages. Also plotted is a cavity frequency scan for reference, as well as a grey dotted reference line. Figure 8.7b is the IQ data projected onto the reference line and histogrammed, with the x -axis the distance d of the data point projection from the midpoint between the ideal position of the states. For this amplifier chain and dispersive frequency shift, clear state discrimination occurs somewhere between 10^6 and 10^7 averages. Taking the standard deviation σ of these histograms and plotting with the number of averages n gives the plot in Figure 8.8.

As the qubit and cavity are tuned further from each other the dispersive shift on the cavity decreases, making distinguishing states more difficult. The cavity IQ and phase plots, sweeping frequency, for two different detunings are shown in Figure 8.9. The data were taken by

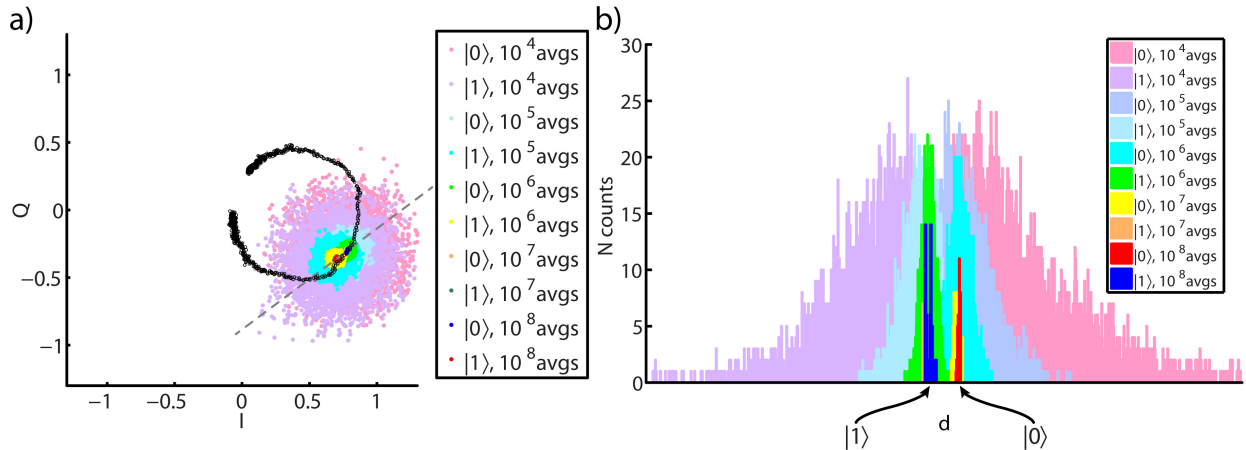


Figure 8.7: IQ noise and state discrimination - a) State discrimination in IQ space for different averaging times at $f_{01} = 7.31$ GHz ($+13g$). The full resonator curve is plotted on top of the data, as is a grey dotted line onto which the data points are projected and histogrammed in b). The axis d is the distance from the center of the line to the projection of a given data point on the line. The contrast is about 6° .

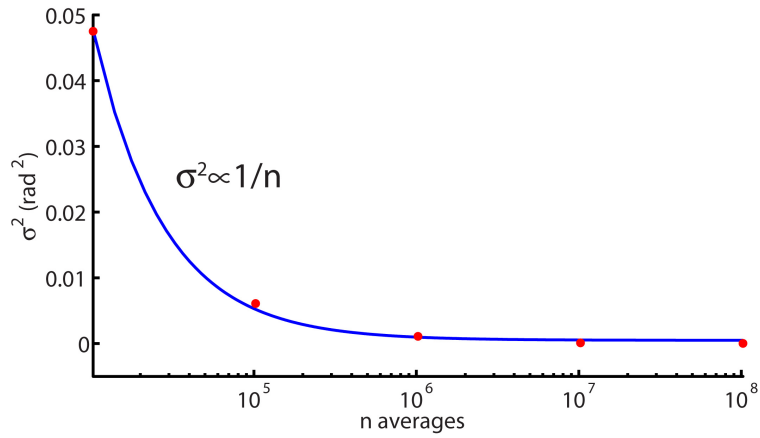


Figure 8.8: IQ noise standard deviation - The square of the standard deviation σ is inversely proportional to the number of averages n , which is expected for an unsaturated amplifier chain.

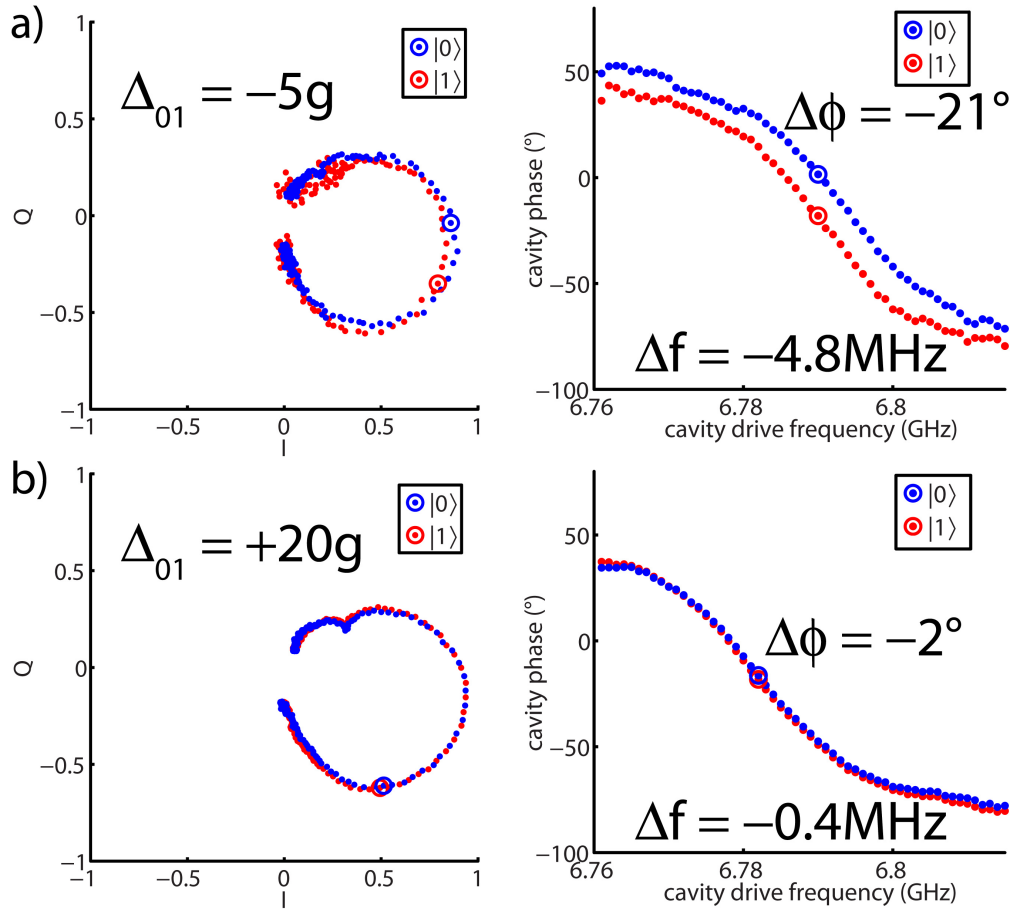


Figure 8.9: State discrimination and detuning - a) State discrimination for the detuning $\Delta_{01} = -5g$, with a dispersive shift of $\Delta f = -4.8$ MHz, $\Delta\phi = -21^\circ$. b) State discrimination data for the detuning $\Delta_{01} = +20g$, giving a dispersive shift of $\Delta f = -0.4$ MHz, $\Delta\phi = -2^\circ$. The large circles are the data points at one drive frequency where the phase slope is steep, from where the phase shift is reported.

putting the qubit in either the $|0\rangle$ or $|1\rangle$ state and sweeping the drive frequency to the tunable cavity. The large circle for each plot indicates the data point at a fixed drive frequency where the $|0\rangle$ state phase curve is steepest. This point is where the phase shift associated with each dispersive frequency shift is measured. The kink in the IQ plots corresponds to the spurious resonance in the tunable cavity spectroscopy at 6.75 GHz, identified in Figure 7.7. The rotation of the IQ circle comes from a phase offset between the measurement plane and ports, and the complex offset comes from crosstalk between feedlines and/or spurious resonance structures, as discussed in Section 3.2.6. These artifacts are still present after a through calibration procedure where the cavity is detuned from the frequency range to be calibrated, the calibration data are taken, then the cavity is returned to the desired frequency. Returning the cavity to the desired frequency for operation changes the impedance environment enough to introduce the complex offset and phase offset. Although it is possible to fit the resonance curves in IQ space and remove these offsets, it is usually unnecessary when measuring the dispersive shift in IQ space since it is a relative shift; offsets do not affect a quadrature measurement. However, if these offsets are large enough then phase or amplitude measurements may lose sensitivity.

Figure 8.9 shows the decrease in the ability to distinguish between the $|0\rangle$ and $|1\rangle$ states as detuning grows. It is also clear from the two phase plots that the slope of the phase change also affects distinguishability. Increasing the overall quality factor Q of the cavity will increase the distinguishability for a given detuning, since the phase shift from the dispersive shift is given by $\delta\phi = \pm \tan^{-1}(2Qg^2/\omega_{01}\Delta\phi_1)$. While this alone suggests that it is advantageous to make the quality factor very large, it is important to remember that the response time of the cavity also increases with Q , as $T_{Cav} = Q_{Cav}/\omega_{Cav}$. The optimal Q to choose will depend on the application, whether a large state discrimination difference or a short cavity rise time is most desirable.

8.5 Dispersive shift data

Dispersive shift data were taken at various points along the qubit spectroscopy with the cavity tuned to its maximum frequency $f_{Cav} = 6.78$ GHz. These data are plotted as red dots in Figure 8.10. Two and three level qubit models are plotted as red dotted and solid lines, respectively. The three level model clearly matches the data best. Also plotted are data where the qubit is held fixed at both $f_{Qu} = 6.28$ GHz and $f_{Qu} = 6.98$ GHz while the cavity is swept, represented as blue and green dots, respectively. The three level model for this swept cavity situation matches the data well. The fixed qubit models (blue and green) models do not lay on top of the fixed cavity model since the anharmonicity of the qubit changes when the cavity is held fixed, but does not change when the qubit is held fixed. The anharmonicity of the qubit enters the dispersive shift expression through the Δ_{12} term that results from using the three-level model.

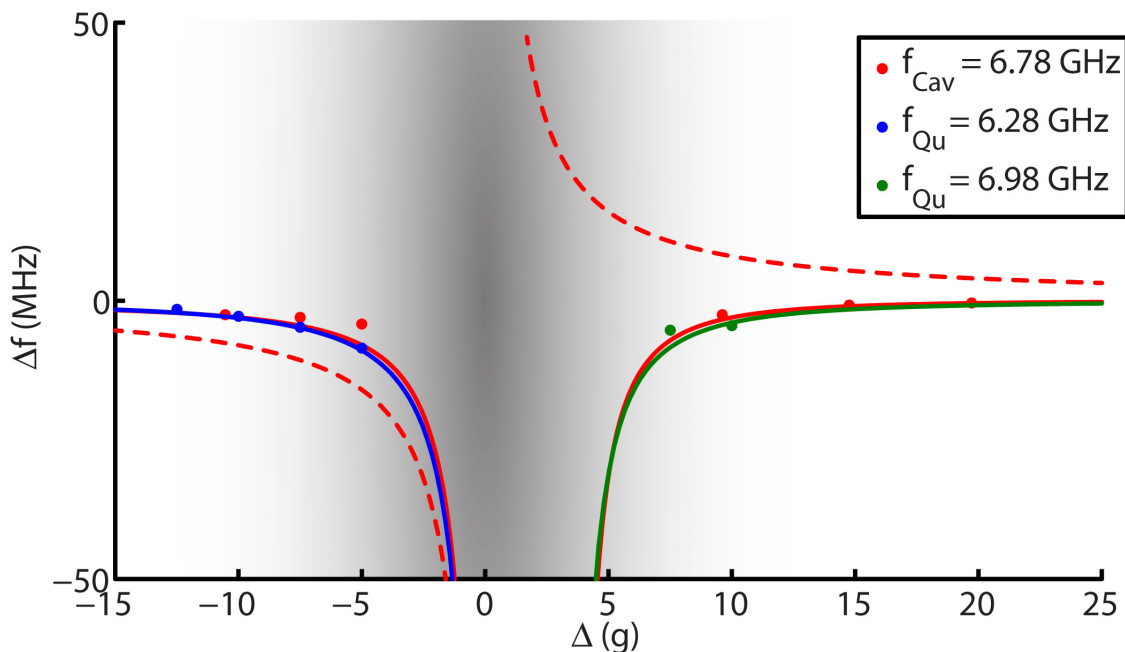


Figure 8.10: Dispersive shift in the tunable cavity - Dispersive shift for holding the cavity fixed at $f_{cav} = 6.78$ GHz and moving the qubit are plotted as red dots, along with the corresponding two and three level models as red dotted and red solid lines, respectively. Data for holding the qubit fixed at $f_{Qu} = 6.28$ GHz and moving the cavity are plotted as blue dots, with the corresponding three level model plotted as a blue line, as well as data for the qubit fixed at $f_{Qu} = 6.98$ GHz and its three level model in green.

9

Conclusions and future work

9.1 Summary of results

9.1.1 Demonstration of full qubit control

Full control over the qubit, meaning the ability to place the qubit in an arbitrary state and fully characterize that state, was shown in Chapter 7, where a metastable phase qubit with via-style Josephson junctions was measured using tunneling measurement and readout using a DC SQUID. The microwaves were generated by custom electronics that controlled pulse amplitude, phase, and duration, with sub-nanosecond resolution. The precession and decay of the initial state $(|0\rangle + i|1\rangle) / \sqrt{2}$ as it was rotated with a z -pulse of varying duration was also measured and mapped onto the Bloch sphere as a demonstration of tomographic measurement. While this demonstration of control over the entire Bloch sphere was not a first in the community, it was an important demonstration of capability for our group.

9.1.2 Tunneling readout with a tunable cavity

The DC SQUID was replaced with a fast tunable cavity on a new metastable phase qubit design with only two fabrication layers. Made from shadow evaporated Josephson junctions, this device

had a greatly improved energy relaxation time. The device was also measured using tunneling during a fast flux pulse, but readout was accomplished with a tunable cavity biased to be flux sensitive. Because of the device's long energy relaxation time, an anti-retrapping measure pulse was used to improve the contrast compared to a simple square measure pulse. Since the readout operation occurs after qubit manipulation and measurement, the tunable cavity was free to be used during qubit manipulation. Energy relaxation data were taken with the cavity at its maximum and minimum frequencies, across 2 GHz of qubit spectroscopy, to see the Purcell effect loss at two different cavity frequencies. This is the first time the loss via the Purcell effect has been controlled by detuning the cavity. This dynamic manipulation of the Purcell effect is a key result of this work, not yet shown in other devices. It is important because the main drawback of previous cQED systems has been fixed loss through the cavity over a useful qubit bandwidth; a tunable cavity allows this region to be used, while still using the cavity to measure.

9.1.3 Tunneling measurement photons in the cavity

The tunable cavity was also used to directly see photons populating the cavity as the metastable phase qubit rang down after a short tunneling measurement. The photons were fed to the cavity as the chirped pulse from the qubit ring down crossed resonance with the cavity, over approximately 200 ns. This was evident because the decay constant of the cavity after the measure pulse was measured as 220 ns, whereas the intrinsic decay time of the cavity was measured as 6.5 ns. Although others have seen evidence for tunneling photons entering the cavity, this is the first time they have been observed directly in the cavity. This clearly shows that tunneling measurement is not a viable measurement scheme for many qubit quantum processors.

9.1.4 Multiplexing tunable cavities

Four tunable cavities were multiplexed and tuned using one common microwave line and one common flux bias line. They were not connected to qubits, and were made using the much less reliable via-style Josephson junctions. Although qubit measurements were not made in a multiplexed way, the device demonstrated that the tunable cavities could be clearly distinguished in frequency space, and required much less wiring. Using only one microwave feedline and only one expensive amplifier chain can minimize noise thermal photons in the system and lower cost.

9.1.5 Dispersive measurement with a tunable cavity

The tunable cavity was also used to perform dispersive measurement of a metastable phase qubit. Spectroscopy, Rabi oscillations, and T_1 measurements were done dispersively. The dispersive shift was measured across the qubit spectroscopy range for one fixed cavity frequency, then twice more by moving the cavity and holding the qubit at two other fixed frequencies. The data show a dispersive shift inconsistent with a two level system, but consistent with a three level system. The metastable phase qubit's weak anharmonicity is responsible for needing the three level model. This is the first dispersive measurement of a metastable phase qubit, and could pave the way for more complex metastable phase qubit processors in the future.

9.2 Future work

9.2.1 Device design/measurement setup improvements

The next generation of devices clearly needs the flux bias line to the qubit to be properly coupled. Since the flux bias line to the tunable cavity was properly coupled, the next qubit bias line should use the same design. This should increase qubit dephasing and energy relaxation times. Along with fixing the bias coil, it may also be advantageous to have all the ground planes tied

together with microfabricated crossovers instead of wirebond crossovers. This would make the devices more consistent, as well as being designed to remove all spurious modes from ground plane potential differences. Although in the device presented in this work most of these modes were suppressed using the wirebonds, a 10 MHz splitting near the top of the tunable cavity spectroscopy at 6.75 GHz was still present. This suggests that the wirebond method can be insufficient to suppress all structural spurious modes, and a more reproducible method should be developed. The drawback to such a method is that it introduces a dielectric layer to the fabrication that both increases fabrication complexity and introduces a new materials system that could make the qubit more lossy, even if all of it is later removed. A simple test for this system would be to use the device design that is already well characterized in this work and deposit and completely remove the wiring insulator before depositing the Josephson junction, then characterize the energy loss. If no difference is seen, the dielectric may be suitable for use in wiring crossovers.

To further increase the qubit energy relaxation time, as well as the tunable cavity internal quality factor, the finger spacing in their interdigitated capacitors could be increased. This decreasing of the electric field spacial density between capacitor plates has been shown in other quantum devices to increase the energy relaxation time[26][76], and should work for these devices as well. Increasing the tunable cavity's external quality factor by decreasing the value of its coupling capacitor should also improve device performance by narrowing the Purcell effect's influence in the frequency domain, as well as increasing the cavity's phase sensitivity to the dispersive shift. This should increase the signal to noise ratio of the measurement for a given detuning.

The measurement setup could also be improved by increasing the attenuation on cold fridge microwave and fast flux lines. Only 16 dB of attenuation may be added cold, since any more attenuation would make the flux bias range too limited to be useful. An improved setup is shown in Table 9.1, which would give a thermal photon number at the mixing chamber of ~ 0.01 . Assuming the mixing chamber can handle up to $1 \mu\text{W} = -30 \text{ dBm}$ of power before warming, and knowing that

Stage	Atten.
4 K	10 dB
Still	10 dB
HXC	0 dB
MXC	20 dB

Table 9.1: Cold attenuators - This heavier attenuation setup would drop the thermal photon number down to ~ 0.01 at the mixing chamber.

the tunable cavity becomes nonlinear at -80 or -90 dBm, it is clear that this attenuation setup on the microwave line will not heat the refrigerator noticeably. More importantly, the attenuators will not be adding many thermal photons due to local heating of the attenuators by the drive. The fast flux line has the potential to put a lot of heat into the fridge through the attenuators as relatively large currents can be on for several microseconds. The voltage limit on the Tektronix AWG5014B is ± 2.25 V into 50Ω , or $+20$ dBm. The 40 dB of attenuation shown in Table 9.1 would put -20 dBm at the mixing chamber if the AWB5014B were oscillating between its voltage limits. While this would most certainly heat the mixing chamber noticeably, it is a worst case scenario that does not occur in practice.

As described in Section 6.2.2, the Tektronix AWG5014B does not generate very sharp or flat step edges. In this work the pulse edge problems were mostly avoided by waiting a few microseconds after the pulse step edge and making a linear ramp to roughly correct for the slow drift, though the problems were still present in the very short measure pulse rising edge. A better solution is to correct for the nonidealities in the instrument by adding the normalized difference between the real pulse and the ideal pulse to be generated.

A final setup improvement is to add a bias tee and a fast flux line to the tunable cavity flux line, and use a DC current source (Yokogawa 7651) for the cavity's slow flux line. This allows the cavity to be quickly moved, just like the qubit, for photon transfer experiments. These flux lines would be a copy of the flux setup for the qubit.

9.2.2 Bifurcation measurement

Measurement and readout of a quantum system is essentially the encoding of the quantum state onto a classical state. For the device used in this work the classical state is either a flux state in the case of the tunneling measurement scheme, or the frequency of a classical resonator in the case of dispersive measurement. Bifurcation measurement involves encoding the quantum state onto the amplitude state of a nonlinear resonator. This is useful because the encoding may be very fast, a few nanoseconds, then the amplitude of the resonator may be decreased so that the latched state may be read out. This is a fast single-shot measurement and readout, something not achievable with traditional dispersive measurement without a near quantum limited amplifier. Bifurcation measurement with a nonlinear cavity has been used on Cooper-pair box qubits[86], flux qubits[87], and stable phase qubits[88]. Bifurcation measurement has also been employed with stable phase qubits using linear cavities by exploiting the natural nonlinearity of the cavity dressed states[89].

A natural next step with the device design presented in this work is to perform bifurcation measurement on the metastable phase qubit using the tunable cavity, thus demonstrating a third measurement protocol using the same device. It would be interesting to compare the contrast achieved with this measurement to the contrast achieved in the tunneling measurement, another single-shot measurement.

9.2.3 Tunable cavity states and anharmonicity

The tunable cavity is an interesting device because it is essentially an anharmonic metastable phase qubit, or a slightly anharmonic harmonic oscillator, all while having a single valued potential well. It becomes fairly anharmonic at its lowest frequency, but since it is never double valued the cavity is stable here. Figure 9.1 is a plot of the relative anharmonicity α_r overlaid on the spectroscopy across one flux quantum. This demonstrates that the tunable cavity may be used as both a harmonic oscillator (where $\alpha_r = 0$) and a qubit with positive or negative relative anharmonicity,

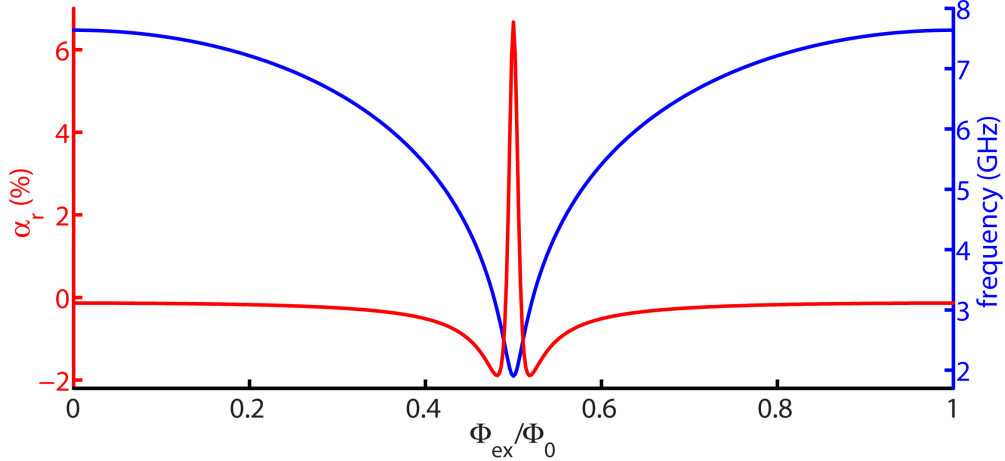


Figure 9.1: Tunable cavity anharmonicity - The tunable cavity relative anharmonicity α_r is plotted over its spectroscopy, across one flux quantum. The cavity becomes somewhat anharmonic at its lowest frequency. This plot was made by solving the Schrödinger equation for a device with $\beta_L = 0.9$ and a large capacitor. The series inductance L_s was not included as the Hamiltonian becomes nontrivial.

as long as its lifetime is sufficiently long in both regimes. Both the internal and external quality factors of the cavity would need to be much higher than the device presented here. One could also load a state into the cavity from the qubit and then probe the state directly using the microwave line. Since these interesting regions are near the low frequency side of the spectroscopy where the slope is steep, it would be crucial to minimize flux noise to the cavity. Likewise, one could also use the qubit as a cavity by operating the qubit in its deep, nearly harmonic potential and directly monitoring it with a microwave feedline.

9.2.4 Multiplexing and cavity damping

Finally, a system of multiplexed metastable phase qubit/tunable cavity pairs could be built, to make a simple quantum processor using only one microwave control line and amplifier chain, though each qubit and each cavity would need its own flux control line. The advantages of multiplexing include saving on precious dilution fridge wiring lines, as well as needing only one expensive amplification and detection chain. Multiplexing is likely to be useful when scaling up to large, complex quantum processors.

The tunable cavity may also be used to damp the qubit, initializing it to the ground state. As

qubit lifetimes increase, the low quality factor tunable cavity could be used when waiting for the natural decay of the qubit to initialize the state is impractical. One could imagine measuring the qubit state using the cavity, as has been done here, then tuning the cavity to be on resonance with the qubit so that the qubit decays to the ground state.

9.3 Final thoughts

By exploiting the tunable nature of superconducting Josephson junction devices, great flexibility may be gained. The ephemeral nature of quantum systems seems to require a multidimensional flexibility that the much more stable, albeit far advanced, semiconductor systems do not. This ephemerality and flexibility hopefully will lead to quantum computers that do powerful things, far beyond today's imaginations can dream. During my 7 1/2 years in this field I have seen advance after advance that has surprised me, and the pace seems to be increasing. I hope I continue to be surprised.

10

Appendix A

10.1 Qubit with DC SQUID process sheet

The device used to demonstrate full tomographic control, made with via-style Josephson junctions (Section 5.2.1.1) and reported on in Section 7.1, was die 1007 from the wafer fabricated by Katarina Cicak and labeled `wfr080330.2xqb16-IDcap-CPW8GHz.kc`. The process sheet for this wafer is reproduced below.

4

ps080330.IM_qubit_EtchAwaySiNx.kc.doc
Date: 3/30/08 kc

wfr080330.2xQB16-IDcap-CPW8GHz.kc

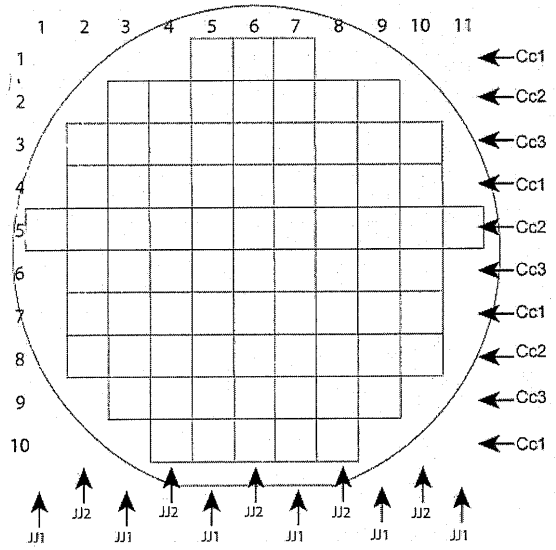
Project name: qb070319.2xqb16HFCoupRes.rws

PROCESS SHEET SUMMARY

Si OR Sapphire wafer (circle one)

Stepper job file: jb080227.IMqubitSiNx.kc

Image → Layer ↓ V	All	JJ1	JJ2	Cc1	Cc2	Cc3
✓ b	ALIGN, 2XHFID-B	2XID8G-CE	2XID8G-CE			
✓ be	2XHFID-BE					
✓ ji		2XHFID-JI	2XID8G-JI			
✓ jc	2XQB16-JC					
✓ wi	2XHFID-WI					
✓ wc	2XID8G-WC 3/24/08 kc					
✓ ie	2XID8G-IE 3/24/08 kc					
rs				2XHFID-RS	2XID8G-SC	2XID8G-SI
se	2XID8G-SE 3/24/08 kc					



JJ1 = Qubit JJ is 6.63 μm^2
 JJ2 = Qubit JJ is 4x1.66 μm^2
 Cc1 = small + small Cc
 Cc2 = small + big Cc
 Cc3 = big + big Cc

Thickness of:	Wafer center:	Wafer edge:
Base layer (Al):	<u>106</u>	<u>94 nm</u>
Insulator (SiNx):	<u>319</u>	<u>307</u>
Top wiring (Al):	<u>97</u>	<u>88</u>

Oxidation parameters:
38.4 torr, 10:00 min:sec, 79.28 ± 61.2%
 Top JJ1 (6.63 μm^2): Rn = ~~158~~ (158) ohm ± ~~21.8~~%
 Top JJ2 (4x1.66 μm^2): Rn = 55.84 (158) ohm ± 62.4%
 Bottom JJ (35.36 μm^2): Rn = 23.12 (30) ohm ± 48.1%
 Jo = 36.51 (28.52) A/cm²

Date: 3/30/08 **DEPOSIT and PATTERN B (Base) and BE (gnd plane holes) LAYERS**

- ✓ Inspect wafer surface under microscope: _____
- ✓ If using Si-wafer record stress before deposition: _____
- Load wafer into Nb system and pump load lock for (5 min) p = 3x10⁻⁷ torr LL

○ Ion mill wafer to clean Nb surface of any oxide in Nb system for ✓ (30 sec)
 Base pressure = _____ torr, Gate valve pressure = 4.6 x 10⁻⁸ torr.

Set:	Other parameters should be near (record):
Ar pressure 1.4 x 10 ⁻⁴ torr ✓	Cathode filament I = <u>2.93</u> (3.37) A
Probe I = 0.15 mA/cm ² ✓	Discharge I = <u>0.50</u> (0.51) A
Beam V = 300 V ✓	Beam I = <u>37</u> (35) mA
Accelerator V = 950 V ✓	Accelerator I = <u>3</u> (2) mA
Emission I = 50 mA (~1.5 x Beam I) <u>57</u>	Discharge V = <u>✓</u> (55.0) V
<u>punch c</u>	Filament I = <u>2.54</u> (3.25) A

○ Sputter Al on the wafer

- Dummy, ~67 nm, ✓ (2:00) min, ✓ (5.0) mTorr Ar, ✓ (200) W, 543V, 0.36 A
- WFR, ~100 nm, ✓ (3:15) min, ✓ (5.0) mTorr Ar, ✓ (200) W, 545 V, 0.36 A

3/31/08
1 kt

- Inspect under microscope: looks good
- If using Si-wafer record stress after deposition: _____
 Calculated stress: _____ MPa () compressive, () tensile

○ Pattern B layer resist

- Clean spinner nozzle with acetone and IPA, and purge it 10 times
- Spin HMDS at 3500 rpm (setting 381) for 35 sec
- Bake on hotplate 95 C for 60 sec with vacuum on
- Spin resist SPR 660L, 3200 rpm → ~1micron, (setting 323), 40 sec
- Bake on hotplate 95 C for 60 sec with vacuum on

Expose on stepper:

- Mask **ALIGN, 2XHFID-B, 2XID8G-CE**
- Job file: **jb080227.IMqubitSiNx.kc**
- Layer ID: **b**
- Exposure dose: **230 mJ/cm²**

- Post-bake on hot plate 110 C for 60 sec with vacuum on
- Spin-develop in MF-701 for 60 sec (make sure settings are as they are labeled on the machine)
- Inspect under microscope: looks good (here and there dust dots)

○ Wet Etch Aluminum:

- Heat Al etchant type A to 48-49 C (set hot plate to ~65-70 C settings). New thermometer
- Use tripod and dip in etchant until 2 sec after it clears (15 sec) 16 sec

- Inspect under microscope: looks good (0.1 μm overetched)

- Ultrasound "dirty" acetone (½ min), Ultrasound "clean" acetone (½ min), spray HEAVELY with ACETONE then IPA while spinning dry. power 60

- Inspect under microscope: looks good

- Measure Al thickness (base qubit layer) using profilometer (100 nm) Edge: 94 Center: 106

○ Pattern BE layer resist

- Clean spinner nozzle with acetone and IPA, and purge it 10 times
- Spin HMDS at 3500 rpm (setting 381) for 35 sec
- Bake on hotplate 95 C for 60 sec with vacuum on

- Spin resist SPR 660L, 3200 rpm → ~ 1micron, (setting 323), 40 sec
- Bake on hotplate 95 C for 60 sec with vacuum on
- Expose on stepper:
 - Mask **2XHFID-BE**
 - Job file: **jb080227.IMqubitSiNx.kc**
 - Layer ID: **be**
 - Exposure dose: **230 mJ/cm²**
- Post-bake on hot plate 110 C for 60 sec with vacuum on
- Spin-develop in MF-701 for 60 sec (make sure settings are as they are labeled on the machine)
- Inspect under microscope: looks good
- Wet Etch Aluminum:
 - Heat Al etchant type A to 48-49 C (set hot plate to ~65-70 C settings).
 - Use tripod and dip in etchant until 2 sec after it clears (¹⁵sec) 20
 - Inspect under microscope: looks good ²⁰ (0.1 μm overetched)
 - Ultrasound "dirty" acetone (2 min), Ultrasound "clean" acetone (2 min), spray HEAVELY with ACETONE then IPA while spinning dry.
 - Inspect under microscope: looks good

DEPOSIT INSULATOR LAYER

- 1) Glue sapphire wafer onto "spider" wafer (skip this step if using Si wafer):
 - a) Mount Teflon chuck and carefully place the sapphire wafer face (polished-side) down on the chuck (to spin resist on back of it).
 - b) **Alternative** if Teflon chuck is not available: Stick adhesive backing-tape used for dicing wafers onto a chuck. Make sure the tape covers the chuck completely. Then with sharp tweezers puncture a small hole through the middle of tape to allow for vacuum grip. Mount the chuck and carefully place the sapphire wafer face (polished-side) down on the chuck.
 - c) Spin "glue" resist SPR 220-3, 2500 rpm, 35 sec (dispense manually). There should be no resist on the face of the sapphire wafer after spin.
 - d) Place the sapphire wafer, resist side down, onto a "spider" wafer with flats aligned, and push the edges together until the two are "glued" together
 - e) Bake on hotplate 95 C for 10 min with vacuum on (sapphire face up)
 - f) Inspect sapphire wafer under microscope for surface cleanliness: _____
 - g) Spin-clean the wafer with acetone and IPA to clean resist from the edges of the wafer.

2) Deposit Insulator using PlasmaQuest ECR:

- a) Run process BIGCLEAN with the cleaning wafer in the machine.
 b) Load wafer and run your process SiNx RFcln (edit deposition time to deposit SiNx for 170 sec)

Record the actual parameter values: RF Clean		Record the actual parameter values: SiNx Deposition	
O2 flow:	✓ (0) sccm	Ar flow:	101.4 (100.2) sccm
Ar flow:	140.8 (139.0) sccm	N2 flow:	15.1 (15.0) sccm
SiH4 flow:	- (0) sccm	SiH4 flow:	133.7 (132) sccm
Upper magnet I:	179.8 (185) A	Upper magnet I:	178.7 (185) A
Pressure:	(5) mTorr	Pressure:	8.8 (5) mTorr
RF power F:	48.8 (50) W	RF power F:	- (0) W
R:	-4.8 (0) W	R:	- (0) W
Dc bias:	210.5 (-200) V	Dc bias:	- (0) V
Microwave power F:	- (0) W	Microwave power F:	1195.9 (1200) W
R:	- (0) W	R:	0.5 (0) W
Backside He press:	4.9 → 4.8 (>4.5) torr	Backside He press:	4.8 (>4.5) torr
Backside He flow:	1.27 → 1.17 (<1.0) sccm	Backside He flow:	1.23 → 1.09 → 0.98 (<1.0) sccm
Clean time:	✓ (60) sec	Deposition time:	170 s ✓ (170) sec
		(dep. rate 100 nm/min)	
		Does SiNx look uniform? If not, draw it →	

had some gripping problems. After some time with plasma on the backside He flow dropped to 0.98. Good.

- 3) Ultrasound "dirty" acetone (1 min), separate wafers (skip this step if using Si wafer).
 4) Ultrasound "dirty" acetone (1 min), Ultrasound "clean" acetone (1 min), spray HEAVELY with ACETONE then IPA while spinning dry.
 5) Inspect under microscope: looks good Few dies around center of wafer have weird SiNx

GOOD STOPPING POINT: mean: cool edges: like SiNx is not sticking well.

4/1/08 KC

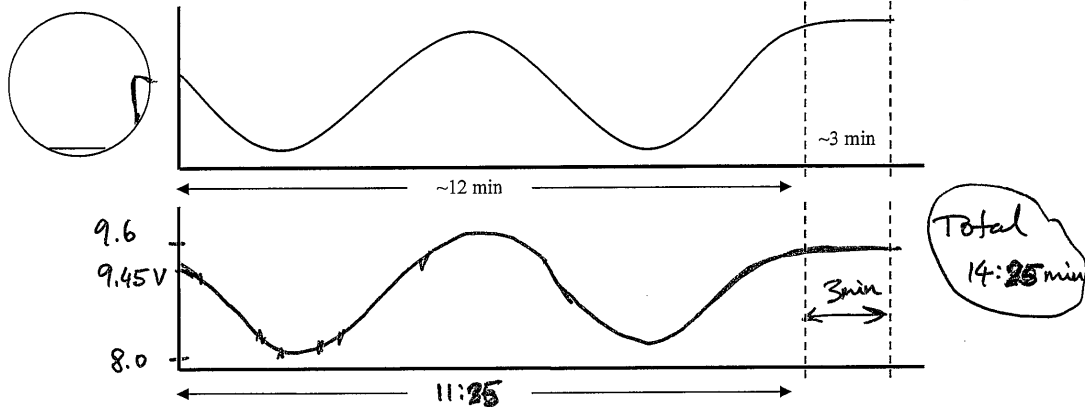
PATTERN JUNCTION INSULATOR (VIA) (JI-LAYER)

- i) Pattern JI-layer resist:
 a) Clean spinner nozzle with acetone and IPA and purge it 10 times.
 b) Spin HMDS and Resist SPR 660L
 i) Thin layer HMDS: 3500 rpm (setting 332?) ✓ → 40 sec
 ii) Bake on hotplate 95 C for 60 sec with vacuum on
 iii) 1.23 micron Resist: 2200 rpm (setting 227) → 40 sec
 iv) Bake on hotplate 95 C for 60 sec with vacuum on.
 c) Expose on stepper:
 i) Masks: 2XHFID-JI and 2XID8G-JI
 ii) Job File: (jb080227.IMqubitSiNx.ke) ✓
 iii) Layer ID: ji
 iv) Expose at 275 mJ/cm²:
 d) Post-bake on hot plate 110 C for 60 sec with vacuum on.
 e) Spin-develop in MF-701 for 60 sec.

See photos taken on 4/8/08

- 2) Inspect under microscope: looks good
 3) Etch through Insulator using AXIC. Use proper recipe (JASnitride.prc) ✓
 a) Use acetone to make clean spot for laser beam thickness monitor. Align beam (8-12 V) 10.68
 b) Condition chamber by running JASnitride.prc for 25 (15-20 min)
 c) Pump to base pressure p = 6x10⁻⁵ torr ✓
 d) Start etch and watch graph for wavy curve (see c)).
 (60 sccm O2) ✓ (50 W(f)) 49
 (42 sccm CF4) ✓ (0 W(r)) 1
 (65 mtorr) 63 (-130 V) -140

Sketch etch curve below and where the laser monitor was relative to the flat on the wfr:



Comments:

- ④ Inspect under microscope: looks good
- ⑤ Strip resist:
 - a) Clean Asher without wafer: 50 sccm O₂ 50 W (subtract any offset) 3:00 min
 - b) Use Asher with wafer: 50 sccm O₂ 50 W (subtract any offset) 3:00 min
 - c) Ultrasound "dirty" acetone (2 min), Ultrasound "clean" acetone (2 min), spray HEAVELY with ACETONE then IPA while spinning dry. Power 70
- ⑥ Inspect under microscope: looks good
- ⑦ Measure etched thickness using profilometer: Center: 319 (270 nm) Edge: 307 (320 nm)

OXIDIZE AND DEPOSIT JUNCTION TOP CONDUCTOR (JC) LAYER

- ① Load wafer into Nb system and pump load lock for (5 min) LL p = 3 x 10⁻⁷ torr
- ② Prepare O₂ line: load wfr in main chamber & pump 1:05 pm - 4 pm.
 - a) close valve on O₂ cylindrical in chase and pump out the line for 5 min. LL p = 1.55 x 10⁻⁴ torr
 - b) Prepare load-lock by setting O₂ flow to 8x10⁻⁴ Torr of O₂ (or until Baratron gauge just starts registering 0.000-0.001 torr) and flush O₂ line for (5) min.
- ③ Ion mill vias to clean surface in Nb system for (60 sec) as follows:
 - a) Base pressure (torr) Gate valve pressure (torr) 4.4 x 10⁻⁸

Set:	Other parameters should be near (record):
Ar pressure 1.4 x 10 ⁻⁴ torr <input checked="" type="checkbox"/>	Cathode filament I = <u>2.58</u> (2.98) A
Probe I = 0.10 mA/cm ² <input checked="" type="checkbox"/>	Discharge I = <u>0.18</u> (0.19) A
Beam V = 800 V <input checked="" type="checkbox"/>	Beam I = <input checked="" type="checkbox"/> (20) mA
Accelerator V = 950 V <input checked="" type="checkbox"/>	Accelerator I = <input checked="" type="checkbox"/> (2) mA
Emission I = 33 mA (~1.5 x Beam I) <u>31</u>	Discharge V = <input checked="" type="checkbox"/> (55.0) V
<u>puck c</u>	Filament I = <u>2.39</u> (3.13) A

- ④ Oxidize junctions in Nb system:
 - a) Record RGA data (Filename)
 - b) Let wafer cool in 5 mTorr of Ar gas for (5 min) 10 min
 - c) Pump out load lock (torr) and transfer wafer into it.
 - d) Oxidize for (2 min) 2 at (8 x 10⁻⁴ torr) 7.3 x 10⁻⁴, baratron = 0.002 torr
 - e) Fill O₂ for 25 (10 sec), and oxidize for 10 (10min), at 38.4 (6 torr).
- ⑤ Sputter Al on the wafer:
 - a) 67 nm Dummy (2:00 min) (5.0 mtorr Ar) (200 W) 519 (V) 0.88 (A)
 - b) 100 nm Wafer (3:15 min) (5.0 mtorr Ar) (200 W) 527 (V) 0.38 (A)
- ⑥ Inspect film under microscope: looks good

$$p_2 t_2 = p_1 t_1 \left(\frac{R_1 A_1}{R_2 A_2} \right)^{\frac{1}{b}} \quad b = -0.516449$$

$$\left. \begin{aligned} R_1 &= 172.86 \, \Omega \\ p_1 &= 49.4 \, \text{torr} \\ t_1 &= 10 \, \text{min} \end{aligned} \right\} \text{previous wafer data}$$

$$t_2 = 10 \, \text{min}$$

$$A_1 = A_2 = 6.63 \, \mu\text{m}^2$$

$$R_2 = 158 \, \Omega$$

$$p_2 = ?$$

$$p_2 = \frac{p_1 t_1}{t_2} \left(\frac{R_1 A_1}{R_2 A_1} \right)^{\frac{1}{b}}$$

$$p_2 = (49.4 \, \text{torr}) \left(\frac{172.86}{158} \right)^{-\frac{1}{0.516449}}$$

$$p_2 = 41.51 \, \text{torr}$$

or from equation

$$J_0 = C E^b$$

$$E = p \cdot t$$

$$\text{want } J_0 = 28.52 \frac{\text{A}}{\text{cm}^2}$$

$$t = 10 \, \text{min}$$

$$p = ?$$

$$J_0 = C (p \cdot t)^b$$

$$\left(\frac{J_0}{t} \right)^{\frac{1}{b}} = p \cdot t$$

$$p = \frac{1}{t} \left(\frac{J_0}{C} \right)^{\frac{1}{b}}$$

$$b = -0.516449$$

$$\log C = 2.715933$$

$$C = 10^{2.715933}$$

$$C = 519.91578$$

$$p = \frac{1}{10 \, \text{min}} \left(\frac{28.52 \frac{\text{A}}{\text{cm}^2}}{519.91578} \right)^{-\frac{1}{0.516449}}$$

$$p = 27.62 \, \text{torr}$$

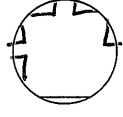
← from fit parameters

$$J_0 \text{ in } \frac{\text{A}}{\text{cm}^2}$$

$$E = p \cdot t$$

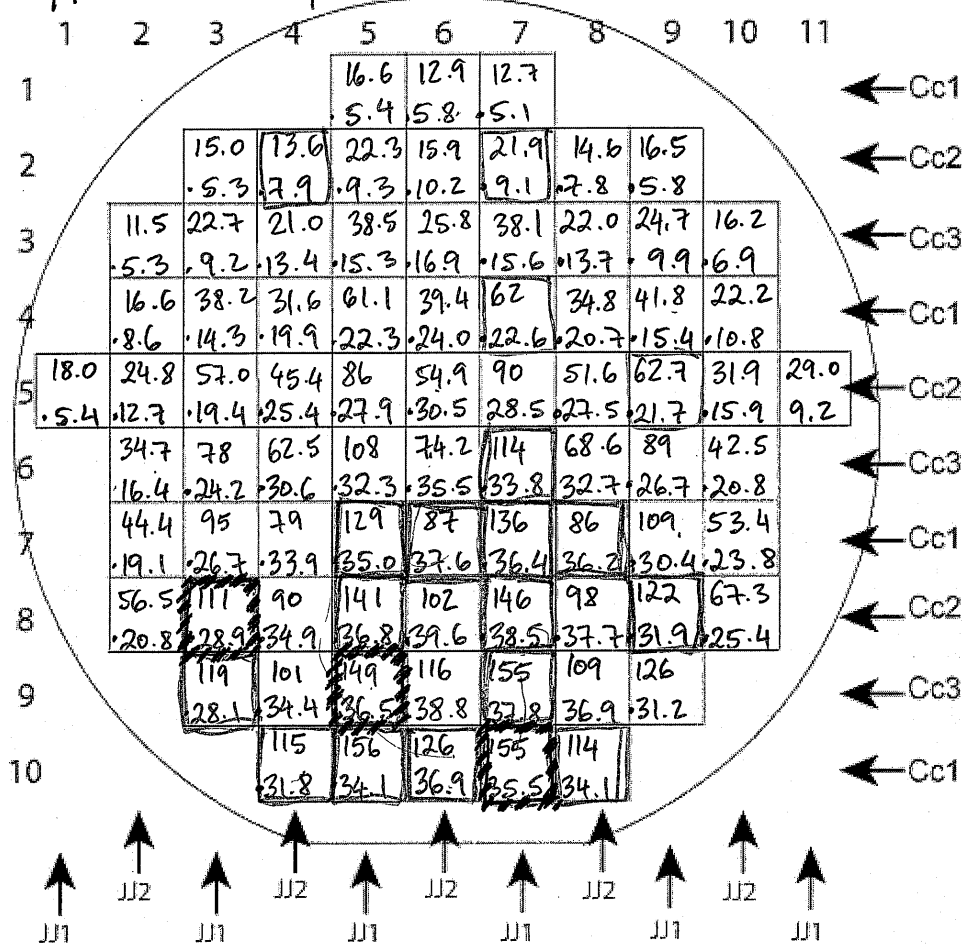
↑ in [min]

PATTERN JUNCTION CONDUCTOR (JC-LAYER)

- 1) Pattern jc-layer resist:
- a) Clean spinner nozzle with acetone and IPA and purge it 10 times.
 - b) Spin HMDS at 3500 rpm (setting 381) for 35 sec
 - c) Bake on hotplate 95 C for 60 sec with vacuum on
 - d) Spin 1 micron resist SPR 660L: 3200 rpm (setting 323) ✓ → 40 sec
 - e) Bake on hotplate 95 C for 60 sec with vacuum on.
 - f) Expose on stepper:
 - ii) Masks: 2XQB16-JC
 - iii) Job File: (jb080227.IMqubitSiNx.kc) ✓
 - Layer ID: jc
 - g) Expose at 230 mJ/cm²: ✓
 - h) Post-bake on hot plate 110 C for 60 sec with vacuum on.
 - i) Spin-develop in MF-701 for 60 sec.
- 2) Inspect under microscope: looks good
- 3) !! Use acetone to clean resist from several spots for future laser beam thickness monitor for future insulator etches !! Sketch where relative to the wafer flat.
- 4) Wet Etch Aluminum: 
- a) Heat Al etchant type A to 48-49 C (set hot plate to ~65-70 C settings).
 - b) Use tripod and dip in etchant until 2 sec after it clears (15 sec) 16
- 5) Inspect under microscope: looks good (0.1 μm overetched)
- 6) Ultrasound "dirty" acetone (1 min), Ultrasound "clean" acetone (1 min), spray HEAVELY with ACETONE then IPA while spinning dry. Power 50
- 7) Inspect under microscope: looks good
- 8) Measure etched thickness using profilometer Center: 97 (100 nm), Edge: 88 (nm)



CHECK TEST JUNCTIONS

1) Use probe station to determine junction resistances. Diode box used: YES NO $B_{grnd} = 0. D/3$
 Date: 4/11/08 KC Time: 6 pm in cleanroom R



Oxidation parameters: 38.4 torr, 10:00 min:sec,
 Top JJ1 (6.63um²): $R_n = \frac{79.28}{(158)} \pm \frac{48.52}{(158)}$ ohm (61.2%)
 Top JJ2 (4x1.66um²): $R_n = \frac{55.84}{(158)} \pm \frac{34.85}{(158)}$ ohm (62.4%)
 Bottom JJ (35.36um²): $R_n = \frac{23.12}{(30)} \pm \frac{11.13}{(30)}$ ohm (48.1%)
 $J_o = (2.9845e4 V)/(A * R_n_bottom) = (2.9845e4 V)/(35.36 \text{ um}^2 * 23.12 \text{ Ohms})$
 $J_o = \frac{36.51}{(28.52)} \text{ A/cm}^2$

34.7% lower R_n for split JJ's

 = in gel box
 = cooled down 4/13/08 KC

Date: 4/4/08 KC **PATTERN WIRING INSULATOR (WI-LAYER)**

1) **Pattern WI layer resist:**

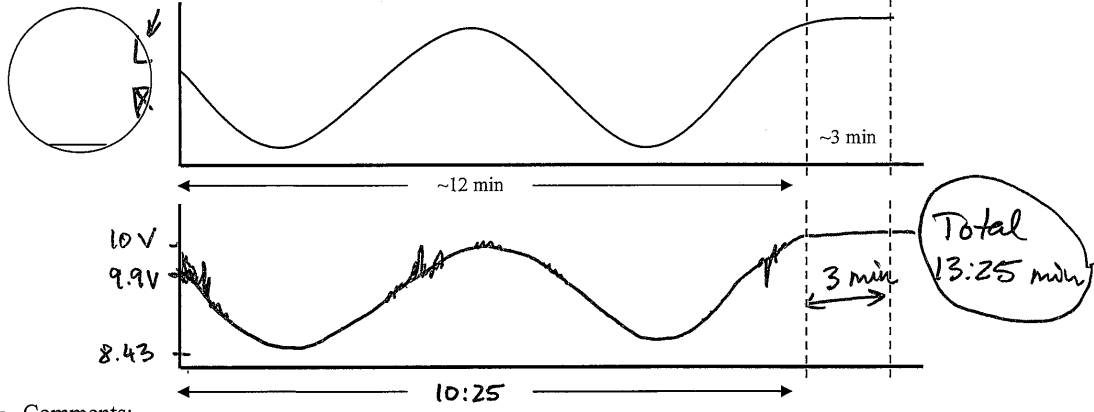
- a) Clean spinner nozzle with acetone and IPA and purge it 10 times.
- b) Spin HMDS and Resist SPR 660L
 - i) Thin layer HMDS: 3500 rpm (setting 332?) _____ → 40 sec
 - ii) Bake on hotplate 95 C for 60 sec with vacuum on
 - iii) 1.23 micron Resist: 2200 rpm (setting 227) ✓ → 40 sec
 - iv) Bake on hotplate 95 C for 60 sec with vacuum on.
- c) Expose on stepper:
 - i) Masks: **2XHFID-WI**
 - ii) Job File: **(jb080227.IMqubitSiNx.kc)** ✓
 - iii) Layer ID: **wi**
 - iv) Expose at **275 mJ/cm²**: _____
- d) Post-bake on hot plate 110 C for 60 sec with vacuum on.
- e) Spin-develop in MF-701 for 60 sec.

2) **Inspect under microscope:** looks good

- 3) **Etch through Insulator using AXIC.** Use proper recipe (**JASnitride.prc**) ✓
- a) Use acetone to make clean spot for laser beam thickness monitor. Align beam (8-12 V) 11.0V
 - b) Condition chamber by running **JASnitride.prc** for 9:20 (15-20 min)
 - c) Pump to base pressure $p = 6 \times 10^{-5}$ torr 7×10^{-5}
 - d) Start etch and watch graph for wavy curve (see c).

(60 sccm O ₂)	✓	(50 W(f))	<u>49</u>
(42 sccm CF ₄)	✓	(0 W(r))	<u>4</u>
(65 mtorr)	<u>64</u>	(-130 V)	<u>-120V</u>

Sketch etch curve below and where the laser monitor was relative to the flat on the wfr:



Comments:

- 4/7/08 KC 4) **Inspect under microscope:** looks good
- 5) **Strip resist:**
 - a) Clean Asher without wafer: 50 sccm O₂ 50 W (subtract any offset) 3:00 min
 - b) Use Asher with wafer: 50 sccm O₂ 50 W (subtract any offset) 3:00 min
 - c) Ultrasound "dirty" acetone (2 min), Ultrasound "clean" acetone (2 min), spray HEAVELY with ACETONE then IPA while spinning dry. power 40
- 6) **Inspect under microscope:** looks good
- 7) **Measure etched thickness using profilometer:** Center: _____ (270 nm) Edge: _____ (320 nm)

DEPOSIT WIRING CONDUCTOR (WC) LAYER


- 1) Load wafer into Nb system and pump load lock for (5 min) $p = 3 \times 10^{-7}$ torr, 7 min
 2) Ion mill vias to clean surface in Nb system for (60 sec) as follows:
 a) Base pressure (torr) Gate valve pressure (torr) 4.5×10^{-8}

Set:	Other parameters should be near (record):
Ar pressure 1.4×10^{-4} torr ✓	Cathode filament I = 2.55 (2.98) A
Probe I = 0.1 mA/cm ² ✓	Discharge I = 0.18 (0.19) A
Beam V = 800 V ✓	Beam I = ✓ (20) mA
Accelerator V = 950 V ✓	Accelerator I = ✓ (2) mA
Emission I = 33 mA (~1.5 x Beam I) 34	Discharge V = ✓ (55.0) V
<i>puke C</i>	Filament I = 2.40 (3.13) A

- a) Let wafer cool in 5 mtorr of Ar gas for (5 min) ✓ 7 min
 3) Sputter Al on the wafer:
 a) 67 nm Dummy ✓ (2:00 min) ✓ (5.0 mtorr Ar) ✓ (200 W) 527 (V) 0.38 (A)
 b) 100 nm Wafer ✓ (3:15 min) ✓ (5.0 mtorr Ar) ✓ (200 W) 534 (V) 0.37 (A)
 5) Inspect film under microscope: ~~XXXXXXXXXX~~

PATTERN CONDUCTOR (WC-LAYER)

1) Pattern WC-layer resist:

- a) Clean spinner nozzle with acetone and IPA and purge it 10 times.
 b) Spin thin layer HMDS: 3500 rpm (setting 332?) ✓ → 40 sec
 c) Bake on hotplate 95 C for 60 sec with vacuum on
 d) Spin 1 micron resist SPR 660L: 3200 rpm (setting 323) ✓ → 40 sec
 e) Bake on hotplate 95 C for 60 sec with vacuum on.
 f) Expose on stepper:
 i) Masks: ~~2X118D-WC~~ 2X1D8G-WC 3/24/08 kc
 ii) Job File: (jb080227.IMqubitSiNx.kc) ✓
 iii) Layer ID: wc
 iv) Expose at 230 mJ/cm²: ✓
 g) Post-bake on hot plate 110 C for 60 sec with vacuum on.
 h) Spin-develop in MF-701 for 60 sec. Bottoms of ~~the~~ vias on left side of wfr
 i) Inspect under microscope: have dots in the via. Don't know why. Last wafer had it too.
 j) Use acetone to clean resist from several spots for future laser beam thickness monitor for future insulator etches !! Sketch where relative to the wafer flat. 
 k) Wet Etch Aluminum:
 a) Heat Al etchant type A to 48-49 C (set hot plate to ~65-70 C settings).
 b) Use tripod and dip in etchant until it 2 sec after it clears (15 sec) 13
 l) Inspect under microscope: looks good (0.1 μm overetched)
 m) Ultrasound "dirty" acetone (1 min), Ultrasound "clean" acetone (1 min), spray HEAVELY with ACETONE then IPA while spinning dry.
 n) Inspect under microscope: looks good
 o) Measure etched thickness using profilometer (100 nm) ✓

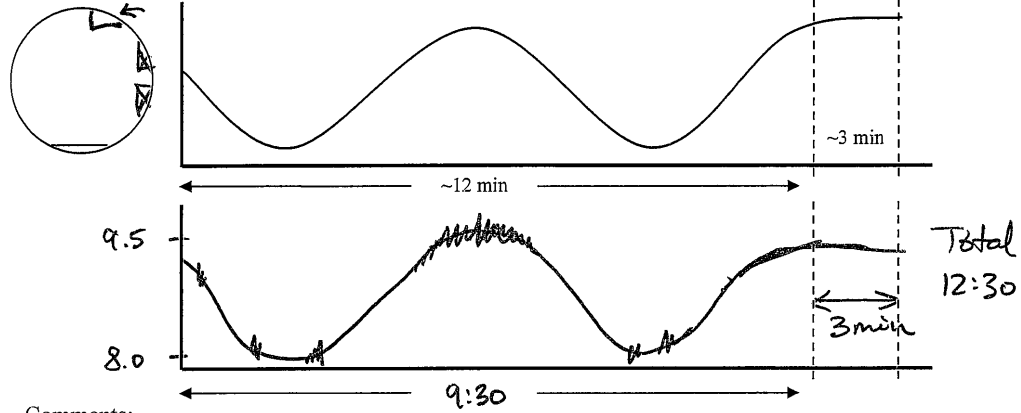
PATTERN INSULATOR ETCH (IE-LAYER)

1) Pattern IE layer resist:

- a) Clean spinner nozzle with acetone and IPA and purge it 5 times.
 b) Spin HMDS and Resist SPR 660L
 i) Thin layer HMDS: 3500 rpm (setting 332) ✓ → 40 sec
 ii) Bake on hotplate 95 C for 60 sec with vacuum on
 iii) 1.23 micron Resist: 2200 rpm (setting 227) ✓ → 40 sec
 iv) Bake on hotplate 95 C for 60 sec with vacuum on.

- (c) Expose on stepper:
 (i) Masks: ~~2XHFID-IE~~ **2XID8G-IE** 3/24/08 kc
 (ii) Job File: (jb080227.IMqubitSiNx.kc)
 (iii) Layer ID: ie
 (iv) Expose at 275 mJ/cm²: ✓
 (d) Post-bake on hot plate 110 C for 60 sec with vacuum on.
 (e) Spin-develop in MF-701 for 60 sec.
 (2) Inspect under microscope: looks good except for previously mentioned look photos
 (3) Etch through Insulator using AXIC. Use proper recipe (JASnitride.prc) ✓
 (a) Use acetone to make clean spot for laser beam thickness monitor. Align beam (8-12 V) 10.83 V
 (b) Condition chamber by running JASnitride.prc for 43 (15-20 min)
 (c) Pump to base pressure p = 6x10⁻⁵ torr ✓
 (d) Start etch and watch graph for wavy curve (see c).
 (60 sccm O₂) ✓ (50 W(f)) 49
 (42 sccm CF₄) ✓ (0 W(r)) 1
 (65 mtorr) 64 (-130 V) -130 V

Sketch etch curve below and where the laser monitor was relative to the flat on the wfr:



- Comments:
 (4) Inspect under microscope: looks good
 (5) Strip resist:
 (a) Clean Asher without wafer: 50 sccm O₂ 50 W (subtract any offset) 3:00 min ^{6 min}
 (b) Use Asher with wafer: 50 sccm O₂ 50 W (subtract any offset) 3:00 min
 (c) Ultrasound "dirty" acetone (2 min), Ultrasound "clean" acetone (2 min), spray HEAVELY with ACETONE then IPA while spinning dry. ^{Power 40}
 (6) Inspect under microscope: looks good
 (7) Measure etched thickness using profilometer: Center ✓ (270 nm) Edge: ✓ (320 nm)

PATTERN CAVITY AND COUPLING CAPS (RS-LAYER)

- (2) Pattern RS-layer resist:
 (a) Clean spinner nozzle with acetone and IPA and purge it 5 times.
 (b) Spin HMDS at 3500 rpm (setting 381) for 35 sec
 (c) Bake on hotplate 95 C for 60 sec with vacuum on
 (d) Spin 1 micron resist SPR 660L: 3200 rpm (setting 323) ✓ → 40 sec
 (e) Bake on hotplate 95 C for 60 sec with vacuum on.
 (f) Expose on stepper:
 (i) Masks: **2XHFID-RS, 2XID8G-SC, and 2XID8G-SI**
 (ii) Job File: (jb080227.IMqubitSiNx.kc) ✓
 (iii) Layer ID: rs

- iv) Expose at **230 mJ/cm²**: ✓
- g) Post-bake on hot plate 110 C for 60 sec with vacuum on.
- h) Spin-develop with MF-701 for 60 sec.
- 3) Inspect under microscope: looks good
- 4) Wet Etch Aluminum:
 - a) Heat Al etchant type A to 48-49 C (set hot plate to ~65-70 C settings).
 - b) Use tripod and dip in etchant until it 2 sec after it clears (15 sec) 15
- 5) Inspect under microscope: looks good (0.5 μm overetched)
- 6) Ultrasound "dirty" acetone (2 min), Ultrasound "clean" acetone (2 min), spray HEAVELY with ACETONE then IPA while spinning dry. Power 40
- 7) Inspect under microscope: looks good

4908 kc

PATTERN SE-LAYER (sacrificial etch)

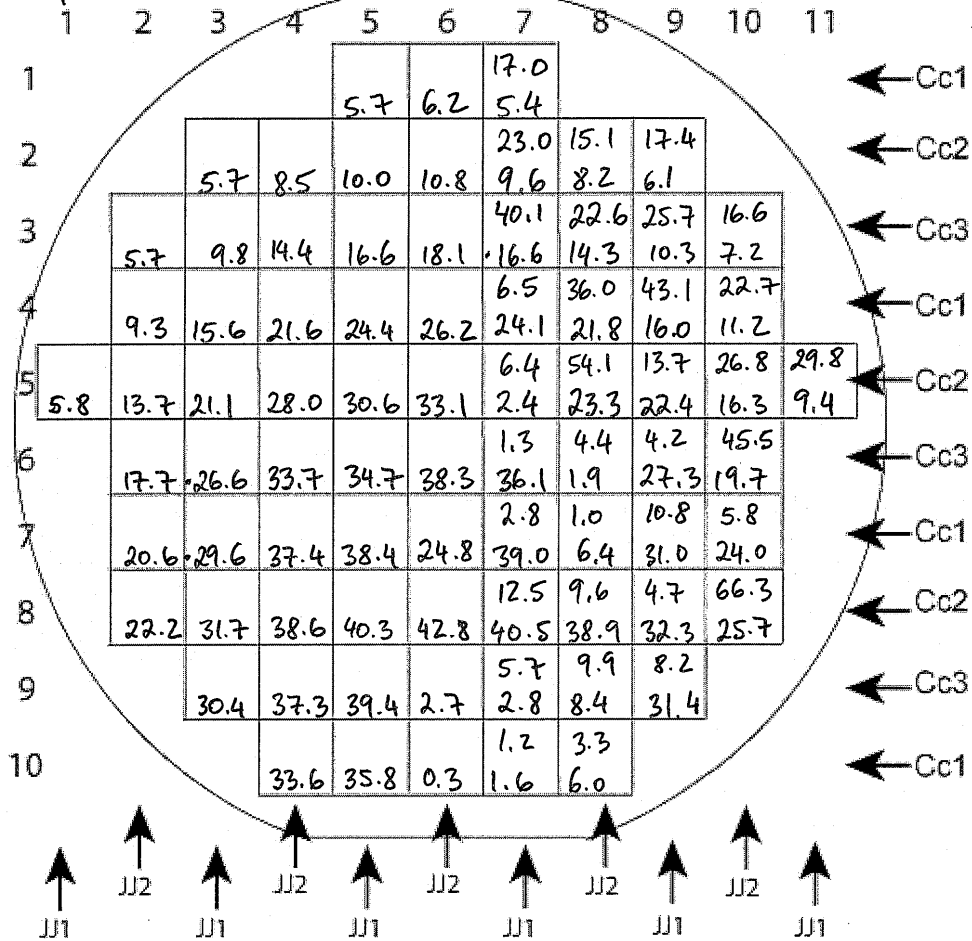
Remove SiNx from wiring crossovers on fishbone cap by high pressure RIE etch

- 8) Pattern SE-layer resist:
 - a) Clean spinner nozzle with acetone and IPA and purge it 5 times.
 - b) Spin HMDS at 3500 rpm (setting 381) for 35 sec
 - c) Bake on hotplate 95 C for 60 sec with vacuum on
 - d) Spin thick resist SPR 660L: 2200 rpm (setting 227) → 40 sec
 - e) Bake on hotplate 95 C for 60 sec with vacuum on.
 - f) Expose on stepper:
 - i) Masks: 2XID8G-SE ← 3/24/08 kc
 - ii) Job File: (jb080227.IMqubitSiNx.kc) ✓
 - iii) Layer ID: se
 - iv) Expose at **275 mJ/cm²**: ✓
 - g) Post-bake on hot plate 110 C for 60 sec with vacuum on.
 - h) Spin-develop with MF-701 for 60 sec.
- 9) Inspect under microscope: looks good
- 10) Dry etch in IPE RIE to remove SiNx from vacuum cross-overs
 - a) Precondition machine by running plasma for 5-10 min without chips, process kcsf6.prc 10 min
 - b) Run process kcsf6.prc to etch SiNx Base p = 3.6 x 10⁻⁶ torr
 - Power f: 98 (100)W,
 - SF₆ ✓ (100) sccm r: 0 (0)W
 - press: ✓ (200) mTorr Voltage: -18 (-20)V Total etch time 23 (20)min
- 11) Inspect under microscope: looks good ← resist still on.
- 12) Strip resist:
 - a) Clean Asher without wafer: 50 sccm O₂ 50 W (subtract any offset) 3:00 min 6 min
 - b) Use Asher with wafer: 50 sccm O₂ 50 W (subtract any offset) 3:00 min
 - c) ~~Ultrasound "dirty" acetone (2 min), Ultrasound "clean" acetone (2 min), spray HEAVELY with ACETONE then IPA while spinning dry.~~
- 13) Ultrasound at **power setting 25** in "dirty" acetone (3 min), Ultrasound at **power setting 25** in "clean" acetone (3 min), spray HEAVELY with ACETONE then IPA while spinning dry. Power settings above 30 destroy/rip vacuum bridges.
- 14) Inspect under microscope: _____

CHECK TEST JUNCTIONS

Bgrnd = 0.076 Ω

2) Use probe station to determine junction resistances. Diode box used: YES NO
 Date: 4/9/08 KC Time: 2:40 pm in cleanroom



Oxidation parameters: _____ torr, _____ min:sec,

Top JJ1 (6.63um²): Rn = _____ (158) ± _____ ohm (_____%)
 Top JJ2 (4x1.66um²): Rn = _____ (158) ± _____ ohm (_____%)
 Bottom JJ (35.36um²): Rn = _____ (30) ± _____ ohm (_____%)
 $J_o = (2.9845e4 V)/(A * Rn_bottom) = (2.9845e4 V)/(_____ um^2 * _____ Ohms)$
 $J_o = _____ (28.52) A/cm^2$

For large JJs: After processing JJ resistances are 5-10% larger.

Date: 4/9/08 KC

DICE WAFER

- Spin protective layer of resist:
 - Spin resist SPR 660L, 3200 rpm → ~ 1micron, (setting 323), 40 sec
 - Bake on hotplate 95 C for 60 sec with vacuum on
- Dice wafer on a dicing saw using resinoid blade and parameters: 060/246/246/8/35/90/100/3000/3.
(or if using Si wafer use Si blade and parameters: 010/246/246/8/35/90/200/3000).
- Select dies to be measured and spin clean them with ACETONE then IPA at power setting 25 for 3 min.
- Inspect under microscope: _____

Date: _____

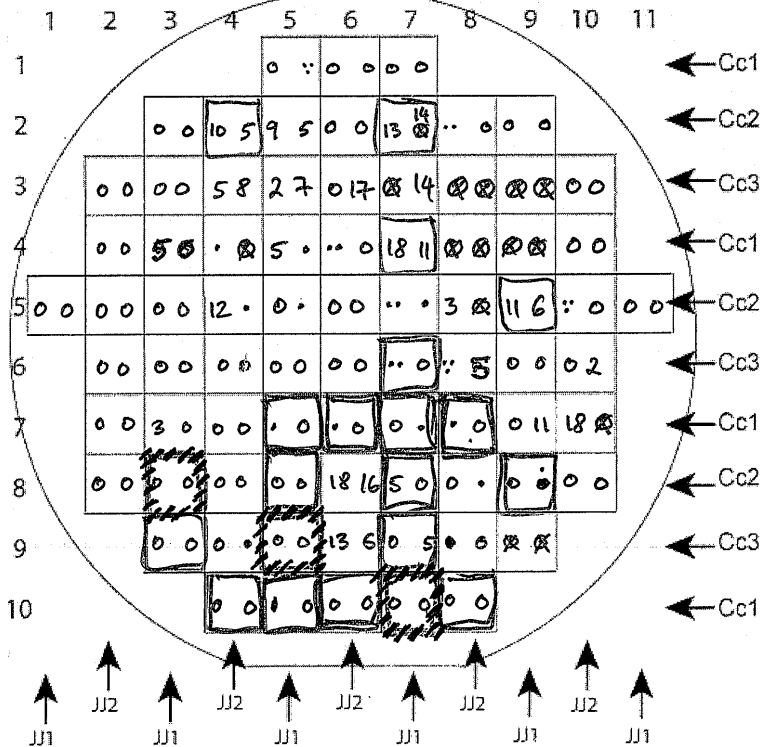
SEM INSPECTION

- Record die name, tilt angle, WD (working distance) and name/number of the generated image.

Date: 4/9/08 KC

FINAL ASSESMENT

Mark dies taken out for cooldown, and write down the date when taken out.



Inspected before spinning dicing resist.

Inspecting vacuum bridges on ID capacitor

- one bridge damaged
- 2 "
- 3 "
- good
- more than 20 broken

□ = in gel box
 [hatched] = cooled down 04/13/08 KC

4/10/08 KC

⊙ Test on dummy chips if vacuum crossovers get destroyed during resist strip

	Before	After Soak	After Spin	After 2+2 min ultrasonic (power 25)
die 0509	11 7	11 7	11 7	11 24 +17
die 0207	13 14	13 14	13 14	15 14 +2
die 0204	10 5	10 5	10 5	10 6 +1

of destroyed/missing bridges

⇒ Drying ^{after} by soaking or by spinning does not rip vacuum bridges.

⇒ Drying by spinning after ultrasonicating (power 25) does!!

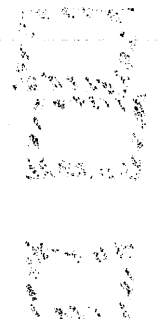
die 0407

18 12	18 12
-------	-------

04/10/08 KC

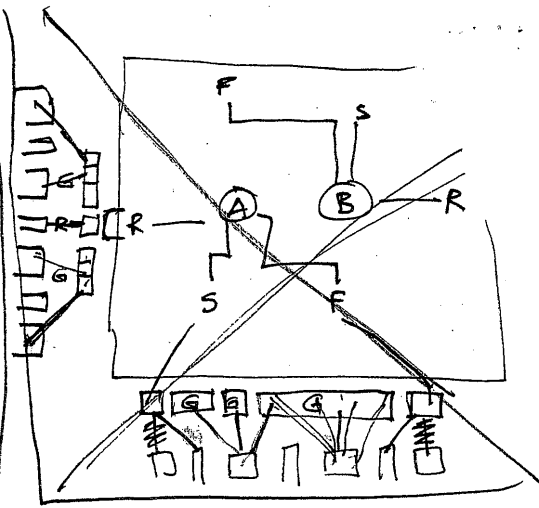
⊙ SEM inspection: see if bridges are collapsed


	tilt	WD	Beam W	image #
die 0204	15°	18.75 mm	5 kV	1 - 10
die 0407	15°	18.75	5 kV	11 - 15



Gel Pack

0509	1004 X	1005	0803 X	0903 X
0207	1006 X	1007	0805	0905
0204	1008	0705	0807 X	0907
0407	0706 X X	0707	0809 X	0807
	0708 X X			




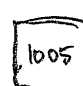
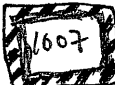



 = cooled down 4/13/08

↑ test, SEM
 ↑ JJ2 Cc1
 ↑ JJ1 Cc1
 ↑ JJ1 Cc2
 ↑ JJ1 Cc3

4/11/08 KC

Soak all except 1st column of chips in acetone and spin dry them

Inspect:

-  - O.K. some sand that cannot be clean near RF coil of one qubit
-  - O.K. (dummy qubit coil broken). One vacuum bridge on R ID cap missing but O.K.
-  - O.K.
-  - O.K.
-  - O.K. but some junk (probably organic) across cavity
-  - O.K. one vacuum bridge gone. but O.K.

0907 - O.K. few vacuum bridges on ϕ missing but ok

10.2 Qubit with tunable cavity process sheet

The device used to demonstrate dispersive measurement, made with shadow evaporated Josephson junctions (Section 5.2.2) and reported on in Sections 7.2-7.2.7 and Chapter 8, was die 0503 from the wafer labeled `wfr110903.SE.jdw`. The device was fabricated by the author. The process sheet for this wafer is reproduced below.

Date: 9/3/11
 ps110822.SE.jdw.odt

wfr110903.SE.jdw

Page: 1-4

Si OR Sapphire wafer (circle one)

→ EPITAXIAL FROM PAPPAS

Stepper job file: jb110822.jdw

Layer	ID	Image	Reticle(s)	Exposure (MJ/cm ²)	Notes
0	PM	0-PM	ALIGN	180	
1	first	TRY1-4	ALIGN, JC1	180	For doing JJ tests on bare wafers
2	B	TRY1-4	B-100 (1,3), B-200 (2,4)	180	
3	JC1	ALL1	JC1	180	
4	JC2	ALL2	JC2	180	Does 100nm shifts in x by row
5	empty				

I. Deposit 100nm Al

→ CHAMBER HAD BEEN VENTED TO FIX RF, SO I BURNED IN AL TARGET FOR 5 MIN W/ WAFER IN LOAD LOCK.

1. Use recipe "QubitBaseCleanAldep" (qb_sub_Clean60W, qb_sub_Aldep100nm)

2. Record parameters for each step:

- (a) **RF cln:** Pressure: 5.0 mT (15.0 mT) Time: 60 s (60s)
 Forward pow: 60 W (60 W) Reflected pow: 0 W (0 W) Bias: 270 V (280 V)
- (b) **Al pre:** Pressure: 5.0 mT (5.0 mT)
 Power: 301 W (300 W) Voltage: 346 V (350 V)
 Current: 0.89 A (0.9 A) Time: 60 s (60 s)
- (c) **Al dep:** Pressure: 5.0 mT (5.0 mT)
 Power: 302 W (300 W) Voltage: 350 V (350 V)
 Current: 0.89 A (0.9 A) Time: 350 s (350 s = 5:50 min, 100nm)

II. Pattern Alignment marks and B layer

1. Pattern resist:

- (a) Temperature: 68.7 °F (68°F) Humidity: 35 % (35%)
 (b) Spin HMDS at 3900 rpm (setting 390) for 35 sec, bake on hotplate 95°C for 60 sec with vacuum on. ✓
 (c) Clean spinner nozzle with acetone and IPA and purge it 3 times. ✓
 (d) Spin 1 micron resist SPR 660L: 2800 rpm 35 sec ✓
 (e) Bake on hotplate 95°C for 60 sec with vacuum on. ✓
 (f) Expose on stepper: Job File: jb110822.jdw ✓
 i. Reticles: ALIGN, Layer 0 "PM" (leave wafer on e-table), B-100, B-200, layer "B" ✓
 ii. Expose at 180 mJ/cm² ✓
 (g) Post-bake on hot plate 110°C for 60 sec with vacuum on. ✓
 (h) Spin-develop with MF-26A for 60 sec. → DEVELOP STATION DOWN; DEVELOPED BY HAND RINSED IN H₂O 60s.

2. **Inspect** under microscope: GOOD, THOUGH DIE 0501 IS MESSED UP. overdev(μm): L=0.2 C=0.2 R=0.2

3. **Etch** Al using Trion etcher

- (a) Use recipe kc_Al_vertical for 26 s (~25s) (3s overetch)
 i. He press: 5.0 torr He flow: 2.0 sccm RIE power: 200 W
 ii. Pressure: 30 torr Cl₂ flow: 10 sccm BCl₃ flow: 30 sccm 5 nm/s (100 nm/20 s)
 (b) **Passivate** in DI water for 2 min, **Sonicate** in DI water for 2 min at 50V, spin dry ✓

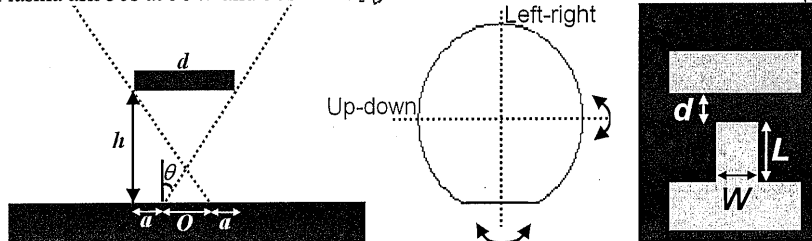
4. **Ultrasound** at 50V in acetone (2 min), IPA (2 min), H₂O washer

5. **Inspect** under microscope: GOOD overdev(μm): L=0.2 C=0.2 R=0.2

6. **Measure** etched thickness with profilometer: L=96 nm, C=107 nm, R=96 nm, Avg=102 nm

III. Al shadow evaporation

1. Spin LOR
 - (a) Apply p-20 primer at 3900 rpm for 35s, bake for 60s at 95°C. ✓
 - (b) Use recipe 7 for LOR 20B ✓
 - i. Step1: speed=500, ramp=500, term time=5s, Step2: speed=3000, ramp=10000, term time=45s, Step3: speed=0, ramp=10000, term time=0s (use step 0 to get back to run screen)
 - ii. Set plate temp to 170°C ✓
 - (c) Pour LOR 20B from bottle, a smooth puddle of half wafer diameter, spin ✓
 - i. While spinning wet a rag with Nano EBR-PG and clean edge during the 3000 rpm spin ✓
 - (d) Bake at 170°C for 5 min ✓
 - (e) Mistakes: strip before bake using Nano EBR-PG. Strip after bake using Remover PG
2. Pattern resist:
 - (a) Temperature: 68.9 °F (68°F) Humidity: 35 % (35%)
 - (b) Clean spinner nozzle with acetone and IPA and purge it 3 times. ✓
 - (c) Spin resist SPR 660L 35 sec at 2800 RPM (1µm) ✓
 - (d) Bake on hotplate 95°C for 60 sec with vacuum on. ✓
 - (e) Expose on stepper: **jb110822.jdw**
 - i. Reticle **JC1** for layer **JC1**, leave on e-table, then do reticle **JC2** in layer **JC2** (for shift) ✓
 - ii. Expose at 180 (180) mJ/cm² ✓
 - (f) Post-bake on hotplate 110°C for 60 sec with vacuum on. ✓
 - (g) Spin-develop with MF-26A: 5s pre-wet, dev for 60s, rinse for 45s, spin dry 20s. ✓
 - (h) Plasma ash 30s at 50W and 50sccm O₂ ✓



DEVELOP SPINNER IS DOWN, SO I HAD TO DEVELOP IN MF-26A FOR 60S & RINSE IN H₂O 60S, SPIN DRY.

3. Geometry: $\tan(\theta) = (d+O)/2h$ $O = (A_{nom} + \Delta A)/W$ $\Delta A = \underline{\quad(-0.2\mu m^2)\quad}$
 4. Inspect under microscope: undercut: 5.5 (3.5µm)
- | Die: | 0501 | 0502 | 0503 | 0504 | 0505 | 0506 | 0507 | 0508 | 0509 | 0510 | 0511 | |
|---------|------|------|------|------|------|------|------|------|------|------|------|-------------|
| d (µm): | 1.96 | 1.94 | 1.97 | 1.98 | 1.99 | 1.93 | 1.93 | 1.93 | 1.93 | 1.88 | 1.85 | d Avg: 1.93 |
| W (µm): | 0.65 | 0.60 | 0.71 | 0.62 | 0.63 | 0.70 | 0.63 | 0.62 | 0.65 | 0.65 | 0.62 | W Avg: 0.64 |
| L (µm): | 2.36 | 2.36 | 2.33 | 2.28 | 2.25 | 2.36 | 2.40 | 2.36 | 2.40 | 2.40 | 2.46 | L Avg: 2.36 |

5. Measure LOR thickness (h) across wafer using profilometer (assume top resist is 1µm thick):
- | Die: | 0501 | 0502 | 0503 | 0504 | 0505 | 0506 | 0507 | 0508 | 0509 | 0510 | 0511 | |
|---------|------|------|------|------|------|------|------|------|------|------|------|-------------|
| h (µm): | 2.79 | 2.74 | 2.76 | 2.74 | 2.77 | 2.76 | 2.74 | 2.74 | 2.75 | 2.76 | 2.75 | h Avg: 2.75 |

AY DEPOSITED 9/4

$\tan^{-1}(\frac{d+O}{2h}) = 23.5^\circ$

$\tan^{-1}(\frac{L}{h}) = 20.0^\circ$

6. Deposit using Joetek (recipe ae110709 - standard X-90's)
 - (a) Ion Mill for 50s in 1.2x10⁻⁴ T Ar, cool in Ar for 1 min after milling
Cathode fil. I: 3.67 (3.67A) Discharge I: 0.44 (0.40A) Beam I: 35 (32mA) Accel I: 2 (2mA) Neut. Emis. I: 55 (51mA)
Discharge V: 55 (55V) Beam V: 300 (300V) Accel V: 950 (950V) Filament I: 3.65 (3.74A)
 - (b) Al thicknesses: 75 (75nm) / 150 (150nm) at 3.8A/s, Angle: ±23.5° (±20°), Axis: + then - 23.50
 - (c) Oxidation pressure: 760 (750mT), oxidation time: 10 (10min) ramp 37.05

LIFT-OFF NEXT NIGHT 9/4-9/5

7. Lift-off (NO ULTRASOUND AT ALL!) * Noted streaks on wafer page 3-4
- (a) Overnight acetone (>3hrs), 5 min acetone x2, 30 min Remover PG (hotplate at 180°F=80°C) x2, 5 min IPA x2, spin dry
8. Inspect under microscope: GREAT. PROFILOMETER ON 5C1/5C2:

DIE	0501	0409	0408	0405	0505	0605	1006	0106
JS MEA:	0.31	0.24	0.23	0.28	0.33	0.46	0.10	0.11

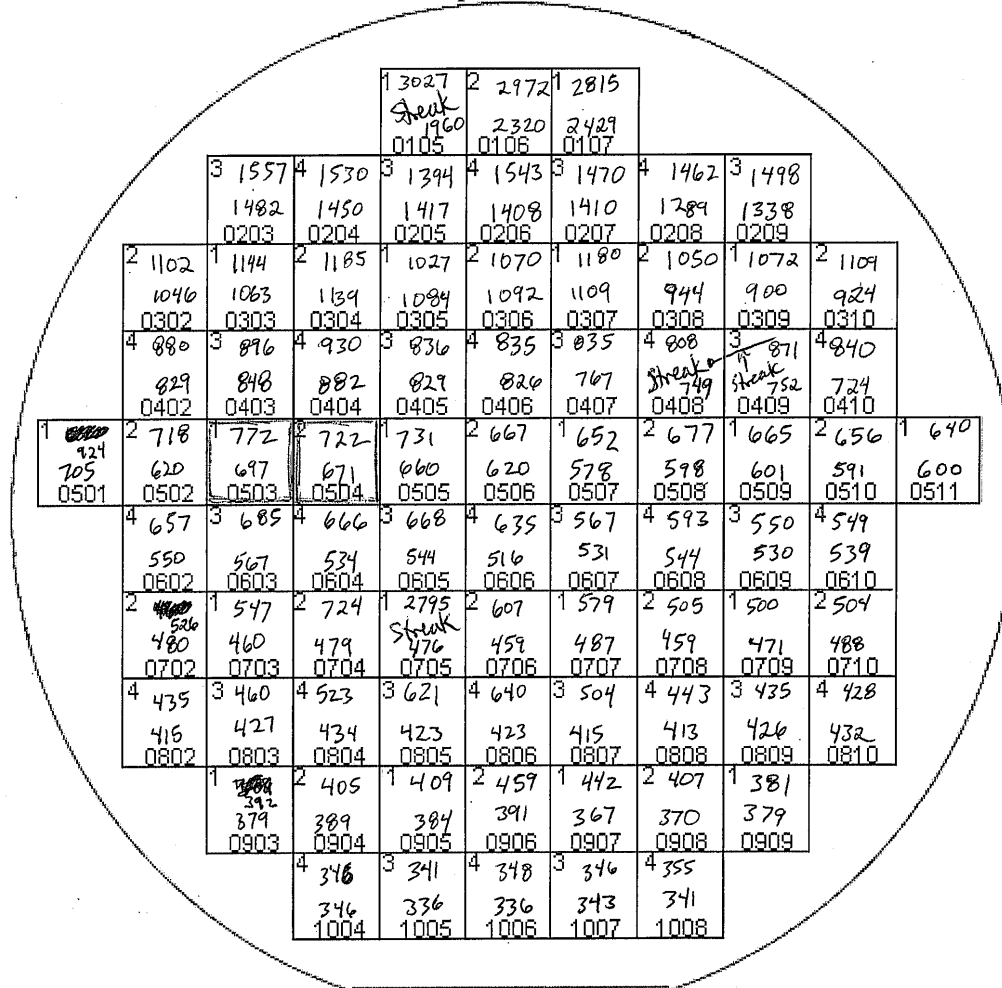
Date: 9/5/11

wfr110903.SE.jdw

Page: 3-4

IV. Record Resistance Measurements

Use lockin amplifier in volt lab, or cleanroom probe station
 If using cleanroom probe stations use diode box and set HP 34401A to 3 digit kOhm precision



$$I_c (\mu A) = J_c A = (370 \pi) / (4 R_N) = 290.60 / R_N$$

Area (um ²)	Mean R (Ω)	Std dev (Ω)	Spread	N	I ₀	J ₀
Top:						
Bottom:						

Measure bias line resistances across wafer

Die: 0501 0502 0503 0504 0505 0506 0507 0508 0509 0510 0511

R_{SQ} (Ω): _____ R_{SQ} Avg: _____

Date: 9/5/11 wfr110903.SE.jdw

Page: 4-4

V. DICE WAFER

1. Spin protective layer of resist:
 - (a) Temperature: 68.7 °F (68°F) Humidity: 35 % (38%)
 - (b) Spin 1 micron resist SPR 660L: 2200 rpm (setting 215) 35 sec ✓
 - (c) Bake on hotplate 95 C for 60 sec with vacuum on. ✓
2. Dice wafer using resinoid blade (sapphire): 060/3000/3000/246/246/4/30/90/100/3/15000 ✓
 (or if using Si wafer use Si blade: ~~010/246/246/8/35/90/200/3000~~)

VI. Die selection/use

Die	Date	Use	R _{top}	R _{bottom}	R _{bias}	Notes
0503	9/6	100 MHz, RES ONLY	772	697	?	
0504	9/6	200 MHz, Au & RES	722	671	?	RUINED BIAS LINE w/ WIRE BOND-JUNK
0502	9/6	200 MHz, Au & RES	719s	620	?	

10.3 Multiplexed tunable cavities process sheet

The device used to demonstrate multiplexed tunable cavities, made with via-style Josephson junctions (Section 5.2.1.1) and reported on in Section 7.2.8, was die 0507 from the wafer labeled wfr090608.MultiSQUIDs.jdw. The device was fabricated by the author, and also included vacuum gap capacitors. The process sheet for this wafer is reproduced below.

Date: 6/18/09
 ps090527.MultiSQUIDSs.jdw.odt
 wfr 090608.MultiSQUIDSs.jdw

PROCESS SHEET SUMMARY

Si OR Sapphire wafer (circle one)

Stepper job file: jb090428.MultiSQUIDSs.jdw, jb090428.TestDie.jdw

Layer	ID	Image	Reticle(s)	Exposure (MJ/cm ²)	Notes
0	PM	0-PM	ALIGN	230	
1	bhpm	TRY1-3	BH, ALIGN	200 250	
2	bh	TRY1-3	BH	200 250	
3	bc	TRY1-3	BC	200 250	
4	se	TRY1-3	SE	200 250	
5	eh	TRY1-3	EH	200 250	
6	b	TRY1-3	B	200 250	
7	caps	TRY1-3	CAPS	200 250	
8	bg	TRY1-3	BG	200 250	
9	ji	TRY1-3	JJ	200 250	
10	jc	TRY1-3	JC	200 250	
11	wi	TRY1-3	WI	200 250	
12	wc	TRY1-3	WC	200 250	
13	ie	TRY1-3	IE	200 250	
14	tt	TRY1-3	TT	~260 ~300	Focus~-0.4
15	th	TRY1-3	TH	~260 ~300	Focus~-0.4
16	test	TRY1-3	TEST	200 250	
17	flood	TRY1-3	FLOOD	200 250	

Stepper job file: endpoint

Layer	ID	Image	Reticle(s)	Notes
0	0	0-PM	*	
1	try1	TRY1	FLOOD	
2	try2	TRY2	FLOOD	
3	try3	TRY3	FLOOD	
4	try4	TRY4	FLOOD	
5	wi	WI	FLOOD	
6	ie	IE	FLOOD	
7	all	ALL	FLOOD	

Junctions:

Label	Area (um ²)	Diameter (um)	Ic (uA)	Rn (Ohms)
SQUID	6.1	2.71	1.22	260
Qubit	10	3.47	2	149
Top test	10	3.47	2	149
Bottom test	6.1	2.71	1.22	260
Test Die				
Top test	10	3.47	2	149
Bottom test	19	4.79	3.8	78.5
Qubit	10	3.47	2	149
JJ res	5.75	2.63	1.15	259
SQUID 1	10	3.47	2	149
SQUID 2	19	4.79	3.8	78.5
SQUID 3	17	4.53	3.4	87.8

Date: 6/8/09

Page: 2-18

I. DEPOSIT Aluminum

1. Run process "shaneBLayer".
2. Record parameters for each step:

RF clean:

Pressure: 15.0 mT (15 mT) Time: 360 s (360s)
Forward power: 110 W (110 W) Reflected power: 0 W (0 W)
Bias voltage: 381 V (380 V)

Al pre:

Pressure: 5.0 mT (5.0 mT) Voltage: 273 V (273 V)
Power: 105 W (105 W) Time: 60 s (60 s)
Current: 0.41 A (0.41 A)

Al dep:

Pressure: 5.0 mT (5.0 mT) Voltage: 274 V (274 V)
Power: 106 W (106 W) Time: 1142 s (1142 s = 19:02 min)
Current: 0.41 A (0.41 A)

II. Pattern Alignment marks

1. Pattern resist:

- (a) Temperature: 60 °F (68°F) Humidity: 37 % (38%)
- (b) Spin HMDS at 3900 rpm (setting 390) for 35 sec ✓
- (c) Evacuate HMDS fumes from spinner/Bake on hotplate 95 C for 60 sec with vacuum on. ✓
- (d) Clean spinner nozzle with acetone and IPA and purge it 5 times. ✓
- (e) Spin 1 micron resist SPR 660L: 3200 rpm (setting 306) 35 sec ✓
- (f) Bake on hotplate 95 C for 60 sec with vacuum on. ✓
- (g) Expose on stepper: Job File: jb090428.MultiSQUIDS.jdw ✓
 - i. Reticles: ALIGN ✓
 - ii. Layer 0 "PM" ✓
 - iii. Expose at 230 mJ/cm² ✓
- (h) Post-bake on hot plate 110 C for 60 sec with vacuum on. ✓
- (i) Spin-develop with MF-26A for 60 sec. ✓

2. Inspect under microscope: Good

3. Etch Al using Trion etcher

- (a) If necessary, clean chamber with Clean10 recipe 10 min (10 min)
- (b) Use recipe kc_Al_vertical 40s
 - i. He press: 5.0 torr He flow: 2.0 sccm RIE power: 200 W
 - ii. Pressure: 30 torr Cl₂ flow: 10 sccm BCl₃ flow: 30 sccm
 - iii. 5 nm/s (100 nm/20 s)
 - iv. Passivate in running DI water for 5 min ✓

4. Inspect under microscope: DIDN'T

5. Ultrasound at 70V "dirty" acetone (2 min), Ultrasound "clean" acetone (2 min), spray HEAVELY with ACETONE then IPA while spinning dry. ✓

6. Inspect under microscope: Good

Date: 6/8/09

III. PATTERN BH and BC (base holes and base conductors) LAYERS

1. Pattern BH- and BC-layer resist:

- (a) Temperature: 68 °F (68°F) Humidity: 36 % (38%)
- (b) Spin HMDS at 3900 rpm (setting 390) for 35 sec ✓
- (c) Evacuate HMDS fumes from spinner/Bake on hotplate 95 C for 60 sec with vacuum on. ✓
- (d) Clean spinner nozzle with acetone and IPA and purge it 5 times. ✓
- (e) Spin 1 micron resist SPR 660L: 3200 rpm (setting 306) 35 sec ✓
- (f) Bake on hotplate 95 C for 60 sec with vacuum on. ✓
- (g) Expose on stepper: Job File: jb090428.MultiSQUIDS.jdw (try1-3), jb090428.TestDie.jdw (try4) ✓
 - i. Reticles: ALIGN, BH, BC, BHtest, BCtest SHOT ~~BH~~ BHs (TRY 1-4), BUT ONLY BCs ON TRY 1-2.
 - ii. Layers 2 & 3 "bh", "bc" ✓
 - iii. Expose at 200 mJ/cm² ✓
- (h) Post-bake on hot plate 110 C for 60 sec with vacuum on. ✓
- (i) Spin-develop with MF-26A for 60 sec. ✓

2. Inspect under microscope: GOOD. SIDECUT < 0.2 um

3. Etch Al using Trion etcher

- (a) If necessary, clean chamber with Clean10 recipe 0 min (10 min)
- (b) Use recipe kc_Al vertical 40s
 - i. He press: 5.0 torr He flow: 2.0 sccm RIE power: 200 W
 - ii. Pressure: 30 torr Cl₂ flow: 10 sccm BCl₃ flow: 30 sccm
 - iii. 5 nm/s (100 nm/20 s)
 - iv. Passivate in running DI water for 5 min ✓ SONICATE AT 50V FOR 2min IN DI WATER ✓

4. Inspect under microscope: GOOD, NO PEELING RESIST

5. **Ultrasound** at 70V "dirty" acetone (2 min), Ultrasound "clean" acetone (2 min), spray HEAVELY with ACETONE then IPA while spinning dry. ✓

6. **Inspect** under microscope: GOOD Record Over etch amount < 0.2 um

7. **Measure** etched thickness using profilometer (100 nm): 93 um

SHOT BC ON TRY 3 & TRY 4, DEVELOPED, THEN ETCHED IN 100ml AL ETCHANT AT 49°C FOR 13 s ✓

INSPECT UNDER MICROSCOPE GOOD ~~OVERETCH: 0.3 um~~ ✓

ULTRASOUND AT 70 V IN ACETONE 2min TWICE. ✓

INSPECT UNDER MICROSCOPE: GOOD OVERETCH: 0.3 um

Date: 6/8/09

IV. DEPOSIT SiN sacrificial layer

1. **Glue** sapphire wafer onto "spider" wafer (skip this step if using Si wafer):
 - (a) Clean teflon chuck with acetone and IPA and blow it dry. ✓
 - (b) Mount teflon chuck and carefully place the sapphire wafer face (polished-side) down on the chuck (to spin resist on back of it). ✓
 - (c) Spin "glue" resist SPR 220-3, 2500 rpm, 35 sec (dispense manually). There should be no resist on the face of the sapphire wafer after spin. ✓
 - (d) Place the sapphire wafer, resist side down, onto a "spider" wafer with flats aligned, and push the edges together until the two are "glued" together. ✓
 - (e) Bake on hotplate 95 C for 10 min with vacuum on (sapphire face up) ✓
 - (f) Inspect sapphire wafer under microscope for surface cleanliness: GOOD, NO SCRATCHES
 - (g) Spin-clean the wafer with acetone and IPA to clean resist from the edges of the wafer. ✓

2. **Ash** 2:00 to make insulator stick better. ✓
3. **Deposit Insulator** using PlasmaQuest ECR:

- (a) Run process BIGCLEAN with the cleaning wafer in the machine.
 - i. Is the chamber manometer zeroed? ✓
 - ii. Is the chamber being heated? ✓

- (b) Run a dummy wafer to get microwave power tuned ✓

- (c) Load wafer and run your process **SiNx RFcln** (edit deposition time to deposit SiNx for ¹¹⁰~~120~~ sec)

Record the actual parameter values: RF Clean		Record the actual parameter values: SiNx Deposition	
O2 flow:	0 (0) sccm	Ar flow:	101.4 (100.0) sccm
Ar flow:	140.8 (139.0) sccm	N2 flow:	15.1 (15.0) sccm
SiH ₄ flow:	0 (0) sccm	SiH ₄ flow:	133.7 (132) sccm
Upper magnet I:	179.8 (185) A	Upper magnet I:	179.0 (185) A
Pressure:	5.0 (5) mTorr	Pressure:	9.5 (9) mTorr
RF power F:	50 (50) W	RF power F:	0 (0) W
R:	0 (0) W	R:	0 (0) W
Dc bias:	-195 (-200) V	Dc bias:	0 (0) V
Microwave power F:	0 (0) W	Microwave power F:	1200 (1200) W
R:	0 (0) W	R:	5 (0) W
Backside He press:	2.4 (>2.5) torr	Backside He press:	2.4 (>2.5) torr
Backside He flow:	1.3 (<1.0) sccm	Backside He flow:	1.2 (<1.0) sccm
Clean time:	120, (120) sec	Deposition time:	110 (120) sec

4. **Ultrasound** at ⁵⁰~~70~~V "dirty" acetone (1 min), separate wafers (skip this step if using Si wafer). ✓
5. **Ultrasound** at ⁵⁰~~70~~V "dirty" acetone (2 min), Ultrasound "clean" acetone (2 min), spray HEAVELY with ACETONE then IPA while spinning dry. ✓
6. **Inspect** under microscope: GOOD, NO PEELING

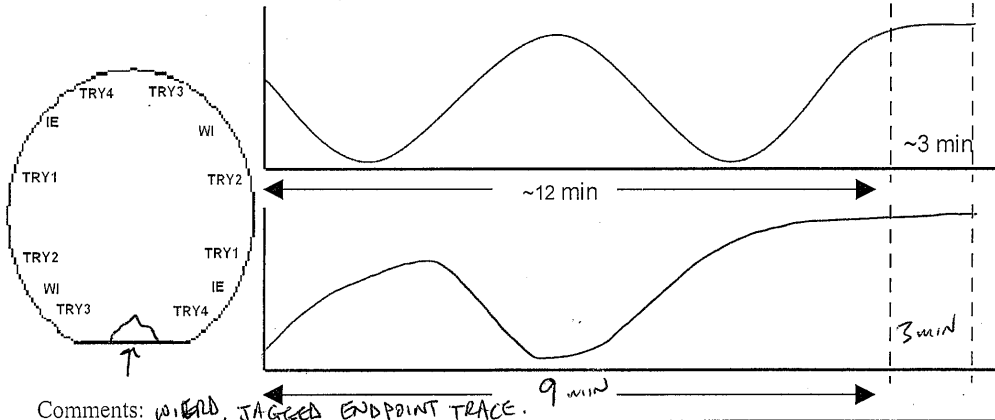
Date: 6/8/09

V. PATTERN SE (Sacrificial Etch) LAYER (and EH for via posts)

1. Pattern SE layer resist
 - (a) Temperature: 69 °F (68°F) Humidity: 35 % (38%)
 - (b) Spin HMDS at 3900 rpm (setting 390) for 35 sec ✓
 - (c) Evacuate HMDS fumes from spinner/Bake on hotplate 95 C for 60 sec with vacuum on. ✓
 - (d) Clean spinner nozzle with acetone and IPA and purge it 5 times. ✓
 - (e) Spin 1 micron resist SPR 660L: 2200 rpm (setting 215) 35 sec ✓
 - (f) Bake on hotplate 95 C for 60 sec with vacuum on. 22
 - (g) Expose on stepper: **jb090428.MultiSQUIDS.jdw** (try1-3), **clearout, jb090428.TestDie.jdw** (try4) ✓
 - i. Reticles: **SE, EH, ALIGN, SEtest, EHtest** ✓
 - ii. Layers 4 & 5 "se", "eh" ✓
 - iii. Expose at 200 mJ/cm² ✓
 - (h) Post-bake on hot plate 110 C for 60 sec with vacuum on ✓
 - (i) Spin-develop in MF-26A for 60 sec (make sure settings are as they are labeled on the machine) ✓
2. Inspect under microscope: GOOD, 0.2 um SIDE CUT
3. Condition chamber by running **JASnitride.prc** for 0 (5 min)
4. Etch through Insulator using **AXIC**. Use proper recipe (**JASnitride.prc**). Use acetone to make clean spot for laser beam thickness monitor. Align beam (8-12 V) 12.5
 - (a) Pump to base pressure $p = 6 \times 10^{-5}$ torr
 - (b) Start etch and watch graph for wavy curve (see c).

(60 sccm O ₂)	<u>60.0</u>	(50 W(f))	<u>49</u>
(42 sccm CF ₄)	<u>42.0</u>	(0 W(r))	<u>1</u>
(65 mtorr)	<u>63.0</u>	(-130 V)	<u>-130</u>

Sketch etch curve below and where the laser monitor was relative to the flat on the wfr:



stopped here 6/8/09 8:22

- (c) Inspect under microscope: GREAT.
- (d) Strip resist:
 - i. Clean asher without wafer: 50 sccm O₂ 50 W (subtract any offset) 3:00 min ✓
 - ii. Ash wafer: 50 sccm O₂ 50 W (subtract any offset) 3:00 min ✓
- (e) Ultrasound "dirty" acetone (2 min), Ultrasound "clean" acetone (2 min), spray HEAVELY with ACETONE then IPA while spinning dry. ✓
- (f) Inspect under microscope: GOOD, 0.4 um SIDE CUT/PEELING?
- (g) Measure etched thickness using profilometer: Left: 172 nm, Center: 170 nm, Right: 158 nm
- (h) Record thickness in ECR log book. Deposition rate: 1.52 nm/s, 90.9 nm/min

Date: 6/10/09

Page: 6-18

VI. DEPOSIT 2nd Aluminum Layer for Base B Layer

1. Run process "shaneBLayer".
2. Record parameters for each step:

RF clean:

Pressure: 15.0 mT (15 mT) Time: 360 s (360s)
Forward power: 110 W (110 W) Reflected power: 0 W (0 W)
Bias voltage: 385 V (380 V)

Al pre:

Pressure: 5.0 mT (5.0 mT) Voltage: 271 V (273 V)
Power: 105 W (105 W) Time: 60 s (60 s)
Current: 0.41 A (0.41 A)

Al dep:

Pressure: 5.0 mT (5.0 mT) Voltage: 272 V (274 V)
Power: 106 W (106 W) Time: 1142 s (1142 s = 19:02 min)
Current: 0.42 A (0.41 A)

VII. PATTERN B, BG, and CAPS LAYERS

1. Pattern B, BG and CAPS-layer resist:

- (a) Temperature: 69 °F (68°F) Humidity: 35 % (38%)
- (b) Spin HMDS at 3900 rpm (setting 390) for 35 sec ✓
- (c) Evacuate HMDS fumes from spinner/Bake on hotplate 95 C for 60 sec with vacuum on. ✓
- (d) Clean spinner nozzle with acetone and IPA and purge it 5 times. ✓
- (e) Spin 1 micron resist SPR 660L: 3200 rpm (setting 306) 35 sec ✓
- (f) Bake on hotplate 95 C for 60 sec with vacuum on. ✓
- (g) Expose on stepper: jb090428.MultisQUIDS.jdw (try1-3), jb090428.TestDie.jdw (try4) ✓
 - i. Reticles: B, BG, CAPS, Btest, BGtest, CAPStest ✓
 - ii. Layers 6, 7 & 8 "b", "caps", "bg" ✓
 - iii. Expose at 200 mJ/cm² ✓
- (h) Post-bake on hotplate 110 C for 60 sec with vacuum on. ✓
- (i) Spin-develop with MF-26A for 60 sec. ✓

2. Inspect under microscope: GOOD. 0.2 um S.DECUT

3. Etch Al using Trion etcher

- (a) If necessary, clean chamber with Clean10 recipe 0 min (10 min)
- (b) Use recipe kc Al vertical 40s
 - i. He press: 5.0 torr He flow: 2.0 sccm RIE power: 200 W
 - ii. Pressure: 30 torr Cl₂ flow: 10 sccm BCl₃ flow: 30 sccm
 - iii. 5 nm/s (100 nm/20 s)
 - iv. Passivate in DI water for 5 min ✓ SONICATE 2min AT 50V IN DI WATER ✓

4. Inspect under microscope: GOOD

5. Ultrasound at 70V "dirty" acetone (2 min), Ultrasound "clean" acetone (2 min), spray HEAVELY with ACETONE then IPA while spinning dry. ✓

6. Inspect under microscope: GOOD Record Over etch amount 0.2 um

7. Measure etched thickness using profilometer (100 nm): 94 nm

INSPECTED IN ~~SEM~~ SEM - EVERYTHING LOOKS GREAT, BUT SAW SOME FAINT "WORM" TRACES.

Date: 6/10/09

VIII. DEPOSIT INSULATOR (SiO₂)

1. Glue sapphire wafer onto "spider" wafer (skip this step if using Si wafer):
 - (a) Clean teflon chuck with acetone and IPA, blow dry ✓
 - (b) Mount teflon chuck and carefully place the sapphire wafer face (polished-side) down on the chuck (to spin resist on back of it). ✓
 - (c) Spin "glue" resist SPR 220-3, 2500 rpm, 35-sec (dispense manually). There should be no resist on the face of the sapphire wafer after spin. ✓
 - (d) Place the sapphire wafer, resist side down, onto a "spider" wafer with flats aligned, and push the edges together until the two are "glued" together. ✓
 - (e) Bake on hotplate 95 C for 10 min with vacuum on (sapphire face up) ✓
 - (f) Inspect sapphire wafer under microscope for surface cleanliness: GOOD, NO SCRATCHES
 - (g) Spin-clean the wafer with acetone and IPA to clean resist from the edges of the wafer. ✓

2. Ash 2:00 to make insulator stick better. ✓

3. Deposit Insulator using PlasmaQuest ECR:

- (a) Run process BIGCLEAN with the cleaning wafer in the machine. ✓
 - i. Is the chamber manometer zeroed? ✓
 - ii. Is the chamber being heated? ✓

(b) ~~Run dummy wafer to get microwaves tuned~~

(c) Load wafer and run your process SiO₂ RFeln (edit deposition time to deposit SiO₂ for ²³⁰~~200~~ sec)

Record the actual parameter values: RF Clean	Record the actual parameter values: SiO ₂ Deposition
O ₂ flow: <u>20</u> (20) sccm	O ₂ flow: <u>18.7</u> (18.4) sccm
Ar flow: <u>140.9</u> (139.0) sccm	Ar flow: <u>140.9</u> (139) sccm
SiH ₄ flow: <u>0</u> (0) sccm	SiH ₄ flow: <u>119.6</u> (118) sccm
Upper magnet I: <u>179.2</u> (185) A	Upper magnet I: <u>179.2</u> (185) A
Pressure: <u>15.1</u> (15) mTorr	Pressure: <u>15.1</u> (15) mTorr
RF power F: <u>30</u> (30) W	RF power F: <u>245</u> (240) W ^{245W}
R: <u>0</u> (0) W	R: <u>0</u> (0) W
Dc bias: <u>-200</u> (-200 to -300) V	Dc bias: <u>-309</u> (~-300) V
Microwave power F: <u>0</u> (0) W	Microwave power F: <u>724.2</u> (725) W
R: <u>0</u> (0) W	R: <u>7.3</u> (0) W
Backside He press: <u>2.4</u> (2.5) torr	Backside He press: <u>2.4</u> (2.5) torr
Backside He flow: <u>1.5</u> (<1.0) sccm	Backside He flow: <u>1.5</u> (<1.0) sccm
Clean time: <u>120</u> (120) sec	Deposition time: <u>230</u> (200) sec ²³⁰

4. ^{50V}Ultrasound at ~~70V~~ "dirty" acetone (1 min), separate wafers (skip this step if using Si wafer). ✓
5. ^{30V}Ultrasound at ~~70V~~ "dirty" acetone (2 min), Ultrasound "clean" acetone (2 min), spray HEAVELY with ACETONE then IPA while spinning dry. ✓
6. Inspect under microscope: (GOOD)

STOPPED HERE 6/10/09 7pm.

Date: 6/11/09

TRY 1

IX. PATTERN INSULATOR for JUNCTION JI LAYER

1. Pattern JI layer resist

- (a) Temperature: 68 °F (68°F) Humidity: 38 % (38%)
- (b) Spin HMDS at 3900 rpm (setting 390) for 35 sec ✓
- (c) Evacuate HMDS fumes from spinner/Bake on hotplate 95 C for 60 sec with vacuum on. ✓
- (d) Clean spinner nozzle with acetone and IPA and purge it 5 times. ✓
- (e) Spin 1 micron resist SPR 660L: 2200 rpm (setting 215) 35 sec ✓
- (f) Bake on hotplate 95 C for 60 sec with vacuum on. 210

2. Expose: jb090428.MultiSQUIDS.jdw (try1-3), endpoint, clearout, jb090428-TestDie.jdw (try4) ✓

- (a) Reticles: **J1, FLOOD, (ALIGN for clearout)** ✓ DID CLEAROUT
- (b) Layer 9 "ji" Try 1 (try1, try2, try3, try4, all)
- (c) Endpoint Layer 1 (1-7) try 1 (fy1, try2, try3, try4, wi, ie, all)
- (d) Exposure dose: 200 mJ/cm² ✓

3. Post-bake on hot plate 110 C for 60 sec with vacuum on ✓

4. Spin-develop in MF-26A for 70 sec (make sure settings are as they are labeled on the machine) ✓

5. Inspect under microscope: GOOD 6.1um² → 6.5um², 10um² → 9.8um²

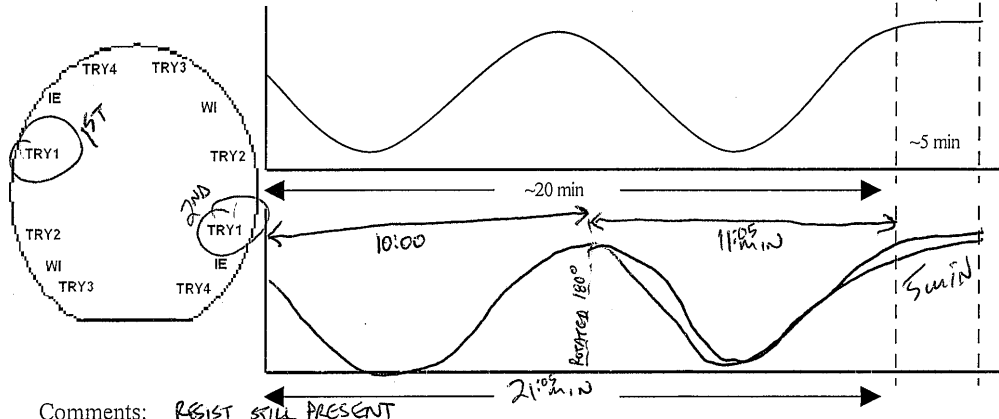
6. Condition Axic chamber by running sio2.prc for 0 (~20 min)

7. Etch through Insulator using AXIC. Use proper recipe (SiO2.prc)

- (a) Pump to base pressure $p = 6 \times 10^{-5}$ torr
- (b) Start etch and watch graph for wavy curve (see c).

(20 sccm O ₂)	<u>20.0</u>	(120 W(f))	<u>119</u>
(50 sccm CHF ₃)	<u>50.0</u>	(0 W(r))	<u>2</u>
(200 mtorr)	<u>103</u>	(-250 V)	<u>-250</u>
Time: (~25min)	<u>26</u>		

Sketch etch curve below and where the laser monitor was relative to the flat on the wfr:



Comments: RESIST STILL PRESENT

8. Strip resist:

- (a) Clean Asher without wafer: 50 sccm O₂ 50 W (subtract any offset) 3:00 min ✓
- (b) Use Asher with wafer: 50 sccm O₂ 50 W (subtract any offset) 3:00 min ✓
- (c) Ultrasound "dirty" acetone (3 min), Ultrasound "clean" acetone (3 min), spray HEAVELY with ACETONE then IPA while spinning dry. ✓

9. Inspect under microscope: GOOD, BUT TEST DIE 6.10um² HAD SOME PROBLEMS - JAGGED CRAP

10. Measure junction areas:

- i. SQUID: 7.58 um² (6.1um²) Qubit: 11.88 um² (10um²) Top: 11.79 um² (10um²)
- Bottom: 7.12 um² (6.1um²) Area = 0.82843 x²

11. Measure thickness with profilometer: 345um

Date: 6/11/09

T2Y1

X. OXIDIZE and DEPOSIT ALUMINUM JC LAYER

- Use recipe "shanejunction" Aim for 16.76 A/cm²
- Choose exposure using $Jc1/Jc2 = (E1/E2)^{-0.51}$ USE P=10 Torr, T=3864s
 - Oxidation from 1/21/09 gave 16.36 A/cm² using 10 Torr, 820s for a 9 um² junction
- Adjust the recipe for the proper exposure
 - Set oxidation time on program line 5310
 - Set oxidation pressure on program line 5260/5280. 1st Pressure: 9.09 2nd Pressure: 10.0
- Record parameters for each step:

RF clean:

Pressure: 0.8 mT (0.8 mT) Time: 360 s (360s)
 Forward power: 249 W (250 W) Reflected power: 0 W (0 W)
 Bias voltage: ~~740~~ V (740 V)

Oxidation:

Pressure: 10 Torr (~~5~~ Torr) Time: 3864 s (~~2484~~ s) Chiller: 18.0 °C (18.0°C)
Fill Time: 80 s

Al pre:

Pressure: 5.0 mT (5.0 mT) Voltage: 271 V (273 V)
 Power: 105 W (105 W) Time: 60 s (60 s)
 Current: 0.41 A (0.41 A)

Al dep:

Pressure: 5.0 mT (5.0 mT) Voltage: 272 V (274 V)
 Power: 106 W (106 W) Time: 1145 s (1145 s = 19:05 min)
 Current: 0.42 A (0.41 A)

Recipe steps: O₂ purge: 3350, RFclean: 1010, Cool: 2320, Oxidize: 5110, Film dep dwell: 6170

LOOKED @ 1 DIE IN SEM - JUNCTIONS LOOK GREAT

XI. PATTERN JC (Junction Conductor) LAYER

STOPPED HERE 6/11/09 5pm

1. Pattern JC-layer resist:

- Temperature: 68 °F (68°F) Humidity: 39 % (38%)
- Spin HMDS at 3900 rpm (setting 390) for 35 sec ✓
- Evacuate HMDS fumes from spinner/Bake on hotplate 95 C for 60 sec with vacuum on. ✓
- Clean spinner nozzle with acetone and IPA and purge it 5 times. ✓
- Spin 1 micron resist SPR 660L: 3200 rpm (setting 306) 35 sec ✓
- Bake on hotplate 95 C for 60 sec with vacuum on. ✓
- Expose: jb090428.MultiSQUIDS.jdw (try1-3), endpoint, jb090428.TestDie.jdw (try4)
 - Reticles: **JC, FLOOD, JCtest**
 - Layer 10 "jc" Try (try1) try2, try3, try4, all
 - Use "all" layer (7) on endpoint to remove Al covering future endpoints
 - Expose at 200 mJ/cm²
- Post-bake on hot plate 110 C for 60 sec with vacuum on. ✓
- Spin-develop with MF-26A for 60 sec. ✓

JC ON TRY 1 ONLY
FLOOD ON TRY 3,4
FORGOT TO DO ENDPOINTS

2. Inspect under microscope: RESIST MISHAPPEN, WILL WORK, 0.2um RESIST SIDE CUT

3. Etch Al using Trion etcher

- If necessary, clean chamber with **Clean10** recipe 0 min (10 min)
- Use recipe **kc_Al_vertical** 60s
 - He press: 5.0 torr He flow: 2.0 sccm RIE power: 200 W
 - Pressure: 30 torr Cl₂ flow: 10 sccm BCl₃ flow: 30 sccm
 - 5 nm/s (100 nm/20 s)
 - Passivate in DI water for 5 min ✓

HAD A HARD TIME TUNING, BUT WORKED.

4. Inspect under microscope: GOOD, NO RESIST REELED

5. Ultrasound at 50V "dirty" acetone (2 min), Ultrasound "clean" acetone (2 min), spray HEAVELY with ACETONE then IPA while spinning dry. ✓

6. Inspect under microscope: GOOD, SOME SINGLED EDGES, RESIST? Record Over etch amount 0.3um

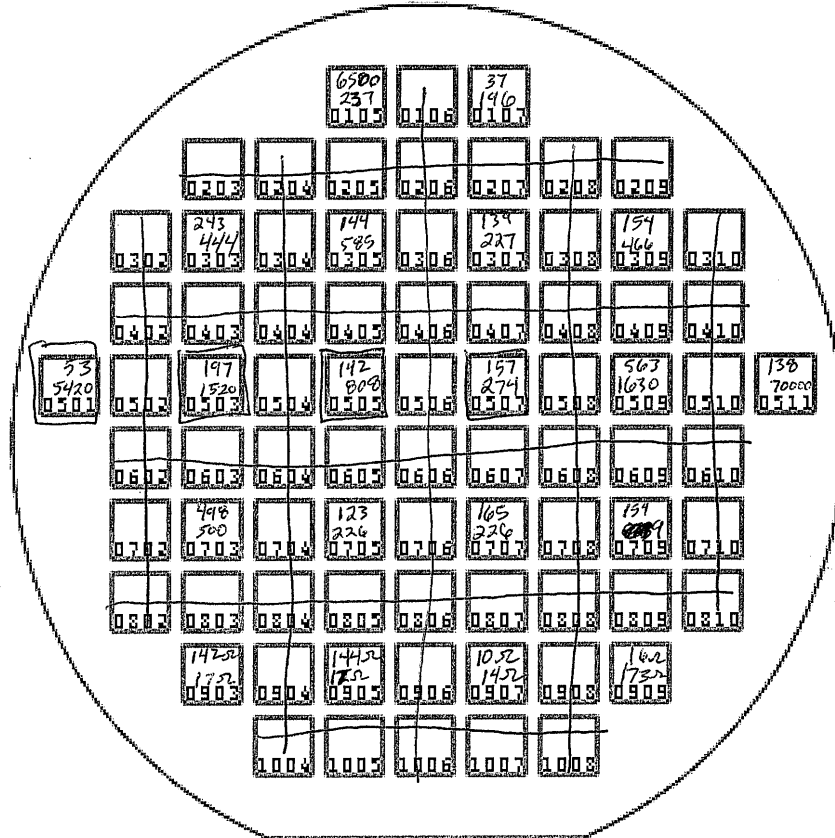
7. Measure etched thickness using profilometer (100 nm): 91um

8. Put on a thick layer of resist and shoot the test layer (using TEST reticle) to protect devices ✓

Date: 6/15/09

TR4 1

Record Resistance Measurements
Use lockin amplifier in volt lab



$$I_c = J_c A = (380 \pi) / (4 R_N) = 298.45 / R_N$$

Area (um ²)	Mean R (Ω)	Std dev (Ω)	Spread	N	I ₀	J ₀
10 (top)	145.64	11.36	7.8%	11	2.05 μA	17.33 A/cm ²
6.1 (bottom)	222.71	31.78	14.27%	7	1.34 μA	18.23 A/cm ²

After returning to the clean room:

1. Ultrasound at 50V "dirty" acetone (2 min), Ultrasound "clean" acetone (2 min), spray HEAVILY with ACETONE then IPA while spinning dry ✓
2. Ash wafer for 2 min at 50 W, 50 sec O₂

→ SHOT ENDPOINTS - ALL etched 40s in Cl etcher STRIPPED RESIST

STOPPED HERE 6/15/09 5pm

TRY 2

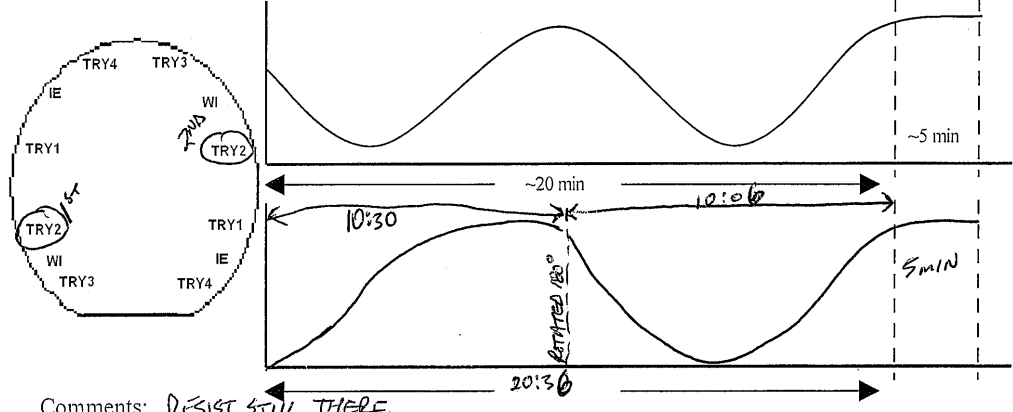
Date: 6/16/09

IX. PATTERN INSULATOR for JUNCTION JI LAYER

1. Pattern JI layer resist
 - (a) Temperature: 69 °F (68°F) Humidity: 36 % (38%)
 - (b) Spin HMDS at 3900 rpm (setting 390) for 35 sec ✓
 - (c) Evacuate HMDS fumes from spinner/Bake on hotplate 95 C for 60 sec with vacuum on. ✓
 - (d) Clean spinner nozzle with acetone and IPA and purge it 5 times. ✓
 - (e) Spin 1 micron resist SPR 660L: 2200 rpm (setting 215) 35 sec ✓
 - (f) Bake on hotplate 95 C for 60 sec with vacuum on. 210 ✓
2. Expose: jb090428.MultiSQUIDS.jdw (try1-3), endpoint, cleanup, jb090428.TestDie.jdw (try4)
 - (a) Reticles: JI, FLOOD, (ALIGN for cleanup)
 - (b) Layer 9 "ji" Try 2 (try1, try2, try3, try4, all) ✓
 - (c) Endpoint Layer (1-7) try 2 (try1, try2, try3, try4, wi, ie, all) ✓
 - (d) Exposure dose: 200 mJ/cm² ✓
3. Post-bake on hot plate 110 C for 60 sec with vacuum on ✓
4. Spin-develop in MF-26A for 70 sec (make sure settings are as they are labeled on the machine) ✓
5. Inspect under microscope: 60 GOOD
6. Condition Axic chamber by running sio2.prc for 0 (~20 min)
7. Etch through Insulator using AXIC. Use proper recipe (SiO2.prc) ✓
 - (a) Pump to base pressure p = 6x10⁻⁵ torr
 - (b) Start etch and watch graph for wavy curve (see c).

(20 sccm O ₂)	20.0	(120 W(f))	119
(50 sccm CHF ₃)	50.0	(0 W(r))	1
(200 mtorr)	103	(-250 V)	-250

Sketch etch curve below and where the laser monitor was relative to the flat on the wfr:



Comments: RESIST STILL THERE

8. Strip resist:
 - (a) Clean Asher without wafer: 50 sccm O₂ 50 W (subtract any offset) 3:00 min ✓
 - (b) Use Asher with wafer: 50 sccm O₂ 50 W (subtract any offset) 3:00 min ✓
 - (c) Ultrasound "dirty" acetone (3 min), Ultrasound "clean" acetone (3 min), spray HEAVILY with ACETONE then IPA while spinning dry. ✓
9. Inspect under microscope: GOOD; NO WEIRD JUNCTIONS SEEN
10. Measure junction areas:
 - i. SQUID: 8.043 um² (6.1um²) Qubit: 12.80 um² (10um²) Top: 12.7 um² (10um²)
Bottom: 8.12 um² (6.1um²) Area = 0.82843 x²
11. Measure thickness with profilometer: X

TRY 2

Date: 6/16/09

Page: 9-18

X. OXIDIZE and DEPOSIT ALUMINUM JC LAYER

- Use recipe "shanejunction"
- Choose exposure using $Jc1/Jc2 = (E1/E2)^{-0.51}$
 - Oxidation from ~~1/21709~~ gave 16.36 A/cm² using 10 Torr, ~~820s~~ ^{600s} for a 776 μ m² junction (286 Ω , $I_c = 1.0455 \mu$ A)
- Adjust the recipe for the proper exposure
 - Set oxidation time on program line 5310 \rightarrow 4577s
 - Set oxidation pressure on program line 5260/5280. 1st Pressure: 9.09 Torr 2nd Pressure: 10.0 Torr
- Record parameters for each step:

RF clean:
 Pressure: 1.0 mT (0.8 mT) Time: 360 s (360s)
 Forward power: 249 W (250 W) Reflected power: 0 W (0 W)
 Bias voltage: 730 V (740 V)

Oxidation:
 Pressure: 10 Torr (10 Torr) Time: 4577 s (4577 s) Chiller: 18.0 °C (18.0 °C)
 O₂ Fill Time: 89 s

Al pre:
 Pressure: 5.0 mT (5.0 mT) Voltage: 271 V (273 V)
 Power: 105 W (105 W) Time: 60 s (60 s)
 Current: 0.41 A (0.41 A)

Al dep:
 Pressure: 5.0 mT (5.0 mT) Voltage: 271 V (274 V)
 Power: 106 W (106 W) Time: 1145 s (1145 s = 19:05 min)
 Current: 0.42 A (0.41 A)

Recipe steps: O₂ purge: 3350, RFclean: 1010, Cool: 2320, Oxidize: 5110, Film dep dwell: 6170

XI. PATTERN JC (Junction Conductor) LAYER

- Pattern JC-layer resist:
 - Temperature: 68 °F (68 °F) Humidity: 36 % (38%)
 - Spin HMDS at 3900 rpm (setting 390) for 35 sec ✓
 - Evacuate HMDS fumes from spinner/Bake on hotplate 95 C for 60 sec with vacuum on. ✓
 - Clean spinner nozzle with acetone and IPA and purge it 5 times. ✓
 - Spin 1 micron resist SPR 660L: 3200 rpm (setting 306) 35 sec ✓
 - Bake on hotplate 95 C for 60 sec with vacuum on. ✓
 - Expose: jb090428.MultisQUIDS.jdw (try1-3), endpoint, jb090428.TestDie.jdw (try4)
 - Reticles: JC, FLOOD, JCtest
 - Layer 10 "jc" Try (try1, try2, try3, try4, all)
 - Use "all" layer (7) on endpoint to remove Al covering future endpoints
 - Expose at 200 mJ/cm²
 - Post-bake on hotplate 110 C for 60 sec with vacuum on. ✓
 - Spin-develop with MF-26A for 60 sec. ✓
- Inspect under microscope: CRAPPY, STRIPED RESIST IN A FEW AREAS SONICATE 2min & RE SHOT AT 230 mJ/cm²
- Etch Al using Trion etcher
 - If necessary, clean chamber with Clean10 recipe 10 min (10 min)
 - Use recipe kc_Al_vertical 40 s
 - He press: 5.0 torr He flow: 2.0 sccm RIE power: 200 W
 - Pressure: 30 torr Cl₂ flow: 10 sccm BCl₃ flow: 30 sccm
 - 5 nm/s (100 nm/20 s)
 - Passivate in DI water for 5 min ✓ SONICATE @ 50V 2min in H₂O
- Inspect under microscope: _____
- Ultrasound at 50V "dirty" acetone (2 min), Ultrasound "clean" acetone (2 min), spray HEAVELY with ACETONE then IPA while spinning dry. ✓
- Inspect under microscope: Good Record Over etch amount 0.3
- Measure etched thickness using profilometer (100 nm): 95 nm
- Put on a thick layer of resist and shoot the test layer (using TEST reticle) to protect devices DIDN'T DO

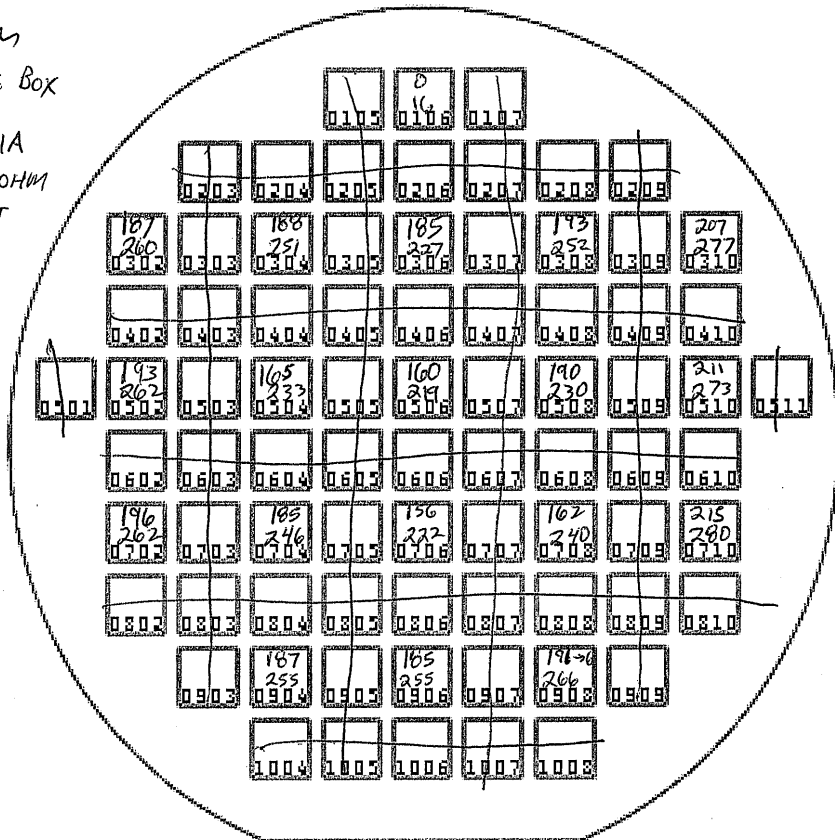
Date: 6/16/09

TR 2

Record Resistance Measurements

Use lockin amplifier in volt lab

DID IN
CLEANROOM
W/ DIODE BOX
& HP 34401A
SET TO KOHM
W/ 3 DIGIT
PRECISION



$$I_c = J_c A = (380 \pi) / (4 R_N) = 298.45 / R_N$$

Area (um ²)	Mean R (Ω)	Std dev (Ω)	Spread	N	I ₀	J ₀
10 (top)	186.44	16.71	8.96%	18	1.60 μA	12.55 A/cm ²
6.1 (bottom)	250.56	18.68	7.46%	18	1.19 μA	14.72 A/cm ²

NOMINAL RATIOS

$$\frac{A_{10}}{A_{6.1}} = \frac{10}{6.1} = 1.639, \quad \frac{R_{6.1}}{R_{10}} = \frac{260}{149} = 1.745$$

MEASURED RATIOS

$$\frac{A_{10}}{A_{6.1}} = 1.578, \quad \frac{R_{6.1}}{R_{10}} = 1.344$$

After returning to the clean room:

NEXT TIME MAKE THE 10 μm² JUNCTION 10.4 μm²

- No resist so I SKIPPED THESE
1. Ultrasound at 50V "dirty" acetone (2 min), Ultrasound "clean" acetone (2 min), spray HEAVILY in xic with ACETONE then IPA while spinning dry
 2. Ash wafer for 2 min at 50 W, 50 sccm O₂

FINISHED HERE 6/16/09 8pm

TRY 384

Date: 6/10/09

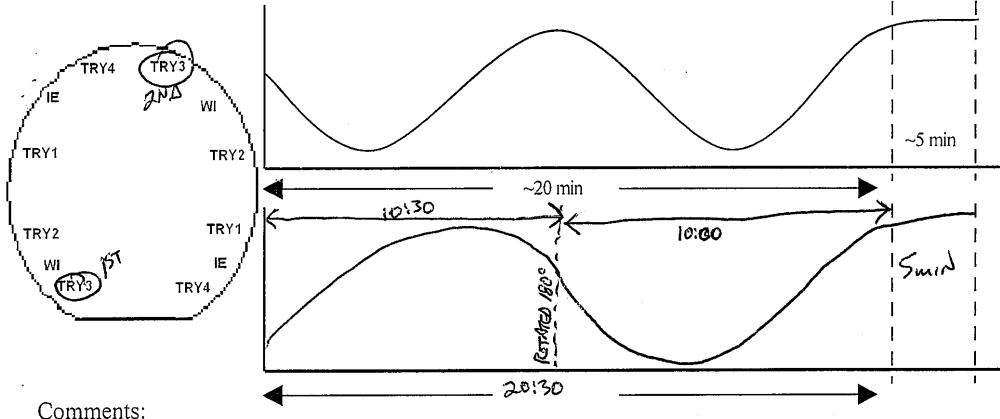
Page: 8-18

IX. PATTERN INSULATOR for JUNCTION JI LAYER

- Pattern JI layer resist
 - Temperature: 60 °F (68°F) Humidity: 37 % (38%)
 - Spin HMDS at 3900 rpm (setting 390) for 35 sec ✓
 - Evacuate HMDS fumes from spinner/Bake on hotplate 95 C for 60 sec with vacuum on. ✓
 - Clean spinner nozzle with acetone and IPA and purge it 5 times. ✓
 - Spin 1 micron resist SPR 660L: 2200 rpm (setting 215) 35 sec ✓
 - Bake on hotplate 95 C for 60 sec with vacuum on. ✓
- Expose: jb090428.MultiSQUIDs.jdw (try1-3), endpoint, ~~clearout~~, jb090428.TestDie.jdw (try4)
 - Reticles: JI, FLOOD, (ALIGN for clearout) N2 CLEAROUT
 - Layer 9 "ji" Try 384 (try1, try2, try3, try4, all)
 - Endpoint Layer (1-7) TRYS (try1, try2, try3, try4, wi, ie, all)
 - Exposure dose: 200 mJ/cm² ✓
- Post-bake on hot plate 110 C for 60 sec with vacuum on ✓
- Spin-develop in MF-26A for 70 sec (make sure settings are as they are labeled on the machine) ✓
- Inspect under microscope: Good - Took PICS
- Condition Axic chamber by running sio2.prc for 0 (~20 min) SHANE DID SIO2.PRC (WIT) RIGHT BEFORE ME.
- Etch through Insulator using AXIC. Use proper recipe (SiO2.prc)
 - Pump to base pressure $p = 8 \times 10^{-5}$ torr ✓
 - Start etch and watch graph for wavy curve (see c).

(20 sccm O ₂)	<u>20.0</u>	(120 W(f))	<u>119</u>
(50 sccm CHF ₃)	<u>50.0</u>	(0 W(r))	<u>2</u>
(200 mtorr)	<u>103</u>	(-250 V)	<u>-250</u>
Time: (~25min)	<u>25:30</u>		

Sketch etch curve below and where the laser monitor was relative to the flat on the wfr:



Comments:

- Strip resist:
 - Clean Asher without wafer: 50 sccm O₂ 50 W (subtract any offset) 3:00 min ✓
 - Use Asher with wafer: 50 sccm O₂ 50 W (subtract any offset) 3:00 min ✓
 - Ultrasound "dirty" acetone (3 min), Ultrasound "clean" acetone (3 min), spray HEAVELY with ACETONE then IPA while spinning dry. ✓
- Inspect under microscope: Good
- Measure junction areas:
 - SQUID: 8.26 um² (6.1um²) Qubit: 12.50 um² (10um²) Top: 12.47 um² (10um²)
Bottom: 6.24 um² (6.1um²) Area = 0.82843 x²
- Measure thickness with profilometer: X

TRY 3d4

Date: 6/18/09

X. OXIDIZE and DEPOSIT ALUMINUM JC LAYER

1. Use recipe "shanejunction"
2. Choose exposure using $Jc1/Jc2 = (E1/E2)^{-0.51}$
 - (a) Oxidation from 1/21/09 gave 16.36 A/cm² using 10 Torr, 820s for a 9 um² junction
3. Adjust the recipe for the proper exposure
 - (a) Set oxidation time on program line 5310
 - (b) Set oxidation pressure on program line 5260/5280. 1st Pressure: 9.09 2nd Pressure: 10.0
4. Record parameters for each step:

RF clean:

Pressure: 1.0 mT (~~0.8~~ mT) Time: 360 s (360s)
 Forward power: 249 W (250 W) Reflected power: 0 W (0 W)
 Bias voltage: 730 V (~~740~~ V)

Oxidation:

Pressure: 10 Torr (~~5~~ Torr) Time: 3591 s (~~2484~~ s) Chiller: 18.1 °C (18.0°C)
 O₂ Fill Time: 88 s

Al pre:

Pressure: 5.0 mT (5.0 mT) Voltage: 270 V (273 V)
 Power: 105 W (105 W) Time: 60 s (60 s)
 Current: 0.41 A (0.41 A)

Al dep:

Pressure: 5.0 mT (5.0 mT) Voltage: 271 V (274 V)
 Power: 106 W (106 W) Time: 1145 s (1145 s = 19:05 min)
 Current: 0.42 A (0.41 A)

Recipe steps: O₂ purge: 3350, RFclean: 1010, Cool: 2320, Oxidize: 5310, Film dep dwell: 6170

XI. PATTERN JC (Junction Conductor) LAYER

1. Pattern JC-layer resist:

- (a) Temperature: 69 °F (68°F) Humidity: 35 % (38%)
- (b) Spin HMDS at 3900 rpm (setting 390) for 35 sec ✓
- (c) Evacuate HMDS fumes from spinner/Bake on hotplate 95 C for 60 sec with vacuum on. ✓
- (d) Clean spinner nozzle with acetone and IPA and purge it 5 times. ✓
- (e) Spin 1 micron resist SPR 660L: 3200 rpm (setting 308) 35 sec ✓
- (f) Bake on hotplate 95 C for 60 sec with vacuum on. ✓
- (g) Expose: jb090428.MultisQUIDS.jdw (try1-3), endpoint, jb090428.TestDie.jdw (try4)
 - i. Reticles: JC, FLOOD, JCtest ✓
 - ii. Layer 10 "jc" Try 1-3 (try1, try2, try3, try4, all) ✓
 - iii. Use "all" layer (7) on endpoint to remove Al covering future endpoints ✓
 - iv. Expose at 200 mJ/cm² ✓
- (h) Post-bake on hot plate 110 C for 60 sec with vacuum on. ✓
- (i) Spin-develop with MF-26A for 60 sec. ✓

TRY 1, 2, 3 - JC
TRY 4 - JCtest

2. Inspect under microscope: GOOD, ~0.2 um SIDE CUT

3. Etch Al using Trion etcher

- (a) If necessary, clean chamber with Clean10 recipe 0 min (10 min)
- (b) Use recipe kc_Al vertical 40 s
 - i. He press: 5.0 torr He flow: 2.0 sccm RIE power: 200 W
 - ii. Pressure: 30 torr Cl₂ flow: 10 sccm BCl₃ flow: 30 sccm
 - iii. 5 nm/s (100 nm/20 s)
 - iv. Passivate in DI water for 5 min ✓

SONICATE SDV 2min in DI H₂O ✓

4. Inspect under microscope: GOOD

5. Ultrasound at 50V "dirty" acetone (2 min), Ultrasound "clean" acetone (2 min), spray HEAVELY with ACETONE then IPA while spinning dry. ✓

6. Inspect under microscope: GOOD Record Over etch amount 0.2 um

7. Measure etched thickness using profilometer (100 nm): 95nm

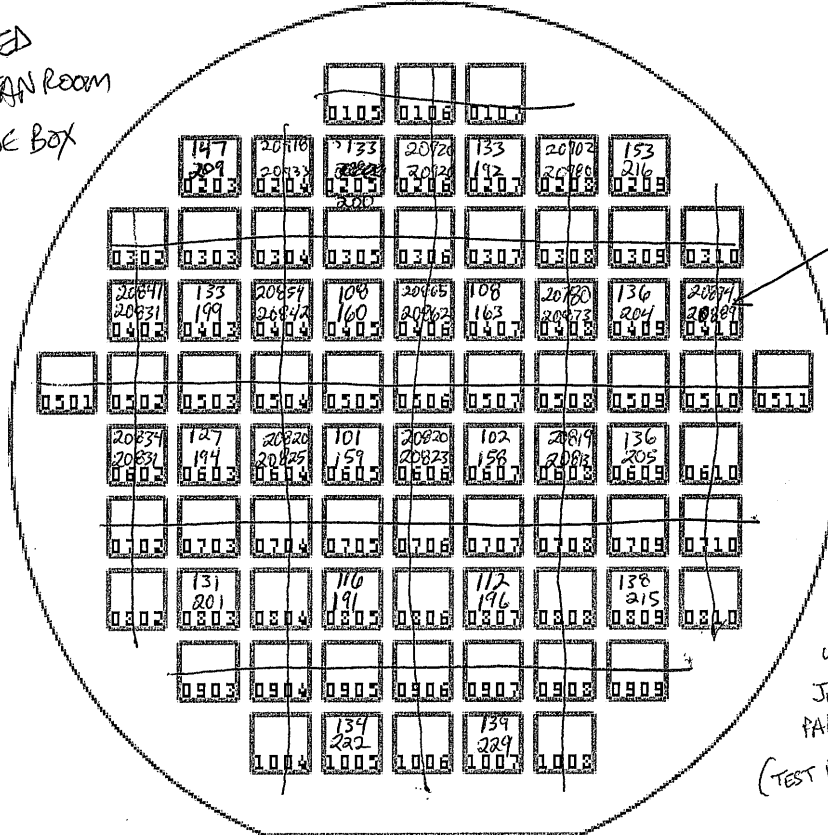
8. Put on a thick layer of resist and shoot the test layer (using TEST reticle) to protect devices DIDN'T DO

TRY 3 & 4

Date: 6/18/09

Record Resistance Measurements
Use lockin amplifier in volt lab

MEASURED
IN CLEAN ROOM
w/ DIODE BOX



I FORGOT TO
HAVE JI
LAYER CUT
THROUGH
TEST PADS!
RE MEASURE
TRY 4 WC
AFTER ~~ETCH~~
ETCH,
ALSO, NEED
WC TO CONNECT
JUNCTIONS TO
PADS FOR TRY 4
(TEST DIE)

3591s

$$I_c = J_c A = (380 \pi) / (4 R_N) = 298.45 / R_N$$

Area (um ²)	Mean R (Ω)	Std dev (Ω)	Spread	N	I ₀	J ₀
10 (top)	127.06	15.43	12.14%	18	2.35 μA	18.81 A/cm ²
6.1 (bottom)	195.17	21.86	11.20%	18	1.53 μA	18.54 A/cm ²

After returning to the clean room:

- Don't do {
1. Ultrasound at 50V "dirty" acetone (2 min), Ultrasound "clean" acetone (2 min), spray HEAVELY with ACETONE then IPA while spinning dry
 2. Ash wafer for 2 min at 50 W, 50 sccm O₂

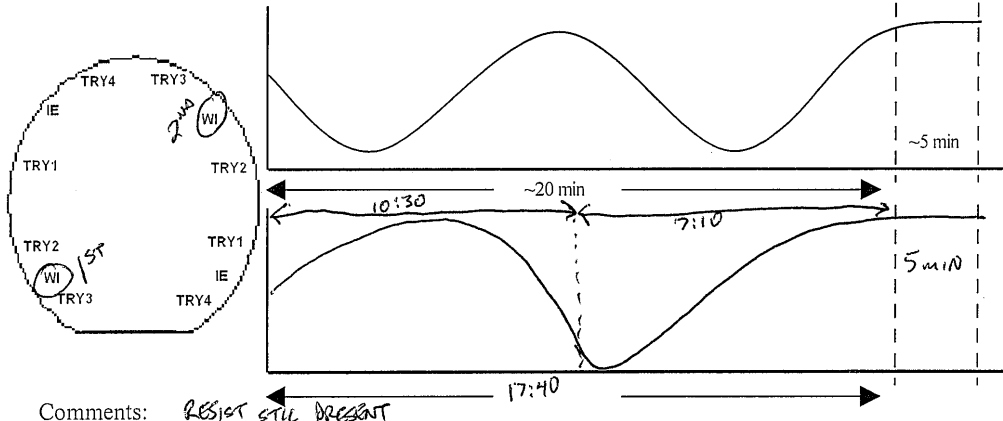
Date: 6/18/09

XII. PATTERN WI (Wiring Insulator) LAYER

1. Pattern WI layer resist
 - (a) Temperature: 69 °F (68°F) Humidity: 35 % (38%)
 - (b) Spin HMDS at 3900 rpm (setting 390) for 35 sec ✓
 - (c) Evacuate HMDS fumes from spinner/Bake on hotplate 95 C for 60 sec with vacuum on. ✓
 - (d) Clean spinner nozzle with acetone and IPA and purge it 5 times. ✓
 - (e) Spin 1 micron resist SPR 660L: 2200 rpm (setting 215) 35 sec ✓
 - (f) Bake on hotplate 95 C for 60 sec with vacuum on. 210
2. Expose: **jb090428.MultisQUIDs.jdw** (try1-3), **endpoint** (wi), **jb090428.TestDie.jdw** (try4) ✓
 - (a) Reticles: **WI, FLOOD, WItest** ✓
 - (b) Layer 11 "wi" Try 1-4 (try1, try2, try3, try4, all) ✓ TRY 1-3 → WI
TRY 4 → WItest
 - (c) Endpoint layer wi (5) ✓
 - (d) Exposure dose: 200 mJ/cm² ✓
3. Post-bake on hot plate 110 C for 60 sec with vacuum on ✓
4. Spin-develop in MF-26A for 60 sec (make sure settings are as they are labeled on the machine) ✓
5. **Inspect** under microscope: Good
6. **Condition** chamber by running **SiO2.prc** for 0 (20 min)
7. **Etch** through Insulator using AXIC. Use proper recipe (**SiO2.prc**) ✓
 - (a) Pump to base pressure $p = 8 \times 10^{-5}$ torr ✓
 - (b) Start etch and watch graph for wavy curve.

(20 sccm O ₂)	<u>20.0</u>	(120 W(f))	<u>119</u>
(50 sccm CHF ₃)	<u>50.0</u>	(0 W(r))	<u>2</u>
(100 mtorr)	<u>103</u>	(-250 V)	<u>-250</u>

Sketch etch curve below and where the laser monitor was relative to the flat on the wfr:



Comments: Resist still present

8. **Inspect** under microscope: _____
9. **Strip resist**:
 - (a) Clean Asher without wafer: 50 sccm O₂ 50 W (subtract any offset) 3:00 min INAS LAST
 - (b) Use Asher with wafer: 50 sccm O₂ 50 W (subtract any offset) 3:00 min ✓ USER
 - (c) Ultrasound at 50V "dirty" acetone (3 min), Ultrasound "clean" acetone (3 min), spray HEAVELY with ACETONE then IPA while spinning dry. ✓
10. **Inspect** under microscope: Good
11. **Measure** etched thickness using profilometer: 170

Date: 6/18/09

Page: 12-18

XIII. DEPOSIT ALUMINUM for WC Layer

1. Run process "shaneBLayer".
2. Record parameters for each step:

RF clean:

Pressure: 15.0 mT (15 mT) Time: 360 s (360s)
Forward power: 110 W (110 W) Reflected power: 0 W (0 W)
Bias voltage: 282 V (380 V)

Al pre:

Pressure: 5.0 mT (5.0 mT) Voltage: 270 V (273 V)
Power: 109 W (105 W) Time: 60 s (60 s)
Current: 0.42 A (0.41 A)

Al dep:

Pressure: 5.0 mT (5.0 mT) Voltage: 271 V (274 V)
Power: 106 W (106 W) Time: 1142 s (1142 s = 19:02 min)
Current: 0.42 A (0.41 A)

STOPPED HERE 8:00pm 6/18/09

XIV. PATTERN WC (Wiring Conductor) LAYER

1. Pattern WC-layer resist:

- (a) Temperature: 70 °F (68°F) Humidity: 36 % (38%)
- (b) Spin HMDS at 3900 rpm (setting 390) for 35 sec ✓
- (c) Evacuate HMDS fumes from spinner/Bake on hotplate 95 C for 60 sec with vacuum on. ✓
- (d) Clean spinner nozzle with acetone and IPA and purge it 5 times. ✓
- (e) Spin 1 micron resist SPR 660L: 3200 rpm (setting 306) 35 sec ✓
- (f) Bake on hotplate 95 C for 60 sec with vacuum on. ✓
- (g) Expose: jb090428.MultiSQUIDS.jdw (try1-3), endpoint (all), jb090428.TestDie.jdw (try4) ✓
 - i. Reticles: WC, FLOOD, WCtest ✓ TRY 1-3 → WC
 - ii. Layer 12 "wc" Try 344 (try1, try2, try3, try4, all) ✓ TRY 4 → WCtest
 - iii. Use "all" layer (7) on endpoint to remove Al covering future endpoints ✓
 - iv. Expose at 200 mJ/cm² ✓
- (h) Post-bake on hot plate 110 C for 60 sec with vacuum on. ✓
- (i) Spin-develop with MF-26A for 60 sec. ✓

2. Inspect under microscope: GOOD, 0.2 um RESIST SIDE CUT

3. Etch Al using Trion etcher

- (a) If necessary, clean chamber with Clean10 recipe 10 min (10 min)
- (b) Use recipe kc_Al vertical 30s ← VERY FAST THIS TIME (USUALLY 40s)
 - i. He press: 5.0 torr He flow: 2.0 sccm RIE power: 200 W
 - ii. Pressure: 30 torr Cl₂ flow: 10 sccm BCl₃ flow: 30 sccm
 - iii. 5 nm/s (100 nm/20 s)
 - iv. Passivate in DI water for 5 min ✓ SONICATE @ 50W 2min in DI H₂O ✓

4. Inspect under microscope: GOOD

5. Ultrasound at 50V "dirty" acetone (2 min), Ultrasound "clean" acetone (2 min), spray HEAVELY with ACETONE then IPA while spinning dry.

6. Inspect under microscope: GOOD, BUT LOTS OF WORMS Record Over etch amount 0.2 um

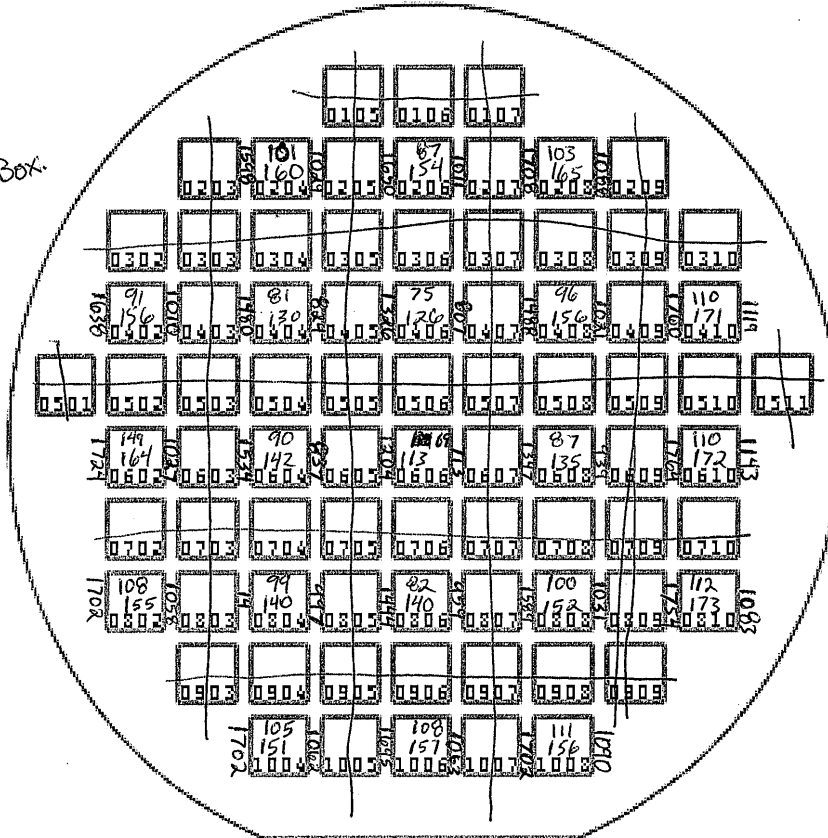
7. Measure etched thickness using profilometer (100 nm): 91nm

Date: 6/19/09

TRY4

Record Resistance Measurements
Use lockin amplifier in volt lab

Did in
CLEAN ROOM
WITH DIODE BOX



$$I_c = J_c \cdot A = (380 \pi) / (4 R_N) = 298.45 / R_N$$

Area (um ²)	Mean R (Ω)	Std dev (Ω)	Spread	N	I ₀	J ₀
19.10 (top)	96.25	12.88	13.4%	20	3.10 μA	
8.1 (bottom)	150.86	15.81	10.5%	21	1.98 μA	
190.0 μm ² (10x19 μm ²)	995.76	112.67	11.3%	21	0.304 A (3.00 μA/10)	
100.0 μm ² (10x10 μm ²)	1590.45	161.78	10.2%	20	0.188 μA (1.88 μA/10)	

After returning to the clean room:

- MINUT Do
1. **Ultrasound** at 50V "dirty" acetone (2 min), Ultrasound "clean" acetone (2 min), spray HEAVELY with ACETONE then IPA while spinning dry
 2. Ash wafer for 2 min at 50 W, 50 sccm O₂

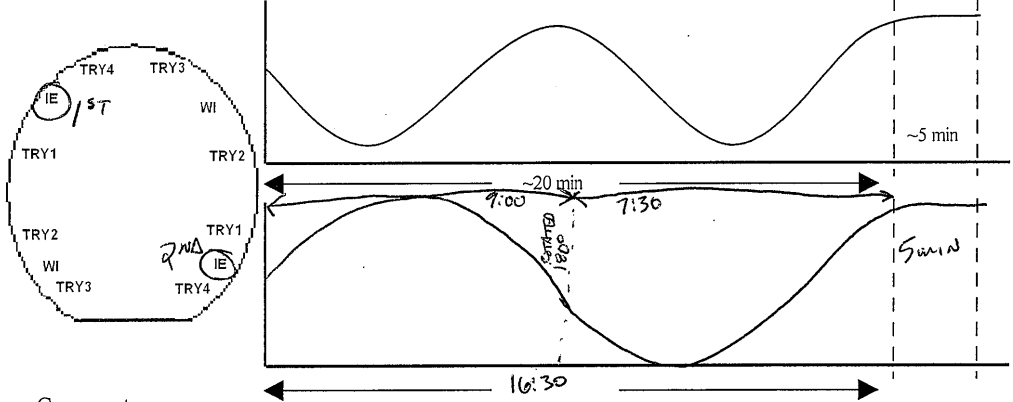
Date: 6/19/09

XV. PATTERN IE (Insulator Etch) LAYER

1. **Pattern IE** layer resist
 - (a) Temperature: 69 °F (68°F) Humidity: 35 % (38%)
 - (b) Spin HMDS at 3900 rpm (setting 390) for 35 sec ✓
 - (c) Evacuate HMDS fumes from spinner/Bake on hotplate 95 C for 60 sec with vacuum on. ✓
 - (d) Clean spinner nozzle with acetone and IPA and purge it 5 times. ✓
 - (e) Spin 1 micron resist SPR 660L: 2200 rpm (setting 215/210) 35 sec ✓
 - (f) Bake on hotplate 95 C for 60 sec with vacuum on. ✓
2. Expose: **jb090428.MultiSQUIDS.jdw** (try1-3), **endpoint (ie)**, **jb090428.TestDie.jdw** (try4) ✓
 - (a) Reticles: **IE, FLOOD, IEtest**
 - (b) Layer 13 "ie" Try (try1, try2, try3, try4), all TRY 1-3 IE
 - (c) Endpoint layer "ie" (6) TRY 4 IEtest
 - (d) Exposure dose: 200 mJ/cm² ✓
3. Post-bake on hot plate 110 C for 60 sec with vacuum on ✓
4. Spin-develop in MF-26A for 60 sec (make sure settings are as they are labeled on the machine) ✓
5. **Inspect** under microscope: A LITTLE OVERDEVELOPED. NEXT TIME USE 250 mJ/cm² (0.8 um step)
6. **Condition** chamber by running **sio2.prc** for 0 (20 min)
7. **Etch** through Insulator using AXIC. Use proper recipe (**sio2.prc**) ✓
 - (a) Align beam (8-12 V) ✓
 - (b) Pump to base pressure $p = 6 \times 10^{-3}$ torr ✓
 - (c) Start etch and watch graph for wavy curve.

(20 sccm O ₂)	<u>20.0</u>	(120 W(f))	<u>119</u>
(50 sccm CHF ₃)	<u>50.0</u>	(0 W(r))	<u>2</u>
(200 mtorr)	<u>103</u>	(-250 V)	<u>-250</u>

Sketch etch curve below and where the laser monitor was relative to the flat on the wfr:



Comments:

GRASS IN CENTER, NO GRASS ON EDGES, WHAT?

8. **Inspect** under microscope:
9. **Strip resist:**
 - (a) Clean Asher without wafer: 50 sccm O₂ 50 W (subtract any offset) 3:00 min ✓
 - (b) Use Asher with wafer: 50 sccm O₂ 50 W (subtract any offset) 3:00 min ✓
 - (c) Ultrasound at 50V "dirty" acetone (3 min), Ultrasound "clean" acetone (3 min), spray HEAVELY with ACETONE then IPA while spinning dry. ✓
10. **Inspect** under microscope: 6.0 um Overetch: 0.6 - TOP
11. **Measure** etched thickness using profilometer: Bottom: 230 nm RIGHT: 219 nm
MIDDLE: 220 nm LEFT: 226
TOP: 230 nm 0.3 - BOTTOM
12. **Inspect** metal surface with SEM - are there goobers?

Date: 6/19/04

XVI. PATTERN TOP HOLE GRADIENT TT LAYER

1. Pattern TT-layer resist:
 - (a) Temperature: 69 °F (68°F) Humidity: 34 % (38%)
 - (b) Spin HMDS at 3900 rpm (setting 390) for 35 sec ✓
 - (c) Evacuate HMDS fumes from spinner/Bake on hotplate 95 C for 60 sec with vacuum on. ✓
 - (d) Clean spinner nozzle with acetone and IPA and purge it 5 times. ✓
 - (e) Spin 1 micron resist SPR 660L: 3200 rpm (setting 306) 35 sec
 - (f) Bake on hotplate 95 C for 60 sec with vacuum on.
 - (g) Expose: jb090428.MultiSQUIDS.jdw (try1-3), endpoint (all); jb090428.TestDie.jdw (try4)
 - i. Reticles: TT ✓
 - ii. Layer 14 "tt" Try ALL (try1, try2, try3, try4, all) ✓ 360
 - iii. Vary focus around -0.4 (Δ=0.2) with Exposure at ~~260~~ (Δ=20) mJ/cm² ✓
 Process Test Batch – Focus/Exposure Matrix Mode ✓
 Center die is at 0606, adding (subtracting) exposure delta for each column to the right (left) ✓
 Adding (subtracting) focus delta for each row down (up) ✓
 - (h) Post-bake on hot plate 110 C for 60 sec with vacuum on. ✓
 - (i) Spin-develop with MF-26A for 60 sec. ✓
2. **Inspect** under microscope: ALL OF THEM LOOK GOOD, BUT THE SAME.
3. **Etch** Al using Trion etcher
 - (a) If necessary, clean chamber with Clean10 recipe 0 min (10 min)
 - (b) Use recipe kc_Al_vertical 40s
 - i. He press: 5.0 torr He flow: 2.0 sccm RIE power: 200 W
 - ii. Pressure: 30 torr Cl₂ flow: 10 sccm BCl₃ flow: 30 sccm
 - iii. 5 nm/s (100 nm/20 s)
 - iv. Passivate in DI water for 5 min ✓ SONICATE 2min @ 50V in DI H₂O ✓
4. **Inspect** under microscope: SOME RESIST PEELLED UP FROM H₂O SONICATION
5. **ULTRASOUND** at 50V "dirty" acetone (2 min), Ultrasound "clean" acetone (2 min), spray HEAVELY with ACETONE then IPA while spinning dry. ✓
6. **Inspect** under microscope: GOOD, THOUGH THEY ALL LOOK THE SAME Record Over etch amount _____

XVII. PATTERN TH (Top Holes) LAYER

1. Pattern TH-layer resist:
 - (a) Temperature: 69 °F (68°F) Humidity: 39 % (38%)
 - (b) Spin HMDS at 3900 rpm (setting 390) for 35 sec ✓
 - (c) Evacuate HMDS fumes from spinner/Bake on hotplate 95 C for 60 sec with vacuum on. ✓
 - (d) Clean spinner nozzle with acetone and IPA and purge it 5 times. ✓
 - (e) Spin 1 micron resist SPR 660L: 3200 rpm (setting 306) 35 sec ✓
 - (f) Bake on hotplate 95 C for 60 sec with vacuum on. ✓
 - (g) Expose: jb090428.MultiSQUIDS.jdw (try1-3), jb090428.TestDie.jdw (try4)
 - i. Reticles: TH, TH test
 - ii. Layer 15 "th" Try 1-4 (try1, try2, try3, try4, all) → TH → TRY 1-3
 - iii. Expose at 360 mJ/cm² and Focus -0.4 → TH test → TRY 4
 - (h) Post-bake on hot plate 110 C for 60 sec with vacuum on. ✓
 - (i) Spin-develop with MF-26A for 60 sec. ✓
2. **Inspect** under microscope: GOOD
3. **Etch** Al using Trion etcher
 - (a) If necessary, clean chamber with Clean10 recipe 0 min (10 min)
 - (b) Use recipe kc_Al_vertical 40s
 - i. He press: 5.0 torr He flow: 2.0 sccm RIE power: 200 W
 - ii. Pressure: 30 torr Cl₂ flow: 10 sccm BCl₃ flow: 30 sccm
 - iii. 5 nm/s (100 nm/20 s)
 - iv. Passivate in DI water for 5 min ✓ SONICATE @ 50V 2min in DI H₂O ✓
4. **Inspect** under microscope: GOOD

Date: 6/19/09

5. **Ultrasound** at 50V "dirty" acetone (2 min), Ultrasound "clean" acetone (2 min), spray HEAVELY with ACETONE then IPA while spinning dry. ✓

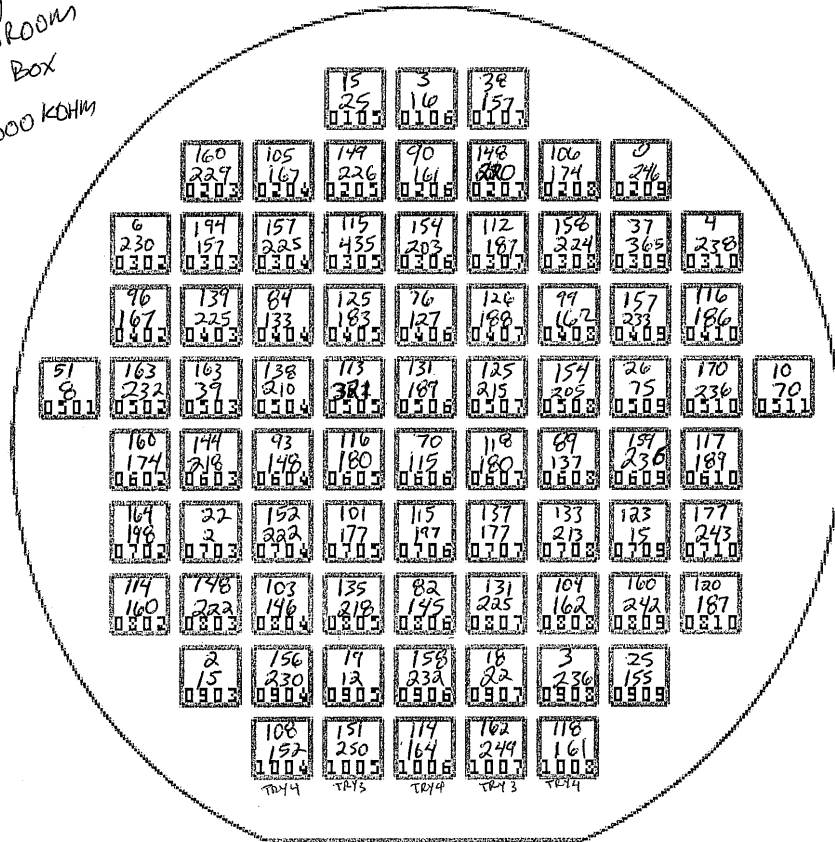
6. **Inspect** under microscope: GOOD Record Over etch amount _____

7. **Put** on a thick layer of resist and shoot the test layer (using TEST reticle) to protect devices DIDN'T DO

Final Resistance Measurements

~~Use lockin amplifier in volt lab~~

USED DMM
IN CLEANROOM
w/ Diode Box
ON 000.000 KOHM
RANGE



$$I_c = J_c A = (380 \pi) / (4 R_N) = 298.45 / R_N$$

Area (um ²)	Mean-R (Ω)	Std dev (Ω)	Spread	N	I ₀	J ₀
10 (top)						
6.1 (bottom)						

After returning to the clean room:

1. **Ultrasound** wafer at 50V in acetone 2 min x2.
2. **Ash** wafer for 2 min at 50 W, 50 sccm O₂

STOPPED HERE 6/19/09 6 PM

Date: 6/22/09

XVIII. DICE WAFER

1. Spin protective layer of resist:
 - (a) Temperature: 70 °F (68°F) Humidity: 43 % (38%) ✓
 - (b) Spin HMDS at 3900 rpm (setting 390) for 35 sec ✓
 - (c) ~~Evacuate HMDS fumes from spinner/Bake on hotplate 95 C for 60 sec with vacuum on.~~ SKIPPED
 - (d) ~~Clean spinner nozzle with acetone and IPA and purge it 5 times.~~
 - (e) Spin 1 micron resist SPR 660L: 2200 rpm (setting 215) 35 sec ✓
 - (f) Bake on hotplate 95 C for 60 sec with vacuum on. ✓
2. Dice wafer on a dicing saw using resinoid blade and parameters: 060/246/246/8/35/90/100/3000/3/24000/499/
 (or if using Si wafer use Si blade and parameters: 010/246/246/8/35/90/200/3000/1798)
 ACCIDENTALLY CUT THROUGH COLUMN 03.

XVIII. DEFINE CAPACITOR SUPPORT POSTS BY DRY ETCHING

6/25/09

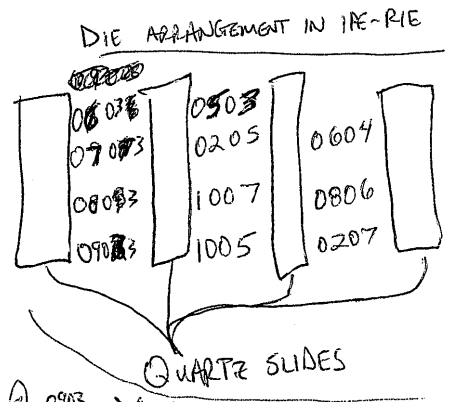
1. Strip resist on a spinner with acetone and IPA from individual chips to be processed further.
 - (a) Prepare several extra dies as some will be needed for etch calibration check. ✓
2. Etch
 - (a) You can either use IPE RIE SF6 etch to remove sacrificial layer and make posts, or use XeF2 dry chemical etcher.
 - (b) **If using IPE RIE SF6 etch (it will heat the whole chip):**
 - (c) Precondition machine by running plasma for 5-10 min without chips, process ksf6.prc NOTE: SHAME WAS LAST USER w/ KCSF6.PRC
 - (d) Run process ksf6.prc to etch SiN

CHF ₃	<u>0</u> (0) sccm	Power f:	<u>100</u> (100)W,
SF ₆	<u>100.1</u> (100) sccm	r:	<u>0</u> (0)W
press:	<u>197</u> (200) mTorr	Voltage:	<u>-18</u> (-20)V

 Total etch time _____ (25)min
 - (e) Remove top plate by either:
 - i. Dip the chip in 48-49 deg. C transine until top layer etches away, and look at it under optical microscope to determine if the posts are small enough. Repeat the RIE etching step as many times as needed.
 - ii. Use Kapton/double sided tape to peel off top capacitor plate
 - (f) **Inspect** under microscope: _____
 - (g) **Repeat** until all the insulator is gone from under the capacitor plate

ALL HAVE VISUAL w/ RESIST -> A

GOOD RESISTANCES	(149)	(260)	(785)	RANK	
	10	6.1	19		
1005	151	250	-	1	} ETCH THESE
1007	162	249	-	2	
0805	135	218	-	6	
0807	131	225	-	5	
0205	149	226	-	3	} ETCH THESE
0207	148	220	-	4	
0806	145	-	82	1	} ETCH THESE
0604	148	-	93	2	
0404	133	-	84	3	
0206	161	-	90	4	



20 min → looked @ 0603 → 15 min → looked @ 0903 → 15 min → looked @ 0503 → ...
 → 10 min → looked @ 0703
 SEM → looked @ 1007 & 0806 AFTER WARMING FROM COOL-DOWN
IVb
 0404 - 6 min
 0404 - 10 min
 0404 - 14 min
 0404 - 18 min
 0404 - 20 min

Date: 6/24/09

VISUAL
XIX. FINAL ASSESMENT (w/ RESIST STILL ON)

MOST DIES HAVE SUPPARE TABS LEFT FROM DICING

ALL DIES HAVE
LOTS OF DEBRIS FROM
BREAKING STREETS

DIES THROUGH
COLUMN

			A 0105	A 0106	B-TEST IS SCRATCH 0107					
	F 0203	A 0204	A 0205	A 0206	A 0207	A 0208	A 0209			
A 0302	F 0303	A 0304	A 0305	A 0306	A 0307	A 0308	A 0309	A 0310		
A 0402	F 0403	A 0404	A 0405	B-TEST? IS SCRATCH 0406	A 0407	B-TEST IS SCRATCH 0408	A 0409	A 0410		
A 0501	A 0502	F 0503	C-SCRAPE? 0504	A 0505	A 0506	A 0507	A 0508	A 0509	A 0510	C-2 SCRATCHES? 0511
A 0602	F 0603	A 0604	A 0605	A 0606	A 0607	A 0608	A 0609	A 0610		
A 0702	F 0703	A 0704	A 0705	B-TEST IS SCRATCH 0706	A 0707	A 0708	A 0709	A 0710		
A 0802	F 0803	A 0804	A 0805	A 0806	A 0807	A 0808	A 0809	A 0810		
	F 0903	A 0904	A 0905	B-TEST IS SCRATCH 0906	A 0907	A 0908	A 0909			
		A 1004	A 1005	A 1006	A 1007	B-TEST SCRATCH? 1008				

Mark imperfections on chart and record dies/dates when checked out in log book!

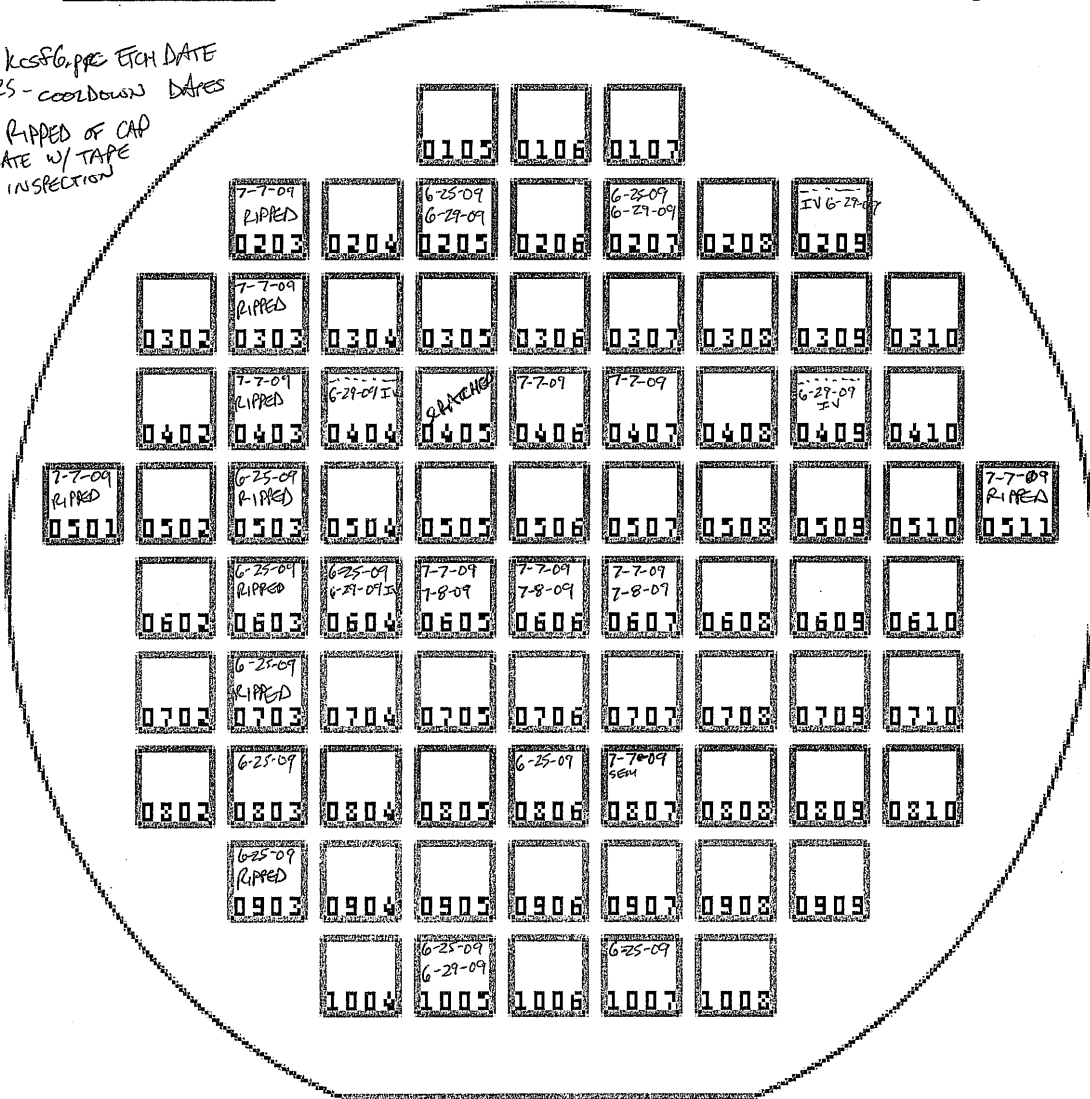
- A: Perfect!
- B: Okay, some imperfections
- C: Don't use if you don't have to
- D: Crap
- F: Government Use Only!

ETCH/COOLDOWN RECORD

Date: _____

Page: 18-18

TOP - KCSFG, PRE ETCH DATE
 OTHERS - COOLDOWN DATES
 RIPPED = RIPPED OFF CAP
 TOP PLATE W/ TAPE
 FOR INSPECTION



Mark imperfections on chart and record dies/dates when checked out in log book!

- A: Perfect!
- B: Okay, some imperfections
- C: Don't use if you don't have to
- D: Crap
- F: Government Use Only!

TRAY 1 AREAS (OPTICAL)

DIE	TEST 6.1um ²	SQUID (6.1um ²)	TEST 10um ²	QUBIT (10um ²)
0105	6.57	7.95	11.17	11.21
0105				
0501	7.73 (screwed up)	7.61	12.52	12.52
0505	6.57 (screwed up)	6.53	11.52	11.79
0511	7.57	7.90	12.56 (screwed up?)	12.67
0905	7.15	7.92	11.17	11.20
AVERAGE:	7.12	7.58	11.79	11.88

AVERAGE:

$$7.35 \text{ um}^2$$

$$11.83 \text{ um}^2$$

J_c NEEDED:

$$J_c = \frac{1.22 \mu\text{A}}{7.35 \text{ um}^2} = 16.60 \text{ A/cm}^2$$

$$\frac{2.0 \mu\text{A}}{11.83 \text{ um}^2} = 16.91 \text{ A/cm}^2$$

$$\text{AVE } J_c \text{ NEEDED} = 16.76 \text{ A/cm}^2$$

J_I -8484.9x
 SYMBOL @ -13664.1y
 COLUMN 07?

J_c SEM QUBIT

10um²: 3.66 um Dia → 11.10 um² → 100 nA → 3.86 um → 12.34 um²
 6.92 um² → 100 nA → 3.09 um → 7.91 um²
 $\frac{3.298.55}{\cos 25} =$
 TEST 6.1um²: 2.90 um Dia → 7.14 um² → 100 nA → 3.10 um → 7.96 um²

SHANE'S 4-21-09 OXIDATION:

10 Torr, 6000s

$$A = 7.76 \mu\text{m}^2$$

$$R = 286 \Omega$$

$$I_c = 1.0435 \mu\text{A}$$

$$J_c = 13.45 \text{ A/cm}^2$$

I WANT 20 A/cm² ← NOMINAL

$$\frac{J_1}{J_2} = \sqrt{\frac{E_2}{E_1}}$$

$$J_1 = 13.45 \text{ A/cm}^2$$

$$J_2 = 20 \text{ A/cm}^2$$

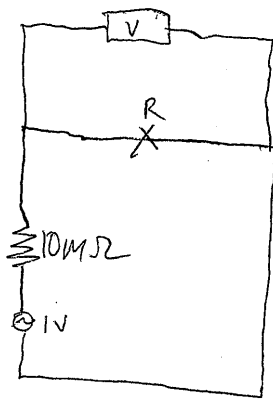
$$E_1 = 60000$$

$$E_2 = \frac{J_1^2 E_1}{J_2^2} = \frac{(13.45)^2 60000}{20^2} = 27135$$

USING MEASURED AREAS I WANT 16.76 A/cm²

$$E_2 = \frac{(13.45)^2 60000}{(16.76)^2} = \frac{180.9025 \cdot 60000}{280.8976} = 38641$$

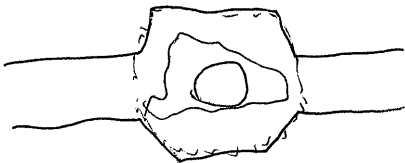
SO USE P = 10 Torr, T = 3864s



$$I = \frac{1V}{10M\Omega} = 10^{-7}A = 0.1\mu A$$

$$R = \frac{V}{I} = \frac{1V}{10^{-7}A} = 10^7\Omega = 10M\Omega$$

$$R = 10V_{\mu V}$$



TRY 2 ETCHED AREAS (OPTICALLY)

DIE	TEST (6.1 μm^2)	SQUID (6.1)	QUBIT (10)	TEST (10.1 μm^2)
0106	7.73	8.24	12.52	12.52
0502	7.57	7.88	12.87	12.56
0506	7.90	7.73	11.95	13.06
0510	8.69	8.69	13.99	12.52
0906	8.73	7.61	12.67	12.87

AVG: $\frac{8.12 + 8.03}{2} = 8.08 \mu\text{m}^2$ $\frac{12.80 + 12.71}{2} = 12.75 \mu\text{m}^2$

J_c needed: $\frac{1.22 \mu\text{A}}{8.08 \mu\text{m}^2} = 15.10 \text{ A/cm}^2$ $\frac{2.0 \mu\text{A}}{12.75 \mu\text{m}^2} = 15.69 \text{ A/cm}^2$

J_c AVG: 15.40 A/cm^2

$E_2 = \frac{J_1^2 E_1}{J_2^2} = \frac{(13.45)^2 \cdot 60000}{(15.40)^2} = \frac{180.9025 \cdot 60000}{237.16} = 45767$

USE $P = 10 \text{ TORR}$, $t = 4577s$

FROM SHANG,
4-21-09
OXIDATION

<u>DIE</u>	<u>TEST (6.1)</u>	<u>SQUID(6.1)</u>	<u>QUBIT(10)</u>	<u>TEST(10)</u>
0205	7.61	7.92	12.52	12.85
0403	8.74	7.61	12.56	11.28
0406	—	—	12.56	13.14 ← TEST DIE (NO 6.1)
0409	7.57	8.82	12.52	12.56

1007	<u>9.04</u>	<u>8.69</u>	<u>12.34</u>	<u>12.52</u>
AVG:	8.24	8.26	12.50	12.47
AVG:	8.25		12.49	

$$J_c \text{ NEEDED: } \frac{1.22 \mu\text{A}}{8.25 \mu\text{m}^2} = 14.79 \text{ A/cm}^2 \quad \frac{2.0 \mu\text{A}}{12.49 \mu\text{m}^2} = 16.02 \text{ A/cm}^2$$

$$\text{AVG } J_c = 15.40 \text{ A/cm}^2$$

From TRY 2, $J_c = 13.64 \text{ A/cm}^2$ w/ $E = 45770$

$$E_2 = \frac{J_1^2 E_1}{J_2^2} = \frac{(13.64 \text{ A/cm}^2)^2 \cdot 45770}{(15.40)^2} = 35906$$

SO USE P=10 Torr, $t = 3591 \text{ s}$

DOWNSTAIRS FRIDGE

DIE 0806 - TO COMPARE VAC GAP QUBIT TO IDC QUBIT, ONLY CONNECTED
FLUX & SQUID LINES ~~10/11/12~~

UPSTAIRS FRIDGE

DIE 1005 - ALL PORTS BONDED,

DIE 0205 - ALL WIRINGS BONDED, SQUID BIAS & 1 FLUX BONDED

DIE 0207 - ALL WIRINGS BONDED, SQUID BIAS & 1 FLUX BONDED

INs

DIE 0209 - $6.1 \mu\text{m}^2$ - SLOT 3 - BOARD LINES ~~9 & 10~~ 9 & 10

DIE 0409 - $10 \mu\text{m}^2$ - SLOT 4 - BOARD LINES 11 & 12

DIE 0404 - $19 \mu\text{m}^2 \times 10$ - SLOTS - BOARD LINES 13 & 14

DIE 0604 - $10 \mu\text{m}^2 \times 10$ - SLOT 6 - BOARD LINES 16 & 17

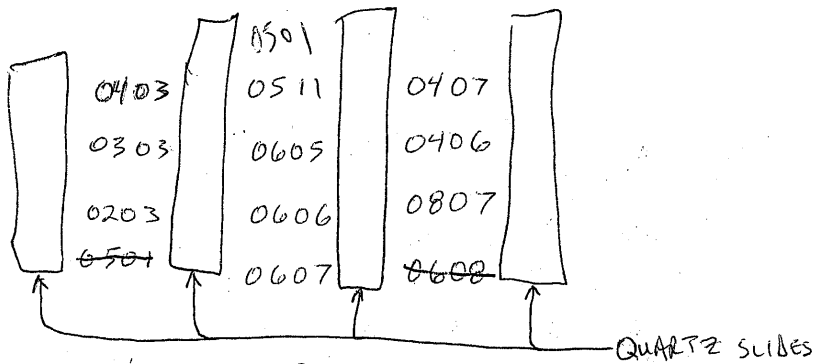
NG A - SLOT 1 - BOARD LINES 3 & 4

NG B - SLOT 2 - BOARD LINES 6 & 7

7/7/89 - PREP DEVICES FOR NEXT COOLDOWN:

ETCH TESTS	DEVICES
0403	0605
0303	0606 ← TEST DIE
0203	0607
0501	0407
0511	0406 ← TEST DIE
	0409 SCRATCHED
	0807 (EV)
	0608 (EV)

- 1) IPA/ACETONE SPIN,
- 2) 18 MIN 50 W 500cm ASH
- 3) KCSF6.pfc



Time	TOTAL	looked @	COMMENT
20 min	20 min	0403	NOT MUCH ETCHED
20 min	40 min	0303	ALMOST TO POSTS (0303 FLIPPED OVER DURING THIS ETCH.)
20 min	60 min	0501, 0303	A FEW POSTS STILL HAVE STUFF ^{NEAR} THEM. ←
10 min	70 min	0511	A FEW POSTS STILL HAVE JUNK AROUND THEM, BUT LESS THAN

LOOKED @ SEM OF 0807 TO CHECK THAT BIAS LINES STILL HAVE INSULATOR UNDER THEM. THEY DO.

BOMBED

- 0607 - u₅IN, u₅OUT, u_QIN, u_QOUT, S, F
- 0605 - u₅IN, u₅OUT, u_QIN, u_QOUT, S, F
- 0606 - u₅, u₅, FI, SI, SB, SV, FV, FSS, SS, SSV, FSV
- THRU - u₅, u₅. Al on Si.

7-21-09

GOOD RESISTANCES

- 0407 - 126, 188 Ω ETCHED 7-7 \rightarrow USE
- 0406 - 76, 127 Ω TEST ETCHED 7-7 \rightarrow USE
- 0405 - 125, 183 Ω \leftarrow ~~DON'T ETCH!~~ SCRATCHED
- 0408 - 79, 162 Ω TEST ~~SCRATCHED~~ \leftarrow USE UNETCHED SCRATCHED
- 0608 - 89, 137 Ω TEST \leftarrow USE UNETCHED
- 0805 - 135, 218 Ω \leftarrow USE UNETCHED
- 0804 - 103, 146 Ω TEST

Bibliography

- [1] A. TONOMURA, J. ENDO, T. MATSUDA, AND T. KAWASAKI. **Demonstration of single-electron buildup of an interference pattern.** *American Journal of Physics*, **57**:117, 1989. [1](#)
- [2] FUJIO SHIMIZU. **Double-slit interference with ultracold metastable neon atoms.** *Physical Review A*, **46**:R17, 1992. [1](#)
- [3] O. CARNAL AND J. MLYNEK. **Young’s Double-Slit Experiment with Atoms: A Simple Atom Interferometer.** *Physical Review Letters*, **66**:2689, 1991. [1](#)
- [4] S. DÜRR, T. NONN, AND G. REMPE. **Origin of quantum-mechanical complementarity probed by a ‘which-way’ experiment in an atom interferometer.** *Nature*, **395**:33, 1998. [1](#)
- [5] P. BERTET, S. OSNAGHI, A. RAUSCHENBEUTEL, G. NOGUES, A. AUFFEVEES, M. BRUNE, J. M. RAIMOND, AND S. HAROCHE. **A complementarity experiment with an interferometer at the quantum-classical boundary.** *Nature*, **411**:166, 2001. [1](#)
- [6] RICHARD P. FEYNMAN. **Simulating Physics with Computers.** *International Journal of Theoretical Physics*, **21**:467, 1982. [2](#)
- [7] DAVID P. DIVINCENZO. **The Physical Implementation of Quantum Computation.** *Fortschritte der Physik*, **48**:771, 2000. [2](#), [11](#), [20](#)
- [8] LIEVEN M. K. VANDERSYPEN, MATTHIAS STEFFEN, GREGORY BREYTA, COSTANTINO S. YANNONI, MARK H. SHERWOOD, AND ISAAC L. CHUANG. **Experimental realization of Shor’s quantum factoring algorithm.** *Nature*, **414**:883, 2001. [2](#)
- [9] D. HANNEKE, J. P. HOME, J. D. JOST, J. M. AMINI, D. LEIBFRIED, AND D. J. WINELAND. **Realization of a programmable two-qubit quantum processor.** *Nature Physics*, **6**:13, 2010. [2](#)
- [10] C. OSPELKAUS, U. WARRING, Y. COLOMBE, K. R. BROWN, J. M. AMINI, D. LEIBFRIED, AND D. J. WINELAND. **Microwave quantum logic gates for trapped ions.** *Nature*, **476**:181, 2011. [2](#)
- [11] PASCAL BÖHI, MAX F. RIEDEL, JOHANNES HOFFFROGGE, JAKOB REICHEL, THEODOR W. HÄNSCH, AND PHILIPP TREUTLEIN. **Coherent manipulation of Bose-Einstein condensates with state-dependent microwave potentials on an atom chip.** *Nature Physics*, **5**:592, 2009. [2](#)

- [12] MARCO ANDERLINI, PATRICIA J. LEE, BENJAMIN L. BROWN, JENNIFER SEBBY-STRABLEY, WILLIAM D. PHILLIPS, AND J. V. PORTO. **Controlled exchange interaction between pairs of neutral atoms in an optical lattice.** *Nature*, **448**:452, 2007. [2](#)
- [13] ALBERTO POLITI, JONATHAN C. F. MATTHEWS, AND JEREMY L. O'BRIEN. **Shor's Quantum Factoring Algorithm on a Photonic Chip.** *Science*, **325**:1221, 2009. [2](#)
- [14] DAVID PRESS, THADDEUS D. LADD, BINGYANG ZHANG, AND YOSHIHISA YAMAMOTO. **Complete quantum control of a single quantum dot spin using ultrafast optical pulses.** *Nature*, **456**:218, 2008. [2](#)
- [15] L. DICARLO, J. M. CHOW, J. M. GAMBETTA, LEV S. BISHOP, B. R. JOHNSON, D. I. SCHUSTER, J. MAJER, A. BLAIS, L. FRUNZIO, S. M. GIRVIN, AND R. J. SCHOELKOPF. **Demonstration of two-qubit algorithms with a superconducting quantum processor.** *Nature*, **460**:240, 2009. [3](#)
- [16] ERIK LUCERO, R. BARENDS, Y. CHEN, J. KELLY, M. MARIANTONI, A. MEGRANT, P. O'MALLEY, D. SANK, A. VAINSENER, J. WENNER, T. WHITE, Y. YIN, A. N. CLELAND, AND JOHN M. MARTINIS. **Computing prime factors with a Josephson phase qubit quantum processor.** *Nature Physics*, **8**:719, 2012. [3](#)
- [17] MARKUS ANSMANN, H. WANG, RADOSLAW C. BIALCZAK, MAX HOFHEINZ, ERIK LUCERO, M. NEELEY, A. D. O'CONNELL, D. SANK, M. WEIDES, A. N. CLELAND, AND JOHN M. MARTINIS. **Violation of Bell's inequality in Josephson phase qubits.** *Nature*, **461**:504, 2009. [3](#)
- [18] V. BOUCHIAT, D. VION, P. JOYEZ, D. ESTEVE, AND M. H. DEVORET. **Quantum coherence with a Single Cooper Pair.** *Physica Scripta*, **T76**:165, 1998. [4](#)
- [19] Y. NAKAMURA, YU. A. PASHKIN, AND J. S. TSAI. **Coherent control of macroscopic quantum states in a single-Cooper-pair box.** *Nature*, **398**:786, 1999. [4](#)
- [20] SIYUAN HAN, R. ROUSE, AND J. E. LUKENS. **Observation of Cascaded Two-Photon-Induced Transitions between Fluxoid States of a SQUID.** *Physical Review Letters*, **84**:1300, 2000. [4](#)
- [21] JONATHAN R. FRIEDMAN, VIJAY PATEL, W. CHEN, S. K. TOLPYGO, AND J. E. LUKENS. **Quantum superposition of distinct macroscopic states.** *Nature*, **406**:43, 2000. [4](#)
- [22] JOHN M. MARTINIS, S. NAM, J. AUMENTADO, AND C. URBINA. **Rabi Oscillations in a Large Josephson-Junction Qubit.** *Physical Review Letters*, **89**:117901, 2002. [4](#), [79](#)
- [23] A. WALLRAFF, D.I. SCHUSTER, A. BLAIS, L. FRUNZIO, J. MAJER, M.H. DEVORET, S.M. GIRVIN, AND R.J. SCHOELKOPF. **Approaching Unit Visibility for Control of a Superconducting Qubit with Dispersive Readout.** *Physical Review Letters*, **95**:060501, 2005. [6](#), [61](#)
- [24] YI YIN, H. WANG, M. MARIANTONI, RADOSLAW C. BIALCZAK, R. BARENDS, Y. CHEN, M. LENANDER, ERIK LUCERO, M. NEELEY, A.D. O'CONNELL, D. SANK, M. WEIDES, J. WENNER, T. YAMAMOTO, J. ZHAO, A.N. CLELAND, AND JOHN M. MARTINIS. **Dynamic quantum Kerr effect in circuit quantum electrodynamics.** *Physical Review A*, **85**:023826, 2012. [6](#)

- [25] JOHN M. MARTINIS, K.B. COOPER, R. MCDERMOTT, MATTHIAS STEFFEN, MARKUS ANSMANN, K.D. OSBORN, K. CİCAK, SEONGSHIK OH, D.P. PAPPAS, R. W. SIMMONDS, AND CLARE C. YU. **Decoherence in Josephson Qubits from Dielectric Loss.** *Physical Review Letters*, **95**:210503, 2005. [9](#), [13](#), [111](#)
- [26] HANHEE PAIK, D.I. SCHUSTER, LEV S. BISHOP, G. KIRCHMAIR, G. CATELANI, A.P. SEARS, B.R. JOHNSON, M.J. REAGOR, L. FRUNZIO, L.I. GLAZMAN, S.M. GIRVIN, M.H. DEVORET, AND R.J. SCHOELKOPF. **Observation of High Coherence in Josephson Junction Qubits Measured in a Three-Dimensional Circuit QED Architecture.** *Physical Review Letters*, **107**:240501, 2011. [9](#), [145](#)
- [27] MICHEL H. DEVORET AND JOHN M. MARTINIS. **Implementing Qubits with Superconducting Integrated Circuits.** *Quantum Information Processing*, **3**(1):1–41, 2004. [10](#)
- [28] R. SHANKAR. *Principles of Quantum Mechanics*. Plenum Press, 2nd edition, 1994. [10](#)
- [29] THEODORE VAN DUZER AND CHARLES W. TURNER. *Principles of Superconductive Devices and Circuits*. Prentice Hall, 2nd edition, 1999. [13](#), [14](#), [15](#)
- [30] R.W. SIMMONDS, K.M. LANG, D.A. HITE, S. NAM, D.P. PAPPAS, AND JOHN M. MARTINIS. **Decoherence in Josephson Phase Qubits from Junction Resonators.** *Physical Review Letters*, **93**(7):077003, 2004. [13](#)
- [31] M.S. ALLMAN, F. ALTOMARE, J.D. WHITTAKER, K. CİCAK, D. LI, A. SIROIS, J. STRONG, J.D. TEUFEL, AND R.W. SIMMONDS. **Time-Domain Detection of Weakly Coupled TLS Fluctuators in Phase Qubits**, 2010. [14](#), [124](#)
- [32] MICHEL H. DEVORET, JOHN M. MARTINIS, DANIEL ESTEVE, AND JOHN CLARKE. **Resonant Activation from the Zero-Voltage State of a Current-Biased Josephson Junction.** *Physical Review Letters*, **53**(13):1260, 1984. [14](#), [36](#)
- [33] T.A. FULTON AND L.N. DUNKLEBERGER. **Lifetime of the zero-voltage state in Josephson tunnel junctions.** *Physical Review B*, **9**(11):4760, June 1974. [14](#)
- [34] MARKUS ANSMANN. *Benchmarking the Superconducting Josephson Phase Qubit: The Violation of Bell's Inequality*. PhD thesis, University of California Santa Barbara, 2009. [18](#), [93](#)
- [35] MICHAEL SHANE ALLMAN. *Coherent Tunable Coupling of Quantum Circuits*. PhD thesis, University of Colorado, 2011. [18](#), [80](#), [90](#), [95](#)
- [36] ALEXANDRE BLAIS, REN-SHOU HUANG, ANDREAS WALLRAFF, S.M. GIRVIN, AND R.J. SCHOELKOPF. **Cavity quantum electrodynamics for superconducting electrical circuits: An architecture for quantum computation.** *Physical Review A*, **69**:062320, 2004. [21](#), [27](#)
- [37] JENS KOCH, TERRI M. YU, JAY GAMBETTA, A.A. HOUCK, D.I. SCHUSTER, J. MAJER, ALEXANDRE BLAIS, M.H. DEVORET, S.M. GIRVIN, AND R.J. SCHOELKOPF. **Charge-insensitive qubit design derived from the Cooper pair box.** *Physical Review A*, **76**:042319, 2007. [22](#), [23](#), [29](#), [30](#), [31](#)

- [38] A. WALLRAFF, D.I. SCHUSTER, A. BLAIS, L. FRUNZIO, R.-S. HUANG, J. MAJER, S. KUMAR, S.M. GIRVIN, AND R.J. SCHOELKOPF. **Strong coupling of a single photon to a superconducting qubit using circuit quantum electrodynamics.** *Nature*, **431**:162, 2004. [25](#)
- [39] J. MAJER, J. M. CHOW, J. M. GAMBETTA, JENS KOCH, B. R. JOHNSON, J. A. SCHREIER, L. FRUNZIO, D. I. SCHUSTER, A. A. HOUCK, A. WALLRAFF, A. BLAIS, M. H. DEVORET, S. M. GIRVIN, AND R. J. SCHOELKOPF. **Coupling superconducting qubits via a cavity bus.** *Nature*, **449**:443, 2007. [25](#), [61](#)
- [40] MIKA A. SILLANPÄÄ, JAE I. PARK, AND RAYMOND W. SIMMONDS. **Coherent quantum state storage and transfer between two phase qubits via a resonant cavity.** *Nature*, **449**:438–442, September 2007. [25](#), [61](#)
- [41] F. ALTOMARE, J.I. PARK, K. CİCAK, M.A. SILLANPÄÄ, M.S. ALLMAN, D. LI, A. SIROIS, J.A. STRONG, J.D. WHITTAKER, AND R.W. SIMMONDS. **Tripartite interactions between two phase qubits and a resonant cavity.** *Nature Physics*, **6**:777, 2010. [25](#), [78](#), [110](#)
- [42] T. WIRTH, J. LISENFELD, A. LUKASHENKO, AND A.V. USTINOV. **Microwave readout scheme for a Josephson phase qubit.** *Applied Physics Letters*, **97**:262508, 2010. [25](#)
- [43] SERGE HAROCHE AND JEAN-MICHEL RAIMOND. *Exploring the quantum*. Oxford University Press, first edition, 2006. [26](#), [31](#), [52](#)
- [44] FREDERICK W. STRAUCH. **Quantum logic gates for superconducting resonator qubits.** *Physical Review A*, **84**:052313, 2011. [29](#)
- [45] MAXIME BOISSONNEAULT, J.M. GAMBETTA, AND A. BLAIS. **Improved qubit bifurcation readout in the straddling regime of circuit QED.** *Physical Review A*, **86**:022326, 2012. [30](#)
- [46] E.M. PURCELL. **Spontaneous Emission Probabilities at Radio Frequencies.** *Physical Review*, **69**:681, 1946. [31](#)
- [47] A.A. HOUCK, J.A. SCHREIER, B.R. JOHNSON, J.M. CHOW, JENS KOCH, J.M. GAMBETTA, D.I. SCHUSTER, L. FRUNZIO, M.H. DEVORET, S.M. GIRVIN, AND R.J. SCHOELKOPF. **Controlling the Spontaneous Emission of a Superconducting Transmon Qubit.** *Physical Review Letters*, **101**:080502, 2008. [31](#)
- [48] A.O. CALDEIRA AND A.J. LEGGETT. **Quantum Tunnelling in a Dissipative System.** *Annals of Physics*, **149**:374, 1983. [36](#)
- [49] MICHAEL A. NIELSEN AND ISAAC L. CHUANG. *Quantum Computation and Quantum Information*. Cambridge University Press, 1st edition, 2000. [38](#)
- [50] J.J. SAKURAI. *Modern quantum mechanics*. Addison-Wesley Publishing Company, Inc., revised edition, 1994. [39](#)
- [51] JOHN M. MARTINIS, S. NAM, J. AUMENTADO, AND K.M. LANG. **Decoherence of a superconducting qubit due to bias noise.** *Physical Review B*, **67**:094510, 2003. [41](#)

- [52] HANHEE PAIK, B.K. COOPER, S.K. DUTTA, R.M. LEWIS, R.C. RAMOS, T.A. PALOMAKI, A.J. PRZYBYSZ, A.J. DRAGT, J.R. ANDERSON, C.J. LOBB, AND F.C. WELLSTOOD. **Measurements of Decoherence in Three dc SQUID phase qubits.** *IEEE Transactions on Applied Superconductivity*, **17**:120, 2007. [41](#)
- [53] H.C. TORREY. **Transient Nutations in Nuclear Magnetic Resonance.** *Physical Review*, **76**:1059, 1949. [41](#)
- [54] MATTHIAS STEFFEN, JOHN M. MARTINIS, AND ISAAC L. CHUANG. **Accurate control of Josephson phase qubits.** *Physical Review B*, **68**:224518, 2003. [42](#)
- [55] ERIK LUCERO, M. HOFHEINZ, M. ANSMANN, RADOSLAW C. BIALCZAK, N. KATZ, MATTHEW NEELEY, A.D. O'CONNELL, H. WANG, A.N. CLELAND, AND JOHN M. MARTINIS. **High-Fidelity Gates in a Single Josephson Qubit.** *Physical Review Letters*, **100**:247001, 2008. [43](#), [52](#), [123](#)
- [56] T. YAMAMOTO, M. NEELEY, E. LUCERO, R.C. BIALCZAK, J. KELLY, M. LENANDER, MATTEO MARIANTONI, A.D. O'CONNELL, D. SANK, H. WANG, M. WEIDES, J. WENNER, Y. YIN, A.N. CLELAND, AND JOHN M. MARTINIS. **Quantum process tomography of two-qubit controlled-Z and controlled-NOT gates using superconducting phase qubits.** *Physical Review B*, **82**:184515, 2010. [44](#)
- [57] P.A.M. DIRAC. *The Principles of Quantum Mechanics*, **27** of *The International Series of Monographs on Physics*. Oxford University Press, 4th edition, 2001. [44](#)
- [58] MATTHIAS STEFFEN, M. ANSMANN, R. McDERMOTT, N. KATZ, RADOSLAW C. BIALCZAK, ERIK LUCERO, MATTHEW NEELEY, E.M. WEIG, A.N. CLELAND, AND JOHN M. MARTINIS. **State Tomography of Capacitively Shunted Phase Qubits with High Fidelity.** *Physical Review Letters*, **97**:050502, 2006. [47](#), [114](#)
- [59] R. McDERMOTT, R.W. SIMMONDS, MATTHIAS STEFFEN, K.B. COOPER, K. CIOK, K.D. OSBORN, SEONGSHIK OH, D.P. PAPPAS, AND JOHN M. MARTINIS. **Simultaneous State Measurement of Coupled Josephson Phase Qubits.** *Science*, **307**:1299, 2005. [50](#), [52](#)
- [60] ABRAHAM G. KOFMAN, QIN ZHANG, JOHN M. MARTINIS, AND ALEXANDER N. KOROTKOV. **Theoretical analysis of measurement crosstalk for coupled Josephson phase qubits.** *Physical Review B*, **75**:014524, 2007. [50](#)
- [61] FABIO ALTOMARE, KATARINA CIOK, MIKA A. SILLANPÄÄ, MICHAEL S. ALLMAN, ADAM J. SIROIS, DALE LI, JAE I. PARK, JOSHUA A. STRONG, JOHN D. TEUFEL, JED D. WHITTAKER, AND RAYMOND W. SIMMONDS. **Measurement crosstalk between two phase qubits coupled by a coplanar waveguide.** *Physical Review B*, **82**:094510, 2010. [50](#), [52](#), [128](#)
- [62] D.I. SCHUSTER, A. WALLRAFF, A. BLAIS, L. FRUNZIO, R.-S. HUANG, J. MAJER, S.M. GIRVIN, AND R.J. SCHOELKOPF. **ac Stark Shift and Dephasing of a Superconducting Qubit Strongly Coupled to a Cavity Field.** *Physical Review Letters*, **94**:123602, 2005. [52](#), [62](#)
- [63] K. B. COOPER, M. STEFFEN, R. McDERMOTT, R.W. SIMMONDS, S. OH, D. A. HITE, D. P. PAPPAS, AND J. M. MARTINIS. **Observation of quantum oscillations between a Josephson phase qubit and a microscopic resonator using fast readout.** *Physical Review Letters*, **93**(18):180401, October 2004. [52](#)

- [64] MATTHEW NEELEY, M. ANSMANN, RADOSLAW C. BIALCZAK, M. HOFHEINZ, N. KATZ, ERIK LUCERO, A. O'CONNELL, H. WANG, A.N. CLELAND, AND JOHN M. MARTINIS. **Transformed dissipation in superconducting quantum circuits.** *Physical Review B*, **77**:180508, 2008. [55](#)
- [65] LAFE SPIETZ, KENT IRWIN, AND JOSÉ AUMENTADO. **Input impedance and gain of a gigahertz amplifier using a dc superconducting quantum interference device in a quarter wave resonator.** *Applied Physics Letters*, **93**:082506, 2008. [61](#), [99](#)
- [66] LAFE SPIETZ, KENT IRWIN, AND JOSÉ AUMENTADO. **Superconducting quantum interference device amplifiers with over 27 GHz of gain-bandwidth product operated in the 4-8 GHz frequency range.** *Applied Physics Letters*, **95**:092505, 2009. [61](#), [99](#), [100](#)
- [67] LAFE SPIETZ, KENT IRWIN, MINHYEA LEE, AND JOSÉ AUMENTADO. **Noise performance of lumped element direct current superconducting quantum interference device amplifiers in the 4-8 GHz range.** *Applied Physics Letters*, **97**:142502, 2009. [61](#), [99](#)
- [68] J. A. CHERVENAK, K. D. IRWIN, E. N. GROSSMAN, JOHN M. MARTINIS, AND C. D. REINTSEMA. **Superconducting multiplexer for arrays of transition edge sensors.** *Applied Physics Letters*, **74**(26):4043, 1999. [61](#)
- [69] JONGSOO YOON, JOHN CLARKE, J. M. GILDEMEISTER, ADRIAN T. LEE, M. J. MYERS, P. L. RICHARDS, AND J. T. SKIDMORE. **Single superconducting quantum interference device multiplexer for arrays of low-temperature sensors.** *Applied Physics Letters*, **78**(3):371, 2001. [61](#)
- [70] J. A. B. MATES, G. C. HILTON, K. D. IRWIN, AND L. R. VALE. **Demonstration of a multiplexer of dissipationless superconduction quantum interference devices.** *Applied Physics Letters*, **92**:023514, 2008. [61](#)
- [71] A. FAY, E. HOSKINSON, F. LECOCQ, L. P. LÉVY, F.W. J. HEKKING, W. GUICHARD, AND O. BUISSON. **Strong Tunable Coupling between a Superconducting Charge and Phase Qubit.** *Physical Review Letters*, **100**:187003, May 2008. [61](#)
- [72] A. PALACIOS-LALOY, F. NGUYEN, F. MALLET, P. BERTET, D. VION, AND D. ESTEVE. **Tunable Resonators for Quantum Circuits.** *Journal of Low Temperature Physics*, **151**:1034, 2008. [61](#)
- [73] M. S. ALLMAN, F. ALTOMARE, J. D. WHITTAKER, K. CİCAK, D. LI, A. SIROIS, J. STRONG, J. D. TEUFEL, AND R. W. SIMMONDS. **rf-SQUID-Mediated Coherent Tunable Coupling between a Superconducting Phase Qubit and a Lumped-Element Resonator.** *Physical Review Letters*, **104**:177004, 2010. [61](#)
- [74] R. C. BIALCZAK, M. ANSMANN, M. HOFHEINZ, M. LENANDER, E. LUCERO, M. NEELEY, A. D. O'CONNELL, D. SANK, H. WANG, M. WEIDES, J. WENNER, T. YAMAMOTO, A. N. CLELAND, AND J. M. MARTINIS. **Fast Tunable Coupler for Superconducting Qubits.** *Physical Review Letters*, **106**:060501, 2011. [61](#)
- [75] R.W. SIMMONDS, M.S. ALLMAN, F. ALTOMARE, K. CİCAK, K.D. OSBORN, J.A. PARK, M. SILLANPÄÄ, A. SIROIS, J.A. STRONG, AND J.D. WHITTAKER. **Coherent interactions between phase qubits, cavities, and TLS defects.** *Quantum Information Processing*, **8**:117, 2009. [65](#)

- [76] K. GEERLINGS, S. SHANKAR, E. EDWARDS, L. FRUNZIO, R.J. SCHOELKOPF, AND M.H. DEVORET. **Improving the quality factor of microwave compact resonators by optimizing their geometrical parameters.** *Applied Physics Letters*, **100**:192601, 2012. 65, 145
- [77] KATARINA CICAČ, DALE LI, JOSHUA A. STRONG, MICHAEL S. ALLMAN, FABIO ALTOMARE, ADAM J. SIROIS, JED. D. WHITTAKER, JOHN D. TEUFEL, AND RAYMOND W. SIMMONDS. **Low-loss superconducting resonant circuits using vacuum-gap-based microwave components.** *Applied Physics Letters*, **96**:093502, 2010. 67
- [78] K.M. LANG, S. NAM, J. AUMENTADO, C. URBINA, AND JOHN M. MARTINIS. **Banishing Quasiparticles From Josephon-Junction Qubits: Why and How to do it.** *IEEE Transactions on Applied Superconductivity*, **13**:989, 2003. 79
- [79] D. VION, A. ASSIME, A. COTTET, P. JOYEZ, H. POTHIER, C. URBINA, D. ESTEVE, AND M.H. DEVORET. **Manipulating the Quantum State of an Electrical Circuit.** *Science*, **296**:886, 2002. 79
- [80] G.J. DOLAN. **Offset masks for lift-off photoprocessing.** *Applied Physics Letters*, **31**:337, 1977. 82
- [81] J. WENNER, M NEELEY, RADOSLAW C BIALCZAK, M LENANDER, ERIK LUCERO, A D O'CONNELL, D SANK, H WANG, M WEIDES, A N CLELAND, AND JOHN M MARTINIS. **Wirebond crosstalk and cavity modes in large chip mounts for superconducting qubits.** *Superconductor Science and Technology*, **24**:065001, 2011. 86
- [82] BLAKE ROBERT JOHNSON. *Controlling Photons in Superconducting Electrical Circuits.* PhD thesis, Yale University, 2011. 95
- [83] DAVID M. POZAR. *Microwave Engineering.* Wiley, 3rd edition, 2005. 96
- [84] PAUL J. PETERSAN AND STEVEN M. ANLANGE. **Measurement of resonant frequency and quality factor of microwave resonators: Comparison of methods.** *Journal of Applied Physics*, **84**:3392, 1998. 97
- [85] JIANSONG GAO. *The Physics of Superconducting Microwave Resonators.* PhD thesis, California Institute of Technology, 2008. 101
- [86] I. SIDDIQI, R. VIJAY, M. METCALFE, E. BOAKNIN, L. FRUNZIO, R. J. SCHOELKOPF, AND M. H. DEVORET. **Dispersive measurements of superconducting qubit coherence with a fast latching readout.** *Physical Review B*, **73**:054510, 2006. 147
- [87] A. LUPASCU, E. F. C. DRIESSEN, L. ROSCHIER, C. J. P. M. HARMANS, AND J. E. MOOIJ. **High-contrast dispersive readout of a superconducting flux qubit using a nonlinear resonator.** *Physical Review Letters*, **96**:127003, 2006. 147
- [88] FRANÇOIS MALLET, FLORIAN R. ONG, AGUSTIN PALACIOS-LALOY, FRANÇOIS NGUYEN, PATRICE BERTET, DENIS VION, AND DANIEL ESTEVE. **Single-shot qubit readout in circuit Quantum Electrodynamics.** *Nature Physics*, **5**:791, 2009. 147
- [89] M. D. REED, L. DICARLO, B. R. JOHNSON, L. SUN, D. I. SCHUSTER, L. FRUNZIO, AND R. J. SCHOELKOPF. **High-Fidelity Readout in Circuit Quantum Electrodynamics Using the Jaynes-Cummings Nonlinearity.** *Physical Review Letters*, **105**:173601, 2010. 147